



Universitat Autònoma de Barcelona

ADVERTIMENT. L'accés als continguts d'aquesta tesi doctoral i la seva utilització ha de respectar els drets de la persona autora. Pot ser utilitzada per a consulta o estudi personal, així com en activitats o materials d'investigació i docència en els termes establerts a l'art. 32 del Text Refós de la Llei de Propietat Intel·lectual (RDL 1/1996). Per altres utilitzacions es requereix l'autorització prèvia i expressa de la persona autora. En qualsevol cas, en la utilització dels seus continguts caldrà indicar de forma clara el nom i cognoms de la persona autora i el títol de la tesi doctoral. No s'autoritza la seva reproducció o altres formes d'explotació efectuades amb finalitats de lucre ni la seva comunicació pública des d'un lloc aliè al servei TDX. Tampoc s'autoritza la presentació del seu contingut en una finestra o marc aliè a TDX (framing). Aquesta reserva de drets afecta tant als continguts de la tesi com als seus resums i índexs.

ADVERTENCIA. El acceso a los contenidos de esta tesis doctoral y su utilización debe respetar los derechos de la persona autora. Puede ser utilizada para consulta o estudio personal, así como en actividades o materiales de investigación y docencia en los términos establecidos en el art. 32 del Texto Refundido de la Ley de Propiedad Intelectual (RDL 1/1996). Para otros usos se requiere la autorización previa y expresa de la persona autora. En cualquier caso, en la utilización de sus contenidos se deberá indicar de forma clara el nombre y apellidos de la persona autora y el título de la tesis doctoral. No se autoriza su reproducción u otras formas de explotación efectuadas con fines lucrativos ni su comunicación pública desde un sitio ajeno al servicio TDR. Tampoco se autoriza la presentación de su contenido en una ventana o marco ajeno a TDR (framing). Esta reserva de derechos afecta tanto al contenido de la tesis como a sus resúmenes e índices.

WARNING. The access to the contents of this doctoral thesis and its use must respect the rights of the author. It can be used for reference or private study, as well as research and learning activities or materials in the terms established by the 32nd article of the Spanish Consolidated Copyright Act (RDL 1/1996). Express and previous authorization of the author is required for any other uses. In any case, when using its content, full name of the author and title of the thesis must be clearly indicated. Reproduction or other forms of for profit use or public communication from outside TDX service is not allowed. Presentation of its content in a window or frame external to TDX (framing) is not authorized either. These rights affect both the content of the thesis and its abstracts and indexes.



Patricia González Callejo

2021

DOCTORAL THESIS

Pleiotropic activity of
Cancer Stem Cells
derived Extracellular Vesicles in cancer

Tutor: Simó Schwartz Navarro
Director: Joaquín Seras Franzoso

Department of Biochemistry
and molecular Biology



Pleiotropic activity of Cancer Stem Cells derived Extracellular Vesicles in cancer

Patricia González Callejo

PhD Thesis

Director: Joaquín Seras Franzoso PhD

Tutor: Simó Schwartz Navarro MD; PhD

Department of Biochemistry and Molecular Biology

Universidad Autònoma de Barcelona

Cibbim-Nanomedicine group

Vall d'Hebron Research Institut

Barcelona, 2021

A mis padres.

Porque cuando me giro, ellos.

Siempre ellos.

TABLE OF CONTENTS

TABLE OF CONTENTS	1
ABBREVIATIONS	7
CHAPTER I. Role of tumor Extracellular Vesicles on cancer cells plasticity and tumor microenvironment re-modeling in Triple Negative Breast Cancer	10
LIST OF FIGURES	11
LIST OF TABLES	13
ABSTRACT	14
GRAPHICAL ABSTRACT	15
INTRODUCTION	16
1 Breast Cancer	17
2 Breast Cancer Heterogeneity	17
2.1 Inter-tumor heterogeneity.....	18
2.2 Intra-tumor heterogeneity.....	19
3 Breast Cancer Stem Cells (BCSC)	22
3.1 Approaches to identify and isolate BCSC	22
3.2 Molecular pathways driving BCSC phenotypes.....	25
3.3 Biological features of BCSC.....	27
3.4 BCSC in TNBC.....	29
4 Cancer cell plasticity model.....	30
5 CSC and DCC dynamic equilibrium	30
6 Tumor Microenvironment (TME) and plasticity.....	32
6.1 Cellular components in TME guiding plasticity	33
6.2 Environmental factors driving plasticity.....	34
7 Extracellular vesicles (EVs)	36
7.1 EVs subtypes.....	36

8	The Role of EVs in Breast Cancer.....	40
8.1	Tumor EVs modulate the TME	40
8.2	Tumor EVs and drug resistance.....	41
8.3	Tumor EVs as drivers of breast cancer metastasis.....	42
	HYPOTHESIS AND OBJECTIVES	47
	MATERIALS AND METHODS	51
1	Cell lines and CSC model generation.....	52
1.1	Parental cell lines	52
1.2	Generation of human breast CSC models	53
1.3	Generation of breast syngenic CSC models	53
1.4	Genetically-modified cell lines	53
2	CSC and DCC characterization	54
2.1	Fluorescence-Activated Cell Sorting (FACS)	54
2.2	RNA Extraction and Quantitative Real Time-PCR (qPCR).....	54
2.3	2D Invasion Assay.....	55
2.4	3D Invasion assay	56
2.5	Mammosphere formation assay	56
2.6	<i>In Vivo</i> experimentation.....	56
3	Phenotypic equilibrium restoration assay	57
4	EVs ^{CSC} and EVs ^{DCC} isolation and characterization.....	57
4.1	Culture Optimization for <i>in vitro</i> pure MDA-MB-231 CSC and DCC maintenance..	57
4.2	EVs Purification	58
4.3	Morphometric assays.....	59
4.4	Stem Protein Array.....	59
4.5	Protein extraction and Western blotting (WB)	59
4.6	EVs Internalization assays	59
5	EVs and cancer cells plasticity studies.....	61
5.1	Effect of EVs ^{CSC} and EVs ^{DCC} on parental cells stem gene expression profile.....	61

5.2	Effect of EVs ^{CSC} on de-differentiation inhibition.....	61
5.3	Effect of EVs on invasion abilities of recipient parental cancer cells.....	61
5.4	Effect on <i>in vivo</i> plasticity of metastatic MDA-MB-231 cells.....	62
6	EVs effect on stromal cells studies.....	63
6.1	EVs effect on fibroblasts as plasticity mediators.....	63
6.2	Myofibroblasts activation studies.....	64
6.3	Tube formation assay.....	66
7	EVs role in pre-metastatic niche (PMN) conditioning studies.....	66
7.1	Biodistribution assay.....	66
7.2	Lung metastasis mice models.....	67
7.3	Immunohistochemistry.....	67
8	Cartoons.....	68
9	Statistical analysis.....	68
RESULTS.....		70
1	Development and validation of BCSC models.....	71
1.1	<i>ALDH1A1:tdTomato</i> reporter tags BCSC.....	71
2	Study of CSC/DCC plasticity.....	77
2.1	Isolated CSC and DCC subpopulations show phenotypic dynamic equilibrium.....	77
3	Role of CSC and DCC derived EVs on guiding plasticity.....	79
3.1	MDA-MB-231 <i>in vitro</i> model set up for CSC and DCC derived EVs isolation.....	79
3.2	MDA-MB-231 CSC-like state dictates EVs protein cargo.....	81
3.3	EVs ^{CSC} and EVs ^{DCC} control tumor cells plasticity towards CSC or DCC phenotypes.....	84
4	Role of EVs ^{CSC} and EVs ^{DCC} on stromal cells functional activation.....	89
4.1	EVs ^{DCC} stimulate fibroblasts cytokine secretory phenotype.....	89
4.2	EVs ^{CSC} increase breast and lung fibroblasts invasiveness.....	92
4.3	EVs ^{CSC} trigger α -SMA+ CAFs activation.....	93
4.4	EVs ^{CSC} trigger angiogenesis.....	95
5	Role of EVs on metastatic niche conditioning.....	96

5.1	EVs ^{CSC} boost the number of lung metastasis.....	96
5.2	EVs ^{CSC} increase the number of CAFs and trigger angiogenesis in the PMN	99
DISCUSSION		102
1	<i>ALDH1A1:tdTomato</i> reporter efficiently tags CSC-like populations in breast cancer...	104
2	CSC and DCC dynamic equilibrium	105
3	EVs dictate cancer cells plasticity.....	106
3.1	EVs ^{CSC} and EVs ^{DCC} present distinct functional cargo	106
3.2	EVs ^{CSC} and EVs ^{DCC} exerted a confronted regulation of DCC/CSC dynamic equilibrium 107	
4	Cancer EVs origin impact on stromal cells response.....	108
4.1	EVs ^{DCC} activate secretory CAFs	109
4.2	EVs ^{CSC} activate α -SMA+ CAFs	110
4.3	EVs ^{CSC} and EVs ^{DCC} dictate CAFs functional heterogeneity	110
4.4	EVs ^{CSC} trigger angiogenesis.....	111
5	EVs and metastatic niche conditioning	111
5.1	EVs ^{CSC} boost metastatic cells engraftment by remodeling resident stromal cells	111
5.2	EVs ^{DCC} create a CSC supportive metastatic niche.....	112
6	Overview and perspectives	113
CONCLUSIONS		116
BIBLIOGRAPHY		118
CHAPTER II Study of the interplay between Cancer Stem Cells derived Extracellular Vesicles and the Tumor Immune Microenvironment in Head and Neck Squamous Cell Carcinoma.....		145
LIST OF FIGURES.....		146
LIST OF TABLES.....		147
ABSTRACT.....		148

INTRODUCTION.....	149
1 Head and Neck Squamous Cell Carcinoma (HNSCC).....	150
2 HNSCC Cancer Stem Cells.....	151
2.1 Current approaches to isolate HNSCC CSC.....	151
2.2 CSC drive tumorigenesis, metastatic spread and drug resistance in HNSCC.....	153
3 The Tumor Immune Microenvironment in HNSCC.....	153
3.1 Components of HNSCC tumors immune microenvironment.....	154
4 The interaction between CSC and Immune cells.....	157
5 Extracellular Vesicles in the HNSCC TIME.....	157
HYPOTHESIS AND OBJECTIVES.....	159
MATERIALS AND METHODS.....	162
1 Lentiviral vectors (LV).....	163
2 Cell lines and culture conditions.....	166
2.1 Parental cell lines.....	166
2.2 Engineered cell lines.....	166
3 <i>In vitro</i> assays.....	167
3.1 LV copy number assay.....	167
3.2 Fluorescence-Activated Cell Sorting (FACS).....	168
3.3 Stem gene profile validation.....	168
3.4 Orosphere formation assay.....	169
4 Animal experimentation.....	169
5 Flow cytometry.....	169
6 Tumors Immunofluorescence imaging.....	173
7 Cartoons.....	173
8 Statistical analysis.....	173
RESULTS.....	174
1 Genetic labeling of CSC derived EVs.....	175
1.1 mEER EVs ^{CSC-GFP+} <i>in vitro</i> model validation.....	175

1.2	MOC2 EVs ^{CSC-GFP+} <i>in vitro</i> model validation.....	177
2	<i>In vivo</i> study of the EVs ^{CSC} - Immune Cells interplay.....	179
2.1	EVs ^{CSC} reporters reveal a specific high interaction rate between EVs ^{CSC} , MHC-II-Macrophages and PD-1+ T cells in the TIME.....	179
3	CSC and TAMs show spatial close localization in the TME.....	186
DISCUSSION.....		190
1	Genetic labeling of CSC derived EVs.....	191
2	Study of the <i>in vivo</i> interactions between CSC and immune cells via EVs.....	192
2.1	EVs ^{CSC} and Macrophages interplay.....	192
2.2	EVs ^{CSC} and PD-1+ T cells interplay.....	194
3	Overview and perspectives.....	194
CONCLUSIONS.....		196
BIBLIOGRAPHY.....		198
APPENDIX.....		207
	Article1.....	208
	Article2.....	248
	Article3.....	260
	Article4.....	271

ABBREVIATIONS

ABC: ATP-binding cassette	ECM: Extracellular matrix
ABs: Apoptotic bodies	ECs: Endothelial cells
ADCC: Antibody-dependent cellular cytotoxicity	EGF: Epidermal growth factor
ALDH: Aldehyde dehydrogenase	eGFP: Green fluorescent protein
APCs: Antigen-presenting cells	EGM: Endothelial growth medium
AS: After Sorting	EMT: Epithelial to mesenchymal transition
BAA: Bodipy-aminoacetate, Bodipy-aminoacetate	EPCs: Endothelial Progenitor Cells
BAAA: Bodipy-aminoacetaldehyde	ER: Estrogen-Receptor
BCA: Bicinchoninic acid assay	ERBB2/HER2: Human epidermal growth factor receptor 2
BCSC: Breast Cancer Stem Cells	ESCRT: Endosomal sorting complex required for transport
BL: Basal-like	ESEs: Early Stage Endosome
BLI: Bioluminescent imaging	EVs: Extracellular Vesicles
BMDC: Bone marrow-derived cells	EVs^{CSC}: CSC derived EVs
BSA: Bovine serum albumin	EVs^{DCC}: DCC derived EVs
BV: Blood vessels	FACs: Flow activated cell sorting
CAFs: Cancer Associated Fibroblasts	FBS: Fetal bovine serum
CE: Cell extracts	FC: Fold Change
CM: Conditioned media	FGFb: Basic fibroblast growth factor
CNRQ: Calibrated Normalized Relative Quantity	FLI: Fluorescent signal
CpC: copies per cell	GPI: Glycosylphosphatidyl-inositol
CryoTEM: Transmission electron cryomicroscopy	Hh: Hedgehog
CSC: Cancer Stem Cells, Cancer Stem Cells	HIFs: Hypoxia-inducible factors
CTCs: Circulating tumor cells	HNSCC: Head and neck squamous cell carcinoma
CXCR: C-X-C Motif Chemokine Receptor	HPV: Human papillomavirus
DCC: Differentiated cancer cells	
DLS: Dynamic light Scattering	

HR: Hormone Receptor

HR+: Hormone Receptor positive

HRP: Horseradish peroxidase

IDC: Invasive Ductal Breast Carcinoma

IFN: Interferon

IHC: Immunohistochemistry

IL: Interleukins

IL-6R: Interleukin 6 receptor

ILVs: Intraluminal vesicles

IM: Immunomodulatory

IMFP: Intramammary fat pat

ISEV: International Society for Extracellular Vesicles

ITG: Integrin

ITS: Insulin-Transferrin-Selenium

iv: Intravenously injected

JAK: Janus kinases

LA: Low-attachment

LSEs: Late Stage Endosomes

LAR: Luminal androgen receptor

lncRNA: Long non-coding RNA

LPETGG: SrtA substrate

LV: Lentiviral

M: Mesenchymal

M1 Mac: M1 macrophages

M2 Mac: M2 macrophages

MAPK: Mitogen-activated protein kinase

MDR: Multidrug efflux transporters

miRNAs: microRNAs

MMPs: Matrix metalloproteinases

MRD: Minimal residual disease

MS: Mean Score

MSCs: Mesenchymal stem cells

MSL: Mesenchymal stem-like

MVB: Multivesicular bodies

MVs: Microvesicles

Neu: Neutrophils

NFs: Normal Fibroblasts

NF- κ B: Nuclear Factor Kappa B

NGS: Normal goat serum

NK: Natural Killer

NKG2D: NK receptor G2

NRQ: Relative normalized quantities,
Relative normalized quantities

NTA: Nanoparticle Tracking Analysis

O₂: Oxygen

OCT: Optimal cutting temperature
compound

ON: Over night

OCCC: Oropharyngeal cell carcinomas

P1: Passage 1

P5: Passage 5

PBS: Phosphate buffered saline

PD-1: Programmed Cell Death 1

PFA: paraformaldehyde

PGK: Phosphoglycerate kinase

P-gp: P-glycoprotein

PI3K: Phosphatidylinositol-3-kinase

PMN: Pre-metastatic niche

PR: Progesterone-Receptor

PTX: Paclitaxel

qPCR: Quantitative polymerase chain
reaction

Res Mo: Resident monocytes

RT: Room temperature

SDF-1: Stroma-derived factor-1

SEM: Standard error of the mean

SFE: Sphere forming efficiency

siRNAs: small interference RNAs

SN: Supernatants

SOC: Standard of care

SP: Side population, Side population

SRE: SMAD Responsive Element

SrtA: Sortase A

STAT: signal transducer and activator of
transcription proteins

STORM: Stochastic Optical Reconstruction
Microscopy

TAMs: tumor associated macrophages,
Tumor-associated macrophages

TANs: Tumor associated neutrophils

TBS: Tris-buffered saline

tdTomato-: Negative tdTomato cells

tdTomato+: Positive tdTomato cells

TF: Transcription factor

TGF- β 1: Transforming Growth Factor β 1

Th: Helper T cell

TIC: Tumor-initiating cells

TILs: tumour-infiltrating lymphocytes

TIME: tumor immune microenvironment

TME: Tumor Microenvironment

TNBC: Triple-Negative Breast Cancer

TRAIL: TNF-related apoptosis-inducing
ligand

Tregs: Regulatory T cells

TSG101: Tumor susceptibility gene 101

UNS: Unspecified

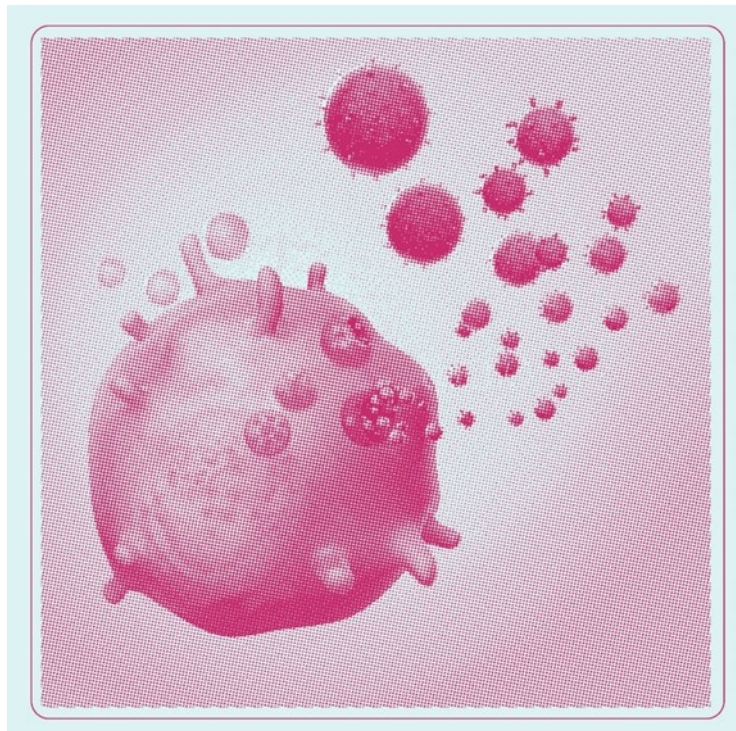
VEGF: Vascular endothelial growth factor

WB: Western Blotting

α -SMA: Alpha-smooth muscle actin

CHAPTER I.

Role of tumor Extracellular Vesicles on cancer cells plasticity and tumor microenvironment re-modeling in Triple Negative Breast Cancer



LIST OF FIGURES

Figure 1: Cancer mortality in women worldwide.	17
Figure 2: Breast cancer inter-tumor heterogeneity	19
Figure 3: Breast cancer intra-tumor heterogeneity.....	20
Figure 4: Intra-tumor heterogeneity determines patient’s prognosis.	20
Figure 5: CSC and clonal evolution models graphical representation.	22
Figure 6: Strategies for the identification and characterization of CSC.....	25
Figure 7: IL-6 and IL-8 signaling pathways in BCSC	27
Figure 8: Biological BCSC features.....	29
Figure 9: Phenotypic dynamic equilibrium between cancer cell subpopulations.	31
Figure 10: CSC plasticity is directed by both intrinsic and extrinsic factors.....	33
Figure 11: Molecular crosstalk between cancer cells and TME cell components fosters plasticity towards BCSC phenotypes..	35
Figure 12: Biogenesis and identity of EVs.	39
Figure 13: Tumor derived EVs foster tumor growth by remodeling surrounding cells in the TME towards pro-tumorigenic phenotypes.	42
Figure 14: Tumor derived-EVs create hospitable distant pre-metastatic niches suitable for metastatic cells engraftment.	46
Figure 15: Vector information for MPRRM42253-LvPM03.....	53
Figure 16: <i>ALDH1A1:tdTomato</i> CSC model <i>in vitro</i> validation.	72
Figure 17: CSC lead the invasive front together with CAFs.....	73
Figure 18: HCC1806 <i>ALDH1A1:tdTomato</i> CSC model <i>in vivo</i> validation.	74
Figure 19: NANOG protein expression in MDA-MB-231 lung metastases.....	75
Figure 20: 4T1 <i>ALDH1A1:tdTomato</i> CSC model <i>in vitro</i> validation..	76
Figure 21: CSC/DCC phenotypic equilibrium.....	78
Figure 22: CSC and DCC culture optimization for MDA-MB-231 EVs ^{CSC} and EVs ^{DCC} isolation	81
Figure 23: EVs ^{CSC} and EVs ^{DCC} characterization.....	83
Figure 24: EVs ^{CSC} and EVs ^{DCC} control tumor cells plasticity <i>in vitro</i>	85
Figure 25: EVs ^{CSC} and EVs ^{DCC} impacts tumor invasive abilities in 3D Matrigel models.....	86
Figure 26: <i>In vivo</i> effect of MDA-MB-231 EVs ^{CSC} and EVs ^{DCC} on the stemness nature of metastatic cancer cells.	87
Figure 27: Scheme summarizing EVs ^{CSC} and EVs ^{DCC} action in MDA-MB-231 cell line depending on the EVs producing cell state.	88

Chapter I

Figure 28. EVs ^{DCC} regulate cancer cells plasticity through stromal fibroblasts.	91
Figure 29. EVs ^{CSC} and EVs ^{DCC} <i>in vitro</i> role in fibroblasts 3D invasive potential.....	92
Figure 30. MDA-MB-231 EVs' effect on fibroblasts activation towards CAFs phenotype.	94
Figure 31 EVs ^{CSC} and EVs ^{DCC} <i>in vitro</i> role angiogenesis.....	95
Figure 32. EVs biodistribution	96
Figure 33. EVs ^{CSC} conditioning boosts lung metastasis <i>in vivo</i>	98
Figure 34. EVs ^{CSC} increase the incidence of CAFs and triggers angiogenesis in lungs.	100
Figure 35. EVs ^{CSC} and EVs ^{DCC} role in tumor maintenance and metastatic progression.....	114

LIST OF TABLES

Table 1. Traditionally used markers to identify BCSC	23
Table 2. Biological characteristics of different EVs subtypes.....	37
Table 3. List of the cell lines used in this study obtained from ATCC.	52
Table 4. Human stemness genes primer sequences.....	55
Table 5. Mice stemness genes primer sequences	55
Table 6. IL-6 and IL-8 primers sequences.....	63
Table 7. Primary Antibodies.....	69
Table 8. Breast cancer models features.....	79

Triple Negative Breast Cancer (TNBC) tumors usually show high grade of intratumor heterogeneity. Among tumor cell subpopulations, Cancer Stem Cells (CSC) emerge as critical cell population that play key roles in tumor initiation, progression, metastasis and tumor relapse after therapy. Indeed, cancer cell plasticity mediates the repopulation of CSC in tumors through de-differentiation processes of differentiated cancer cells (DCC) towards CSC phenotypes.

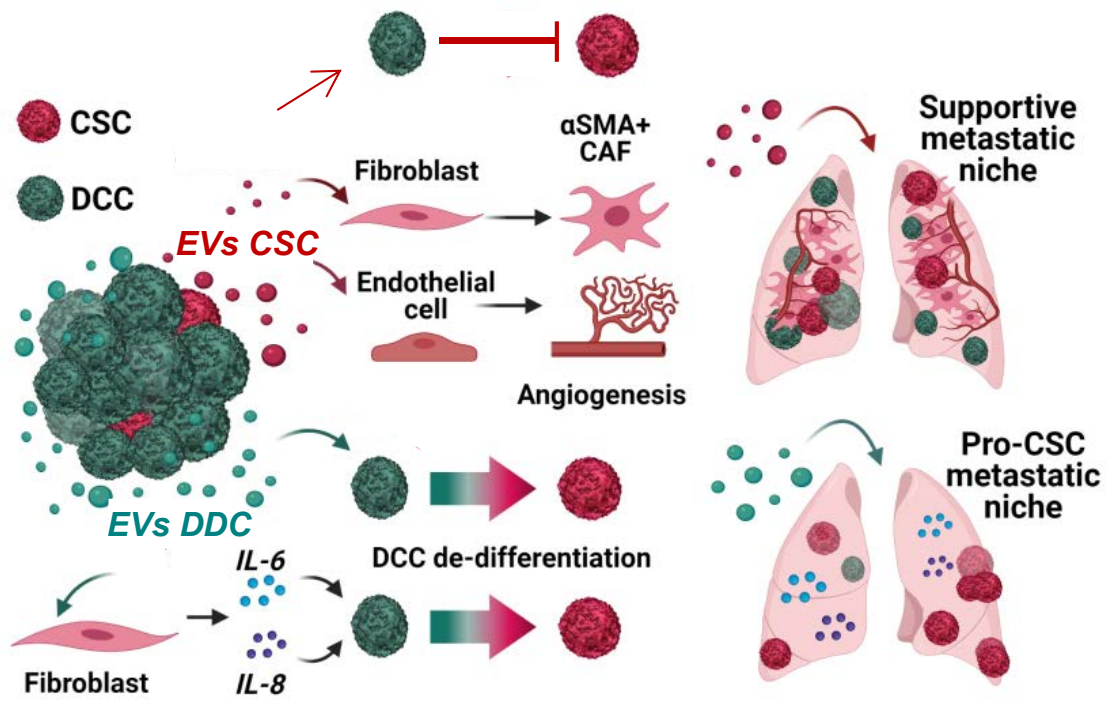
Extracellular Vesicles (EVs) released by tumor cells are known to play a relevant role in the inter-cellular communication and cancer disease. However, the particular contribution of EVs secreted by either CSC or DCC (EVs^{CSC} and EVs^{DCC}) to tumor progression remains elusive.

Here we isolated and characterized EVs^{CSC} and EVs^{DCC} subpopulations, released by TNBC models. Specifically, we showed that both tumor secreted EVs^{CSC} and EVs^{DCC} establish an exclusive communication crosstalk with CSC, DCC and stromal cells present in the tumor microenvironment. Remarkably, we exposed the unique role of tumor derived EVs^{CSC} and EVs^{DCC} in guiding cancer cells plasticity and in mediating distant activation of stromal cells at future metastatic sites. Furthermore, we addressed that TNBC derived EVs^{CSC} and EVs^{DCC} exerted opposite roles in directing tumor cell plasticity. While EVs^{CSC} promoted cancer cells differentiation towards DCC phenotypes, EVs^{DCC} induced tumor cells transitions towards CSC-like states. This plasticity regulation seems to be a mechanism to maintain tumor CSC/DCC dynamic equilibrium in tumors.

Interestingly, we demonstrated that EVs^{CSC} and EVs^{DCC} mediate cancer associated fibroblasts (CAFs) activation in two functional and unique ways. On one hand, EVs^{DCC} activated cytokine secretory CAFs phenotype, triggering IL-6/IL-8 signaling and sustaining CSC phenotype maintenance. On the other hand, EVs^{CSC} produced the *in vitro* and *in vivo* activation of myofibroblastic CAFs subpopulations displaying enhanced invasive potential. Moreover, EVs^{CSC} were able to remodel endothelial cells to promote angiogenesis.

Lastly, we show that exogenously administered EVs^{CSC} prompted the formation of receptive lung metastatic niches supporting macrometastasis growth whilst EVs^{DCC} induced the secretion of pro-stem signals in the niche.

GRAPHICAL ABSTRACT



INTRODUCTION

INTRODUCTION

1 BREAST CANCER

Breast cancer is the most prevalent cancer among women worldwide and the leading cause of cancer death in women. In 2018, nearly 2.1 million (11.6 %) new cases of breast cancer were diagnosed in women and about 627 thousand (6.6 %) of women died from this disease¹. Outcomes for breast cancer vary depending on the cancer type, the extent of disease, and the person's age. Although several advances have been made regarding breast cancer treatment in the last decades, these figures indicate that breast cancer is still in many cases an incurable disease with a devastating female mortality rate (**Figure 1**)²⁻⁴.

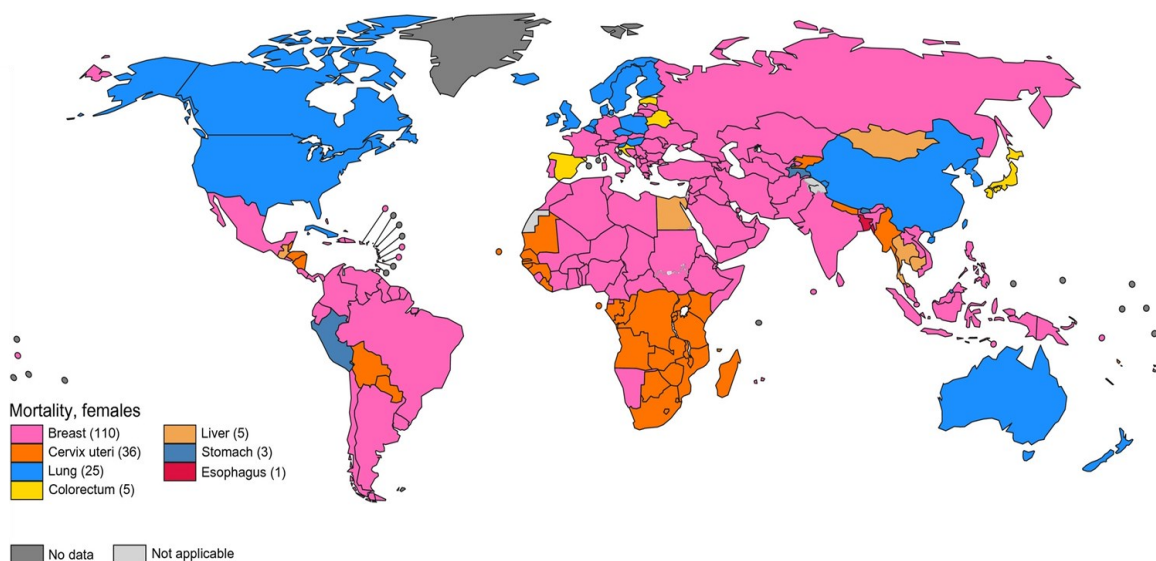


Figure 1: Cancer mortality in women worldwide. Obtained from Globocan, 2020¹.

2 BREAST CANCER HETEROGENEITY

Breast cancer is characterized as an heterogeneous disease. Molecular, phenotypic, and functional diversity among tumors from different patients (inter-tumor heterogeneity) and within a patient's tumor (intra-tumor heterogeneity) are features that complicate disease diagnosis and challenge therapy^{2,5-11}.

2.1 INTER-TUMOR HETEROGENEITY

Inter-tumor heterogeneity is observed in breast carcinomas from different individuals and among patients with discordant primary tumors and matched metastatic lesions. This heterogeneity is usually determined by the differences in tumors receptor status and by tumors molecular classification⁵⁻⁸ (**Figure 2**).

2.1.1 RECEPTOR STATUS AND MOLECULAR PROFILING OF TUMORS

Breast tumors often present differing histopathological features traditionally identified by immunohistochemistry (IHC)⁹. Among them, estrogen-receptor (ER), progesterone-receptor (PR) and/or human epidermal growth factor receptor 2 (ERBB2/HER2) receptor status represents established prognostic and predictive factors. The expression of these receptors in breast carcinomas is critical in guiding assessment for all breast cancers as it determines the suitability of using targeted treatments^{6,10,11}. Newer approaches categorize breast cancer tumors into several conceptual molecular subtypes that generally correspond to IHC receptor status¹². Tumors heterogeneity at molecular profiling by integrated genomic and transcriptomic analysis of tumors revealed at least six subgroups with distinct clinical outcomes: normal like, luminal A, luminal B, HER2 enriched, claudin low, and basal like¹³. These expression profiles usually reflect different clinical prognoses and responses to therapy^{6,13,14}.

2.1.2 CLINICAL MANAGEMENT OF HETEROGENEOUS TUMORS

The outcomes for patients diagnosed with hormone receptor positive (HR+) and/or HER2+ breast cancers improved with the development of targeted therapies. ER+ cancer cells, which depend on estrogen for their growth, are treated with drugs that reduce either the effect of estrogen (e.g. tamoxifen) or the actual level of estrogen (e.g. aromatase inhibitors)¹⁵. HER2+ tumors can be treated with antibodies directed against HER2 receptor and blocking its action (Trastuzumab)¹⁶. Patients treated with these targeted therapies generally have a better prognosis and an increased overall survival¹⁵⁻¹⁸. However, patients whose tumors do not express HR or HER2 usually lack of targeted therapies against their tumors and represent the group with the worst prognosis¹⁹.

2.1.3 TRIPLE-NEGATIVE BREAST CANCER

Basal-like breast cancer subtype, known as triple-negative breast cancer (TNBC), accounts for 15%–20% of all breast cancer cases and is considered to be the most aggressive breast cancer subtype. TNBC can be sub-divided into 6 subtypes: basal-like (BL1 and BL2), mesenchymal (M),

mesenchymal stem-like (MSL), immunomodulatory (IM), and luminal androgen receptor (LAR), as well as an unspecified group (UNS)²⁰. More than 50 % of patients diagnosed with TNBC at an early stage have a recurrence of the disease, and 37 % of these patients die within the first 5 years²¹. TNBC is characterized by reduced expression of ER and HER2 and consequently, hormone therapy and anti-HER2 drugs are not effective choices for this type of cancer. Thereby, chemotherapy still remains the standard of care (SOC) for TNBC, followed by surgery. However, response to treatment is usually short in duration and followed by rapid relapse¹⁹. Currently, there is no established molecular-based targeted therapy for TNBC. Such clinical unmet need makes TNBC one of the highest priorities of contemporary breast cancer research²².

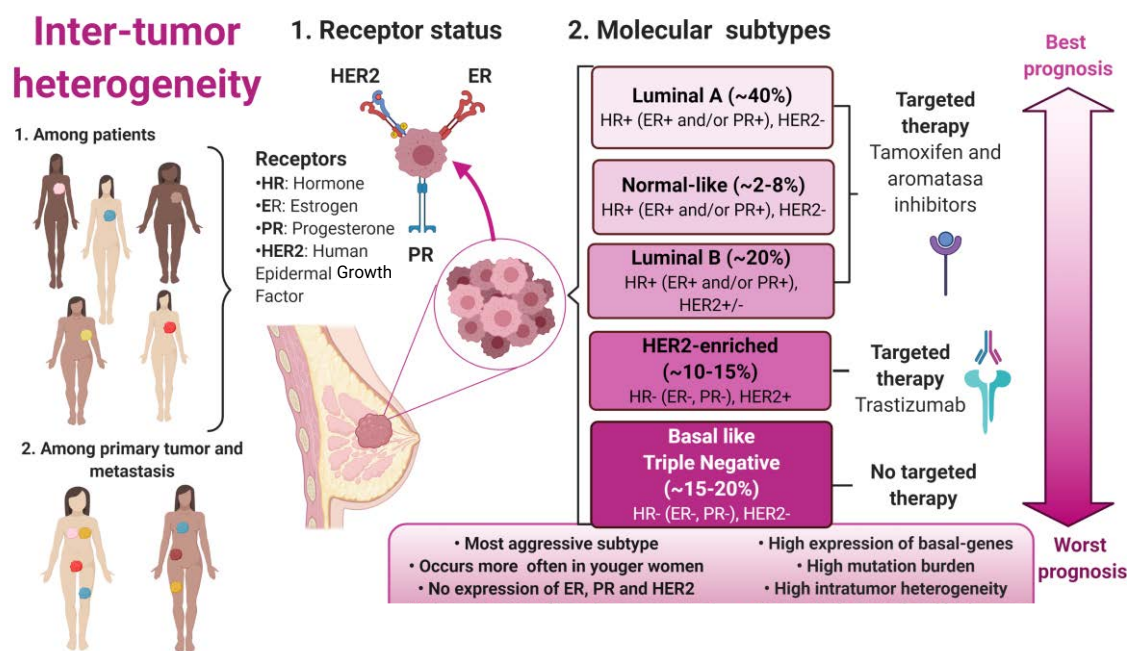


Figure 2. Breast cancer inter-tumor heterogeneity. Variation between breast tumors can be observed among different patients or between impairing primary and metastatic lesions. Breast tumors are usually classified depending on their **(A)** HR status and their **(B)** molecular subtype, being TNBC the group with worst prognosis^{6,8,19}.

2.2 INTRA-TUMOR HETEROGENEITY

TNBC tumors frequently show significant intratumor heterogeneity consisting on the presence of distinct cell populations within a patient's individual tumor^{8,23,24}. These heterogeneous cell populations present differing phenotypes with unique functions and characteristics, including tumorigenicity, resistance to treatment and metastatic potential^{5,7} (**Figure 3**).

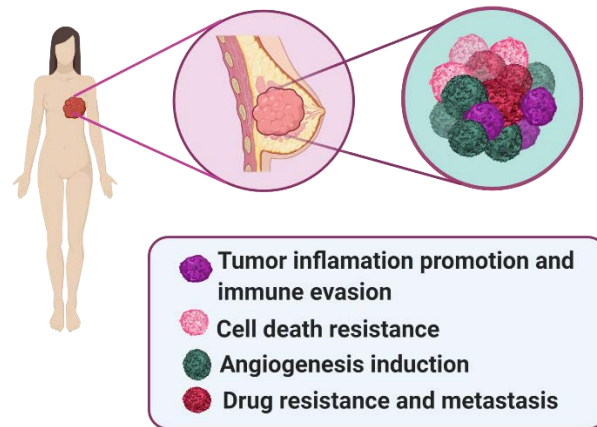


Figure 3. Intra-tumor heterogeneity.

This intratumor heterogeneity seems to reflect the tumor's ability to adapt to new microenvironmental conditions e.g. hypoxia or chemotherapeutic treatment^{25–27}. Note that cancer cells are continuously under selective pressure due to attacks by the immune system or administered therapies^{25,26,28}. Intra-tumoral heterogeneity arises through complex genetic, epigenetic, and protein modifications that drive phenotypic selection to specific subclones, conferring them competitive advantages to survive²⁹ (**Figure 4**). Importantly, understanding the molecular basis of TNBC heterogeneity is crucial for the development of precision therapy to specifically attack the different cellular subtypes present in TNBC tumors, which can easily adapt to the unfavorable microenvironment after therapy^{19,30,31}.

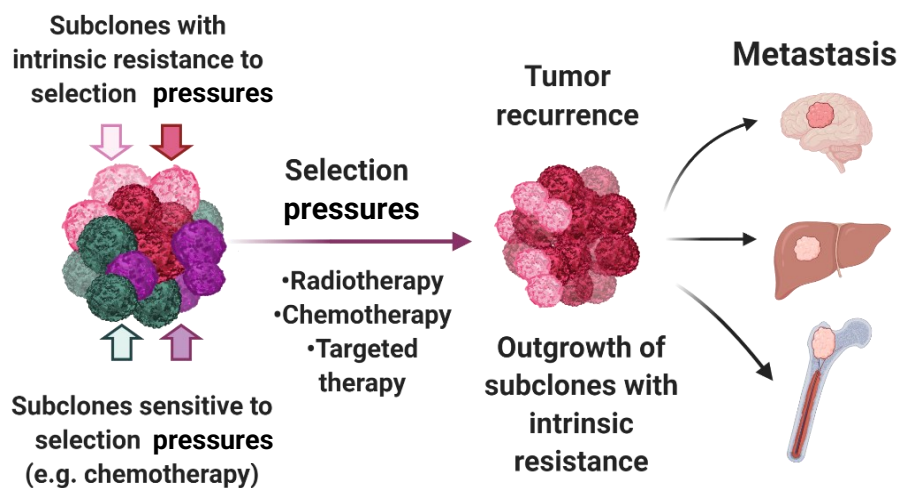


Figure 4. Intra-tumor heterogeneity determines patient's prognosis. Different tumor cell subtypes can have intrinsic resistance to therapeutic treatment and give rise to tumor recurrence and metastasis after treatment. Based on^{5,25}.

The development of intra-tumoral cell diversity has been widely attributed to two processes: the clonal evolution and the Cancer Stem Cell (CSC) models^{32–34} (**Figure 4**).

2.2.1 THE CLONAL EVOLUTION MODEL

The clonal evolution model, also referred to as the stochastic model, was first proposed in 1976 by Peter Nowell, who postulated that tumor development is a Darwinian process driven by the accumulation of spontaneous (epi-) genetic mutations followed by successive selection of specific clones³⁵. This model states that the intrinsic differences observed between tumor cancer cells are based on differing genetic and epigenetic programs as well as on the influence of the tumor microenvironment (TME). Those genetic and epigenetic changes occur over time in cancer cells, and if such changes confer a selective advantage, the fitter clones are selected and contribute to the diversity of the whole tumor cell populations³⁶. Accordingly, all the cells in the tumor will have similar tumorigenicity potential^{34–38}.

2.2.2 THE CANCER STEM CELL MODEL

The CSC model proposes that tumors may be hierarchically organized in the same manner as normal tissues³⁹. During normal development, the change from stem cell to lineage-committed cell is a multiphase gradual process that causes stem cells to progressively lose developmental potential until they reach their final differentiated state⁴⁰. Similarly, tumors would be organized in a hierarchical style, with a rare multipotent and tumorigenic subset of cancer cells (termed CSCs) situated at the top of the hierarchy, and transient, differentiated cancer cells (DCC) forming the bulk of the tumor^{34,39,41}. Consequently, CSCs with high renewal potential would undergo genetic modifications forming phenotypically diverse DCC that would progressively lose the tumorigenic capacity. Thus, the small fraction of CSC subpopulation will be the one driving tumor initiation, progression, metastatic and therapeutic resistance of the entire tumor^{34,42}. Under this rationale, in order to eliminate tumors, it would be imperative to focus on CSC.

The concept of CSCs revealed the possible cellular origin, tumor heterogeneity, maintenance, and progression of breast cancer⁴³. Especially, the CSC theory provided a new insight into the management of TNBC since the heterogeneity, aggressive progression and recurrence of TNBC tumors have been attributed to the presence of breast cancer stem cells (BCSCs) within TNBC tumors³⁰.

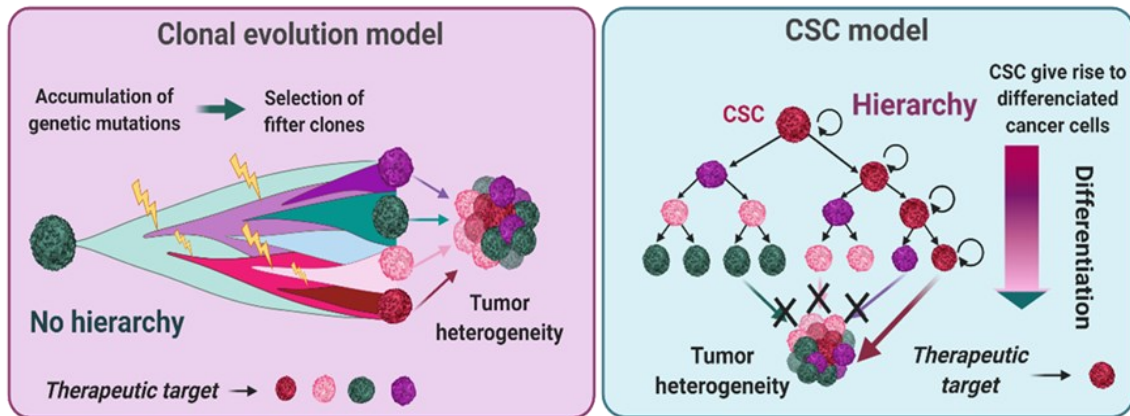


Figure 5. Schematic representation of CSC and clonal evolution models ^{33,34,37}.

3 BREAST CANCER STEM CELLS (BCSC)

BCSCs represent a limited group of tumor-initiating cells (TIC) which possess properties of self-renewal and differentiation potential capable of recapitulating intra-tumoral cell heterogeneity of breast tumors. BCSC are important drivers of tumor initiation, progression and metastasis⁴³⁻⁴⁵. Clinically, BCSCs are considered to be responsible for the development of resistance to treatment and cancer relapse⁴⁵⁻⁴⁷.

3.1 APPROACHES TO IDENTIFY AND ISOLATE BCSC

Development of BCSC-specific biomarkers together with BCSC isolation strategies has facilitated the identification, validation and functional study of BCSC in breast cancer in vitro models and xenografts, as well as in patients^{48,49}.

3.1.1 APPROACHES BASED ON MOLECULAR MARKERS EXPRESSION

Tumorigenic potential is regarded as the ability of cancer cells to form tumors in xenografts and re-establish tumor heterogeneity and it has been the gold standard to identify CSC populations in heterogeneous cancer cell lines and tumors^{50,51}. To assess the tumorigenicity of a specific cell population, tumor cancer cells need to be isolated, usually by Flow Activated Cell Sorting (FACs), based on the expression of specific markers⁵². These cells are then xenotransplanted into mice and the tumorigenicity potential and their biological features can be further examined⁵³. Following this strategy, BCSC were first discovered in 2003 when Al-Hajj et al., identified that the cell fraction with the CD44+/CD24- phenotype in breast cancer patient tissues could recapitulate tumor burden in mice⁵⁴. Later, Ginestier et al. discovered that a subpopulation of cells that displayed high aldehyde dehydrogenase (ALDH) activity also referred high tumorigenic potential⁵⁵.

Since then, the CD44⁺/CD24^{-/lo} phenotype and high ALDH activity have become the reference signature for BCSC isolation and this phenotype is the most commonly used method to isolate CSCs from heterogeneous breast tumor cell populations^{56,57}. Characteristics of these markers are detailed in **Table 1**.

Marker	Authors	Marker description
CD44 ⁺ /CD24 ^{-/lo}	Al-Hajj et al. ⁵⁴	<p>CD44: a family of non-kinase, single span transmembrane glycoproteins expressed on embryonic stem cells and in various levels on other cell types including connective tissues and bone marrow. CD44 expression is also upregulated in subpopulations of cancer cells and is recognized as a molecular marker for cancer stem cells (CSC)⁵⁸.</p> <p>CD24: a small mucin-like glycosylphosphatidylinositol (GPI)-linked cell surface protein that localizes in lipid rafts. Regulates expression of the stem cell controller Nanog⁵⁹.</p>
ALDH1 ⁺	Ginestier et al. ⁵⁵	<p>ALDH1: aldehyde dehydrogenase 1, a detoxifying enzyme for the oxidation of intracellular aldehydes, functions in early differentiation of stem cells through its role in oxidizing retinol to retinoic acid^{55,60}.</p>

Table 1. Traditional markers for BCSC identification, tagged from breast cancer cell lines and patient-derived tumors. Adapted from ⁴⁴.

3.1.2 APPROACHES BASED ON FUNCTIONAL ASSAYS

CSCs refer multiple intrinsic and functional features that are applied to develop efficient CSCs isolation and identification strategies^{48,49}.

3.1.2.1 ALDH ACTIVITY

ALDHs are a group of cytosolic isoenzymes that are involved in oxidizing intracellular aldehyde⁶¹. Among all those isoenzymes, ALDH1 isoform function consists in catalyzing the conversion of retinol to retinoic acid in normal and malignant stem cells^{55,60}. High cytosolic ALDH1 activity has

been widely reported in BCSC as well as in CSC of different types of solid tumors⁶⁰. This enzyme is involved in the regulation of proliferation and differentiation of CSC, induces activity of Wnt/ β -catenin by stimulating the Akt signaling pathway and its activity is also associated with CD44 expression⁶². Furthermore, resistance to chemotherapy results in ALDH1 overexpression⁶³.

The Aldefluor assay can identify and isolate cells with high ALDH activities⁵⁵. This assay is based on the principle that ALDH can convert the ALDH-substrate, Bodipy-aminoacetaldehyde (BAAA) into Bodipy-aminoacetate (BAA), which is retained inside viable cells. Cells with high levels of ALDH become brightly fluorescent and are identified by flow cytometry. Those cells display increased sphere formation capability, self-renewal properties, tumorigenicity and high expression of stemness genes compared to ALDH1-negative cells⁶⁴.

3.1.2.2 MAMMOSPHERE FORMATION ASSAY

BCSCs are resistant to anoikis, a programmed cell death that occurs in anchorage-dependent cells⁶⁵, so when BCSCs are stimulated to proliferate in low adherence tissue culture dishes they give rise to spheroids which are commonly defined as “mammospheres”⁶⁶. Cells forming those mammospheres in low attachment (LA) conditions exhibit activation of stem cell related signaling pathways⁶⁷⁻⁶⁹. Furthermore, the formation rate of mammospheres correlates with the tumorigenicity of the parental cancer cell line in xenografts⁶⁷. Thus, mammosphere formation assays can be used to calculate sphere forming efficiency (%SFE) of BCSCs derived from both primary tissue and breast cancer cell lines⁷⁰.

3.1.2.3 COLONY FORMATION ASSAY

Colony formation assay is a commonly used method for identification of CSCs by the evaluation of how adherent cells grow in a two-dimensional culture⁷¹. It consists in an *in vitro* quantitative technique to evaluate the capacity of a single cell plated in soft-agar to self-renew into the colony of 50 or more cells through clonal expansion⁷². Colonies derived from CSCs frequently display bigger size and higher numbers than the colonies derived from DCC⁷¹.

3.1.2.4 SIDE POPULATION (SP) ASSAY

CSC present high expression of ATP-binding cassette (ABC) and multidrug efflux transporters (MDR) that are usually located within their cell membrane, resulting a crucial protective mechanism against cytotoxic substances⁷³. Consequently, this method uses the capacity of cells to efflux DNA-binding dyes, including Hoechst 33342 or Rhodamine 123, via those transporters to isolate CSC⁷⁴. Hoechst or Rhodamine-treated cancer cells can be analyzed by flow cytometry. The side population (SP) corresponds to a small (typically <2%) fraction of cells that represent

the double-negative group. Cells within SP population present the highest dye efflux and least amount of dye and usually refer tumorigenicity, multipotency and chemoresistance⁷⁵.

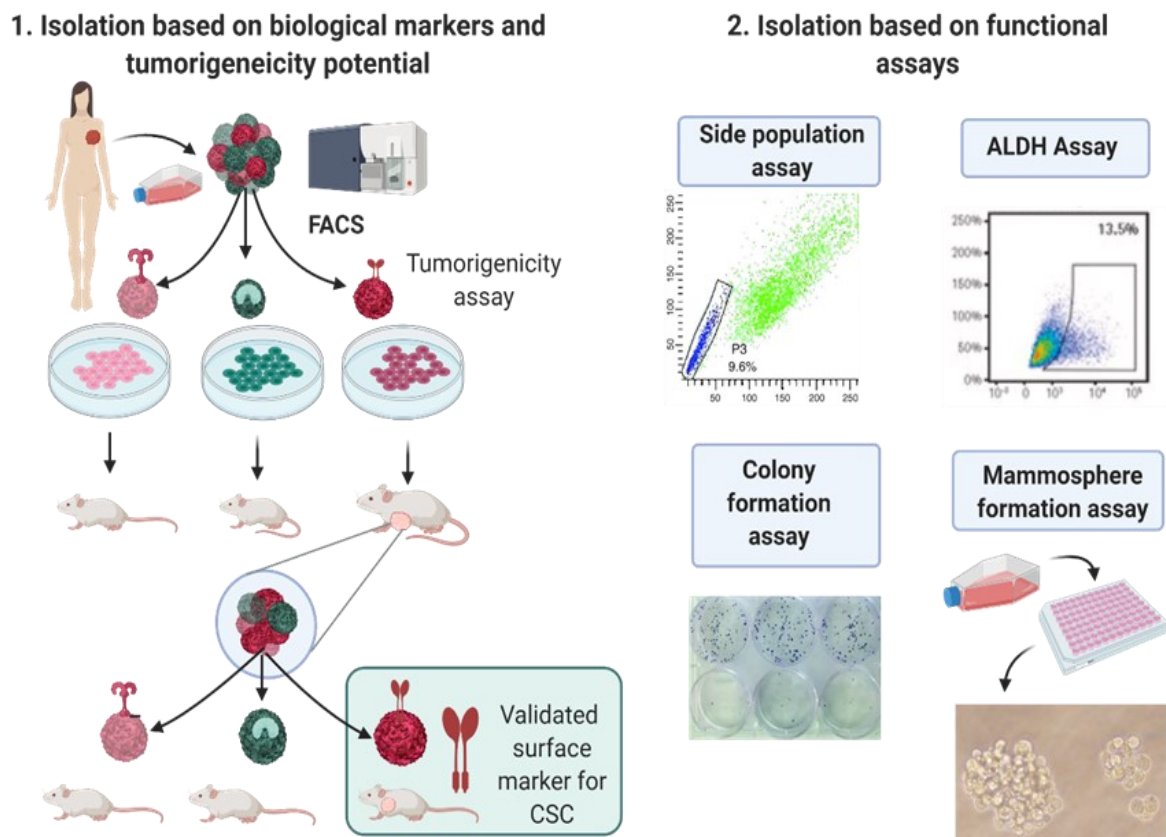


Figure 6. Strategies for the identification, isolation and characterization of CSC. The most common used approaches are based on the identification of CSC based on biological surface markers followed by tumorigenicity assays **(1)** or on functional assays based on CSC intrinsic properties **(2)**⁴⁹.

3.2 MOLECULAR PATHWAYS DRIVING BCSC PHENOTYPES

The best characterized signaling pathways controlling self-renewal and differentiation in normal stem cells are frequently aberrantly regulated in BCSCs, which leads to the acquisition of the stem-cell phenotype⁷⁶.

- **Notch** signaling is a complex and highly conserved pathway involved in embryogenesis, cell fate determination, proliferation and maintenance of stem cells. Notch signaling via Notch4 is crucial for normal mammary gland development⁷⁷. Aberrant Notch4 signaling is involved in tumor formation through deregulated mammary gland stem cell self-renewal⁷⁸. Notch4 expression is an indicator of poor prognosis in breast cancer, correlating with BCSC markers and shorter disease-free survival^{79–82}.

- **The Hedgehog (Hh)** family regulates many embryonic signaling processes to control cellular proliferation, fate determination, and patterning and is frequently deregulated in cancer⁸³. The Hh signaling pathway is required for the maintenance and self-renewal of BCSC⁸⁴, becoming activated in most TNBC and positively correlates with aggressive tumors⁸⁵.
- **Wnt family** of proteins operate a complex signaling pathway fundamental in regulation of proliferation, cell fate determination and cellular migration⁸⁶. Wnt proteins represent key players in CSC in mammary tumorigenesis⁸⁷. High levels of Wnt/ β -catenin signaling in BCSC result in more tumorigenic potential⁸⁸⁻⁹⁰ and its activation is widely associated with TNBC metastasis⁹¹⁻⁹³.
- **Pluripotency Transcription Factors (TF)** that play key roles in maintaining the self-renewal capacity and pluripotency of embryonic stem cells are also widely described biomarkers for BCSC. Similarly, BCSC phenotype is characterized by the expression of pluripotency-associated OCT-4, KLF4, SOX-2 and NANOG TFs. These TF play key roles in maintaining the self-renewal capacity and pluripotency of BCSC⁹⁴⁻⁹⁷.
- **The Nuclear Factor Kappa B (NF- κ B)** refers to a family of TF that control the expression of many genes related to immune responses, survival, proliferation, angiogenesis, and metastasis^{98,99}. BCSC overexpress NF- κ B signaling pathway components and induce constitutive NF- κ B activation and proliferation in the tumor^{100,101}. Moreover, NF- κ B pathways also regulate the gene expression of pro-stemness interleukins (IL) IL-6 and IL-8 cytokines in TNBC, creating a paracrine loop essential for BCSC maintenance^{102, 103}.

Cytokines such as IL-6 and IL-8 and their signaling pathways have been demonstrated to have important roles in BCSC maintenance, function and resistance to therapy¹⁰⁴⁻¹⁰⁸.

- **IL-6** is a pro-inflammatory small glycopeptide that is secreted by a wide variety of cells including lymphocytes and monocytes, endothelial cells (EC), fibroblasts, keratinocytes and adipocytes¹⁰⁹. Several tumor cells, including breast cancer tumors, also generate this cytokine¹¹⁰. Interaction of IL-6 with its receptor IL-6R leads to the activation of STAT3¹¹¹. The IL-6/JAK/STAT3 pathway modulates the expression of several genes involved in the maintenance of BCSC^{112,113}.
- **IL-8** is a pro-inflammatory chemokine that is physiologically produced by monocytes, EC and various epithelial cells and fibroblasts¹¹⁴. Tumor cells also secrete IL-8 and higher circulating IL-8 levels seem to correlate with higher stage, grade and

tumor burden¹¹⁵. IL-8 regulates the breast CSC activity through its receptors C-X-C Motif Chemokine Receptor (CXCR1 and CXCR2) activating different signaling cascades such as the activation of phosphatidylinositol-3-kinase (PI3K) and mitogen-activated protein kinase (MAPK) that leads to NF- κ B activation¹¹⁶.

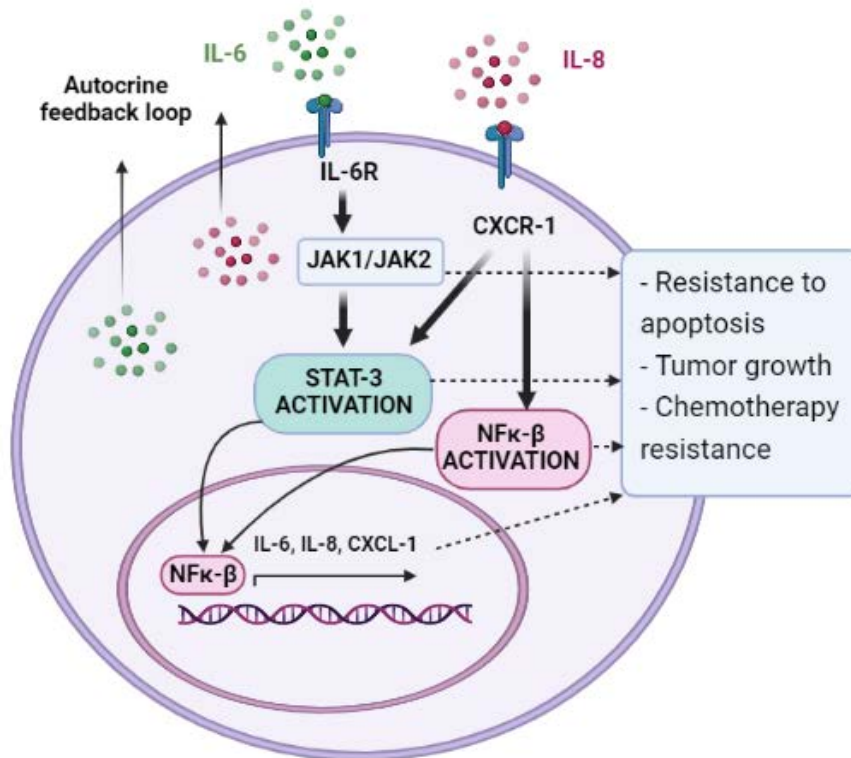


Figure 7. IL-6 and IL-8 signaling pathways in BCSC. Based on¹⁰².

3.3 BIOLOGICAL FEATURES OF BCSC

3.3.1 BCSC AND ANGIOGENESIS

Tumor vascularization is essential for supplying nutrients and O₂ to support dynamically growing tumor and thus, the formation of a vascular network is extremely important for tumor growth and metastasis¹¹⁷. Angiogenesis refers to endotheliosis and the formation of new blood vessels at or around tumor sites using the original blood vessels as a template¹¹⁸. In this regard, BCSCs actively promote angiogenesis by secreting various proangiogenic factors like the stroma-derived factor-1 (SDF-1) and the vascular endothelial growth factor (VEGF)¹¹⁹⁻¹²¹.

3.3.2 BCSC AND HYPOXIA

The lack of O₂ (hypoxia) is a common scenario in growing tumors and hypoxia-sensing pathways play a significant role in the maintenance of the BCSC phenotype that allow these cells to survive

in this stressful condition¹²². Reduced oxygen availability leads to increased production of reactive oxygen species (ROS), which activates hypoxia-inducible factors (HIFs)¹²³. Upon exposure to hypoxia, the HIF α subunits accumulate in the nucleus of cancer cells and bind to target genes that participate in the proliferation, apoptosis, metabolism and invasion, as well in the resistance of cancer cells to therapy¹²⁴. Thereby, increasing evidence indicates that HIFs regulate the sub-populations of BCSCs^{123,125–128}.

3.3.3 BCSC AND DRUG RESISTANCE

BCSC also exhibit multiple drug resistance mechanisms¹²⁹. BCSCs chemotherapy evasion is possibly due to the presence of ABC transporters in their membranes⁷³. Increased levels of ABCG2 in BCSCs enables the expulsion of antitumor cytotoxic drugs¹³⁰. ALDH1A1 and ALDH3A1 are also important in the protection and the differentiation of BCSC as ALDH1 has the ability of metabolizing toxic chemotherapeutic agents into nontoxic molecules⁶³. Alteration of cell cycle kinetics is another alternative intrinsic mechanism of drug resistance reported in BCSC, as BCSC can enter in a quiescent state. This feature enables BCSC to evade death due to chemotherapeutic agents targeting rapidly dividing cells^{131,132}. In this regard, following conventional chemotherapy, it is thought that resistant and surviving BCSCs and stromal cells constitute the minimal residual disease (MRD)^{133–135}. These resistant BCSCs can expand and undergo multilineage differentiation repopulating the heterogeneous tumor and being responsible for relapsed disease after long-time periods¹³⁶.

3.3.4 BCSC, EMT AND METASTASIS

Metastasis, re-location of tumor cells from the original to a secondary site, involves cancer cells loss of adhesion, phenotypic alteration, migration, and invasion^{137–140}. In this scenario, epithelial to mesenchymal transition (EMT) represents an essential phenomenon for initiating metastasis as the transition to a mesenchymal phenotype bestows cells with migratory and invasive capabilities^{141–144}. EMT is induced by activation of EMT transcription factors (EMT-TFs), such as TWIST, ZEB1, SNAIL and SLUG. The major function of EMT-TFs is to downregulate genes involved in cell adhesion, such as E-cadherin, and to upregulate those responsible for migration and invasion^{145,146}. The majority of circulating tumor cells (CTCs) in invasive ductal breast cancer display mesenchymal characteristics, suggesting that primarily cancer cells with mesenchymal phenotype enter the blood stream and disseminate to remote organs¹⁴⁷. Importantly, EMT contributes to the acquisition of stem-like features^{147–149}, as EMT activates BCSC typical stemness signaling pathways¹⁵⁰. Indeed, high expression levels of BCSC markers have been found in CTCs^{151–153}. For

example, the CD44⁺/CD24^{-/low} phenotype has been reported among cancer cells spread into the bone marrow or the lung of patients with breast cancer^{154,155}.

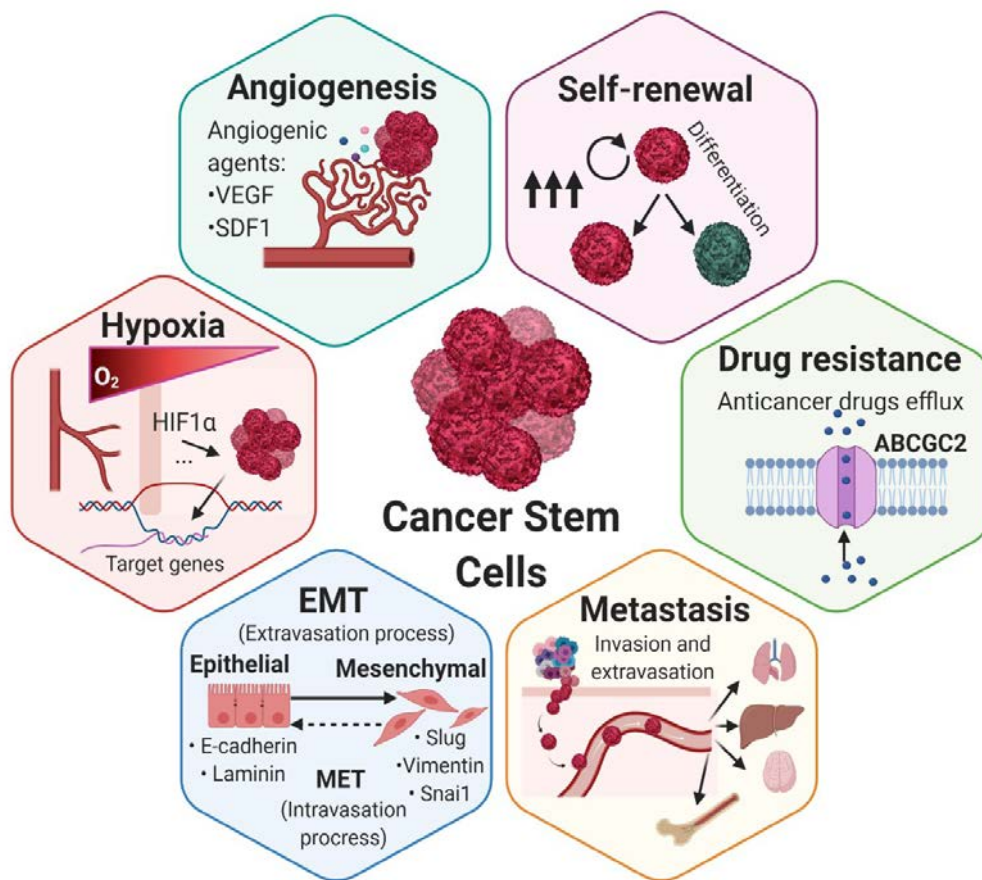


Figure 8. Biological CSC features in breast cancer.

3.4 BCSC IN TNBC

Histopathological analyses of breast cancer patients revealed TNBC tumors are enriched in ALDH1 activity and CD44⁺/CD24⁻ expression signatures^{156–158}. Furthermore, TNBC cell lines have been reported to form mammospheres at a higher degree than non-TNBC cells, exhibiting high % SFE¹⁵⁹. At the transcriptional level, pluripotency-related TFs SOX2, MYC, OCT-4 and NANOG have been shown overexpressed in TNBC and displayed a positive correlation with poor prognosis. From this data it has been hypothesized that TNBC presents an enrichment in CSC¹⁶⁰.

4 CANCER CELL PLASTICITY MODEL

Gathering such a number of tumor malignancy enhancing features, to be able to target BCSCs would be very prospective in order to develop an effective anti-TNBC treatment^{20,136,161}. However, CSC hierarchies are much more plastic than previously believed^{162,163}.

Cellular plasticity is defined as the ability of adult tissue cells to undergo a differentiation or dedifferentiation process to adopt new phenotypic and functional identities⁴⁰. The concept of cancer cell plasticity has added additional complexity to the CSC and clonal evolution models, combining elements of both and adding complexity to explain intra-tumor heterogeneity¹⁶⁴. In agreement with the CSC model, it proposes that tumor heterogeneity is the result of hierarchical organization of phenotypic cell states. However, in contrast to the CSC model, it proposes that DCC may “dedifferentiate” back into CSC, a process denoted as bidirectional interconversion³². Nowadays, the models to explain tumor heterogeneity have evolved taking in account cancer cells plasticity model^{165,166} as multiple studies have addressed that not all cancers follow the unidirectional model of CSC hierarchy, both in breast cancer and many other cancer types^{167–170}.

Emerging evidence has shown that DCC could be reprogrammed and transform into CSC-like cells, which indicates that both CSCs and DCC show plasticity between both cell states¹⁶⁹. For example, an study showed that when environmental stimuli were altered, stem cell–, basal–, and luminal-like phenotypes were equally tumorigenic, and each tumor cell subpopulation could efficiently generate xenografts¹⁶⁸. This demonstrated that the luminal and basal fractions generated functional stem-like cells *in vivo* supporting cell-state interconversion, reinforcing the idea of transitions from DCC to CSCs¹⁶⁶. Further studies demonstrated that while existing CSCs disappeared, new CSCs were formed from DCC during mammary tumor development¹⁶². Similarly, studies with colon cancer cell lines demonstrated that colon DCC restored the LGR5+ CSC pool *in vivo*, providing accurate signs of plasticity^{171,172}. Therefore, stemness should be considered as a cell state that can be reversibly gained or lost through cell plasticity¹⁷³.

5 CSC AND DCC DYNAMIC EQUILIBRIUM

As the proper development of multicellular organisms depends on the balanced equilibrium between cells with stem-like features and differentiated cells committed to tissue lineages, CSCs and their more differentiated progeny (DCC) also seem to co-exist in a dynamic equilibrium state. This notion was first exemplified by Gupta et al., who studied cell populations displaying

stem cell-, basal-, or luminal-like phenotypes from breast cancer cell lines. After isolating and separately culturing those subpopulations, their studies revealed that all three subpopulations were able to generate cells of the other two phenotypes restoring the initial phenotypic proportions of the parental cancer cell line¹⁷⁴. Later, mathematical studies in this area provided an explanation for these phenomena and stated that phenotypic proportions of cancer cells will tend to constants regardless of their initial population states¹⁷⁵. Besides, parallel work performed with colon cell lines demonstrated that, as with breast tumor models, the conversion of DCC into CSCs is necessary for the transient dynamic regulation of cell population structure¹⁷⁶.

These reports not only showed that CSCs can differentiate to more committed cancer cells (DCC), but also that DCC can also acquire stemness traits, which results in a dynamic relationship between the two populations: CSCs and DCC are capable of undergoing phenotypic transitions in response to appropriate stimuli.

In an attempt to clarify how stochastic transitions are directed, Olmeda and collaborators recently postulated that cancer cells plasticity towards CSC phenotypes is directed by an unknown molecular activator of tumor cells dedifferentiation. According to their model, this activator would be triggered when the CSC population density in tumors approached to 0. However, the biological nature of the activator remains unknown¹⁷⁷.

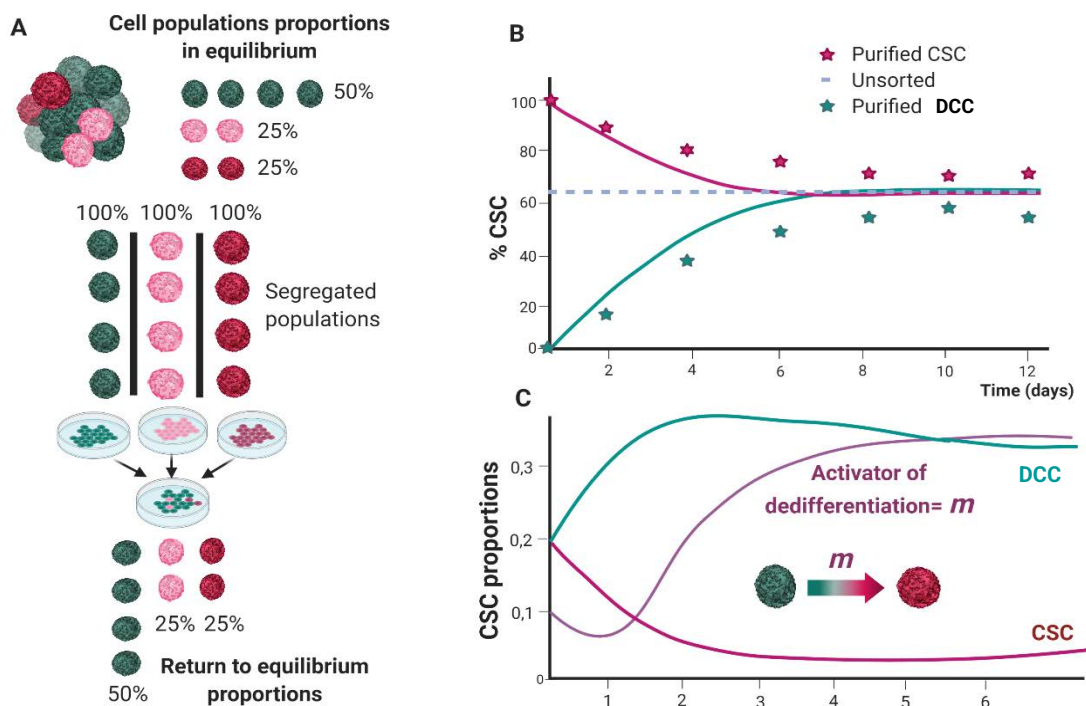


Figure 9. Phenotypic dynamic equilibrium between cancer cell subpopulations. (A) Phenotypically isolated cancer cell subpopulations tend to return to their initial proportions. Scheme

adapted from Gupta et al. work¹⁷⁴. **(B)** Scheme showing experimental results of long-term equilibrium CSC proportions from initial purified CSCs and DCCs, showing the stochastic transition from DCC to CSC. Adapted from a figure of Wang et al. work¹⁶⁸. **(C)** Model proposed to explain DCC conversion towards CSC phenotype. When CSC proportion is under a tiny value, the return to equilibrium of CSC proportions is driven by a molecular activator of DCC de-differentiation towards stem phenotypes. Scheme adapted from Omeda et al. mathematical model¹⁷⁷.

6 TUMOR MICROENVIRONMENT (TME) AND PLASTICITY

Breast tumors are comprised by a variety of different cell populations including DCC, CSCs, mesenchymal stem cells (MSCs), ECs, fibroblasts, inflammatory cells, bone marrow-derived cells (BMDC), among others¹⁷⁸. These cells are embedded in microenvironmental factors that include vasculature and the extracellular matrix (ECM), which is formed by a network of polysaccharides and proteins secreted by cells that serves as a structural tissue element^{179,180}. The combination of these cellular and non-cellular factors conforms the tumor niche or usually called TME, which creates a complex network of intercellular communication. The TME plays a crucial role in tumor development, metastasis, and response to therapy¹⁸¹.

Importantly, microenvironmental stimuli in the TME have great impacts in dictating the phenotype of cancer cells, as BCSC plasticity is controlled by both cell-intrinsic and cell-extrinsic factors. Thus, BCSC function and plasticity seems to be regulated by complex cellular and non-cellular interactions arising in the tumor niche¹⁸².

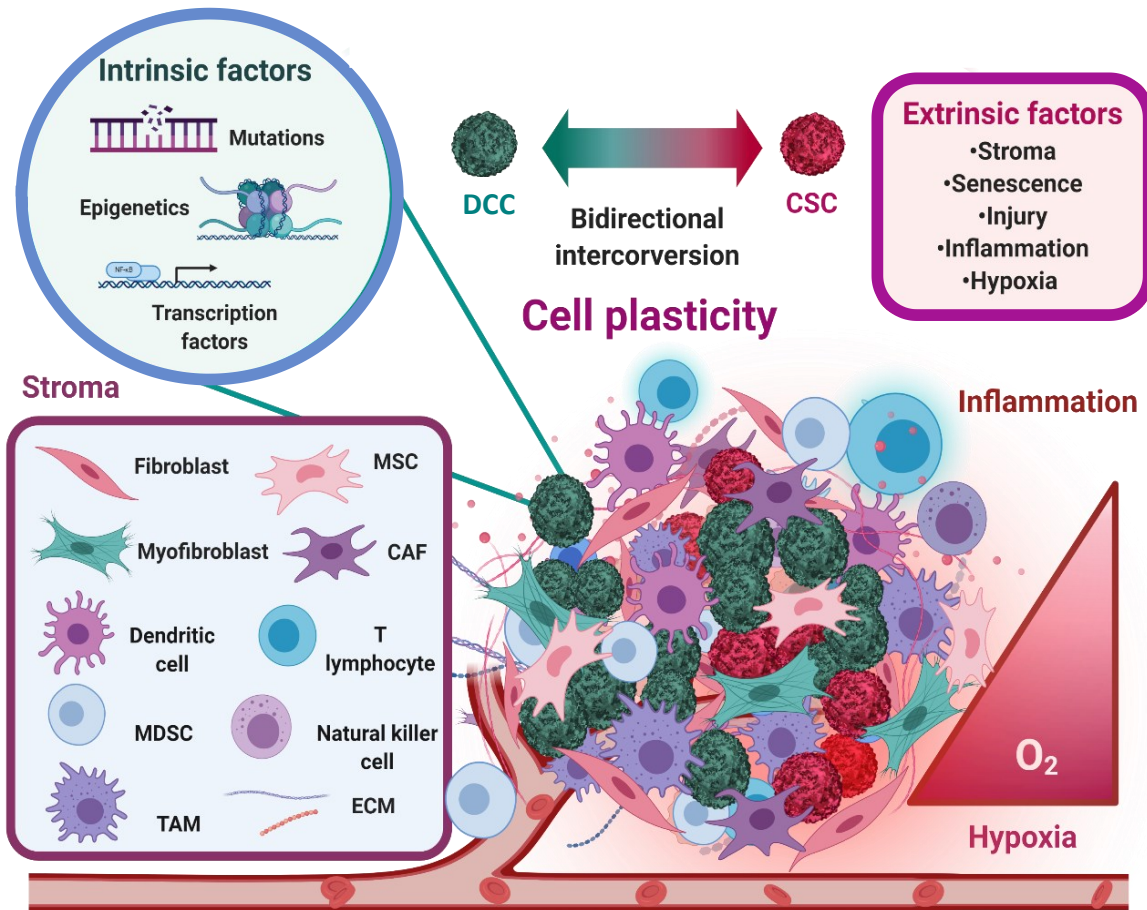


Figure 10. CSC plasticity is directed by both intrinsic and extrinsic factors. Various environmental stimuli can drive cancer cells plasticity towards CSC phenotypes. A tumor is a highly complex heterogeneous dynamic entity that involves cellular components (CSCs, DCCs, fibroblasts, immune cells, mesenchymal cells, etc), cell-secreted functional molecules and the ECM. The TME maintains the equilibrium state of the tumor as a whole biological system guiding cell plasticity to ensure tumor progression^{28,155,163,165}.

6.1 CELLULAR COMPONENTS IN TME GUIDING PLASTICITY

6.1.1 TUMOR CELLS

Tumor cells with DCC phenotypes also take part in maintaining CSC niche as they secrete factors such as IL-6 and IL-8 that sustain cancer cells stemness^{107,183–185}. Interestingly, it has been shown that DCC subpopulations with lower fitness can stimulate growth of other tumor cells (mainly CSC) by inducing tumor-promoting microenvironmental changes¹⁶⁵.

6.1.2 CANCER-ASSOCIATED FIBROBLASTS

Cancer Associated Fibroblasts (CAFs) and their collagen matrix products are a major component of the stroma of breast and many other solid tumors, comprising a substantial proportion of the

tumor mass^{186–189}. CAFs can have different precursors and they mainly differentiate from local normal fibroblasts (NF) and MSCs^{190,191}. CAFs precursors usually acquire a transitional, activated phenotype that corresponds to the expression of alpha-smooth muscle actin (α -SMA). CAFs show an increased secretory phenotype of collagens and fibronectin which provides structural support and anchorage to cancer cells^{190–192}.

CAFs are heterogeneous and display diverse functions among different tumor types^{193–197}. They maintain an active cross-talk with cancer cells which fosters tumor cell growth, angiogenesis and invasion by secreting paracrine factors and by remodeling the ECM^{198–203}. CAFs also foster an immunosuppressive TME by promoting the expansion of regulatory T cells²⁰⁴. Importantly, CAFs are key regulators of cancer cells plasticity displaying pro-stemness activities^{108,184,203,205–208}. Moreover, cytotoxic drugs stimulation also leads to CAFs to secrete pro-stemness cytokines or chemokines to further enhance tumor stemness and aggressiveness following therapy in TNBC²⁰⁹.

6.1.3 MESENCHYMAL STEM CELLS

MSCs are multipotent stromal cells present in the TME that foster cancer cells proliferation and metastasis. They are involved in the restoration of BCSCs via paracrine secretion of a variety of cytokines e.g. CXCL12, IL-6, and IL-8, promoting CSC phenotypes and chemoresistance^{107,210–213}.

6.1.4 INFLAMMATORY CELLS

The breast TME is characterized by displaying an immunosuppressive microenvironment^{214–216}. Numerous immune cell types recruited by chemokines and cytokines that are secreted by cancer cells contribute to this immunosuppression^{216,217}. Cytokines released by those immune components such as Transforming Growth Factor β 1 (TGF- β 1) and IL-6 also promote CSC plasticity transforming DCC into CSCs^{218,219}.

6.2 ENVIRONMENTAL FACTORS DRIVING PLASTICITY

6.2.1 HYPOXIA

Hypoxia is another hallmark of TME¹²⁷. Stemness of BCSCs is maintained by hypoxia in multiple ways: (1) induction of EMT, (2) ROS activated responses to stressors, (3) activation of stemness-related signaling (4) activation of stemness-related genes (5) suppression of differentiation-related genes and (6) alteration of glucose metabolism of CSC^{220–225}. Recently, direct evidence has

assessed that the hypoxic TME favors enrichment and/or maintenance of the BCSC-like tumor cells *in vivo*²²⁶.

6.2.2 THERAPY AND INJURY

There is a direct relationship between stemness and the reaction to stress stimuli. Indeed, an enrichment of the CSC population can be observed after therapy that frequently leads to tumor recurrence^{227–230}. Chemotherapy and radiotherapy enhance expansion of BCSC by inducing stemness phenotypes through Notch and Wnt activation and upregulation of TFs such as OCT-4, NANOG and SOX2^{231,232}.

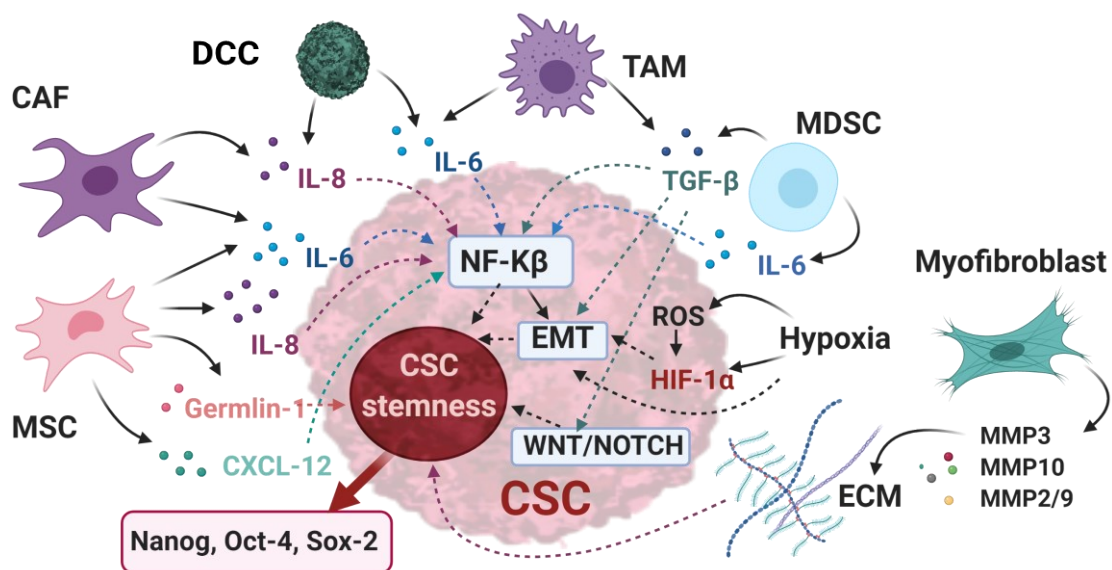


Figure 11. Molecular crosstalk between cancer cells and TME cell components fosters plasticity towards BCSC phenotypes. Adapted from¹⁸².

As detailed before, there is a complex signaling network in TME between cancer cells and TME components that operates to maintain BCSC plasticity. This information exchange functions in a bidirectional way, as cancer cells within tumors may modify their microenvironment to amplify niche-derived signals that in turn support and replenish the pool of BCSC. Understanding the molecular basis of this communication network holds great promise in terms of managing TNBC disease. In this sense, previous studies showed that cancer cells can release and uptake small Extracellular Vesicles (EVs) within the TME, which leads to reprogramming of recipient cells, including the induction of CSC phenotypes. EVs gather such a battery of unique features that make them to stand out among the possible potential candidates to act as signaling transducers of cell state plasticity operating in tumor cell state equilibrium maintenance²³³.

7 EXTRACELLULAR VESICLES

Cell-to-cell communication is essential for physiologic and metabolic processes in all pluricellular organisms²³⁴. In this regard, intercellular communication mediated by the transfer of EVs has been demonstrated to be of remarkable importance in many biological systems²³⁵.

EVs are defined as a heterogeneous collection of lipid bilayer membrane-enclosed vesicles naturally secreted by both prokaryotic and eukaryotic cells. Those membrane-bound carriers show complex biological functional cargoes including: mRNAs, lipids, metabolites, proteins, non-coding RNAs, and even DNA fragments. Of note, such biological cues can induce phenotypic reprogramming when transferred to recipient cells^{236–244}. In addition, EVs have the ability to protect internal cargo due to their high membrane stability²⁴⁵.

EVs of varying size, mode of biogenesis, and cargo can be released from a single cell, and moreover, EVs secretion pattern and EVs content can change with the physiologic state of the cell^{246,247}. Different cell types also produce distinct repertoires of vesicles^{248,249}. Once released, EVs can interact with cells in the immediate vicinity or at distant locations. Those interaction mechanisms include ligand–receptor recognition, release of vesicle contents in the extracellular space by bursting, direct fusion with the plasma membrane, and endocytosis into the cell^{248–250}.

7.1 EVS SUBTYPES

Although the classification of EVs is continuously evolving, EVs are traditionally divided into major categories according to the International Society for Extracellular Vesicles (ISEV). ISEV is a globally scientific organization focused on the study of EVs. According to their guidelines, the terms apoptotic bodies (ABs), Microvesicles (MVs), and exosomes have been traditionally used for cataloging the main EVs subpopulations. This traditional classification is based on EVs origin, size, and specific markers²⁵¹. Characteristics of each EVs populations are detailed in **Table 2**.

Features	Exosomes	MVs	ABs
Cell source	Live/stimulated cells	Live/stimulated cells	Dying cells
Biological origin	MVBs	Plasma membrane	Plasma membrane
Biogenesis and release	Inward budding within endosomal pathway / release upon fusion of MVBs with the plasma membrane	Outward budding from the plasma membrane followed by a fission	Outward blebbing of cell membrane
Density (g/ml)	1.13-1.19	1.032-1.068	1.16-1.18
Size (nm)	30-150	50-1000	50-5000
Morphology	Cup-shaped	Cup-shaped	Heterogeneous
Molecular cargo	proteins, lipids and nucleic acids	proteins, lipids and nucleic acids molecules	Nuclear fractions, cellular organelles
Associated markers	CD9, CD63, CD81 and CD82, Alix, annexin, TSG101.	TyA, C1q	-

Table 2. Biological features of different EVs subtypes. Based on ²⁵².

7.1.1 EXOSOMES

Exosomes constitute a group of EVs characterized by exhibiting typical sizes ranging between 30 and 200 nm in diameter. They are originated from the invagination of the endosomal membrane in form of intraluminal vesicles (ILVs). Such endosomes containing ILV are known as multivesicular bodies (MVB) and release their exosome cargo by membrane fusion with the plasmatic membrane²⁵³. Particularly, the biogenesis of exosomes involves the recruitment of the endosomal sorting complex required for transport (ESCRT) machinery to ubiquitinated proteins in the early endosome (ESCRT-dependent)^{254,255}. ESCRT machinery is comprised by four protein complexes (ESCRT-0, -I, -II, and -III) along with accessory proteins (Alix, VPS4, and VTA-1) that sequentially act to bind future exosome cargoes and form ILVs incorporating those cargoes^{253,256-260}. Note that other mechanisms ESCRT-independent for exosome formation have also been identified²⁶³. Proteins, such as tetraspanins, also participate in exosome biogenesis and protein loading. Tetraspanins, especially CD81, are essential for sorting receptors and intracellular components towards exosomes^{261,262}. In this regard, recent studies have shown the existence of several specialized mechanisms ensuring the specific sorting of bioactive molecules into exosomes, either by ESCRT-dependent or -independent pathways²⁶⁰.

Exosomes exhibit certain common characteristics regardless of their source: they usually sediment between $\sim 70,000\text{--}200,000 \times g$ and they are surrounded by a phospholipid membrane containing lipids characteristic of their cellular origin²⁶³. The main distinctive proteins present in exosomes fractions are components involved in MVB biogenesis such as proteins of the ESCRT complex such as Alix and tumor susceptibility gene 101 (TSG101). The presence of tetraspanins (CD9, CD63, CD81 and CD82) and cytosolic proteins involved in promoting exosome dockage and membrane fusion procedures, such as Rabs, Annexins, proteins involved in the regulation of membrane cytoskeleton dynamics and membrane fusion events, are also characteristically components present on exosomes^{244,251,253,264}.

Exosomes molecular cargo usually consists of proteins, lipids and nucleic acid molecules. Remarkably, exosomes present functional active nucleic acid cargo such as non-coding RNAs, including microRNA and long non-coding RNAs (lncRNAs), tRNA fragments, small-interfering RNAs (siRNAs), structural RNAs (stRNAs), small RNA transcripts and RNA-protein complexes as well as DNA^{265–267}.

Exosomes show substantial heterogeneity regarding their size, content, functional effect on recipient cells, and cellular origin²⁶⁸. Microenvironmental factors and the intrinsic nature of the cells can influence exosomes cargo and exosomes normally reflect the original nature of their cell of origin. For example, the proteome of breast cancer cells exosomes can determine whether the cell of origin is epithelial like or mesenchymal like^{246,269}.

7.1.2 MICROVESICLES

MVs constitute a group of EVs secreted by direct outward budding of the plasma membrane. MVs are budded as small membrane protrusions around a small portion of cytoplasm being released from cell membrane surface to the extracellular space through calpain activation, calcium influx, and cytoskeleton reorganization²⁷⁰. Their size can vary from $\sim 50 \text{ nm}$ up to $\sim 1000 \text{ nm}$ ^{275,276}. The main markers used for detecting MVs are integrins, selectins, and CD40. Their membrane composition is the same as plasmatic membrane^{271–273}. Microvesicles also show different functional cargo such as DNA and RNA, including mRNAs, miRNAs, siRNAs, and lncRNAs from the intracellular environment. Therefore, MVs can exert various functions in intercellular communication, signal transduction and immune regulation, as the transfer of their cargo to recipient cells affect their target cell phenotype^{274–276}.

7.1.3 APOPTOTIC BODIES

ABs consist of EVs released by the outward budding, blebbing, or fragmentation of the plasma membrane during cell apoptosis and are usually larger in size, ranging from 50 nm to 5 μm ²⁸¹. Their content varies depending on cellular origin, but they usually can be distinguished by the presence of organelles, proteins, lipids, and genetic materials²⁵².

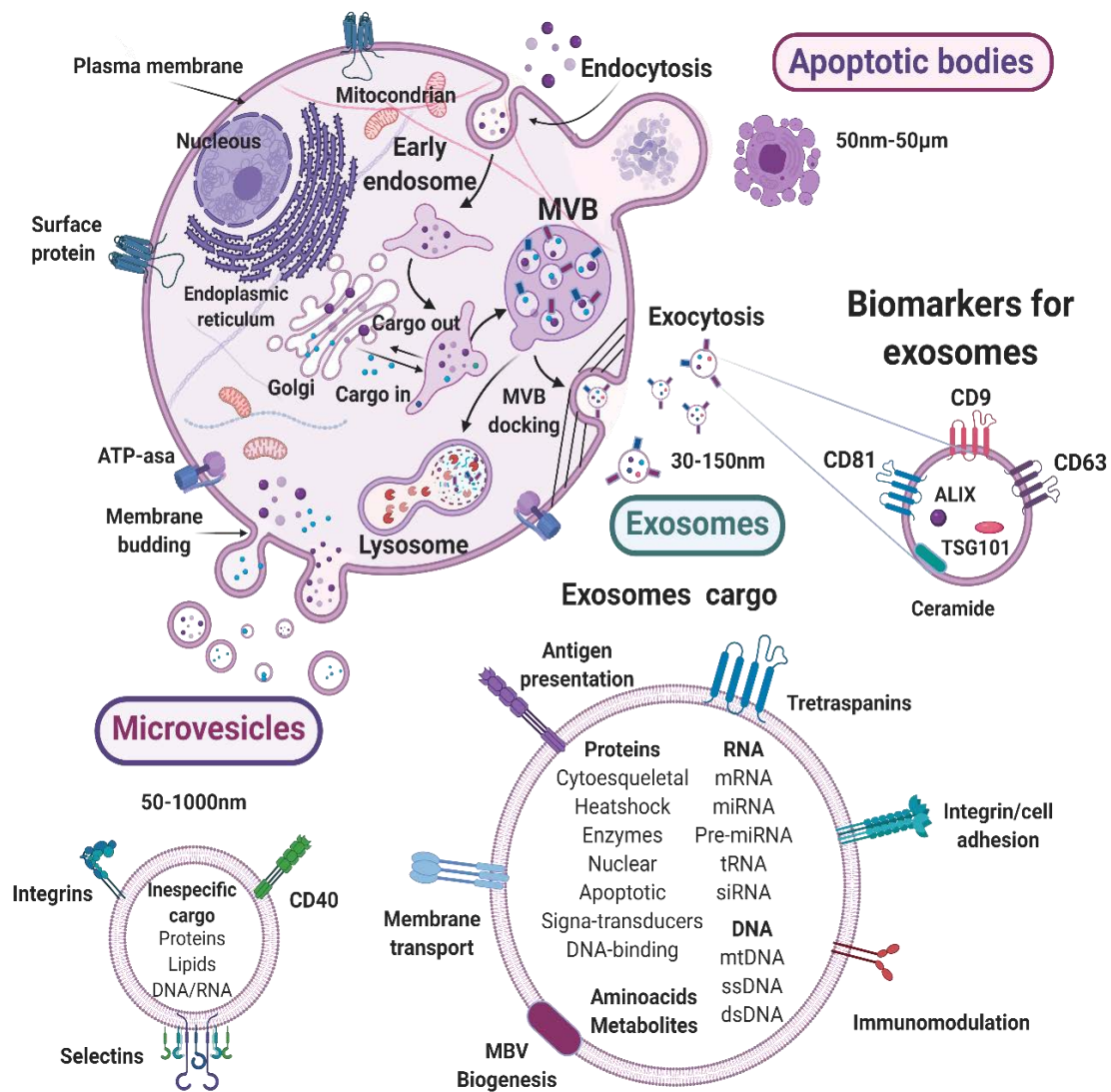


Figure 12. Biogenesis and identity of EVs. The three major categories of EVs are AB, MVs and exosomes. ABs are released by the outward budding, blebbing, or fragmentation of the plasma membrane during cell apoptosis and are usually larger in size, ranging from 50 nm to 5 μm . Microvesicles are released through plasma membrane budding and are in the size range of ~ 50 nm to 1 μm . Exosomes originate from the endosomal pathway by the formation of the Early Stage Endosomes (ESEs), Late Stage Endosomes (LSEs), and ultimately Multivesicular Bodies (MVBs), which contain Intraluminal Vesicles (ILVs). When MVBs fuse with the plasma membrane, exosomes are released (size range ~ 30 to 150 nm). Exosomes exhibit several common markers (CD9,

CD81, CD63, flotillin, TSG101, ceramide, and Alix). Exosome surface proteins include tetraspanins and they can contain different types of biological cargo. Based on ²⁵³.

8 THE ROLE OF EVs IN CANCER

Accumulating evidence suggests that breast tumors-derived EVs play crucial roles in all steps of cancer progression ^{269,278–280}.

8.1 TUMOR EVs MODULATE THE TME

EVs exert a pivotal role in cell-cell communication between tumor and surrounding cells in the primary TME. These particles participate in multiple steps during tumor growth, invasive processes and also contribute to metastatic dissemination. The transfer of the oncogenic cargo via tumor EVs impacts on stromal cells such as fibroblasts, ECs and immune cells. In this sense, tumor EVs can educate these recipient cells towards a tumor-promoting phenotype fostering cancer hallmarks ^{252,278,281–285}.

8.1.1 EVs EFFECT ON SURROUNDING CANCER CELLS

Tumor EVs can transfer oncogenic molecules that increase the aggressiveness of recipient cancer cells. Various studies have shown that EVs purified from breast cancer cells reach the surrounding cancer cells and promote tumor development ^{286–291}. Specifically, EVs isolated from the TNBC cell line Hs578T were proved to increase proliferation, growth and migration of recipient cancer cell lines ²⁹².

8.1.2 EVs EFFECT ON CAFs AND THEIR PRECURSORS

As detailed in previous sections, both activated fibroblasts and fully differentiated CAFs strongly influence cancer initiation and progression ¹⁹². Tumor derived EVs actively promote the conversion of MSCs and NF to activated fibroblast or CAF-like phenotypes through the transmission of different molecular activators ²⁹³. In this regard, EVs from different tumors, including breast cancer, carry TGF- β to fibroblasts, what leads in their differentiation towards a CAF-like phenotype ^{294–296}. A recent report also showed that breast cancer cell-derived Survivin in EVs upregulates SOD1 expression in fibroblasts transforming them into myofibroblasts ²⁹⁷. Moreover, breast cancer-EVs transport different RNA species capable of modifying the properties of recipient CAF precursors in the TME. Particularly, breast cancer EVs miR-21 is known as a critical regulator of CAFs formation promoting the proliferation and invasion of CAFs in breast tumors ²⁹⁸. EVs-mediated delivery of miR-9 also induces CAF-like properties in human breast fibroblasts ²⁹⁹.

This crosstalk is bidirectional, and once CAFs are activated by tumor derived EVs they display distinct phenotypic profiles and functions, secreting pro-tumor factors that in turn affect recipient cancer cells³⁰⁰. In particular, some breast CAFs subsets are well-described to enhance tumor invasion, stimulate cancer cell proliferation, EMT and migration^{301–309}.

8.1.3 EVS EFFECT ON ENDOTHELIAL CELLS PROMOTES ANGIOGENESIS

The development of de novo vasculature is essential for tumor growth. In this sense, the ability of tumor-derived EVs to sustain angiogenesis by promoting communication between cancer cells and endothelial cells has been described in many cancer types^{310,311}. Specifically, breast cancer cells exhibit an increase in EVs release under hypoxic conditions that play key roles in supporting the creation of new vessels³¹². In detail, miR-210 and Annexin II carried in breast cancer EVs can induce angiogenic responses of EC towards a capillary-like network formation *in vitro* and *in vivo*³¹³.

8.2 TUMOR EVS AND DRUG RESISTANCE

EVs can also confer chemo-resistance by transferring drug-resistant features between cells. As examples, EVs derived from chemo-resistant TNBC HCC1806 cells were able to induce proliferation and confer drug resistance to MCF10A breast cells, indicating that chemoresistance can be transferred between cells via EVs³¹⁴. Similarly, Docetaxel and Cisplatin resistant breast cancer cells released EVs which conferred a drug-resistant phenotype to recipient cells by the effective deliver of miRNAs^{291,315,316}.

Ejecting chemotherapeutic drugs via EVs from cancer cells is another mechanism of drug resistance. Exosomal transport of P-glycoprotein (P-gp) has been described as another possible mechanism in exosome-mediated drug resistance in breast cancer, as P-gp concentrations are higher in exosomes derived from drug-resistant cells than in drug-sensitive cells³¹⁷. MDR1/P-gp can be transported from docetaxel-resistant cells to sensitive cells via exosomes enabling the expulsion of drugs from recipient cancer cell lines³¹⁸.

Stromal cells are also implicated in drug resistance transmission. For example, EVs from stromal cells can mediate therapeutic resistance in TNBC after treatment with radiotherapy or chemotherapy by STAT-1 and NOTCH3 activation resulting in the expansion of therapy resistant CSC-like cells³¹⁹.

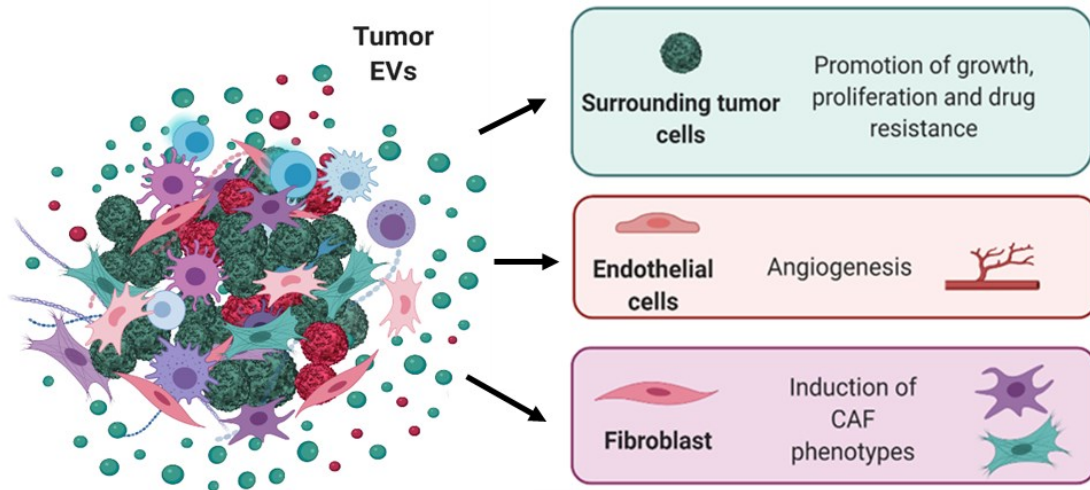


Figure 13. Tumor derived EVs foster tumor growth by remodeling surrounding cells in the TME towards pro-tumorigenic phenotypes.

8.3 TUMOR EVs AS DRIVERS OF BREAST CANCER METASTASIS

Cancer cells secreted EVs support several pathological features of metastasis. There is a strong body of evidence depicting an intricate crosstalk between cancer cells and TME elements mediated by tumor EVs. Such signaling at the primary tumor site and also at future metastatic sites is responsible for driving the metastatic process^{278,320,321}.

8.3.1 EVs MEDIATE REMODELING OF ECM AND INVASION

The early steps of the metastatic cascade are conducted by cancer cells proliferating, migrating and invading the surrounding tissues. At this point, ECM remodeling is essential to promote the invasive phenotype of tumors^{322,323}. In this regard, tumor secreted EVs directly contribute to this event by remodeling the ECM and thus enhancing the migratory capacity of cancer cells³²⁴. Tumor EVs carry ECM degradation factors such as matrix metalloproteinases (MMPs), which are capable of degrading collagen, laminin, and fibronectin thus affecting ECM remodeling^{324,325}. For example, metastatic breast cancer cells EVs activates MMP2-9, leading to degradation of ECM components, release of growth factors, and promotion of cancer cell invasion³²⁶. ECM remodeling, in turn, induces the release of cytokines and growth factors that affect other cells on TME like fibroblast which acquire activated phenotypes to favor cell migration and invasion^{305,327}.

8.3.2 EVs MEDIATE EMT

Tumor EVs also participate in EMT, a crucial step to initiate metastatic cascade^{328,329}. Tumor EVs carry pro-EMT molecular cargoes such as TGF- β , HIF 1 α , β -catenin or miRNAs, which are able to confer mesenchymal properties to recipient cells and directly enhance their invasive and migratory potential^{330–334}. For example, EVs isolated from breast cancer cells could promote EMT process in mammary epithelial cells MCF10A³³⁵.

8.3.3 EVs SET UP FUTURE METASTATIC NICHES

The “*seed and soil hypothesis*” is a well-established theory of cancer metastasis that postulates that a pre-metastatic niche (PMN) is required for tumor cells to engraft onto secondary sites of the body^{336–339}. The PMN is defined by the development of an environment distant from the primary tumor that is suitable for the survival and outgrowth of incoming CTCs. Therefore, in addition to the intrinsic properties of metastatic CTCs, the formation of a hospitable microenvironment in the future metastatic niche is critical to determine whether these CTCs will survive, will remain dormant, or will form macrometastases to spawn a secondary tumor growth^{339,340}. Among the changes required in the PMN for metastatic cells engraftment, there are pre-requirements that play an important role. Such changes include a vascular leakiness, modification of the ECM, remodeling of the vasculature, bone marrow immune cell infiltration with the formation of an immunosuppressive environment and the transformation of resident ECs and fibroblasts^{278,341}.

Importantly, tumor secreted EVs have been shown to play important roles in setting up the PMN. The systemic transfer of EVs from tumors to metastatic sites has been visualized *in vivo*, providing direct proof for the ability of tumor-derived EVs to signal over long ranges³³⁰. In this sense, primary tumor secreted EVs travel through the systemic circulation and are taken up by distal target cells, where they start the formation of pre-metastatic niches through mediating the “reprogramming” of multiple resident cell types^{281,342,343}.

8.3.3.1 EVs INCREASE VASCULAR PERMEABILITY IN THE PMN

To initiate metastasis, cancer cells from the primary tumor have to intravasate nearby blood vessels, travel through these vessels, and then extravasate the vessels at distant tissues to form secondary tumors^{344–348}. Tumor EVs influence the processes of intravasation and extravasation whereby cancer cells enter or leave the blood (or lymphatic) stream, respectively. ECs in the EC layer are connected by tight junctions that maintain vascular barrier function, and it has been described that tumor EVs can impair these junctions. This phenomenon increases vascular

permeability for further EVs and metastatic cells entry into the metastatic tissue parenchyma^{349–351}. miRNAs carried by breast cancer EVs can induce vascular permeability *in vitro* and *in vivo* favoring metastasis to the brain through the destabilization of the blood brain barrier (BBB)^{352,353} and to the lungs and liver through the disruption of the vascular endothelial barrier³⁵⁴. These studies demonstrate that breast tumor EVs promote vascular leakiness at different metastatic sites.

8.3.3.2 EVs PROMOTE ANGIOGENESIS IN THE PMN

Neoangiogenesis is a fundamental process for tumor metastasis as new vessels are needed in distant metastatic sites to provide metastatic arriving cancer cells with the necessary nutrients and oxygen³⁵⁵. Tumor EVs can favor neovascularization at distant organs through the transfer of proangiogenic factors such as VEGF and miRNAs to resident endothelial cells as well as by inducing the secretion of angiogenic factors from stromal cells like CAFs^{356–362}.

8.3.3.3 EVs INDUCE IMMUNE SUPPRESSION IN THE PMN

Recruitment of pro-tumor immune cells is a hallmark of PMN establishment, as these cells have been shown to have immunosuppressive abilities. Primary tumor derived EVs affect the immune response in PMN promoting the recruitment of suppressive immune cells or impairing cytotoxic immune cells function³⁴². Tumor EVs can upregulate the expression of proinflammatory factors like chemokines and cytokines to recruit tumor associated macrophages (TAMs), tumor associated neutrophils (TANs), regulatory T cells (Tregs) and MDSCs to distant secondary sites³⁴¹. Interestingly, tumor derived EVs induced recruitment of BMDCs to lung PMNs promoting accumulation of MDSC cells and directly suppressing anti-tumor T and Natural Killer (NK) cells in lungs and liver of mice lacking tumors³⁵¹. Inflammation signaling from TAMs promotes tumor growth and metastasis at distant sites³⁶³. Tumor EVs can also cause NK cell dysfunction, inhibit antigen-presenting cells, block T cell activation, and enhance T cell apoptosis to block adaptive immune responses^{364,365}. Interestingly, it has been recently confirmed that cancer cells release EVs carrying PD-L1. When binding to PD-1 on T cells EVs can inhibit the proliferation of CD8+ T cells, thus promoting tumor growth. Therefore, EVs carrying PD-L1 can reach the PMN and inhibit anti-tumor immune response³⁶⁶.

8.3.3.4 EVs REMODEL FIBROBLASTS AND ECM IN THE PMN

The survival of cancer cells that metastasize from primary tumors to secondary sites depends on the PMN stroma. Fibroblasts in distant organs are common target stromal cells for primary tumor EVs. During PMN establishment, tumor EVs trigger ECM changes by educating fibroblasts and other stromal cells in multiple ways consequently creating a permissive environment for

CTC seeding and growth³⁶⁷⁻³⁷². Functionally, EVs can reprogram tissue resident fibroblasts to acquire a CAF phenotype favoring metastatic cells arrival^{280,356,373-376}.

8.3.3.5 EVs DETERMINE ORGANOTROPISM IN METASTASIS

Tumor EVs can also dictate the future sites of metastasis through specific integrins present on their membranes. An elegant study conducted by Hoshino et al. found that different types of tumor EVs were involved in organ-specific metastasis. They showed that tumor-derived exosomes expressing particular integrin patterns partially dictated future PMNs at the lung, liver, and brain. Specifically, they described that EVs derived from the TNBC MDA-MB-231 cell line, expressing the integrins $\alpha6\beta4$ and $\alpha6\beta1$, specifically bound to lung resident fibroblasts and epithelial cells mediating lung tropism while EVs expressing $\alpha\nu\beta5$ mainly directed metastasis to the liver. These results indicated that the different integrin expression on exosomes of organotropism³⁷⁵. All the above-mentioned studies highlight the crucial role of EVs in PMN development and further metastasis growth.

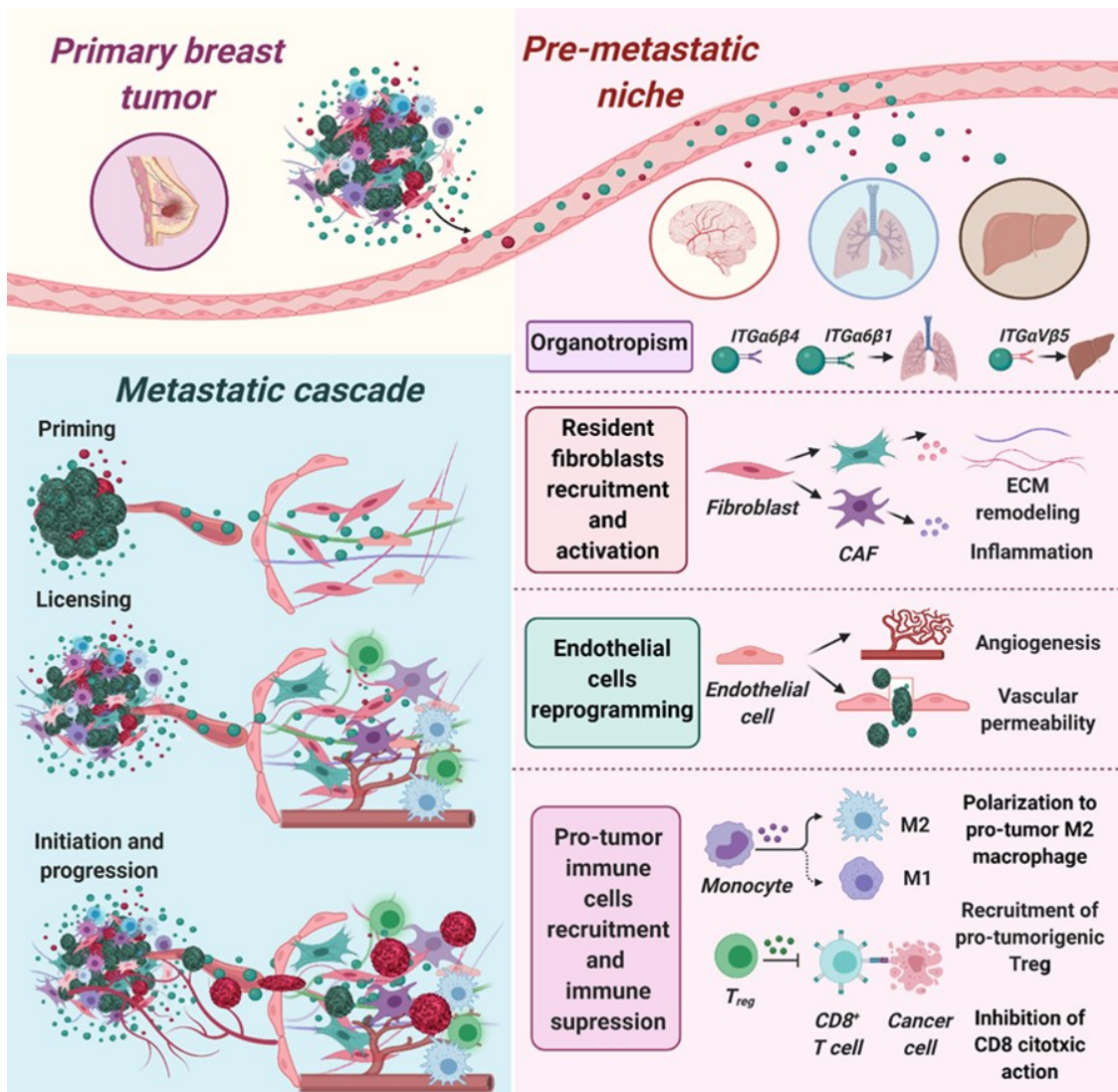


Figure 14. Tumor derived-EVs create hospitable distant pre-metastatic niches suitable for metastatic cells engraftment

HYPOTHESIS AND OBJECTIVES

HYPOTHESIS AND OBJECTIVES

Intra-tumoral phenotypic heterogeneity gives rise to different cancer subpopulations such as CSC and DCC^{8,23,24}. Despite it is well documented that those populations can be autoregulated and maintain a dynamic equilibrium between both phenotypic states through cancer cells plasticity events the scientific basis of this phenomena remains unknown¹⁷⁴. Recent work has elucidated the role of TME stromal cells on regulating cancer cells plasticity, and moreover, tumor secreted EVs have stood out as critical regulators of cancer-stroma inter-cellular communication^{252,278,281–285}. This molecular crosstalk has proven to be crucial to accomplish multiple cancer hallmarks bringing on tumor maintenance, progression, invasion and metastasis^{278–280}. Moreover, tumor EVs relevance for metastatic niche accommodation has been widely documented^{281,342,343}. However, the study of EVs in cancer has generally disregarded the phenotypic state of the EVs-secreting cancer cells. Considering that EV cargo has been proven largely determined by the cell source^{246,247} and the unique role of CSC subpopulations in breast cancer disease^{45–47}, the specific study of the implications of CSC secreted EVs becomes imperative.

Here, we aimed to evaluate the role of TNBC tumor EVs on the basis of their cell state origin (CSC vs. DCC) in mediating cancer cells plasticity to balance tumor dynamic equilibrium. Additionally, we also aimed to explore the role of TNBC secreted DCC and CSC EVs on stromal cells activation and in the creation of supportive PMNs.

Hypothesis 1

TNBC CSC and DCC secrete unique EVs reflecting their phenotypic state in their molecular cargo.

To test this hypothesis the following objectives were established:

Objectives:

1. Develop and validate breast fluorescent CSC models for the isolation and characterization of CSC and DCC from a panel of heterogeneous breast cancer cell lines.

2. Study DCC and CSC subpopulations cell plasticity and dynamic equilibrium between both cell states.
3. Develop a rational design to isolate CSC and DCC EVs from a TNBC cell line.
4. Isolate and characterize TNBC CSC and DCC EVs.

Hypothesis 2

EVs secreted by TNBC CSC and DCC regulate cancer cells plasticity

To test this hypothesis the following objectives were established:

Objectives:

1. Elucidate the role of TNBC CSC and DCC EVs on driving cancer cells plasticity towards DCC or CSC phenotypes, respectively.
2. Explore the functional cell response of TNBC cells challenged with either EV^{DCC} or EV^{CSC}.
3. Explore the role of CSC and DCC EVs in reprogramming stromal cells (fibroblasts) to drive cancer cells plasticity.

Hypothesis 3

TNBC CSC and DCC EVs have distinct effects on stromal cells remodeling

To test this hypothesis the following objectives were established:

Objectives:

1. Investigate the effect of breast EV^{CSC} and EVs^{DCC} in breast and lung fibroblasts activation *in vitro* and *in vivo*.
2. Study the 3D invasive capabilities of breast and lung fibroblast previously challenged with tumor EVs.
3. Explore the effect of EV^{CSC} and EV^{DCC} on endothelial cells and angiogenesis.

Hypothesis 4

TNBC CSC and DCC EVs have a distinct role in the conditioning of receptive PMNs.

To test this hypothesis the following objectives were established:

Objectives:

1. Study EV^{CSC} and EVs^{DCC} effect on metastasis.
2. Assess EV^{CSC} and EV^{DCC} impact on PMN conditioning.

MATERIALS AND METHODS

MATERIALS AND METHODS

1 CELL LINES AND CSC MODEL GENERATION

1.1 PARENTAL CELL LINES

Human breast MDA-MB-231, MCF-7 and HCC1806 cell lines, murine breast 4T1 cells and human lung CCD19 were obtained from American Type Culture Collection (ATCC), references detailed in **Table 3**.

Human CAFs from Invasive Ductal Breast Carcinoma (IDC) were isolated from patient tissue samples and immortalized by pBABE-Hygro-HTERT retroviral transfection (Courtesy of Erik Sahai, Francis Crick Institute, UK).

MDA-MB-231, MCF-7 and HCC1806 cells were routinely maintained in RPMI 1640 Medium supplemented with 10% fetal bovine serum (FBS), 2 mM L-Glutamine, 1x Non-essential aminoacids, 1x antimycotic-antibiotic solution.

Murine 4T1 cells were maintained in RPMI 1640 Medium supplemented with 10% fetal bovine serum (FBS).

CCD19 cells were cultured in DMEM/High Glucose supplemented with 10% FBS, 1x antimycotic-antibiotic solution and 1x Insulin-Transferrin-Selenium (ITS).

Outgrowth Endothelial Progenitor Cells (EPCs) were isolated from stroke patients as previously described³⁸² and cultured in fibronectin-coated flasks with endothelial growth medium (EGM2, Lonza) supplemented with the factors included in the kit and 10% FBS.

All the media and media supplements were purchased from Gibco.

Name	ATCC® number	Origin
MDA-MB-231	HTB-26™	Breast (TNBC)
MCF-7	HTB-22™	Breast (ER+)
HCC1806	CRL-2335™	Breast (TNBC)
4T1	CRL-2539™	Murine Breast (TNBC)
CCD19	CCL-210™	Lung fibroblasts

Table 3. List of the cell lines used in this study obtained from ATCC.

1.2 GENERATION OF HUMAN BREAST CSC MODELS

CSC models were generated from breast tumor cell lines as previously reported by our group^{378,379}. Briefly, tdTomato reporter cDNA was cloned under the minimal *ALDH1A1* promoter using a pENTRtm 5'-TOPO® TA Cloning Kit (Thermo Fisher Scientific) and tdTomato fluorescent protein was used as a reporter of *ALDH1A1* promoter activity. Cells were transfected with Lipofectamine 2000 (Thermo Fisher Scientific), and cultured under selective pressure with 10 µg/mL Blasticidin for two weeks. Positive tdTomato cells (tdTomato+) were sorted by fluorescence-activated cell sorting (FACS) in a FACS Aria cell sorter to determine the stemness profile of cells. Negative tdTomato (tdTomato-) sorted cells were also collected and cultured in regular maintenance medium to be used in cell state equilibrium experiments.

1.3 GENERATION OF BREAST SYNGENIC CSC MODELS

tdTomato reporter cDNA was commercially cloned under the murine *ALDH1A1* promoter using the MPRRM42253-LvPM03 vector by Genecopoeia company. The tdTomato fluorescent protein was used as a reporter of *ALDH1A1* promoter activity. Cells were transfected with Lipofectamine 2000 (Thermo Fisher Scientific), and cultured under selective pressure with 20 µg/mL Puromycin for two weeks. Same isolation procedure detailed in the previous section was then used to obtain the tdTomato+ and tdTomato- cell subpopulations. The stemness nature of isolated tdTomato+ cells was then assessed.

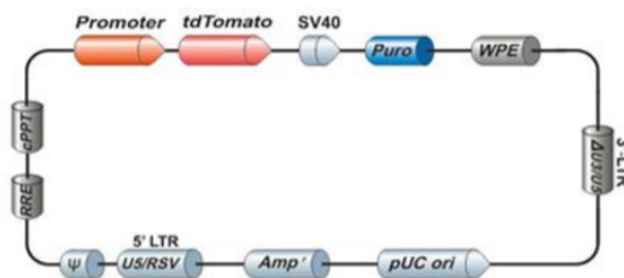


Figure 15. Vector information for MPRRM42253-LvPM03.

1.4 GENETICALLY-MODIFIED CELL LINES

MDA-MB-231, MCF-7 and HCC1806 *ALDH1A1:tdTomato* cell lines were generated as *in vitro* CSC-like models previously described and cultured under the same conditions than parental cancer cell lines plus 10 µg/mL Blasticidin (Gibco), which was used as a selective antibiotic for those engineered cell lines.

MDA-MB-231:*Fluc2-C19* cells were routinely cultured as described for the parental cell line with the addition of neomycin at 500 µg/mL.

4T1 *ALDH1A1:tdTomato* was maintained in supplemented conventional RPMI 1640 Medium plus 20 µg/mL Puromycin (Gibco) as selective antibiotic.

All cell cultures were propagated at 37°C and 5% CO₂ in a humidified incubator.

2 CSC AND DCC CHARACTERIZATION

2.1 FLUORESCENCE-ACTIVATED CELL SORTING (FACS)

FACS was used to sort CSC and DCC subpopulations from a heterogeneous population of MCF-7, MDA-MB-231, HCC1806 and 4T1 cells. For cell sorting, a starting amount of 5x10⁶ cells were used. Cells were detached and resuspended in phosphate buffered saline (PBS; Lonza), supplemented with 10% Fetal Bovine Serum (FBS). DAPI (1 µg/mL, Life Technologies) was used for vital staining (Life Technologies). Cells were sorted according to tdTomato and DAPI fluorescence intensity in a FACS Aria cell sorter (BD Biosciences, CA, USA). Sorted cells were collected in complete medium without antibiotic and used for subsequent experiments.

2.2 RNA EXTRACTION AND QUANTITATIVE REAL TIME-PCR (qPCR)

300,000 tdTomato+ and tdTomato- (identified as CSC and DCC, respectively) were sorted from MDA-MB-231, MCF-7, HCC1806 and 4T1 *ALDH1A1:tdTomato* cell lines and total RNA was extracted for quantitative polymerase chain reaction (qPCR) analysis of different stemness markers. Total RNA was extracted from 300,000 cells using the RNeasy Micro Kit (Qiagen) and the RNA obtained was reverse transcribed using a High Capacity cDNA Reverse Transcription Kit (Thermo Fisher Scientific) according to the manufacturer's instructions. The cDNA reverse transcription product was amplified with specific primers (**Tables 4 and 5**) by qPCR using SYBR Green to label and quantify double strand DNA (Thermo Fisher Scientific). The reaction was performed in triplicate in a 7500 Real time PCR system (Applied Biosystems). Relative normalized quantities (NRQ) of mRNA expression were calculated using the comparative Ct method ($2^{-\Delta\Delta Ct}$) through Qbase™ software with two reference genes (hGAPDH and hActin) used as endogenous controls.

Gene	Primer sequence (5' - 3')
<i>Actin-F</i>	CATCCACGAAACTACCTTCAACTCC
<i>Actin-R</i>	GAGCCGCCGATCCACAC
<i>GAPDH-F</i>	ACCCACTCCTCCACCTTTGAC
<i>GAPDH-R</i>	CATACCAGGAAATGAGCTTGACAA
<i>ALDH1A1-F</i>	CGCAAGACAGGCTTTTCAG
<i>ALDH1A1-R</i>	TGTATAATAGTCGCCCCCTCTC
<i>NANOG-F</i>	AGATGCCTCACACGGAGACTG
<i>NANOG-R</i>	TTGACCGGGACCTTGCTTC
<i>OCT4-F</i>	CCTGCACCGTCACCCCT
<i>OCT4-R</i>	GGCTGAATACCTTCCCAAATAGAAC
<i>ABCG2-F</i>	AGCTCAGATCATTGTACAGTCGT
<i>ABCG2-R</i>	GAACCCCAGCTCTGTTCTGG
<i>NOTCH4-F</i>	GCCCCTCTGGTTTCACAGG
<i>NOTCH4-R</i>	AGTTGGCCTTGTCTTTCTGGTC

Table 4. Human stemness genes primer sequences.

Gene	Primer sequence (5' - 3')
<i>Actin-F</i>	CATTGCTGACAGGATGCAGAAGG
<i>Actin-R</i>	TGCTGGAAGGTGGACAGTGAGG
<i>GAPDH-F</i>	CATCACTGCCACCCAGAAGACTG
<i>GAPDH-R</i>	ATGCCAGTGAGCTTCCCGTTTCAG
<i>ALDH1A1-F</i>	GGAATACCGTGGTTGTCAAGCC
<i>ALDH1A1-R</i>	CCAGGGACAATGTTTACCACGC
<i>NANOG-F</i>	GAACGCCTCATCAATGCCTGCA
<i>NANOG-R</i>	GAATCAGGGCTGCCTTGAAGAG
<i>OCT4-F</i>	CAGCAGATCACTCACATCGCCA
<i>OCT4-R</i>	GCCTCATACTCTTCTCGTTGGG
<i>SOX2-F</i>	AACGGCAGCTACAGCATGATGC
<i>SOX2-R</i>	CGAGCTGGTCATGGAGTTGTAC
<i>NOTCH4-F</i>	GGAGATGTGGATGAGTGTCTGG
<i>NOTCH4-R</i>	TGGCTCTGACAGAGGTCCATCT

Table 5. Mice stemness genes primer sequences.

2.3 2D INVASION ASSAY

The invasiveness of each cancer cells subpopulation was assessed using the CytoSelect™ Laminin Cell Invasion Assay Kit (Cell Biolabs). Briefly, inserts were placed in a 24 well plates and cell suspensions containing 1×10^6 cells/mL of tdTomato+ and tdTomato- cells were added to each insert. After 48 h incubation, invasive cells were dissociated from the lower side of the membranes, lysed, and quantified using CyQuant® GR Fluorescent Dye (Cell Biolabs).

2.4 3D INVASION ASSAY

200,000 MDA-MB-231 CSC and DCC were seeded in P10 plates separately. In parallel, 200,000 CAFs IDC were seeded in a P10 plate. Then, MDA-MB-231 CSC, DCC and CAFs IDC cells were trypsinized to single-cell suspension, centrifuged and resuspended with 3 mL of culture medium containing 2 μL of CellTracker™ staining solution. Each suspension was labeled with a different color of CellTracker™. After 30 min of incubation, cells were washed, counted and resuspended to reach a final concentration of 75×10^5 cells/mL. Hence, a cell suspension containing the three cell types at a 1:1:2 (CSC/DCC/CAFs) ratio and 0.25% methylcellulose solution in DMEM was prepared and 3D invasion assay was performed as described by Labernadie et al³⁸⁰. Briefly, 20 μL droplets of mixed cells were plated onto the lid of a 10 cm culture dish and allowed to form spheroids over night (ON) in a 37°C, 5% CO₂ incubator. The spheroids were then embedded in a Rat tail collagen type I /Matrigel gel mix at in 24-well glass-bottomed cell culture plates (MatTek) and incubated at 37°C and 5% CO₂ until invasive strands were formed. 60 hours later, the spheroids were imaged with a spinning disk confocal microscope at a magnification of $\times 10$, $\times 20$ and $\times 40$. Z stack images spanning 100–150 μm were collected and image stacks were analyzed with ImageJ software.

2.5 MAMMOSPHERE FORMATION ASSAY

A maximum of 10.000 cells/mL of MDA-MB-231 and 4T1 tdTomato+ and tdTomato- cells were seeded in 2 mL in ultra-low attachment P6 plates in serum-free RPMI 1640 Medium for 7–10 days. The serum-free RPMI 1640 Medium was supplemented with 6% glucose, 2 mM L-Glutamine, 1X AA, 4 $\mu\text{g}/\text{mL}$ heparin (Sigma-Aldrich), 2 mg/mL Bovine serum albumin (BSA) (Sigma-Aldrich), 0.02 $\mu\text{g}/\text{mL}$ epidermal growth factor (EGF) (Sigma-Aldrich), 0.01 $\mu\text{g}/\text{mL}$ basic fibroblast growth factor (FGFb) (Thermo Fisher Scientific), 10 $\mu\text{g}/\text{mL}$ putrescin (Sigma-Aldrich), 0.1 mg/mL apo-transferrin (Sigma-Aldrich), 25 $\mu\text{g}/\text{mL}$ insulin (Sigma-Aldrich) and 20 μM progesterone (Sigma-Aldrich). Resulting mammospheres were then counted and imaged by conventional confocal microscopy.

2.6 *IN VIVO* EXPERIMENTATION

Six-week-old female NOD/SCID mice (NOD.CB-17-Prkdcscid/Rj) were obtained from Janvier Laboratories (Le Genest-Saint-Isle, France), housed under specific pathogen-free conditions and provided with food and water ad libitum and used at six to eight weeks of age. Animal care was handled in accordance with the Guide for the Care and Use of Laboratory Animals of the Vall

d'Hebron University Hospital Animal Facility, and the experimental procedures were approved by the Animal Experimentation Ethical Committee at the institution.

2.6.1 HCC1806 CSC TUMORIGENICITY ASSAY

1,000, 10,000 and 100,000 cells of either tdTomato+ or tdTomato- cells (n=5) were inoculated orthotopically in six-week-old female NOD/SCID mice by intramammary fat pad (IMFP) inoculation in a 1:1 mixture with Matrigel (Corning). Tumor incidence and growth was monitored up to 4 weeks post-inoculation. At the endpoint of the experiment tumors were resected and imaged.

2.6.2 MDA-MB-231 CSC LUNG METASTATIC MODEL

1 x 10⁶ cells/mice of either MDA-MB-231.Fluc2-C19. ALDH1:tdTomato+ or tdTomato- cells were intravenously injected (iv) into the tail vein of NOD/SCID mice. When metastasis were observed in lungs, lungs were excised and further fixed in Bouin solution and processed for immunohistochemical analysis of NANOG. IHC procedures are detailed in the 7.3 IMMUNOHISTOCHEMISTRY section.

3 PHENOTYPIC EQUILIBRIUM RESTORATION ASSAY

500,000 MDA-MB-231, MCF-7 and HCC1806 tdTomato+ (CSC) and tdTomato- sorted cells (DCC) were seeded in adherent plates of 10 cm diameter. Cultured CSC were analyzed by FACS every 2 passages to assess the drop in the % of tdTomato+ cells over time. Isolated DCC total RNA was extracted and used for subsequent qPCR analysis at different passages: after sorting (AS), passage 1 (P1) and passage 5 (P5), to monitor changes in the stem gene expression profile of this subpopulation.

4 EVs^{CSC} AND EVs^{DCC} ISOLATION AND CHARACTERIZATION

4.1 CULTURE OPTIMIZATION FOR *IN VITRO* PURE MDA-MB-231 CSC AND DCC MAINTENANCE

4.1.1 MDA-MB-231 CSC

CSC subpopulations from MDA-MB-231 *ALDH1A1:tdTomato* were isolated according to their tdTomato expression in a FACS Aria cell sorter as described before. Two consecutive sorting rounds were employed for CSCs cell enrichment. tdTomato+ cells from the first sorting round

were collected and expanded in complete RPMI 1640 medium for re-sorting. Re-sorted tdTomato⁺ cells displayed high extents of CSC-like cells (99%) were cultured in serum-free RPMI 1640 Medium supplemented with 6% glucose, 2 mM L-Glutamine, 1X AA, 4 µg/mL heparin (Sigma-Aldrich), 2 mg/mL BSA (Sigma-Aldrich), 0.02 µg/mL EGF (Sigma-Aldrich), 0.01 µg/mL FGFb (Thermo Fisher Scientific), 10 µg/mL putrescin (Sigma-Aldrich), 0.1 mg/mL apo-transferrin (Sigma-Aldrich), 25 µg/mL insulin (Sigma-Aldrich), 20 µM progesterone (Sigma-Aldrich) to prevent cell differentiation. This cell line was employed for CSC derived EVs (EVs^{CSC}) production along the study.

4.1.2 MDA-MB-231 DCC

MDA-MB-231 *ALDH1A1:tdTomato* (DCC) cell line stably exhibiting a low content of CSC (1-2%), (artificially mixed proportions), was maintained as described for the parental cell line with the addition of blasticidin at 10 µg/mL (Gibco). This cell line was employed for DCC derived EVs (EVs^{DCC}) production along the study.

4.2 EVS PURIFICATION

Supernatants (SN) coming from MDA-MB-231 CSC and DCC optimized cell cultures, after 48h incubation in EV-depleted medium, were centrifuged at 300 g at 4°C for 10 min in order to remove dead cells. Additional centrifugation steps at increasing centrifugation speed 2,000 g, 10 min 4°C and 10,000 g 20 min 4°C were carried out to eliminate potential sub-cellular debris. Clarified SNs were concentrated through centrifugation at 5,000 g, 15 min, 4°C, using 300,000 KDa VIVAspin devices (Sartorius). The concentration factor varied from 50X to 100X depending on the sample. EVs were then precipitated from concentrated SN by the addition of “Total Exosome Isolation Reagent” (Invitrogen) according to manufacturer’s instructions. Samples were centrifuged at 16,000 g for 1 h at 4°C and pellets containing the EVs resuspended in phosphate buffered saline (PBS). Purified EVs were stored at 4°C. Same process was used to obtain EVs^{CSC} and EVs^{DCC} isolated from HCC1806 and MCF-7 CSC and DCC cultures, respectively.

Note that prior to every EVs purification batch a qPCR control was performed to assess the maintenance of differences in the stemness expression profile of *ALDH1A1*, *Nanog* and *Oct-4* in CSC and DCC cultured cells.

4.3 MORPHOMETRIC ASSAYS

Transmission electron cryomicroscopy (CryoTEM) morphometric assessment and particle size distribution and concentration were further studied by Dynamic light Scattering (DLS) and Nanoparticle Tracking Analysis (NTA) as described by Seras-Franzoso and co-workers³⁸¹.

4.4 STEM PROTEIN ARRAY

Human pluripotent stem cell antibody array (R&D Systems, ARY010) was performed in accordance with the manufacturer's instructions. Briefly, approximately 500 µg of total-EVs^{CSC} and EVs^{DCC} lysates were incubated with array membranes O.N. at 4 °C. Membranes were then washed and incubated with a streptavidin–horseradish peroxidase-coupled antibody (1:2000) for 30 min at RT and developed using Chemi-Reagent Mix. The immunoblot images were captured and visualized using the LI-COR Odyssey Fc imaging system and dot intensity was measured using ImageJ NIH software.

4.5 PROTEIN EXTRACTION AND WESTERN BLOTTING (WB)

Cell extracts (CE) pellets and EVs samples were lysed with Cell Lytic M reagent (Sigma-Aldrich) containing a protease inhibitor cocktail (Sigma-Aldrich). Proteins in crude lysates were quantified using the bicinchoninic acid assay (BCA) Protein Assay (Pierce Biotechnology). A total of 20 µg of whole-cell lysates were separated by SDS-PAGE and transferred onto PVDF membranes (Merck Millipore). Membranes were blocked in 5% non-fat dry milk (w/v) in Tris-buffered saline (TBS) buffer, 1h at RT. Targeted proteins were probed using primary antibodies (**Table 7**), ON at 4°C. Horseradish peroxidase (HRP)-conjugated secondary antibodies, anti-mouse (P0447, Dako) or anti-rabbit (P0217, Dako), were then added as requested and incubated for 1 h at room temperature. Extensive washing in TBS-Tween (0.05% v/v) was performed between blocking and antibodies incubation steps. Membranes were developed using Immobilon® HRP substrate (Merck Millipore) in a LI-COR Odyssey Fc imaging system. Band intensity on the blots was quantified using the ImageJ NIH software.

4.6 EVs INTERNALIZATION ASSAYS

4.6.1 EVs FLUORESCENT LABELING

DiOC/DiD or DiR (Invitrogen™) were supplemented to EVs^{CSC} and EVs^{DCC} to a concentration of 250 µg/mL and 500 µg/mL respectively, for 30 min at 37°C. Samples were then dialyzed (Slide-A-Lyzer™ MINI Dialysis Device, 3.5K MWCO, 0.1 mL, Thermo Scientific) against PBS, ON at 4°C.

4.6.2 STOCHASTIC OPTICAL RECONSTRUCTION MICROSCOPY (STORM)

Parental MDA-MB-231 cells were seeded in an 8 chambered coverglass and incubated with 2.5 µg/mL DiD labeled EVs^{CSC} or EVs^{DCC} ON in cell culture conditions. Cell medium was removed and cells were stained with 5 µg/mL WGA-AF488 (Thermo Fischer Scientific) and fixed in 4% paraformaldehyde (PFA). Samples were imaged in STORM buffer (5% w/v glucose, 100 mM cysteamine, 0.5 mg/mL glucose oxidase and 40 µg/mL catalase in PBS) to ensure an adequate photoswitching of the fluorophores. DiD-labeled EVs^{CSC} and EVs^{DCC} and MDA-MB-231 cells incubated with DiD-labeled EVs were imaged with a 647nm laser (160 mW) using NIS-Elements software in Nikon Eclipse Ti microscope (Nikon Europe, Amsterdam). The sample was illuminated using a total internal reflection fluorescence (TIRF) alignment for EVs structure imaging or a highly inclined and laminated optical (HILO) alignment for intracellular imaging. The z-level was kept constant by Nikon perfect focus system. Fluorescence was collected by a Nikon 100x, 1.49 NA oil immersion objective and images acquired with a Hamamatsu 19 ORCA-Flash 4.0 camera. For each channel 20,000 frames were acquired and analyzed by fitting a 2D Gaussian function to obtain the localizations of fluorophores. Resulting images were then analyzed with ImageJ NIH.

4.6.3 CONFOCAL MICROSCOPY

MDA-MB-231 cells and CCD19 cells were seeded in an 8 chambered coverglass (Lab-Tek®II, Eppendorf) and incubated 24 h at 37°C and 5% CO₂. Then, 2.5 µg/mL DiD-labeled EVs^{CSC} and DiOC-labeled EVs^{DCC} were added to MDA-MB-231 CSC or DCC cells and incubated for 12 h while DiD-labeled EVs^{CSC} or EVs^{DCC} were added to CCD19 cells and also incubated for 12 h. Cell medium was removed and cell membranes fluorescently tagged. Samples were fixed in 4% PFA prior to visualization. Note that, MDA-MB-231 cell membranes were counterstained with 5 µg/mL WGA-AF488 (Thermo Fischer Scientific), 10 min at 37°C and visualized using Nikon Eclipse Ti microscope (Nikon) with 100X/1.49 NA oil immersion objective. While CCD19 cell membranes were stained with 5 µg/mL Cell Mask™ (Invitrogen), 10 min at 37°C and image acquisition was carried out in a spectral confocal microscope FV1000 (Olympus) with a PLAPON 40XO objective. Further image processing was performed using ImageJ NIH software in both cases.

4.6.4 INTERNALIZATION KINETICS ASSAY BY FACS

DiD labeled EVs^{CSC} or EVs^{DCC} were added to MDA-MB-231 CSC or DCC cell cultures, 2.5 µg EVs/mL, and incubated for 15 min, 4h, 8h and 24h. After incubation cells were treated with trypsin 0.05 % (w/v) (Biological Industries) to detach cells, and neutralized in complete RPMI medium supplemented with DAPI (1 µg/mL final concentration). Cell fluorescence intensity was analyzed in

a LSR Fortessa flow cytometer (Beckton Dickinson). Data was further processed using FCS express 4 software (De novo software) and median fluorescence intensity represented.

5 EVS AND CANCER CELLS PLASTICITY STUDIES

5.1 EFFECT OF EVs^{CSC} AND EVs^{DCC} ON PARENTAL CELLS STEM GENE EXPRESSION PROFILE

50,000 MDA-MB-231, MCF-7 or HCC1806 parental cells were seeded in 2 mL of complete RPMI medium in 6-well plates. Then, 25 µg/mL of either EVs^{CSC} or EVs^{DCC} were added to each well for 3 consecutive days (150 µg total EVs/well). After 72h in culture, total RNA was extracted and used for subsequent qPCR analysis and changes in the stemness reporters *ALDH1A1*, *Oct-4* and *Nanog* were studied.

5.2 EFFECT OF EVs^{CSC} ON DE-DIFFERENTIATION INHIBITION

500,000 HCC1806 tdTomato- flow sorted DCC were seeded in attachment conditions in P10 plates and incubated with 25 µg/mL of EVs^{CSC}. In parallel, flow sorted DCC without EVs were cultured as control. Cells were maintained in culture, diluted when they reached confluence and reseeded in a new P10 plate. Each time that cells were reseeded in a P10 plate 25 µg/mL of EVs^{CSC} were added to the cell culture. After 5 passages, total RNA was extracted and used for subsequent qPCR analysis and changes in the stemness reporters *ALDH1A1*, *Oct-4* and *Nanog* were studied.

5.3 EFFECT OF EVS ON INVASION ABILITIES OF RECIPIENT PARENTAL CANCER CELLS

5.3.1 2D INVASION ASSAY

50,000 parental MDA-MB-231, MDA-MB-231 CSC and MDA-MB-231 DCC cells were seeded in 6 well plates. Then, 25 µg/ml of either EVs^{CSC} or EVs^{DCC} were added to parental MDA-MB-231 for 3 consecutive days (150 µg total EVs/well). On the third day, the invasiveness of EVs educated MDA-MB-231 parental cells and MDA-MB-231 CSC and DCC cell subpopulations was assessed using the CytoSelect™ Laminin Cell Invasion Assay Kit (Cell Biolabs). Briefly, inserts were placed in a 24 well plate and cell suspensions containing 1×10^6 cells/mL of MDA-MB-231 CSC and DCC cells and parental MDA-MB-231 cells previously treated with EVs^{CSC} or EVs^{DCC}, added to the

insert. After 48 h incubation, invasive cells were dissociated from the lower side of the membranes, lysed, and quantified using CyQuant[®] GR Fluorescent Dye (Cell Biolabs).

5.3.2 3D INVASION ASSAY

200,000 parental MDA-MB-231 were seeded in P10 plates and 25 µg/mL of either EVs^{CSC} or EVs^{DCC} were added to growing cells for 3 consecutive days. In parallel, 200,000 CAFs IDC were seeded in a P10 plate. Then, MDA-MB-231 and CAFs IDC cells were trypsinized to single-cell suspension, centrifuged and resuspended with 3 mL of culture medium containing 2 µL of CellTracker[™] staining solution. After 30 min of incubation, cells were washed, counted and resuspended to reach a final concentration of 75×10^5 cells/mL. Hence, a cell suspension containing the two cell types at a 1:1 ratio and 0.25% methylcellulose solution in DMEM was prepared and 3D invasion assay was performed as described by Labernadie et al.^[36,51]. Briefly, 20 µL droplets of mixed cells were plated onto the lid of a 10 cm culture dish and allowed to form spheroids in a 37°C, 5% CO₂ incubator O.N. The spheroids were then embedded in a Rat tail collagen type I /Matrigel gel mix at in 24-well glass-bottomed cell culture plates (MatTek) and incubated at 37°C and 5% CO₂ until invasive strands were formed. Sixty hours later, the spheroids were imaged with a spinning disk confocal microscope at a magnification of ×10, ×20 and ×40. Z stack images spanning 100–150 µm were collected and image stacks were analyzed with ImageJ software.

5.4 EFFECT ON *IN VIVO* PLASTICITY OF METASTATIC MDA-MB-231 CELLS

To study the effect of EVs^{CSC} and EVs^{DCC} in the *in vivo* stemness nature of metastatic MDA-MB-231 cells, 4×10^6 Luciferase-expressing MDA-MB-231.Fluc2-C19 cells seeded in 20 mL of RPMI complete medium were exposed to 25 µg/mL of EVs^{CSC} or EVs^{DCC} for 3 consecutive days. Cells were then *iv* injected into the tail vein of NOD-SCID mice. When metastasis were observed in lungs, lung tissues were collected and further fixed in Bouin solution and processed for immunohistochemical analysis of NANOG (detailed in 7.3 IMMUNOHISTOCHEMISTRY section). NANOG labeling was qualitatively assessed in 3 random sections at 4X, 10X and 20X magnifications. Representative images were displayed.

Non-treated MDA-MB-231.Fluc2-C19 cells were also *iv* administered as control.

6 EVS EFFECT ON STROMAL CELLS STUDIES

6.1 EVS EFFECT ON FIBROBLASTS AS PLASTICITY MEDIATORS

6.1.1 CYTOKINE ARRAY

Cytokine antibody-pair-based assays were performed using human cytokine array kit (R&D Systems, ARY005B) according to the manufacturer's protocol. In brief, 100,000 CCD19 fibroblasts seeded in 6-well plates were cultured alone or treated with either EVs^{CSC} or EVs^{DCC}, 25 µg/mL per day during 3 days. Culture supernatants were next collected (CM) and centrifuged at 13,000 rpm during 10 min to remove cell debris. Array membranes, previously spotted with capture antibodies by the manufacturer, were incubated with 0.5 mL of CM ON at 4 °C. Membranes were then washed three times with 50 mL of washing buffer at room temperature (RT), incubated with a streptavidin–horseradish peroxidase-coupled antibody (1:2000) for 30 min at RT and revealed using Chemi-Reagent Mix. The immunoblot images were captured and visualized using the LI-COR Odyssey Fc imaging system and dot intensity was measured using ImageJ NIH software.

6.1.2 EFFECT OF EVs^{CSC} AND EVs^{DCC} ON CCD19 IL-6 AND IL-8 EXPRESSION

50,000 CCD19 cells were seeded in 2 mL of complete DMEM medium in 6-well plates. Then, 25 µg/ml of either EVs^{CSC} or EVs^{DCC}, were added to each well for 3 consecutive days (150 µg total EVs/well). After 72h in culture, total RNA was extracted and used for subsequent qPCR analysis of IL-6 and IL-8 expression. Primers employed are detailed in **Table 6**. Conditioned Media (CM) of cultured CCD19 cells was collected for subsequent experiments.

Gene	Primer sequence (5'- 3')
<i>IL-8-F</i>	TTTCTGCAGCTCTGTGTGAAGG
<i>IL-8-R</i>	GGGTGGAAAGGTTTGGAGTATGT
<i>IL-6-F</i>	ACTCACCTCTTCAGAACGAATTG
<i>IL-6-R</i>	CCATCTTTGGAAGGTTTCAGGTTG

Table 6. IL-6 and IL-8 primers sequences.

6.1.3 EFFECT OF FIBROBLASTS CM ON MDA-MB-231 PARENTAL CELLS STEM GENE EXPRESSION PROFILE

2 mL of fibroblasts EVs^{CSC}-CM and EVs^{DCC}-CM were collected (as described above) and added to 6-well plates seeded with 50,000 MDA-MB-231 parental cells. After 48h in culture, 100,000 MDA-MB-231 cells were collected and total RNA was extracted for qPCR analysis and stemness genes were analyzed. The rest of the collected cells were used for MTT assays.

6.1.4 EFFECT OF IL-6 AND IL-8 ON STEM GENE EXPRESSION PROFILE IN PARENTAL MDA-MB-231

20 ng/mL of either recombinant soluble IL-8 or IL-6 (R&D Systems) were added to 50,000 MDA-MB-231 parental cells seeded in 6-well plates. After 48h in culture, total RNA was extracted and qPCR analysis was performed.

6.1.5 DRUG RESISTANCE ASSAY

Resistance to Paclitaxel (PTX) of MDA-MB-231 cells previously treated with either EVs^{CSC}-CM and EVs^{DCC}-CM was assessed by MTT assay. 5,000 cells/well were seeded in 96-well plate and incubated for 24h at 37°C, 5% CO₂. 0.04µM of PTX (Teva) was then added to growing cells. Complete medium was used as negative control and 10% DMSO as positive control of cytotoxicity. After 48h of incubation, 0.5 mg/mL 3-(4,5-dimethylthiazol-2-yl)-2,5-diphenyl tetrazolium bromide (MTT) was added to each well. Plates were incubated for additional 4 h at 37°C, cell media removed and 180 µL of DMSO (Sigma) was added to each well. The absorbance at 590 nm of each well was read on a microplate reader ELx800 (BioTek). Cell viability was calculated using a minimum of 3 biological replicates with 6 technical replicates for each assay.

6.2 MYOFIBROBLASTS ACTIVATION STUDIES

6.2.1 DETECTION OF EVs CONTENT IN α -SMA BY WESTERN BLOTTING

CSC and DCC cell pellets and EVs samples were processed as previously described in the 4.5 *PROTEIN EXTRACTION AND WESTERN BLOTTING* section. Mouse anti- α SMA primary antibody was used as primary antibody at 1:1000 dilution.

6.2.2 *IN VITRO* α -SMA IMMUNOFLUORESCENT DETECTION IN CCD19 CELLS

For α -SMA immunofluorescence detection, 15,000 CCD19 cells/well were seeded on 8-well coverslips (Lab-Tek®II, Eppendorf) and treated with either EVs^{CSC} or EVs^{DCC}, 25 μ g/mL per day during 3 days. After 72 h of incubation, cells were fixed in 4% PFA for 15 min, permeabilized with 0.1% SDS in PBS for 10 min and blocked in PBS-Tween 0.3% with 5% BSA for 30 min. Samples were then incubated with anti- α -SMA antibody diluted in PBS-Tween 0.3% with 5% BSA O.N. at 4 °C. Cells were washed 3 times in PBS-Tween 0.3% and further incubated with secondary goat antibody anti-mouse conjugated to Alexa Fluor™ 488, 1:1000 (Invitrogen). 30 min at RT in PBS-Tween 0.3% with 5% BSA. Samples were further washed 3 times in PBS-Tween 0.1%. Finally, a drop of antifading mounting medium ProLong (Thermo Fischer Scientific) was added and slides examined using an FV1000 confocal microscope (Olympus) with a 40 \times objective. Images (at least five random positions per condition) were acquired with identical exposure times and settings. Fluorescence intensity was quantified using Image J NIH software.

6.2.3 *IN VIVO* α -SMA IMMUNOFLUORESCENT DETECTION IN LUNG SECTIONS

5 μ m thick OCT microsections from the lungs of animals treated with either EVs^{CSC} or EVs^{DCC}, 300 μ g EVs for 24h, were mounted on glass slides for α -SMA immunofluorescent labeling. Briefly, samples were fixed in ice-cold methanol, 30 min at -20°C. After fixation samples were washed once in PBS followed by 3 washing steps in PBS-Tween 0.3%. Primary antibody, anti- α -SMA (1:500), was supplemented in PBS/BSA 3 % (w/v) and incubated ON at 4°C. Samples were further washed 3 times PBS-Tween 0.3% before the addition of secondary antibody. Goat anti-mouse conjugated to Alexa Fluor™ 488, 1:1000 (Invitrogen) was incubated 1h at RT. Then slides were washed again 3 times in PBS-Tween 0.3% and cell nuclei counterstained with DAPI at 1 μ g/mL, 5 min, RT. Finally, samples were washed in PBS-Tween 0.3% and a drop of antifading mounting medium ProLong (Thermo Fischer Scientific) added. Images were acquired in a confocal spectral LSM980 microscope (Zeiss) operating at high resolution, XY = 120 nm and Z = 350 nm, using the Airy Scan mode and a plan apochromat 63X/1.40 oil objective. 12 random sections with a fluorescence intensity dynamic range of 16 bytes were further quantified using Image J NIH software. SMA fluorescent signal was normalized in front of the number of cell nuclei per section.

6.2.4 *IN VIVO* α -SMA DETECTION IN MDA-MB-231 ORTHOTOPIC MODEL

A total number of 1,000 cells of either MDA-MB-231.Fluc2-C19. CSC or DCC were orthotopically inoculated IMFP (n = 8) in a PBS:Matrigel 1:1 solution. Tumor growth was monitored twice a

week by conventional caliper measurements. When tumors reached a volume range between 250–450 mm³, tumors were excised and paraffin embedded for histological analysis. Standard trichrome Masson staining and α -SMA immunodetection (further detailed in 7.3 section) were performed in order to visualize α -SMA+ infiltrating fibroblasts.

6.2.5 FIBROBLASTS 3D INVASION ASSAY

1×10^5 cells/mL of either CCD19 human lung fibroblasts or CAFs IDC were seeded in P10 plates and 25 μ g/mL of either EVs^{CSC} or EVs^{DCC} were added to growing cells for 3 consecutive days. Then, lung fibroblasts and CAFs were trypsinized to single-cell suspension, centrifuge and resuspended with 3 mL of culture medium containing 2 μ L of CellTrackerTM staining solution. Then, same procedure for 3D invasion assays described before was followed, with the peculiarity that no cancer cells but only EVs educated fibroblasts were used in this experiment.

6.3 TUBE FORMATION ASSAY

Capacity to promote vessel-like tube formation was assessed as described elsewhere^[49]. Briefly, human EPCs were resuspended in basal medium without growth factors (EBM2, Lonza) and seeded at 20,000 cells per well in growth factor reduced Matrigel (Corning) following manufacturer's protocol. Note that Matrigel was thawed at 4°C, dispensed in the microslides (Ibidi) and allowed to polymerize at 37°C till producing a uniform semisolid ECM cell-support prior. Immediately after cell seeding cells were treated with either 25 μ g/mL EVs^{CSC} or EVs^{DCC} suspensions or basal media (as control condition). After ON incubation at 37°C and 5% CO₂ images were taken at 4x and analyzed blindly using Wimtube online tool. Tube length, branching points and total loops were quantified as relevant features for tube formation capacity. Tubulogenesis parameters of the control condition (basal media) were used as a reference value for the EVs treatments.

7 EVS ROLE IN PRE-METASTATIC NICHE CONDITIONING STUDIES

7.1 BIODISTRIBUTION ASSAY

EVs^{CSC} and EVs^{DCC} biodistribution studies were performed by intravenously administration of 300 μ g DiR-labeled EVs^{CSC} or EVs^{DCC} through the mouse tail vein. After 24 h, animals were euthanized and *ex vivo* DiR-EVs localization was assessed using an IVIS[®] Spectrum equipment for image acquisition and Living Image SoftwareTM to further quantify the fluorescent signal (FLI). FLI was normalized to the weight of the wet tissue and represented as the percentage of total FLI per

animal. Lung tissues were collected, embedded in optimal cutting temperature compound (OCT) following standard procedures and stored at -80°C till further analysis.

7.1.1 LUNGS DiR-LABELED EVs ANALYSIS BY HIGH RESOLUTION CONFOCAL MICROSCOPY

OCT blocks from the biodistribution assay were processed into 5 µm thick sections using a cryostat Leica CM3050. Tissue slices were mounted on microscopy glass slides and fixed in ice-cold methanol, 30 min at -20°C. After fixation samples were immunolabeled against α-SMA and the nuclei were fluorescently dyed with DAPI, as previously described. Images were acquired in a confocal spectral LSM980 microscope (Zeiss) operating at high resolution, XY = 120 nm and Z = 350 nm, using the Airy Scan mode and a plan apochromat 63X/1.40 oil objective. 12 random sections with a fluorescence intensity dynamic range of 16 bytes were further quantified using Image J NIH software. Briefly, DiR fluorescent signal was transformed to a binary image in order to identify and count the number of particles per field. DiR labeled particle number was normalized in front of the number of cell nuclei per section.

7.2 LUNG METASTASIS MICE MODELS

In order to examine the roles of EVs^{CSC} and EVs^{DCC} in lung metastasis models, 3 total doses of 75 µg of EVs^{CSC} or EVs^{DCC} were intravenously injected into female nude mice through the tail vein every other day. On the 5th day, 1x10⁶ firefly luciferase-expressing MDA-MB-231.Fluc2-C19 cells were intravenously injected through the tail vein. After 2 months, lung metastasis were measured and quantified by ex vivo bioluminescent imaging (BLI) using IVIS Spectrum (PerkinElmer) and lung tissues were recovered for manual macrometastasis and micrometastasis counting and further processed for hematoxylin-eosin staining analysis and evaluation by a trained histopathologist.

7.3 IMMUNOHISTOCHEMISTRY

The presence of Vimentin, α-SMA and NANOG proteins were assessed in paraffin-embedded formalin fixed sections. Slides were incubated with 10% normal goat serum (NGS) in antibody diluent (1% BSA (w/v) in 100 mM Tris buffer) and then primary antibodies were added, ON at 4°C (see Table 7). Next horseradish peroxidase-conjugated secondary antibody, anti-Mouse o anti-Rabbit, as required, was added to the samples (Dako, EnVision+ System-HRP Labeled Polymer). Finally, the sections were developed with diaminobenzidine (DAB) colorimetric reagent

solution (Dako) and counterstained with Harris hematoxylin (Sigma-Aldrich). Extensive washing in PBS/Tween 20, 1% (v/v) was performed before and after antibody incubations steps.

7.3.1 IHC LABELING EVALUATION

Evaluation of **vimentin** labeling to assess MDA-MB-231 metastatic cells dissemination was determined by the allocation of staining score values from 0 (0 % staining coverage) to 3 (100 % staining coverage) to the individual sections and subsequent mean score (MS) calculation for each group. 18 random sections in a 4X magnification per mice group (8 mice/group) were analyzed and total lungs sections area covered by vimentin positive cells was qualitatively scored and represented.

Evaluation of **α -SMA** labeling was used to assess the number of infiltrated CAFs and blood vessels in lung metastatic lesions. 18 random sections in a 4x magnification per mice group were analyzed for each parameter. For CAFs infiltration assessment, total lungs sections area covered by α -SMA positive fibroblasts like cells was qualitatively scored and represented, staining score values ranging from 0 (0 % positive area) to 3 (100 % positive area). Each evaluation was made blindly by 3 independent observers. The number of blood vessels was quantitatively assessed by manually counting the number of α -SMA positive blood vessels in 18 random lung sections per mice group. Subsequent mean score for both parameters was then calculated for each group.

NANOG labeling was qualitatively assessed in 3 random sections at 4X, 10X and 20X magnifications. Representative images were displayed.

8 CARTOONS

All the images, schemes and figures presented in this thesis were manually created with Biorender.com online application.

9 STATISTICAL ANALYSIS

Bar graphs display mean value \pm standard error of the mean (SEM). Statistical analysis consisted in normality data distribution assessment by Kolmogorov-Smirnov test. If data fitted into a normal distribution, unpaired Student's t-test, for single comparison of means, or one-way ANOVA

for multiple comparisons was then applied. Otherwise, non-parametric Mann-Whitney test or Tukey test were employed for single and multiple mean comparisons respectively.

Data represented as Fold Change (FC) were normalized following the $X = \text{Log}(\text{FC})$ function. Columns statistics were then used to assess the mean difference in comparison to a theoretical $\text{Log}(\text{FC})$ value equal to 0. The significance threshold was established at $p < 0.05$, and significance levels were schematically assigned $^*(0.01 \leq p < 0.05)$, $^{**}(0.001 \leq p < 0.01)$, $^{***}(0.0001 \leq p)$. All the analyses and graphs were performed using GraphPad Prism 6 software (GraphPad, San Diego).

Target protein	Origin	Application	Dilution	Reference
<i>CD81</i>	Mouse	WB	1:300	Santa Cruz, sc-7637
<i>Tsg101</i>	Rabbit	WB	1:1000	Abcam, ab30871
<i>ALIX</i>	Rabbit	WB	1:1000	Abcam, ab76608
<i>β-Tubulin</i>	Mouse	WB	1:2000	Invitrogen, BT7R
<i>ALDH1A1</i>	Mouse	WB	1:500	Santa Cruz, sc-374149
<i>CD44</i>	Mouse	WB	1:1000	Cell Signaling, 156-3C11
<i>NANOG</i>	Rabbit	WB/IHC	1:1000/1:500	Thermo Fisher, PA1-097X
<i>SOX9</i>	Rabbit	WB	1:1000	Sigma-Aldrich, AB5535
<i>ITGB1</i>	Rabbit	WB	1:5000	Abcam, ab179471
<i>ITGα6</i>	Mouse	WB	1:300	Santa Cruz, sc-374057
<i>αSMA</i>	Mouse	WB/IHC/IF	1:1000/1:400/1:500	Sigma-Aldrich, A2547
<i>Vimentin</i>	Rabbit	IHC	1:200	Abcam, ab92547

Table 7. Primary Antibodies.

RESULTS

RESULTS

1 DEVELOPMENT AND VALIDATION OF BCSC MODELS

1.1 *ALDH1A1:tdTOMATO* REPORTER TAGS BCSC

1.1.1 BREAST CSC MODEL *IN VITRO* VALIDATION

In order to tag and isolate CSC from heterogeneous cancer cell populations we used the CSC model previously established in our group^{378,379}. This CSC model allows the identification and separation of CSC-like cells from heterogeneous cancer cell subpopulations using a CSC reporter vector. In this vector, the expression of the tdTomato fluorescent protein (tdTomato+) is under the control of the CSC specific *ALDH1A1* promoter. Besides, cancer cells that do not express the fluorescent reporter (tdTomato-) are considered to constitute the DCC population.

To further validate our CSC model, breast cancer MCF-7 and TNBC MDA-MB-231 and HCC1806 cell lines were stably transfected with *ALDH1A1:tdTomato* reporter. Once the cell lines were stably transfected, CSC and DCC cell subpopulations were obtained by FACS according to their tdTomato fluorescence (**Figure 16A**) and the stemness profile of tdTomato expressing cells (CSC) was explored. Expectedly, after isolation, cultured tdTomato+ cells displayed red fluorescence while no fluorescence was observed in cultured tdTomato- cells (**Figure 16B**). Gene expression analysis of MCF-7, MDA-MB-231 and HCC1806 tdTomato+ cells revealed a significant upregulation of stemness gene reporters *ALDH1A1*, *Nanog*, *Oct-4*, *ABCG2* and *Notch* in comparison to the tdTomato- cell subpopulation (**Figure 16C-E**). Moreover, MCF-7, MDA-MB-231 and HCC1806 tdTomato+ cancer cells displayed significantly higher relative invasive capacities in 2D invasion models than isolated tdTomato- cells (**Figure 16F-H**). Besides, MDA-MB-231 tdTomato+ cells also formed mammospheres displaying red fluorescence when cultured in LA conditions (**Figure 16I**). Accordingly, previous data from our group showed that MCF7 and MDA-MB-231 tdTomato+ cells exhibited higher expression of stemness and EMT related genes and displayed higher mammosphere formation efficiency than the tdTomato- cell subpopulation^{378,379}.

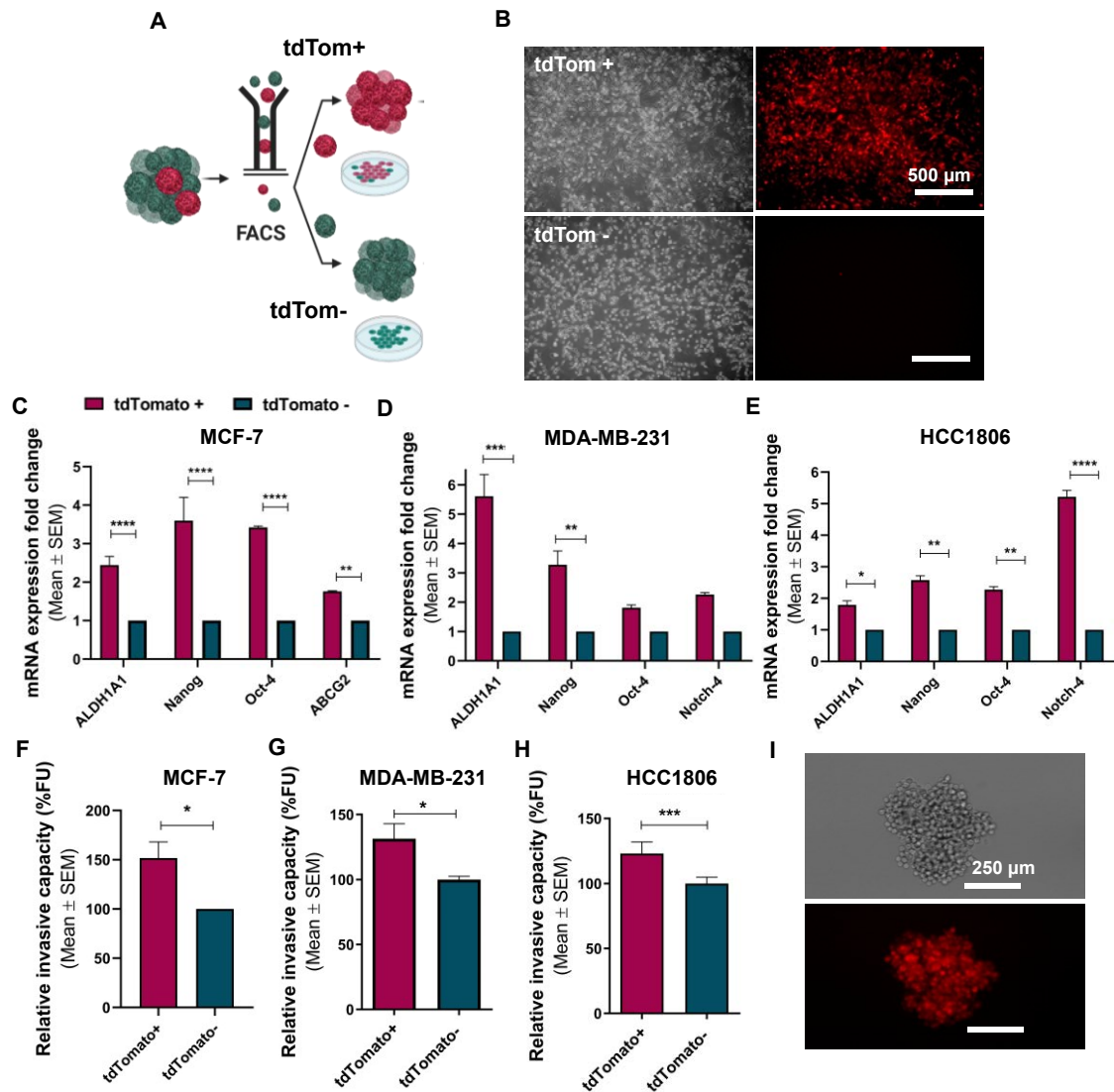


Figure 16. *ALDH1A1:tdTomato* CSC model *in vitro* validation. (A) After stable transfection with the reporter vector, MDA-MB-231 CSC express the fluorescent protein under the CSC-specific promoter (*ALDH1A1*), which allows CSC identification and isolation from phenotypically heterogeneous cancer cell populations by FACS. (B) MDA-MB-231 isolated cells showing red fluorescence in culture (*tdTom*⁺) correspond to the CSC subpopulation, while cells which do not present *tdTomato* fluorescence (*tdTom*⁻) would conform the bulk cancer cell DCC subpopulation. (C-E) Stemness gene expression profile assessed by RT-qPCR of *tdTomato*⁺ cell population (CSC) compared to *tdTomato*⁻ cell population (DCC) in MCF-7, MDA-MB-231 and HCC1806 breast cancer cell lines. Samples were obtained by cell sorting according to *tdTomato* fluorescence (P0). (F-H) Relative invasiveness of MCF-7, MDA-MB-231 and HCC1806 *tdTomato*⁺ cells compared to *tdTomato*⁻ cells assessed by 2D invasion assays. (I) Representative confocal microscopy image of a mammosphere formed by MDA-MB-231 *tdTomato*⁺ displaying red fluorescence when cultured in LA conditions.

Additionally, and on the basis of a recent study showing that mechanically active heterotypic adhesions between CAFs and cancer cells enables cooperative tumor invasion³⁸⁰, we used

multifactorial 3D invasion models to study differences between MDA-MB-231 tdTomato+ and tdTomato- (CSC and DCC) behavior in coordination with stromal cells. As CSC populations are believed to lead the invasive front in tumors³⁸², we aimed to study if either MDA-MB-231 CSC or DCC subpopulations preferentially guided tumor invasion together with CAFs. To this end, a mix of fluorescently labeled breast CAFs, CSC and DCC cell populations were embedded in Matrigel® plus collagen matrix which allowed to form 3D spheroids (**Figure 17A**). After 48h spheroids invaded the surrounding 3D matrix by forming invasive cell strands as they degraded artificial ECM components (**Figure 17B**). A profound analysis of the spheroids imaged with confocal microscopy showed that CAFs preferentially associated with CSC-like cells to guide the invasive strands. Specifically, CSC were found leading the invasive strand together with CAFs in nearly 70 % of cases while the association between CAFs-DCC was only observed in 35% of cases (**Figure 17C**). Those results confirmed the invasive nature of isolated tdTomato+ cells according to their CSC-like phenotypes.

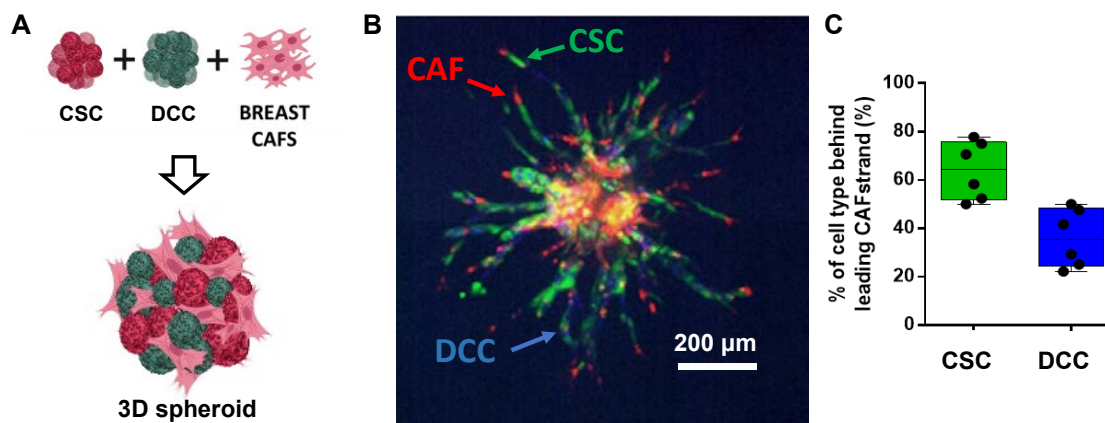


Figure 17. CSC lead the invasive front together with CAFs. (A) Schematic representation of experiment design. **(B)** Representative Z stack projection of a spheroid conformed by CAFs, CSC and DCC invading the surrounding 3D Matrix. **(C)** Graph representing the % of cases in which CSC or DCC were leading the invasive front of strands together with CAFs.

BREAST CSC MODEL *IN VIVO* VALIDATION

1.1.1.1 HCC1806 ORTHOTOPIC MODEL

CSC phenotype of HCC1806 tdTomato+ cells was further validated *in vivo* by our group (data not published). HCC1806 tdTomato+ cells were able to generate tumors in xenografts at low density concentrations more efficiently than their tdTomato- counterpart. Orthotopic IMFP injection of nude immunodeficient mice with growing amounts of either HCC1806 tdTomato+ or tdTomato- cells (1,000, 10,000 and 100,000) revealed differences in the tumor incidence between groups.

Specifically, the tumor incidence was 100% for both groups inoculated with 100,000 and 10,000 of sorted tdTomato+ and - cells. However, the tumor incidences obtained for the group inoculated with 1,000 tdTomato- cells was 20% while for the group inoculated with 1,000 tdTomato+ cells remained at 100% (**Figure 18**). These results supported the CSC-like nature of isolated tdTomato+ cells. Of note, MCF7 tdTomato+ cells also displayed higher tumorigenic potential when they were transplanted into mammary xenograft model³⁷⁹.

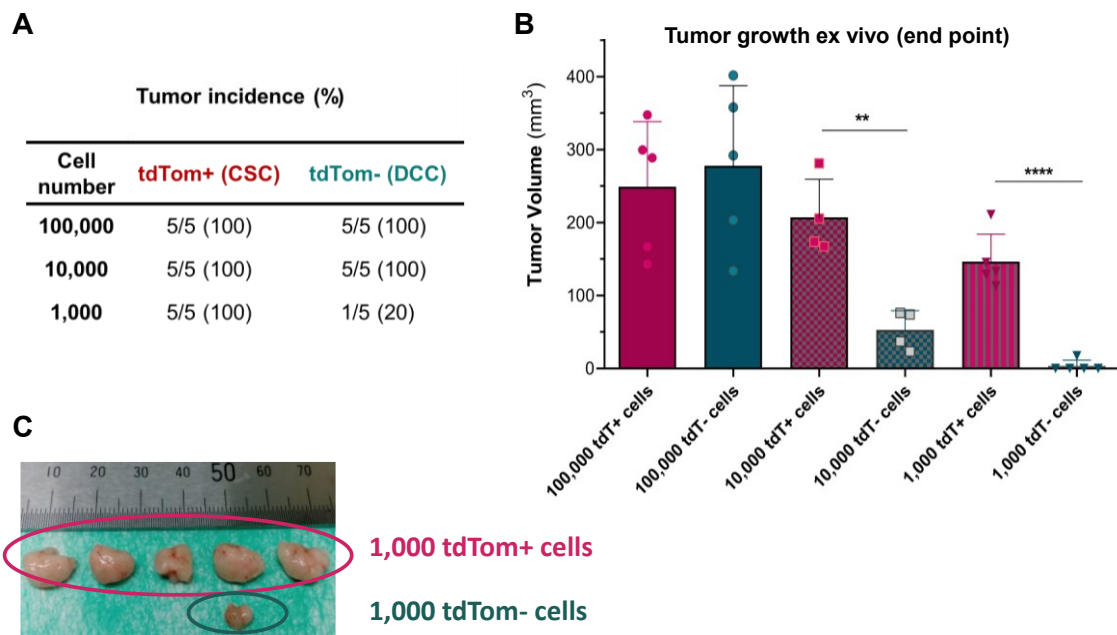


Figure 18. HCC1806 ALDH1A1:tdTomato CSC model *in vivo* validation. (A) Tumor incidence in mice orthotopically inoculated with serial cell dilutions of HCC1806 tdTomato+ cells and HCC1806 tdTomato- cells, respectively. (B) Ex *in vivo* tumor growth at the endpoint of the experiment. Statistically significant differences were detected between groups inoculated with 1,000 and 1,000 cells of tdTomato+ and tdTomato- cells, respectively. (C) Images of tumors formed in mice initially challenged with 1,000 cells are presented.

1.1.1.2 MDA-MB-231 METASTATIC MODEL

To finally explore if the initial stemness nature of inoculated CSC vs DCC was maintained in a lung metastasis model, MDA-MB-231 isolated tdTomato+ (CSC) and tdTomato- (DCC) populations were i.v. injected into BalbC NOD/SCID mice. At the end of the experiment lungs were collected and the stemness nature of MDA-MB-231 CSC and DCC derived metastatic lesions were evaluated (**Figure 19A**). Nanog IHC performed in lung tissues revealed clear differences in the expression of this stemness reporter, as MDA-MB-231 metastatic cells CSC exhibited higher signal than their DCC counterparts. These results confirmed that the stemness nature of inoculated tdTomato+ cells was also maintained, at least partially, in metastatic sites (**Figure 19B, C**).

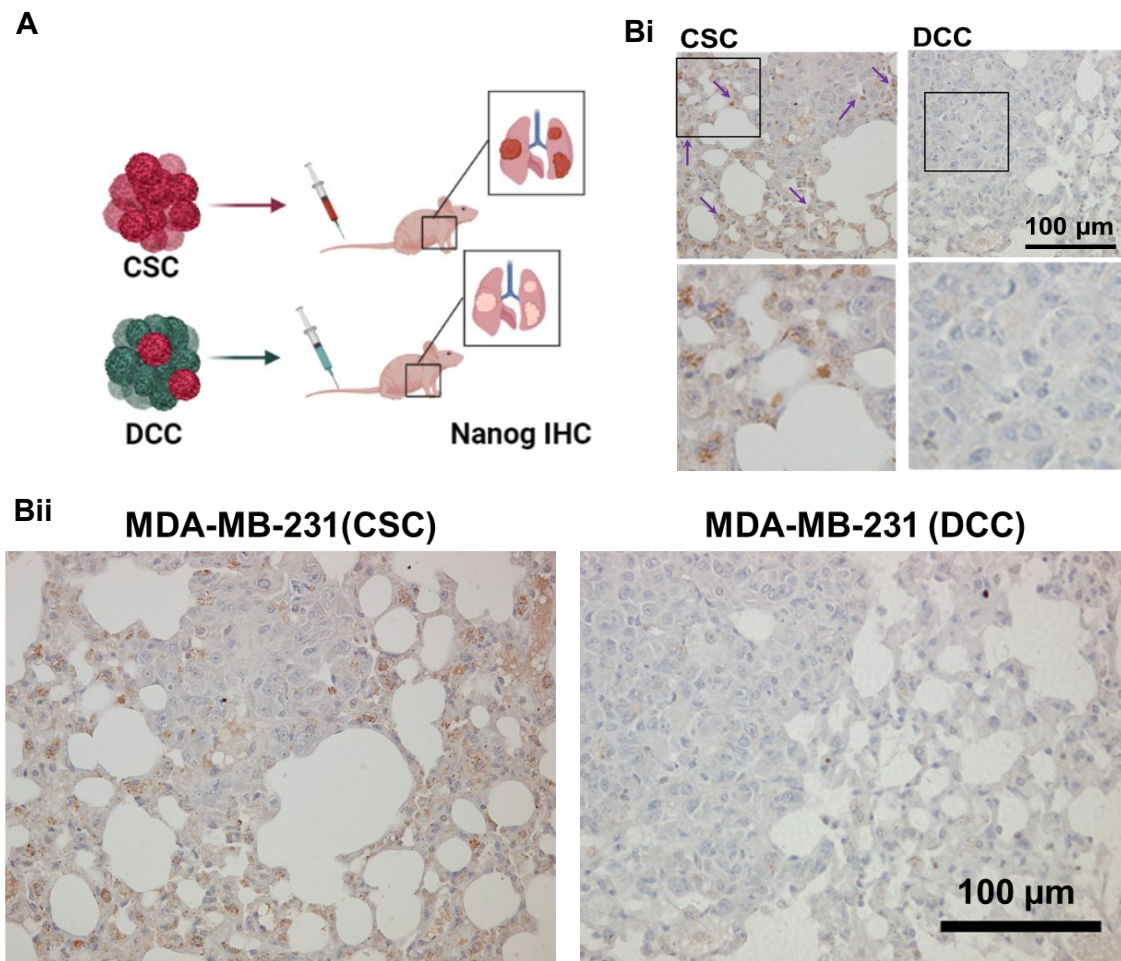


Figure 19. NANOG protein expression in MDA-MB-231 lung metastases. (A) Scheme displaying the distinct conditions tested with the lung metastasis mouse model. Specifically, CSC or DCC cells isolated from MDA-MB-231:ALDH:tdTomato cells were injected into the tail vein and metastasis let to grow for 2 months., At the experimental endpoint lungs were excised and processed for histological analysis. **(Bi, Bii)** NANOG protein expression in metastatic lungs of mice i.v. injected with MDA-MB-231 CSC and DCC cells. Scale bars= 100 μm.

1.1.2 GENERATION OF TNBC SYNGENIC CSC MODEL

We further aimed to generate a new syngenic TNBC CSC model following the same strategy used for human BCSC models. For this purpose, 4T1 cell line was stably transfected with a murine *ALDH1A1:tdTomato* reporter. After transfection, tdTomato⁺ cells were observed in culture (**Figure 20A**). TdTomato⁺ subpopulation displaying red fluorescence was isolated by FACS (**Figure 20B**) and stemness features were examined. As expected, tdTomato⁺ cells displayed stem-associated characteristics when compared to unsorted parental 4T1 cancer cell line. Specifically, 4T1 tdTomato⁺ isolated cells showed typical stemness gene expression signature showing increased expression of pluripotency genes *ALDH1A1*, *Nanog*, *Oct-4*, *Sox-2* and *Notch-4* compared

to parental cell line (**Figure 20C**). Moreover, tdTomato⁺ cells also exhibited increased relative invasive capacity (**Figure 20D**) and higher mammosphere formation efficiency when compared to parental cancer cells (**Figure 20E**). Thus, these results confirmed the CSC-like phenotype of isolated tdTomato⁺ cells, validating this strategy to efficiently identify CSC populations within this heterogeneous murine breast cancer cell line.

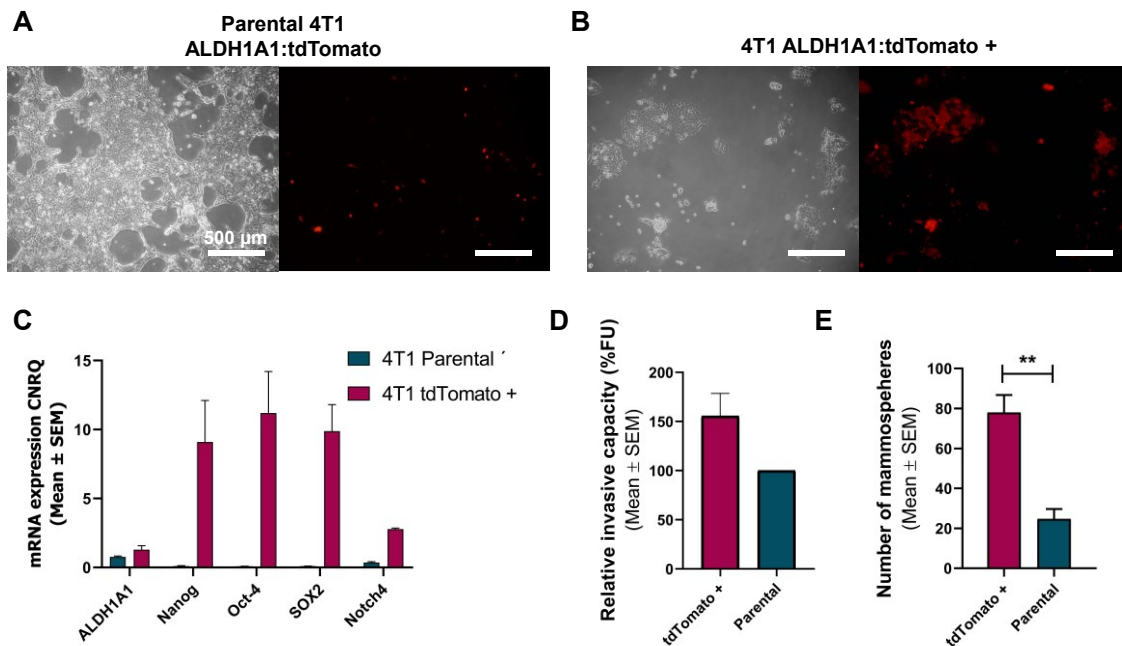


Figure 20. 4T1 ALDH1A1:tdTomato CSC model in vitro validation. (A) Representative images of 4T1 parental cell line stably transfected with ALDH1A1:TdTomato reporter. (B) Representative image of flow sorted 4T1 ALDH1A1:tdTomato⁺ cell subpopulation. (C) Stemness gene expression profile 4T1 parental cells and isolated 4T1 tdTomato⁺ cells assessed by qPCR. (D) Invasive capacity of parental and tdTomato⁺ cells assessed by 2D invasion assay. (E) Mammosphere formation efficiency of 4T1 parental and tdTomato⁺ cell subpopulations.

2 STUDY OF CSC/DCC PLASTICITY

2.1 ISOLATED CSC AND DCC SUBPOPULATIONS SHOW PHENOTYPIC DYNAMIC EQUILIBRIUM

Numerous studies indicated that CSC and DCC showed plasticity and tended to reach a dynamic equilibrium between both phenotypic states¹⁷³⁻¹⁷⁷. In order to assess if previously characterized tdTomato⁺ (CSC) and tdTomato⁻ (DCC) subpopulations followed this dynamic equilibrium model, MCF-7, MDA-MB-231 and HCC1806 CSC and DCC were cultured in attachment conditions and the % of tdTomato⁺ cells and the stemness expression signature of each subpopulation was tracked over cell passages (**Figure 21A**). As expected, CSCs isolated from MDA-MB-231, MCF-7 and HCC1806 ALDH1A1:tdTomato cell lines lost red fluorescence over time, showing a drop in the % of tdTomato⁺ cells over passages as CSC differentiated into DCC and reached the appropriate % of CSC in equilibrium (**Figure 21C-E**). Indeed, MDA-MB-231 CSC significantly decreased stemness gene expression after a few passages, denoting a fast tendency to differentiate into DCC (**Figure 21B**). Interestingly, DCCs isolated from MDA-MB-231, MCF-7 and HCC1806 tumor cells progressively acquired stem features in culture. Specifically, a boost in stem gene expression was observed for DCC subpopulations of each cancer cell line over cell passages, from P0 AS to P5, when they were grown in the absence of CSC population (**Figure 21F-H**). Of note, red fluorescence was also re-detected over time in culture (**Figure 21I**). Those results suggested that cancer cells undergo cell state transitions between CSC and DCC subpopulations to restore initial population equilibrium (**Figure 21J**).

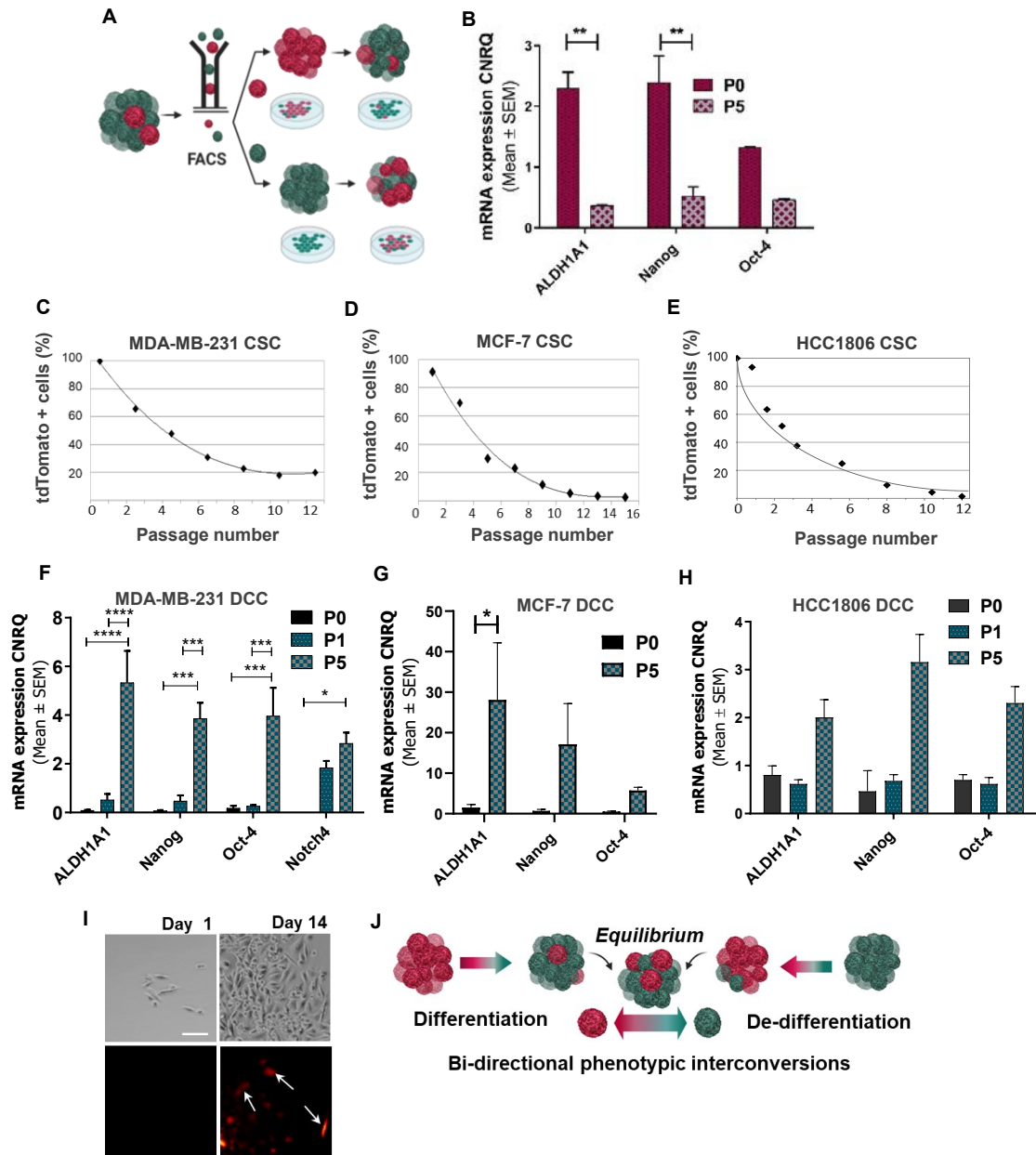


Figure 21. CSC/DCC phenotypic equilibrium. (A) Schematic representation of CSC and DCC behavior in attachment culture conditions after FACS isolation. (B) Stemness gene expression profile of MDA-MB-231 CSC at P0 (after sorting) and P5 assessed by RT-qPCR analysis. (C-E) % of red fluorescent cells in isolated MDA-MB-231, MCF-7 and HCC1806 CSC population over cell passages assessed by flow-cytometry. (F-H) Stemness gene expression profile of isolated MDA-MB-231, MCF-7 and HCC1806 DCC at P0, P1 and P5 AS assessed by RT-qPCR analysis. (I) Representative fluorescent images of MDA-MB-231 DCC at Days 1 and 14 AS. (J) Scheme showing bidirectional interconversion between CSC and DCC phenotypic states to restore initial CSC/DCC equilibrium.

3 ROLE OF CSC AND DCC DERIVED EVs ON GUIDING PLASTICITY

3.1 MDA-MB-231 *IN VITRO* MODEL SET UP FOR CSC AND DCC DERIVED EVs ISOLATION.

Among the panel of breast CSC models developed and validated, MDA-MB-231 cell line represents the TNBC cell line with the most aggressive phenotype in concomitance with the lower differentiated nature³⁸⁸. Besides, MDA-MB-231 cells usually overexpress EMT-related markers, and previous studies carried by our group showed that not only CSC but also DCC were equally tumorigenic, denoting also the plastic nature of this cancer cell line³⁷⁸. Besides, MDA-MB-231 cell line showed a higher % of CSC in the equilibrium (10-15%) compared to the other cell lines studied (less than 5% of CSC). Additionally, the MDA-MD-231 cell line represents a well-established model for breast cancer metastasis research³⁸³. Accordingly, we decided to principally focus our EVs research on this challenging TNBC cell line. In parallel, some additional experiments were also performed with MCF-7 and HCC1806 EVs to complement and support our main research line.

Cell line	Origin	Phenotype	%CSC	Plasticity	Tumorigenicity
MDA-MB-231	Breast (Triple Negative)	Mesenchymal	High	Yes	CSC and DCC are equally tumorigenic
HCC1806	Breast (Triple Negative)	Mesenchymal	Low	Yes	CSC are more tumorigenic
MCF-7	Breast (ER+)	Epithelial	Low	Yes	CSC are more tumorigenic
4T1	Mouse breast (Triple Negative)	Mesenchymal	High	Unknown	Unknown

Table 8. Breast cancer models features.

The phenotypic state transitions observed in regular cell culture for MDA-MB-231 CSCs and DCCs hindered the maintenance of pure CSC and DCC subpopulations. While isolated MDA-MB-231 tdTomato+ cells tended to differentiate in continuous culture, flow sorted and cultured MDA-MB-231 ALDH:tdTomato- cells could not be maintained as DCC over time due to their tendency to re-acquire stemness features in order to restore the CSC population. Therefore, prior to EVs production, MDA-MB-231 CSC and MDA-MB-231 DCC *in vitro* cell propagation was optimized. Specifically, we developed a strategy to efficiently mitigate the differentiation and de-differentiation processes for a certain period, allowing the cell subpopulations of interest to grow with limited loss of their initial features. Briefly, FACS isolated tdTomato+ cells were cultured to

expand the CSC subpopulation and then resorted to obtain 100% pure CSC cells. On one hand, the use of a specific stemness media (serum-free media supplemented with a growth factor cocktail, fully detailed in M&M section) allowed us to maintain pure CSCs in culture over passages avoiding their differentiation (**Figure 22A**). On the other hand, DCCs cultured in presence of a minimal fraction (1-2%) of CSCs avoided their de-differentiation towards stem phenotypes (**Figure 22B**). This protocol is meticulously detailed in M&M section. Under this setup, we obtained two different MDA-MB-231 cell subpopulations according to their content of tdTomato+ cells, namely high tdTomato+ cells (99%), (CSC), and low tdTomato+ cells (1-2%), (DCC). When stemness markers were studied, MDA-MB-231 CSC showed significantly higher mRNA levels of prevalent stemness gene reporters, *ALDH1A1*, *Nanog*, and *Oct-4*, than MDA-MB-231 DCC ($p=0.0017$; $p=0.0002$ and $p=0.0001$, respectively). Specifically, using these culture conditions *ALDH1A1* gene expression in CSCs was increased from 0.5789 ± 0.07208 CNRQ (Calibrated Normalized Relative Quantity) up to 12.19 ± 2.472 NRQ, *Nanog* from 0.495 ± 0.029 CNRQ up to 10.24 ± 2.911 CNRQ and *Oct-4* from 0.716 ± 0.069 CNRQ up to 7.236 ± 2.375 CNRQ in comparison to DCCs. (**Figure 22C**). Isolated populations also showed clear differences in red fluorescence (**Figure 22D**).

Given the significant differences observed in stemness markers expression between both cell populations, we reliably proceeded to EVs isolation. CSC EVs isolated from the CM of MDA-MB-231 CSC subpopulation were accordingly named EVs^{CSC} while EVs isolated from the CM of MDA-MB-231 DCC subpopulation were designated as EVs^{DCC} (**Figure 22E**). Parallely, EVs from HCC1806 and MCF-7 with CSC and DCC stemness profiles were also isolated for complementary studies. EVs isolation protocols are detailed in M&M section. Of note, prior to each EVs production batch MDA-MB-231 CSC and MDA-MB-231 DCC stemness gene reporter expression was confirmed.

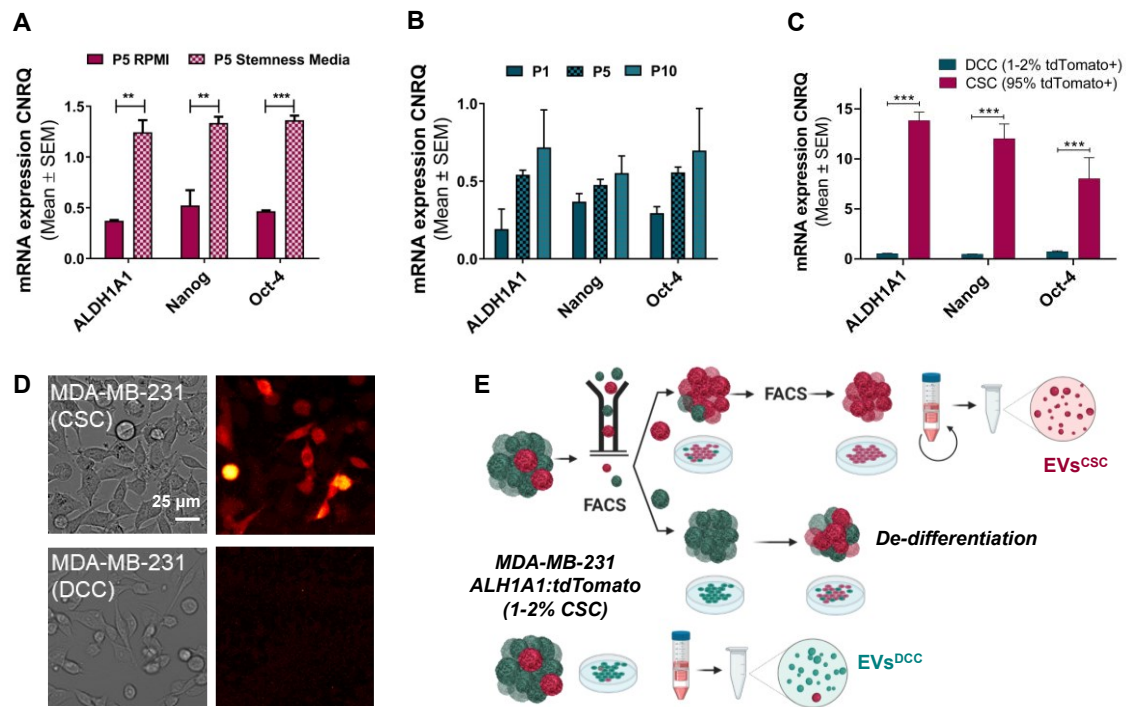


Figure 22. CSC and DCC in vitro culture optimization for MDA-MB-231 EVs^{CSC} and EVs^{DCC} isolation. (A) Stem gene expression of MDA-MB-231 tdTomato⁺ cells at passage 5 (P5) after cell sorting in different culture conditions: RPMI conventional media vs. stemness media. (B) Stem gene expression profile of MDA-MB-231 with 1-2% content of tdTomato⁺ cells maintained in culture at different passages (1, 5 and 10). (C) Gene expression of stemness reporters *ALDH1A1*, *Nanog* and *Oct-4* in CSC and DCC detected by qPCR. (D) Representative fluorescence images of CSCs and DCCs, scale bar = 25 μm. (E) Schematic illustration of EVs isolation procedure. Briefly, MDA-MB-231 tdTomato⁺ cells were cultured with stem cell maintenance media. EVs^{CSC} were isolated from the CM of these MDA-MB-231 CSC cells, which presented high expression of stemness reporters. Due to tdTomato⁻ sorted cells tendency to de-differentiate into CSC, EVs^{DCC} were isolated from a stable MDA-MB-231 cell subpopulation with a minimal content in CSC (1-2%) that exhibited low expression of stemness reporters, as most cells were DCC.

3.2 MDA-MB-231 CSC-LIKE STATE DICTATES EVs PROTEIN CARGO

EVs secreted from both MDA-MB-231 CSC (EVs^{CSC}) and MDA-MB-231 DCC (EVs^{DCC}) were successfully isolated by charge neutralization-based precipitation. Both types of EVs presented pseudo-spherical morphologies as observed by CryoTEM and STORM imaging (Figure 23A, B) with a size distribution ranging from 100 to 300 nm in diameter. EVs^{CSC} and EVs^{DCC} DLS analysis revealed the mean peak around 200 nm diameter while NTA placed the main peak at 145 nm in diameter for both types of vesicles although a minor population of bigger particles could be detected in all samples (Figure 23C, D). The presence of typical EV protein markers such as CD81, TSG101 and ALIX indicated that the isolated EVs were enriched with the exosome fraction (Figure 23E). Low

β -tubulin occurrence in EVs samples confirmed them free from significant cell debris contamination. Furthermore, to investigate possible differences in the internalization of EVs derived from CSC and DCC, the uptake of fluorescently labeled EVs^{CSC} and EVs^{DCC} into parental MDA-MB-231 cells and CCD19 lung fibroblasts was assessed. Fluorescently labelled EVs were supplemented into parental MDA-MB-231 and CCD19 cell cultures. After 6 h of incubation, confocal fluorescence microscopy imaging of fixed cells revealed a spotted fluorescent signal pattern in both, tumor cells and fibroblasts, suggesting that EVs entered into recipient cells. **(Figure 23F, G)**. These rounded structures probably corresponded to clusters of EVs being gathered within endosomal vesicles. Nevertheless, detail provided by STORM imaging also showed much smaller structures within cell cytoplasm matching the size of individual EVs **(Figure 23H)**. Moreover, further analysis performed by flow cytometry revealed no differences in the uptake kinetics profile between EVs^{CSC} and EVs^{DCC} by MDA-MB-231 CSC and DCC cells, respectively **(Figure 23I)**. These data suggested that EVs^{CSC} and EVs^{DCC} internalization into recipient cells was not mediated by specific receptors present in the membrane of recipient CSC or DCC cells, respectively. Interestingly, despite their similarities in size, shape, delivery capacity and even protein EVs signature, differences in the stemness specific protein cargo were clearly detected. EVs^{CSC} presented higher levels of typical stemness protein markers such as ALDH1A1, CD44, SOX9, NANOG, OCT4 and E-Cadherin than EVs^{DCC} **(Figure 23J)**. These data confirmed that EVs reflected their original cell state nature.

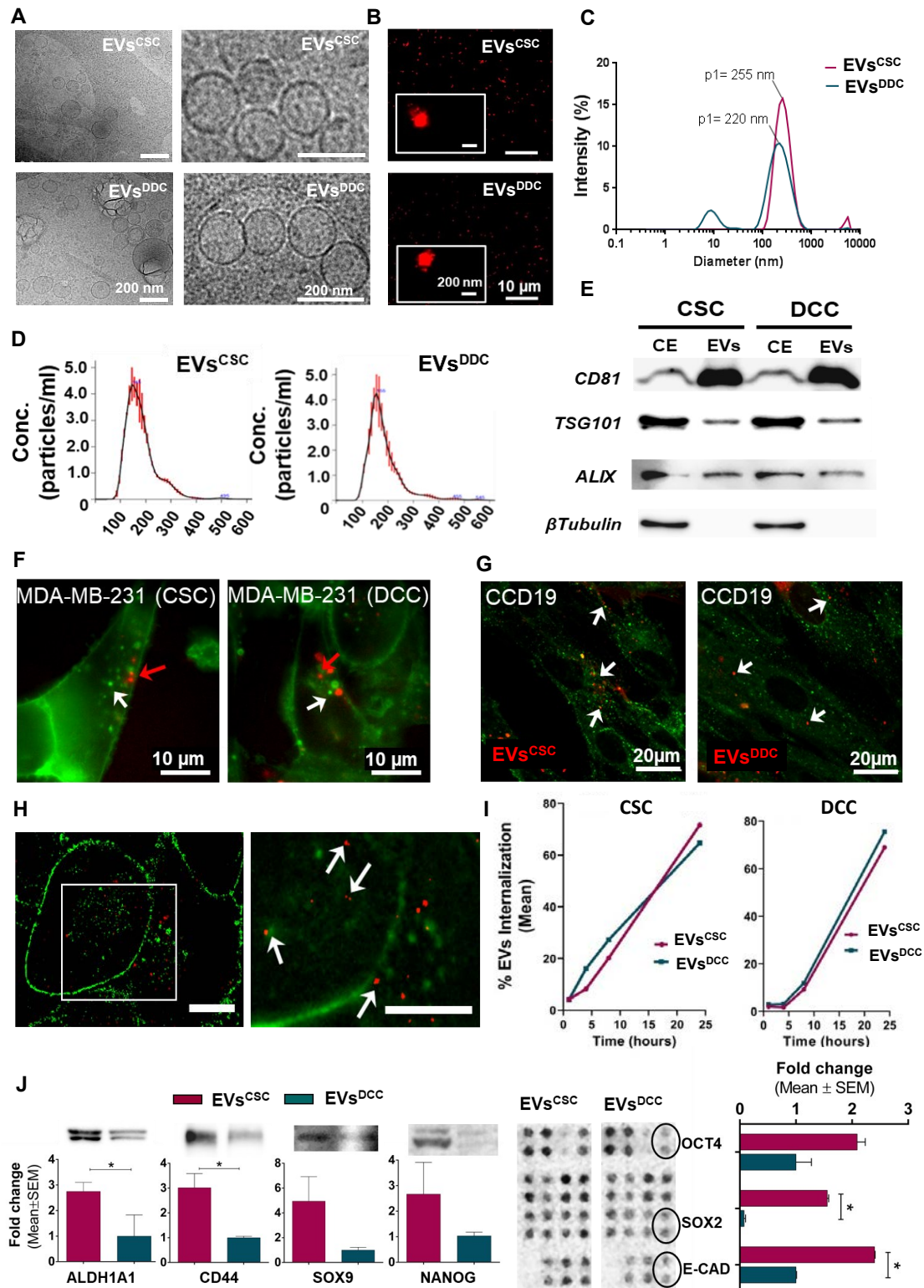


Figure 23. EVs^{CSC} and EVs^{DCC} characterization. (A) CryoTEM imaging of isolated EVs^{CSC} and EVs^{DCC}. (B) STORM imaging of isolated EVs previously labeled with DiD. (C) EVs^{CSC} and EVs^{DCC} DLS analysis (D) NTA analysis of isolated particles. (E) Molecular characterization by WB of EVs typical markers, CD81, TSG101 and ALIX and cell lysate control, β-tubulin. 20 μg of total protein was loaded per lane (F, G) Representative images from fluorescence microscopy of DiD-labeled EVs^{CSC} (red) and DiOC-labeled EVs^{DCC} (green) inside MDA-MB 231 cells (green), *left panel* and DiD-labeled EVs^{CSC} and EVs^{DCC} (red) in CCD19 cells (green), *right panel*. Arrows indicate EVs. (H) STORM

detailed images of EVs internalization into MDA-MB-231 parental cells. Arrows indicate DiD labeled EVs (red). Scale bar=10 μm . **(I)** Internalization kinetics of EVs^{CSC} and EVs^{DCC} in MDA-MB-231 DCC and CSC subpopulations, respectively. **(J)** EV^{CSC} and EVs^{DCC} stem-related protein cargo. ALDH1A1, CD44, SOX9 and NANOG examined by WB and OCT4, SOX2 and E-Cadherin extracted from Human Pluripotent Stem Cell Array Kit. Results are expressed as the FC in the band/dot blot intensity for EVs^{CSC} in respect to EVs^{DCC}. Array results are expressed as integrated density intensity (*p < 0.05).

3.3 EVs^{CSC} AND EVs^{DCC} CONTROL TUMOR CELLS PLASTICITY TOWARDS CSC OR DCC PHENOTYPES

Our previous results showed that in adherent cultures, CSCs divide asymmetrically, reaching a final steady state with a stable CSC population rate. In addition, CSCs tended to appear in flow sorted DCC cultures after a few days in order to regenerate the missing CSC population. These phenomena suggested that phenotypic interconversion occurred between both CSC and DCC states as response to different situations in which either CSC or DCC cell populations were predominant. In order to unravel the biological cues directing cancer cells behavior, we hypothesized that in each case, either EVs^{CSC} or EVs^{DCC} will be predominant and could mediate specific signaling in recipient cancer cells dictating cancer cells plasticity towards the appropriate phenotype to maintain CSC/DCC homeostasis. In order to test this hypothesis, we overstimulated the parental MDA-MB-231 cell line, displaying a stable number of CSCs over time (10-15%) with either EVs^{CSC} or EVs^{DCC} for 3 days. Remarkably, gene expression analysis revealed a significant reduction in the stem gene reporters' expression for tumor cells treated with EVs^{CSC}. Specifically, mRNA levels of *ALDH1A1*, *Nanog* and *Oct-4* were reduced >2-fold. Interestingly, EVs^{DCC} exerted the opposite effect (p<0,001), increasing the relative expression of *ALDH1A1*, *Nanog* and *Oct-4* >50% (**Figure 24A**). Of note, similar stem genes regulation tendency was observed in parental HCC1806 and MCF-7 cell lines incubated with EVs. HCC1806 cancer cells treated with EVs^{CSC} also decreased the level of stemness genes expression (**Figure 24B**). Moreover, the addition of EVs^{CSC} to flow sorted HCC1806 DCC in continuous cell culture tended to mitigate the boost in stemness gene expression at P5 due to DCC de-differentiation (**Figure 24D**). Finally, MCF-7 EVs^{DCC} significantly enhanced the expression of stemness reporters *ALDH1A1* and *Oct-4* in the MCF-7 parental cell line (**Figure 24C**).

Next, the impact of EVs on cell invasiveness, a largely relevant trait in tumor cell malignancy and usually associated with CSCs-like phenotype was studied. First, a 2D invasion assay was performed in cell lines supplemented with either EVs^{CSC} or EVs^{DCC}. Note that results of 2D invasion assays performed with EV producing cells, CSC and DCC, respectively, showed that MDA-MB-

231, MCF-7 and HCC1806 CSC had significantly higher invasive ability than their DCC counterparts (**Figure 24D-F**). MDA-MB-231 cells conditioned with EVs^{CSC} displayed 4,07-fold lower invasion capacity compared to untreated MDA-MB-231 cells ($p = 0.0126$) while EVs^{DCC} showed a tendency to increase invasiveness capacities, exhibiting significant ($p < 0,05$) differences when compared with EVs^{CSC} treated cells (**Figure 24E**). Similarly, we observed significant ($p < 0,05$) differences between the invasive abilities of MCF-7 parental cells treated with EVs^{CSC} and EVs^{DCC}, as while EVs^{DCC} increased cell invasion capacity, EVs^{CSC} tended to reduce this ability (**Figure 24F**). These findings supported the role of EVs^{CSC} and EVs^{DCC} on directing cancer cells plasticity towards specific CSC or DCC phenotypes.

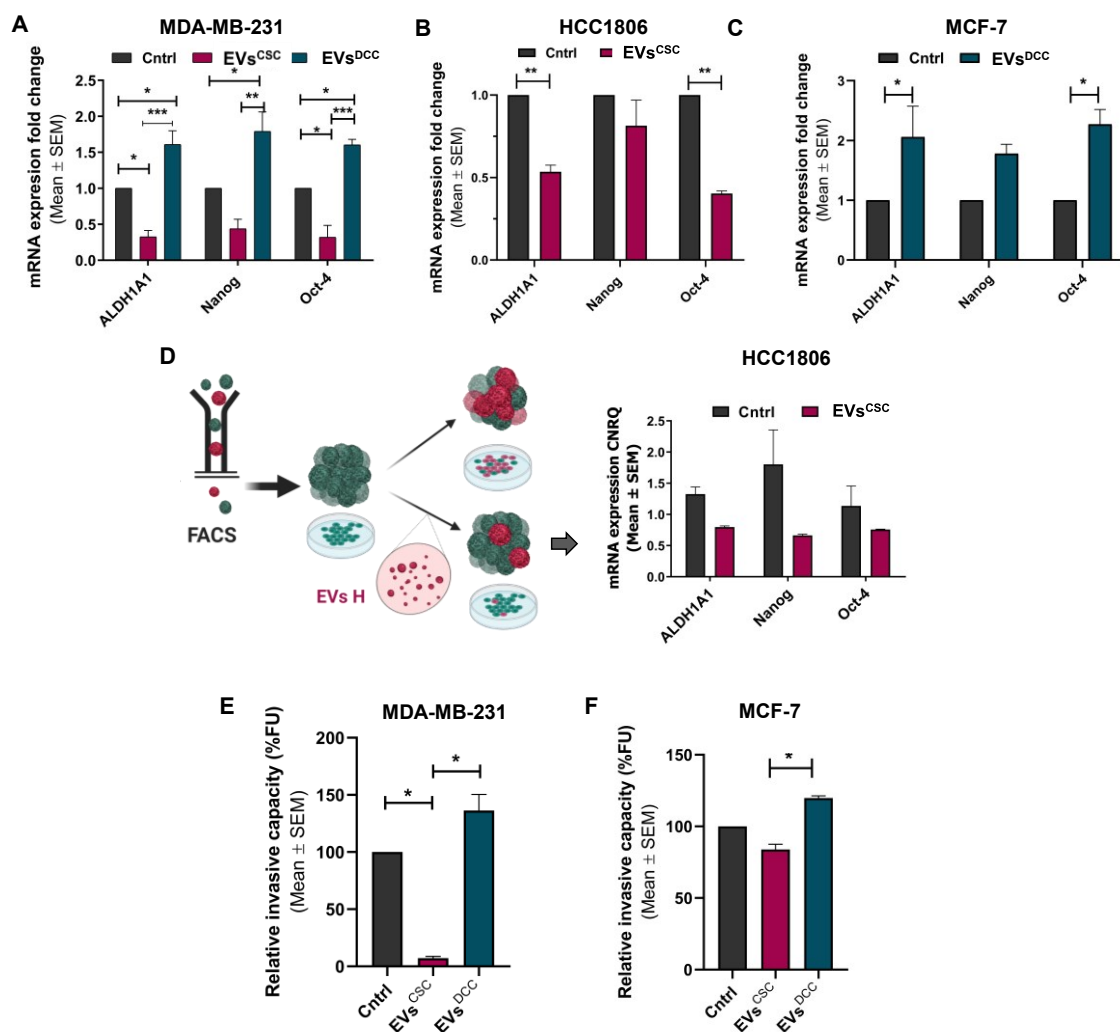


Figure 24. EVs^{CSC} and EVs^{DCC} control tumor cells plasticity *in vitro*. (**A-C**) Relative stem gene expression (qPCR) of MDA-MB-231, HCC1806 and MCF-7 cells treated with either EVs^{CSC} or EVs^{DCC} for 3 days. (**D**) Stem gene expression of FACS isolated HCC1806 DCC at P5 AS receiving EVs^{CSC} doses at each passage. (**E, F**) 2D laminin invasion assay performed with MDA-MB-231 and MCF-7 cells previously pre-treated with EVs^{CSC} or EVs^{DCC}.

We further aimed to study the influence of EVs on cancer plasticity in a more complex scenario. Previous results indicated that CSC-like cells cooperated with CAFs to lead the invasive strands in 3D models, denoting the ability of CSC to degrade the ECM matrix and lead tumor spheroids invasive front. Here, we focused on the invasive capabilities of MDA-MB-231 parental cancer cell line after EVs^{CSC} and EVs^{DCC} education. Briefly, MDA-MB-231 cells were pre-treated for 48 h with either EVs^{CSC} and EVs^{DCC} and afterwards together with CAFs were embedded in Matrigel® plus collagen matrix which allowed to form the previously described 3D cultures of spheroids (**Figure 25A**). Interestingly, confocal imaging of the spheroids (**Figure 25B**) showed that EVs^{DCC} pre-treated cancer cells presented significantly higher amounts of invasive strands compared to untreated cells, MS = 2.73 and 2.1 respectively ($p = 0.015$). On the contrary, EVs^{CSC} treated cells significantly formed less invasive strands, MS = 1.16, ($p=0.0001$), compared to untreated cells (**Figure 25C**). These results suggested that EVs^{DCC} tended to increase the invasive nature of cancer cells promoting CSC phenotypes while EVs^{CSC} appeared to induce the opposite effect.

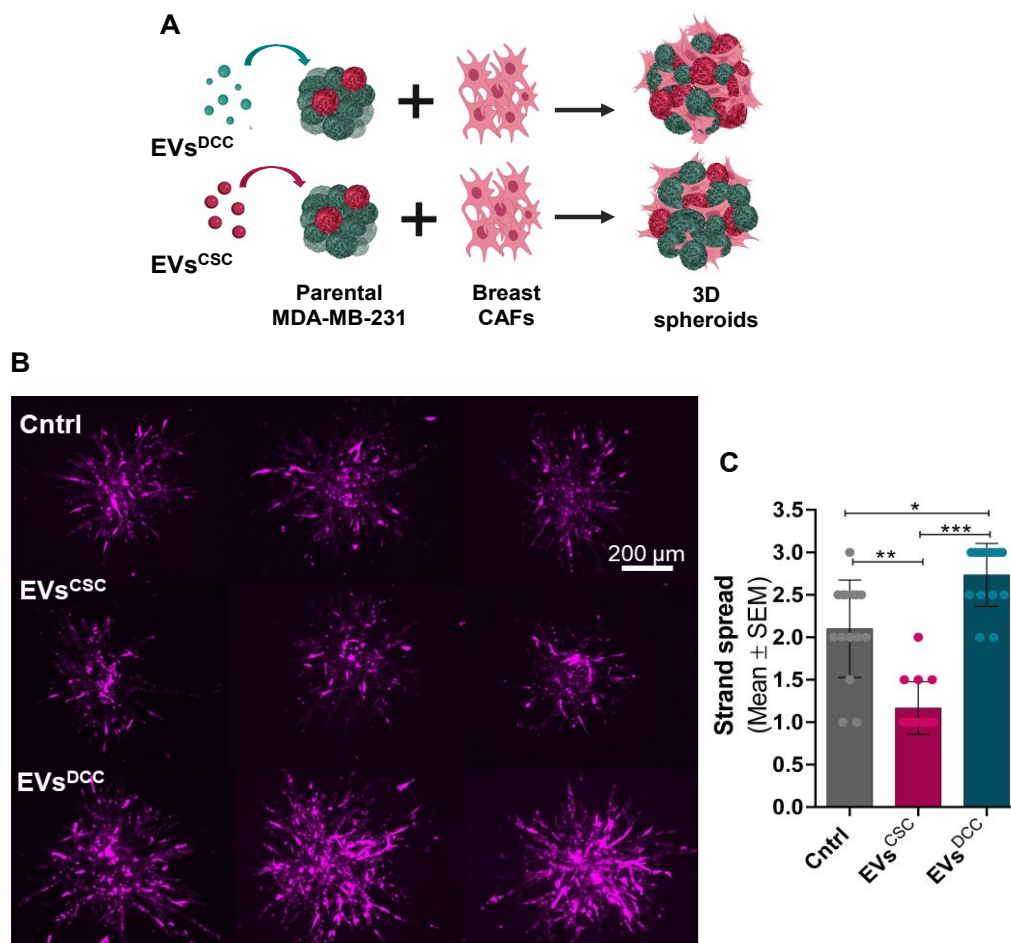


Figure 25. EVs^{CSC} and EVs^{DCC} impacts tumor invasive abilities in 3D Matrigel models. **(A)** Illustrative scheme representing experiment design. **(B)** Representative images of 3D invasion model of spheroids, embedded in Matrigel® plus collagen, formed by MDA-MB-231 previously reprogrammed with EVs^{CSC} and EVs^{DCC}, in purple cells stained with CellTracker™. **(C)** Qualitative score

of 3D invasion images according to spread of invasive strands. (* $p < 0.05$; ** $p < 0.01$; *** $p < 0.001$).

Next, we studied if the effect of EVs^{CSC} and EVs^{DCC} conditioning of MDA-MB-231 cells *ex vivo* altered the stemness profile of metastatic cells when injected *in vivo*. For this aim, MDA-MB-231 cells were pre-treated with either EVs^{CSC} and EVs^{DCC} for 3 days and then i.v. injected into BalbC NOD/SCID mice. At the end of the experiment, lungs were collected and the stemness nature of MDA-MB-231 metastatic lesions were evaluated by assessing NANOG expression by IHC in collected lung tissues (**Figure 26A**). Note that NANOG IHC performed in lung metastatic sections of mice i.v. inoculated with MDA-MB-231 CSC or DCC revealed clear differences in the expression of this stemness reporter, as MDA-MB-231 metastatic CSC exhibited higher signal than their DCC counterparts (**Figure 19**). According with our previous *in vitro* results, MDA-MB-231 lung metastatic cells that were pre-treated with EVs^{DCC} before injection showed more signal for NANOG than cells pre-treated with EVs^{CSC} (**Figure 26B**).

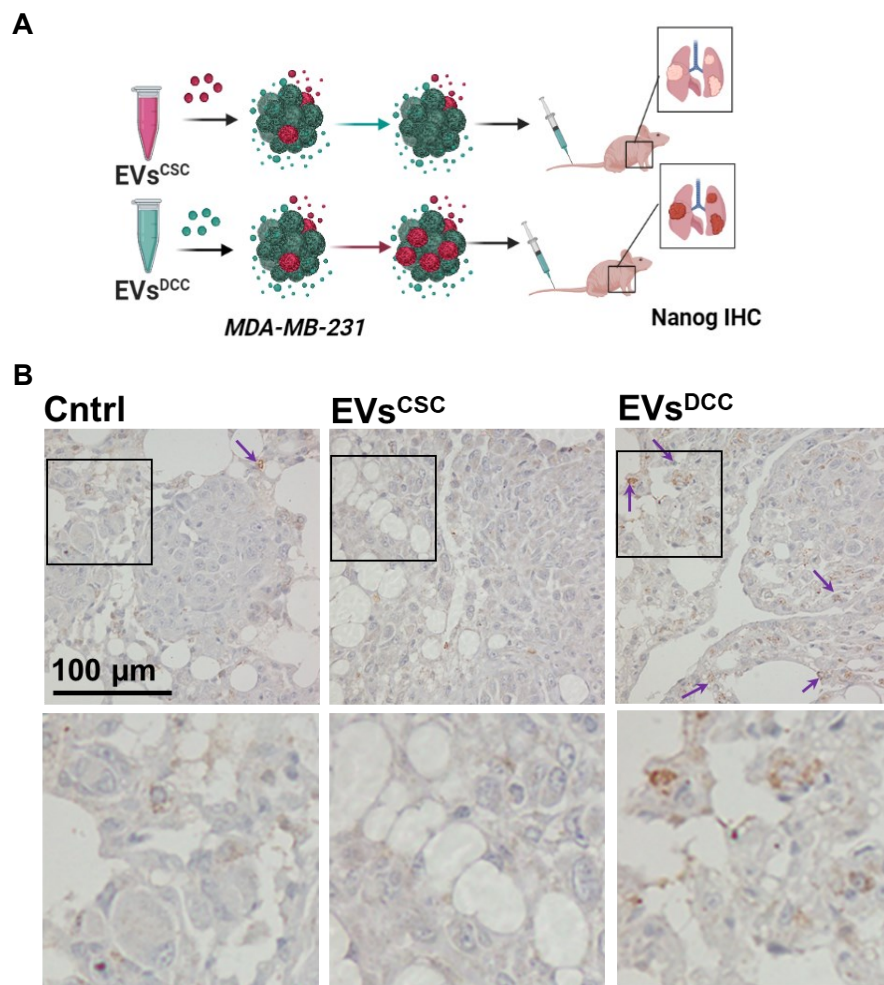


Figure 26. *In vivo* effect of MDA-MB-231 EVs^{CSC} and EVs^{DCC} on the stemness nature of metastatic cancer cells. (A) Representative IHC 20X images of NANOG expression in metastatic lungs

of mice i.v. injected with MDA-MB-231 CSC and DCC cells. Scale bars = 100 μ m. **(B)** Representative IHC 20X images of NANOG expression in metastatic lungs of mice i.v. injected with MDA-MB-231 cells that were previously treated with EVs^{CSC} or EVs^{DCC}, respectively. Changes in NANOG expression derived from EVs effect on MDA-MB-231 cells prior injection could be observed in lung metastatic lesions. Scale bars= 100 μ m.

Altogether our results suggested that EVs from the same cell source but phenotypically distant in the CSC axis may act as modulators of cancer cell plasticity exerting opposed regulation in the stemness profile of recipient cancer cells (**Figure 27**).

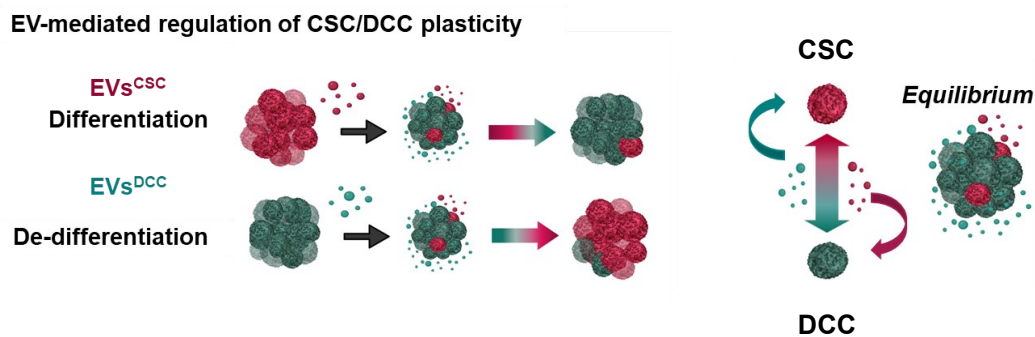


Figure 27. Scheme summarizing EVs^{CSC} and EVs^{DCC} action in MDA-MB-231 cell line depending on the EVs producing cell state.

4 ROLE OF EVs^{CSC} AND EVs^{DCC} ON STROMAL CELLS FUNCTIONAL ACTIVATION

4.1 EVs^{DCC} STIMULATE FIBROBLASTS CYTOKINE SECRETORY PHENOTYPE

Our previous results showed that CSC and DCC secreted EVs are critical regulators of cell plasticity in recipient cancer cells. However, stromal cells present in TME have also been described as essential modulators of plasticity and CSC phenotypes. Therefore, we next aimed to unveil how MDA-MB-231 CSC and DCC interact via EVs with a fibroblast-rich TME and how the TME feedback signaling itself modulates cancer cell plasticity. To this end, CCD19 fibroblasts were incubated with either EVs^{CSC} or EVs^{DCC} and after 72h, cell cultures were then washed and media replaced to remove EVs and allow conditioned fibroblasts to secrete bioactive factors. CCD19 CM were collected for analysis and further supplemented to MDA-MB-231 cells to determine the role of CCD19 secreted factors in cancer cell plasticity, scheme displayed in **Figure 28A**. This strategy allowed us to explore the EV mediated communication between fibroblasts, CSC and DCC.

Cytokine arrays were used to assess expression changes in CCD19 CM and showed that EVs^{DCC} triggered the secretion of cytokines IL-8, IL-6 and CXCL1. Specifically, IL-8 and IL-6 levels increased 61.5- and 2.7-fold, respectively, when compared to untreated controls. Treatment of CCD19 cells with EVs^{DCC}, also induced the release of CXCL1, which was undetectable in the control CM. Conversely, incubation of CCD19 cells with EVs^{CSC} caused a decrease in IL-6 secretion compared to untreated cells (**Figure 28B**). These results were further confirmed by, IL-6 and IL-8 gene expression analysis on CCD19 cells exposed to EVs. EVs^{DCC} promoted higher mRNA levels of *IL-6* and *IL-8*, 6.4- and 100-fold, respectively, while EV^{CSC} induced much milder increases (1.4-fold for *IL-6* and 4.3-fold for *IL-8*) (**Figure 28C**).

Furthermore, the response of MDA-MB-231 cells was also analyzed when challenged with either EVs^{CSC}-CM or EVs^{DCC}-CM, obtained from CCD19 fibroblasts (scheme displayed in **Figure 28A**). MDA-MB-231 cells cultured in EVs^{DCC}-CM showed a remarkable boost in the expression of *ALDH1A1*, *Nanog* and *Oct-4*, with 3.6 ± 0.7 ; 5.54 ± 0.4 and 4.6 ± 0.4 times higher expressions than the untreated control, respectively. Of note, EVs^{CSC}-CM did not display any relevant effect on the stemness gene expression profile of MDA-MB-231 cells (**Figure 28D**). Moreover, when supplementing MDA-MB-231 cell cultures with recombinant IL-8 and IL-6, the two main cytokines upregulated by EVs^{DCC} in CCD19 cells, the expression of stemness related genes was also raised. Specifically, IL-6 significantly increased the expression of *ALDH1A1*, *Nanog* and *ABCGC1*

while IL-8 exerted a substantial upregulating effect on *Nanog* (**Figure 28E**). In agreement with the previous results, MDA-MB-231 *ALDH1A1:tdTomato* cells cultured with EVs^{DCC}-CM displayed a higher number of tdTomato+ cells, as a result of the activation of the ALDH1A1 promoter (**Figure 28F**).

To further study the EVs^{DCC} - TME mediated drift of MDA-MB-231 cells towards a stem-like state, we investigated resistance to a reference chemotherapeutic drug such as paclitaxel (PTX). Note that drug resistance is a major hallmark for CSCs. We observed that MDA-MB-231 parental cells supplemented with EVs^{DCC}-CM were more resistant to PTX, showing a significant increase in cell viability at 0.04 μ M PTX when compared to control cells (14.14%) and to MDA-MB-231 cells cultured in EVs^{CSC}-CM (14.76%) (**Figure 28G**). Remarkably, MDA-MB-231 cells incubated with EVs^{CSC}-CM did not show any difference in cell viability in comparison to the control (**Figure 28G**). Conclusively, these results highlighted the relevance of EVs^{DCC} on regulating cancer cells plasticity towards CSC phenotypes through stromal cells education.

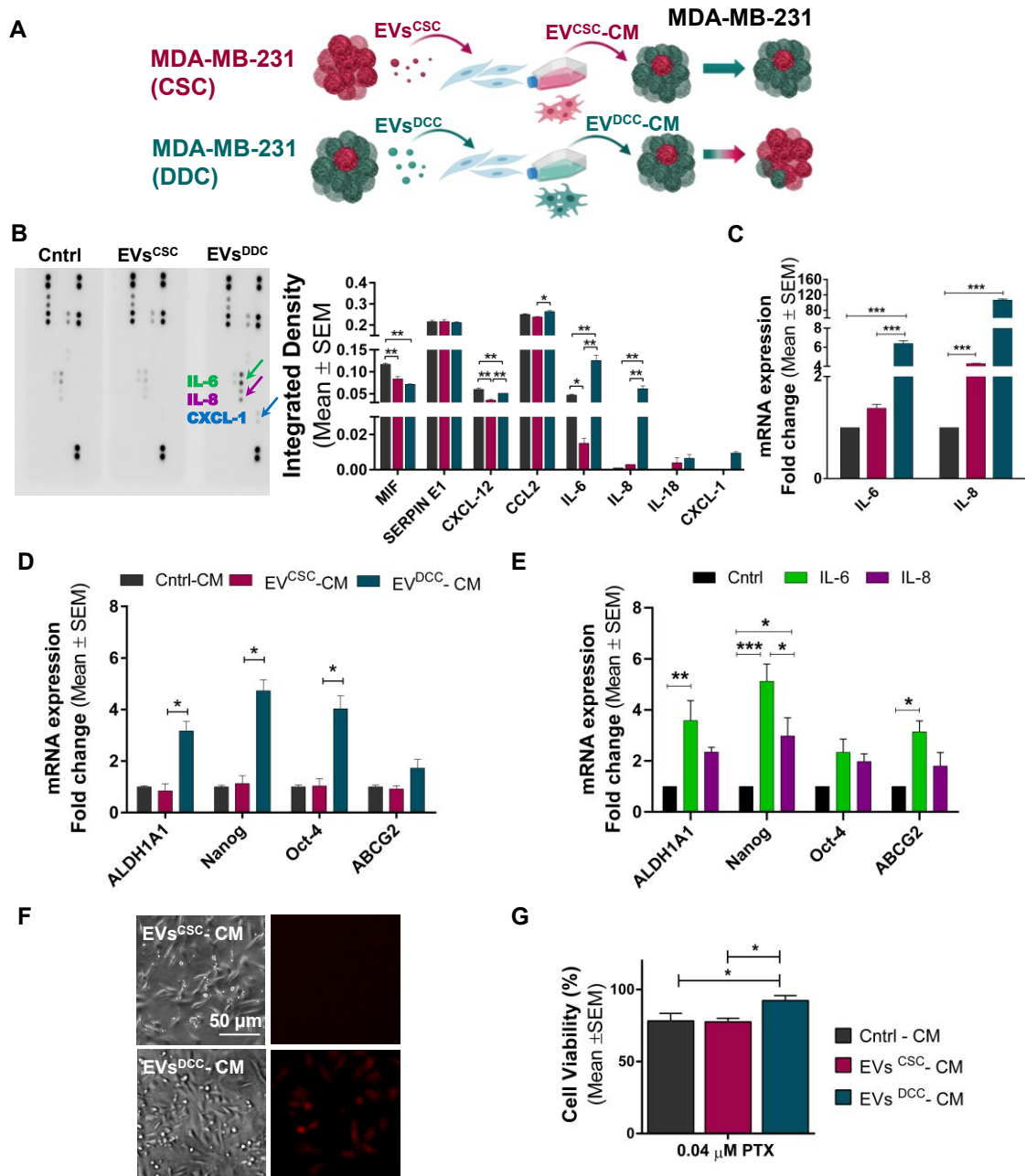


Figure 28. EVs^{DCC} regulate cancer cells plasticity through stromal fibroblasts. (A) Scheme of the experimental approach, CCD19 fibroblasts were educated with either MDA-MB-231 EVs^{CSC} or EVs^{DCC} and CCD19 CM were collected for analysis and further supplemented to MDA-MB-231 parental cells. **(B)** Total Human Profiler Cytokine array performed in CCD19 CM and densitometric quantification of the obtained signal. **(C)** Gene expression of IL-6 and IL-8 in CCD19 cells conditioned with MDA-MB-231 EVs^{CSC} or EVs^{DCC} by qPCR. **(D)** Effect of CCD19 CM obtained after treatment with MDA-MB-231 EVs^{CSC} or EVs^{DCC} in parental MDA-MB-231 stemness gene expression by qPCR. **(E)** Gene expression in MDA-MB-231 cells treated with 20 ng/mL of recombinant IL-8 or IL-6 by qPCR. **(F)** Representative images of tdTomato⁺ cells in MDA-MB-231 ALDH1A1:tdTomato cells after treatment with CCD19-CM. **(G)** MTT cell viability assay of MDA-MB-231 cells incubation with CCD19 CM and different concentrations of PTX (* $p < 0.05$; ** $p < 0.01$; *** $p < 0.001$).

4.2 EVs^{CSC} INCREASE BREAST AND LUNG FIBROBLASTS INVASIVENESS

Fibroblasts are the most abundant cell type present in TME, displaying multiple pro-tumor functions due to their well described functional heterogeneity^{193–197}. Considering this point, and once we established that EVs^{DCC} triggered a pro-CSC cytokine secretory phenotype-like fibroblasts, we explored whether EVs^{CSC} could impact other functional capabilities of fibroblasts. To this end, Breast CAFs or lung fibroblasts (CCD19) were treated with EVs^{CSC} and EVs^{DCC} for 48 h. Then, educated fibroblasts were used to form spheroids and 3D invasion assays were performed. 3D invasive capacity of educated fibroblasts was associated with the number and the length of strands branched by those spheroids into the surrounding Matrigel® / collagen matrix. As observed in **Figure 29A**, CAFs IDC spheroids treated with EVs^{CSC} formed more, 27 ± 0.964 and longer strands $260.7 \pm 6.724 \mu\text{m}$, than the ones supplemented with the EVs^{DCC} fraction, strand number, 22.7 ± 0.804 and strand length, $238.4 \pm 5.8 \mu\text{m}$ (**Figure 29B, C**). Similarly, lung fibroblast spheroids treated with EVs^{CSC} also displayed a significant higher strand number, 58 ± 2.838 and strand length, $156.8 \pm 3.4 \mu\text{m}$ when compared to untreated spheroids and to EVs^{DCC} treated ones (**Figure 29D-E**). These findings suggested that EVs^{CSC} dictated the activation of recipient fibroblasts towards a myfibroblastic pro-invasive phenotype with higher capacity to degrade and remodel ECM components.

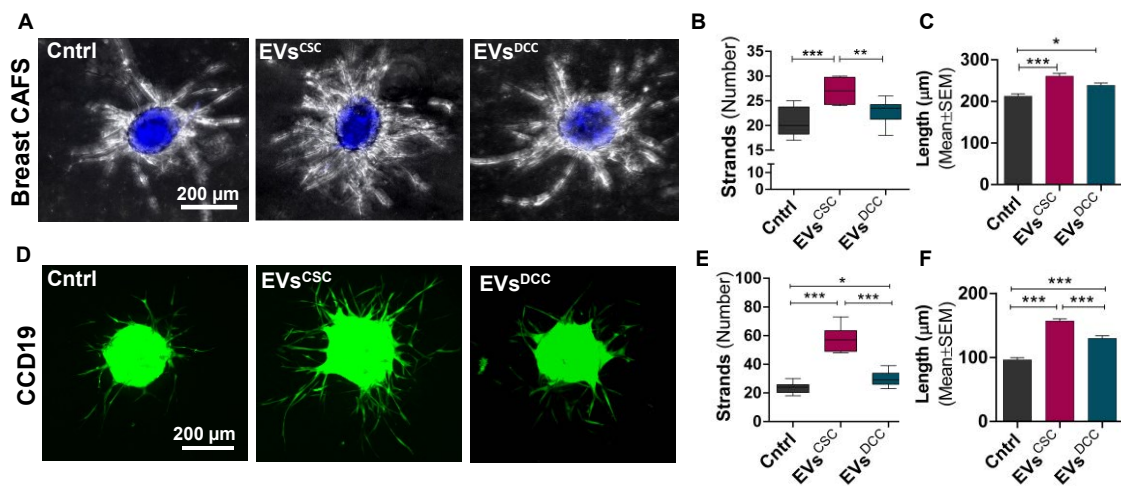


Figure 29. EVs^{CSC} and EVs^{DCC} *in vitro* role in fibroblasts 3D invasive potential. (A) Representative Z stack projection images of 3D invasive spheroids of breast CAFs educated with EVs^{CSC} or EVs^{DCC}. Graphs displaying the number **(B)** and length **(C)** of invasive strands from breast CAFs spheroids. Box plots corresponding to the representation of the number of strands show the median value as an horizontal line. Bar charts display the mean value as indicated in y axis. **(D)** Representative Z stack projection images of 3D invasive spheroids lung CCD19 fibroblasts educated with EVs^{CSC} or EVs^{DCC}. Graphs displaying the number **(E)** and length **(F)** of invasive strands from CCD19 spheroids represented as described above. (* $p < 0.05$; ** $p < 0.01$; *** $p < 0.001$).

4.3 EVs^{CSC} TRIGGER α -SMA+ CAFs ACTIVATION

To further support our previous results we explored the presence of α -SMA, a relevant marker of myofibroblastic phenotype activation³⁰⁵, in CCD19 fibroblasts. Immunofluorescence of CCD19 lung fibroblasts revealed higher α -SMA levels after treatment with EVs^{CSC} in comparison to EVs^{DCC} treated cells (**Figure 30A**). Moreover, when α -SMA cargo in EVs was investigated we assessed that the own EVs^{CSC} payload exhibited a clear enrichment of the α -SMA protein compared to EVs^{DCC} (**Figure 30B**).

Given that EVs^{CSC} seem to have a greater effect in activating fibroblasts towards α -SMA+ phenotype, we next explored potential *in vivo* differences in the CAFs activation patterns using orthotopic primary tumors grown from the injection of either MDA-MB-231 CSC or DCC (**Figure 30C**). We assumed that CSC primary tumors would secrete higher amounts of EVs^{CSC} in comparison to DCC tumors, in which EVs^{DCC} signaling would be predominant. Interestingly, histological analysis by Masson's trichrome staining and α -SMA+ immunolabelling showed a clearer pattern of fibroblast infiltration and stronger signal of α -SMA+ tagging breast CAFs in CSC primary tumors when compared to DCC samples (**Figure 30D, E**).

Next, we investigated whether primary tumor secreted EVs^{CSC} could also trigger the activation of α -SMA+ CAFs subpopulation in future lung **metastatic** niches. To evaluate the presence of activated fibroblasts in lungs derived from EVs education, α -SMA IF was performed in lung tissues from healthy animals previously conditioned with either EVs^{CSC} or EVs^{DCC} for 24h (**Figure 30F**). Our results confirmed that α -SMA IF signal was significantly higher in lung tissues of healthy animals administered with EVs^{CSC} in comparison to EVs^{DCC} and untreated mice, indicating a EVs^{CSC} based action into lung cells towards CAFs phenotypes (**Figure 30G**).

Altogether these results suggest that EVs^{CSC} promote fibroblasts activation towards pro-tumor myofibroblastic phenotypes in both primary tumor and metastatic tumor sites.

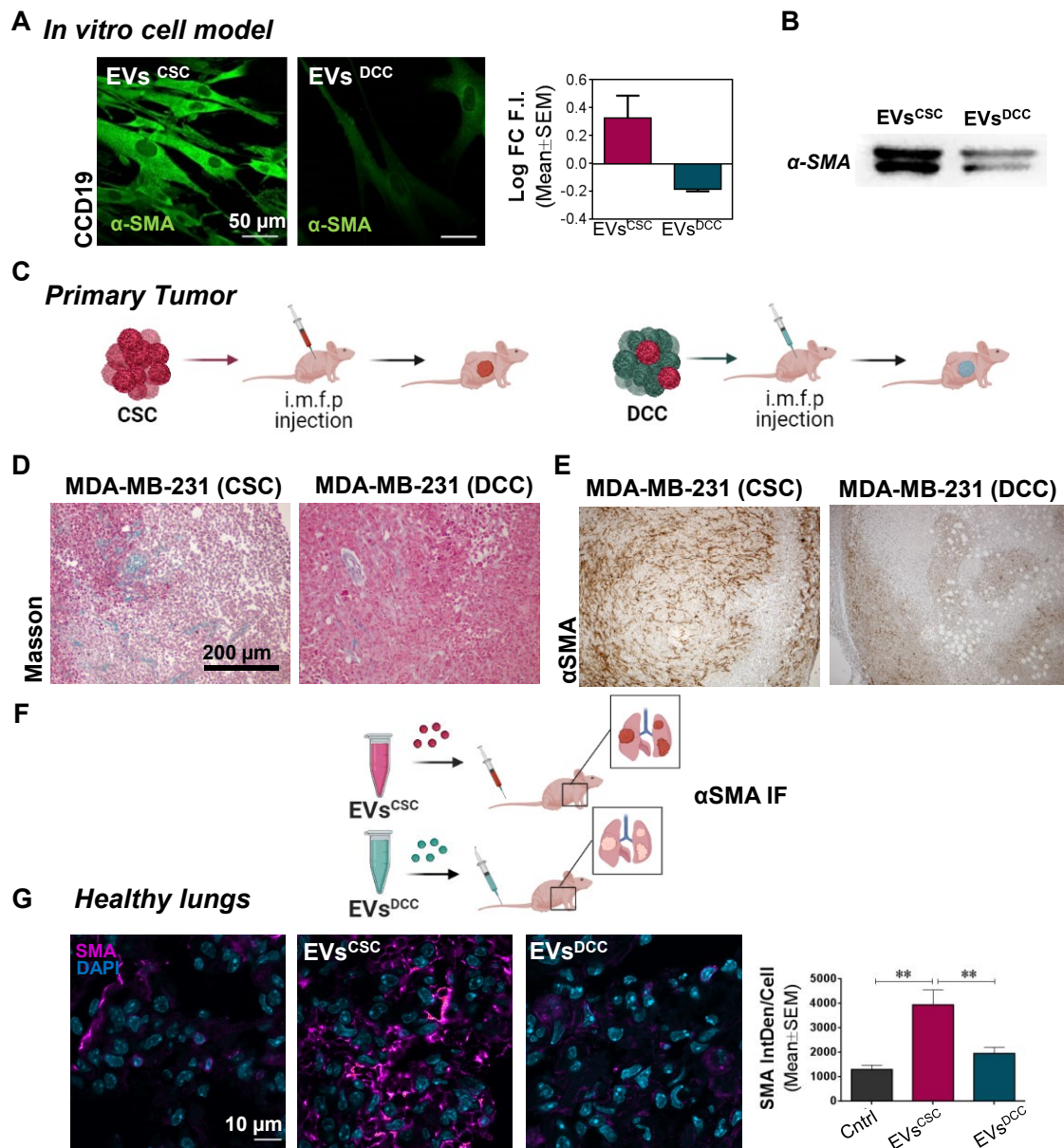


Figure 30. MDA-MB-231 EVs' effect on fibroblasts activation towards CAFs phenotype. (A) Representative images and quantification of fluorescence immunostaining for α -SMA in CCD19 cells educated with MDA-MB-231 EVs^{CSC} and EVs^{DCC} analyzed by confocal microscopy. Scale bar = 50 μ m. (B) EVs^{CSC} and EVs^{DCC} α -SMA cargo examined by WB. (C) Schematic representation of the orthotopic breast cancer mouse model generation. CSC and DCC isolated from MDA-MB-231 ALDH:tdTomato cells were inoculated IMFP. Tumors were let to grow till achieving >250 mm³, excised and processed for histological studies (panels D and E). (D) Masson's Trichrome staining and (E) α -SMA expression in primary tumors of mice orthotopically inoculated into the right mammary fad pad with MDA-MB-231 CSC or MDA-MB-231 DCC and euthanized 9 weeks post-inoculation. Scale bar = 200 μ m. (F) Schematic representation of the lung niche activation model design (G) Representative images and quantification of fluorescence immunostaining for α -SMA in lung sections of healthy mice i.v. inoculated with MDA-MB-231 EVs^{CSC} and EVs^{DCC} after 24h. (** $p < 0.01$).

4.4 EVs^{CSC} TRIGGER ANGIOGENESIS

Tumors are dependent on angiogenesis for their progression, and it has been widely corroborated that tumor EVs activate EC^{320,321}. We next aimed to explore possible differences derived from EVs^{CSC} and EVs^{DCC} influence on EC activation. Thus, the influence of EVs^{CSC} and EVs^{DCC} on angiogenesis was assessed by challenging EPC with both types of EVs and recording the *in vitro* tube formation capability of EC. Results showed that EVs^{CSC} significantly enhanced the formation of new tubes in terms of length ($p = 0.0459$), and complexity of the network, as displayed by the relative increase in the number of branching points ($p = 0.0347$) and the number of total loops completed ($p = 0.0176$), in comparison to EPC treated with EVs^{DCC} (**Figure 31A-D**).

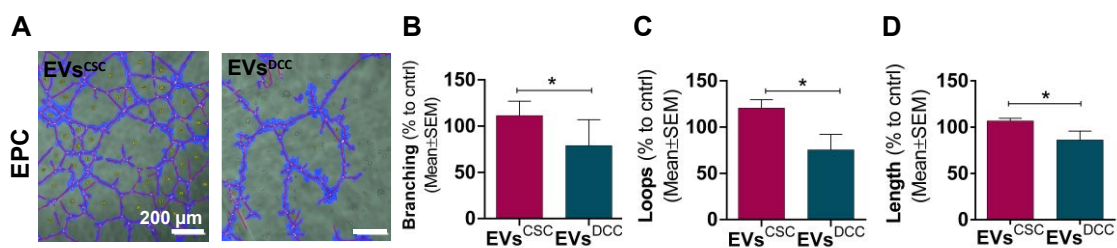


Figure 31 EVs^{CSC} and EVs^{DCC} *in vitro* role angiogenesis. (A) Representative images of *in vitro* tube formation assay performed with EPC treated with either EVs^{CSC} or EVs^{DCC}, the number of branching points (B), total loops (C) and tubes length (D) referred to those in non-treated control cells are represented in the graphs. (* $p < 0.05$; ** $p < 0.01$; *** $p < 0.001$).

Altogether these results highlighted the unique role of EVs^{CSC} in dictating a functional activation of CAFs and EC, processes closely related to local tumor spread and to the construction of receptive niches supportive for metastatic growth.

5 ROLE OF EVs ON METASTATIC NICHE CONDITIONING

5.1 EVs^{CSC} BOOST THE NUMBER OF LUNG METASTASIS

Finally, we aimed to study the function of MDA-MB-231 EVs^{CSC} and EVs^{DCC} in modulating metastasis. For this aim, the biodistribution profile of DiR labeled EVs was analyzed 24h after intravenous administration. As shown in **Figure 32A** similar EVs *in vivo* distribution patterns were observed for both EVs^{CSC} and EVs^{DCC}, with a major accumulation in lungs. Interestingly, EVs^{DCC} displayed a higher tendency than EVs^{CSC} to target the lungs ($p = 0.0153$). Histological analysis confirmed that significantly higher numbers of EVs^{DCC} were able to reach the lung compared to EVs^{CSC}. Specifically, 3.87 ± 1.011 particles per cell were detected in the case of EVs^{DCC} versus the 1.675 ± 0.256 particles per cell observed for EVs^{CSC} (**Figure 32C**). This difference in lung tropism was in accordance with the integrin (ITG) $\alpha 6\beta 1$ expression for both EVs types. The presence of ITG $\alpha 6\beta 1$ heterodimer has been previously shown important for EVs lung tropism³⁷⁵ and although ITG $\beta 1$ expression was similar in EVs^{CSC} and EVs^{DCC}, higher amounts of ITG $\alpha 6$ were clearly displayed on EVs^{DCC} (**Figure 32B**).

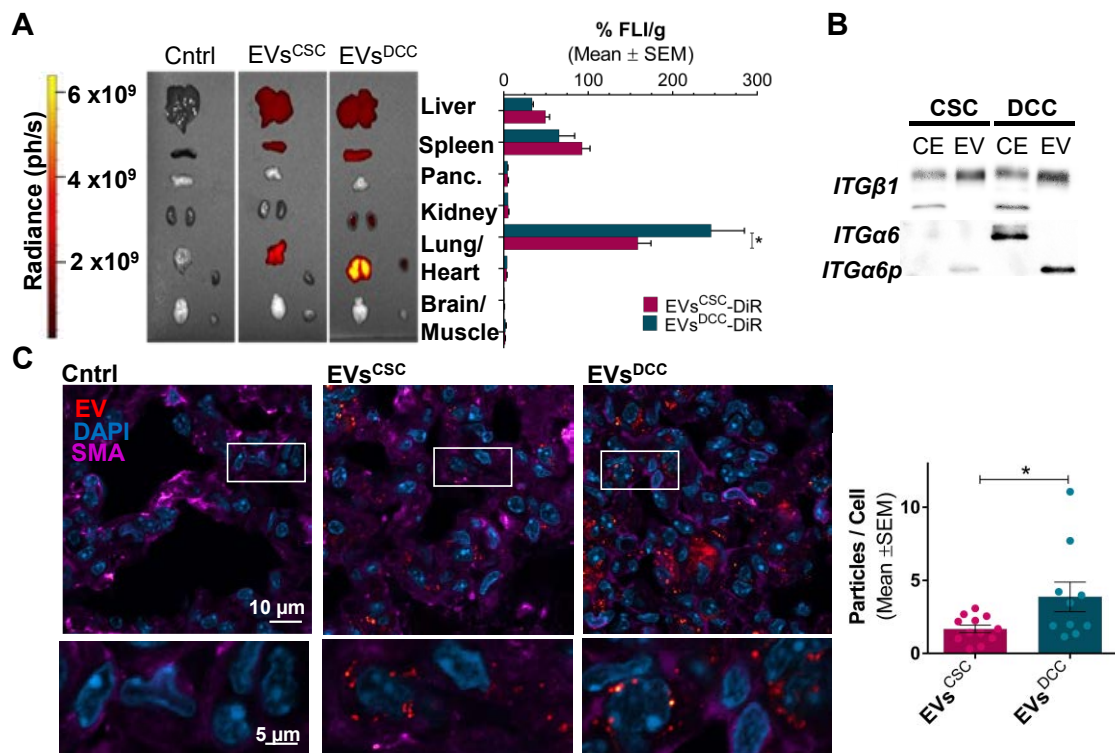


Figure 32. EVs biodistribution (A) FLI analysis of the DiR-labeled EVs after 24h upon tail vein injection of 300 μ g of either EVs^{CSC} or EVs^{DCC}. *Left panels*, representative ex-vivo FLI images of the studied organs for each group. *On the right*, graph displaying ex-vivo FLI values normalized with respect to the untreated controls and represented as % of the total FLI/g. **(B)** WB immunodetection of ITG $\beta 1$ and ITG $\alpha 6$ for CE, EVs^{CSC} and EVs^{DCC}. 20 μ g of total protein was loaded per

lane. **(C)** *On the left*, representative IF images of lung sections 24h after intravenous administration with 300 μg of DiR-labeled EVs. *On the right*, DiR labeled particle quantification from IF images normalized by cell number for EVs^{CSC} and EVs^{DCC} treated mice.

After confirming that EVs in circulation preferably reached the lungs, we proceeded with the functional study of lungs pre-metastatic niche conditioning. To this end, two groups of NOD/SCID mice received i.v. administrations of 75 μg of either EVs^{CSC} or EVs^{DCC} every other day during 5 days. Mice from the control group were administered with equivalent volumes of PBS following the same regimen. Subsequently, luciferase expressing MDA-MB-231 cancer cells were i.v. injected into the tail vein and lung metastasis was evaluated over time (**Figure 33A**). *In vivo* BLI showed that mice preconditioned with EVs^{CSC} displayed significantly more BLI signal in the lungs than control mice or those pre-treated with EVs^{DCC} (**Figure 33B**). These results were confirmed by *ex vivo* BLI determination. Accordingly, lungs excised from animals treated with EVs^{CSC} reached $1.50 \pm 0.16 \times 10^8$ ph/s, while lungs from EVs^{DCC} pre-treated mice displayed only $3.62 \pm 1.34 \times 10^7$ ph/s, in the same range than untreated animals, $5.7 \pm 0.51 \times 10^7$ ph/s (**Figure 33C**).

Furthermore, the number of lung metastasis was individually counted in each of the lungs and results revealed a remarkable impact of EVs^{CSC} on the macrometastatic burden (metastatic foci > 2 mm). Precisely, the number of lung macrometastasis per mouse achieved 137 ± 21 for EVs^{CSC} treated group while EVs^{DCC} treated group and untreated animals produced significantly lower numbers 64 ± 24 and 79 ± 19 , respectively. No relevant differences in the micrometastasis count were detected (**Figure 33D**). Additionally, results on lung BLI intensity and macroscopic metastasis counting were confirmed by histopathological evaluation on hematoxylin-eosin sections (**Figure 33E**) and by immunohistochemistry against vimentin, a relevant marker of MDA-MB-231 cells (**Figure 33F**). Notably, the group injected with EVs^{CSC} presented an almost total coverage of lungs by metastatic lesions.

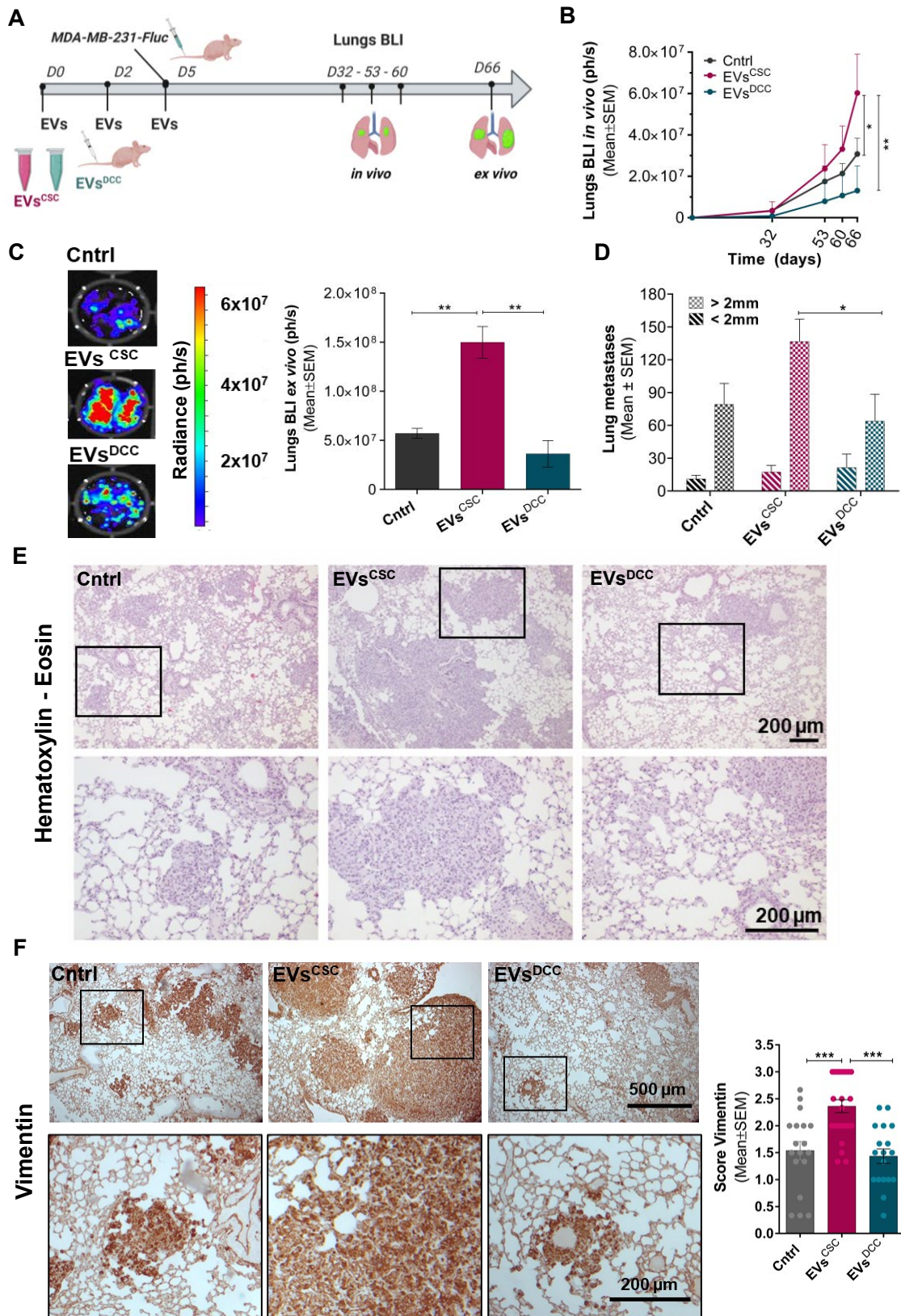


Figure 33. EVs^{CSC} conditioning boosts lung metastasis in vivo. (A) Schematic representation of experimental design for the *in vivo* study of MDA-MB-231. EVs^{CSC} and EVs^{DCC} conditioning effect on lung metastasis. (B) Lung metastasis evolution monitored by *in vivo* luciferase-based BLI of mice pre-treated with EVs^{CSC} and EVs^{DCC} and injected with MDA-MB-231 expressing luciferase cells along the time. (C) *On the left*, representative *ex vivo* BLI images of lungs at the end point

for each condition. *On the right*, BLI ex-vivo quantification of lungs at the endpoint. **(D)** Total number of macro and micrometastasis in the lungs manually counted for control, EVs^{CSC} and EVs^{DCC} preconditioned animals. **(E)** Representative Hematoxylin-Eosin IHC images in lung sections from different mice groups **(F)** *Left panels*, Vimentin staining on lungs showing metastatic foci in different treatment groups. *On the right*, graph displaying vimentin semi-quantitative scoring of the extension of vimentin staining (ranging from 0 -0 % covered area- to 3 -100 % covered area-). (* $p < 0.05$; ** $p < 0.01$; *** $p < 0.001$).

5.2 EVs^{CSC} INCREASE THE NUMBER OF CAFs AND TRIGGER ANGIOGENESIS IN THE PMN

Next, we explored the *in vivo* effect of EVs^{CSC} and EVs^{DCC} on lung fibroblasts and vascular EC. To evaluate the presence of activated fibroblasts derived from EVs education in metastatic lesions, α -SMA immunostaining was performed in lung tissues from animals previously conditioned with either EVs^{CSC} or EVs^{DCC} and subsequently injected with MDA-MB-231 cells (**Figure 34A**). Detail of α -SMA immunostaining of fibroblast like cells can be observed in **Figure 34B**. A higher presence of α -SMA-labeled cells displaying distinctive fibroblast morphologies within the metastatic lesions, MS for α -SMA staining = 2.125, denoted a remarkable occurrence of CAFs in the lungs of animals treated with EVs^{CSC}. Control animals and mice conditioned with EVs^{DCC} also showed a clear signal for the α -SMA marker, but with significantly lower scores, (MS of 0.85; and 1.38, respectively; **Figure 34C**). Additionally, MDA-MB-231 cells pre- treated with EVs^{CSC} or EVs^{DCC} prior to i.v. administration exhibited similar lung metastatic growth irrespective of the EVs type (data not shown). These results suggest that EVs^{CSC} have a stronger effect in lung resident cells than into the MDA-MB-231 cancer cells injected to generate the experimental metastasis model.

Moreover, α -SMA also tagged vascular endothelial cells, and enabled thus to assess EVs impact on angiogenesis. Blood vessels (BV) structures, detailed in **Figure 34D**, were counted in random lung sections. Concomitantly with the previous results, lungs from animals injected with EVs^{CSC} exhibited the highest BV number (40.61 ± 1.833 BV/field), compared to EVs^{DCC} injected animals lungs (29.83 ± 2.22 BV/field) and control animals (33.38 ± 2.02 BV/field,) (**Figure 34E**).

On the other hand, although no significant *in vivo* effect of EVs^{DCC} was observed in terms of functional TME activation favoring metastatic cells engraftment, we could detect a marked labeling pattern for the NANOG protein (**Figure 34F**). This signal was more intense and widely distributed all over the lung than the one displayed by EVs^{CSC} conditioned mice or untreated animals. Those results supported our previous findings indicating a key role of EVs^{DCC} in educating stromal cells to support CSC phenotypes. Altogether these discoveries suggest a major

contribution of EVs^{CSC} to functional activation of the metastatic niche while EVs^{DCC} would perform a role as mediators of cancer cell plasticity towards CSC phenotypes.

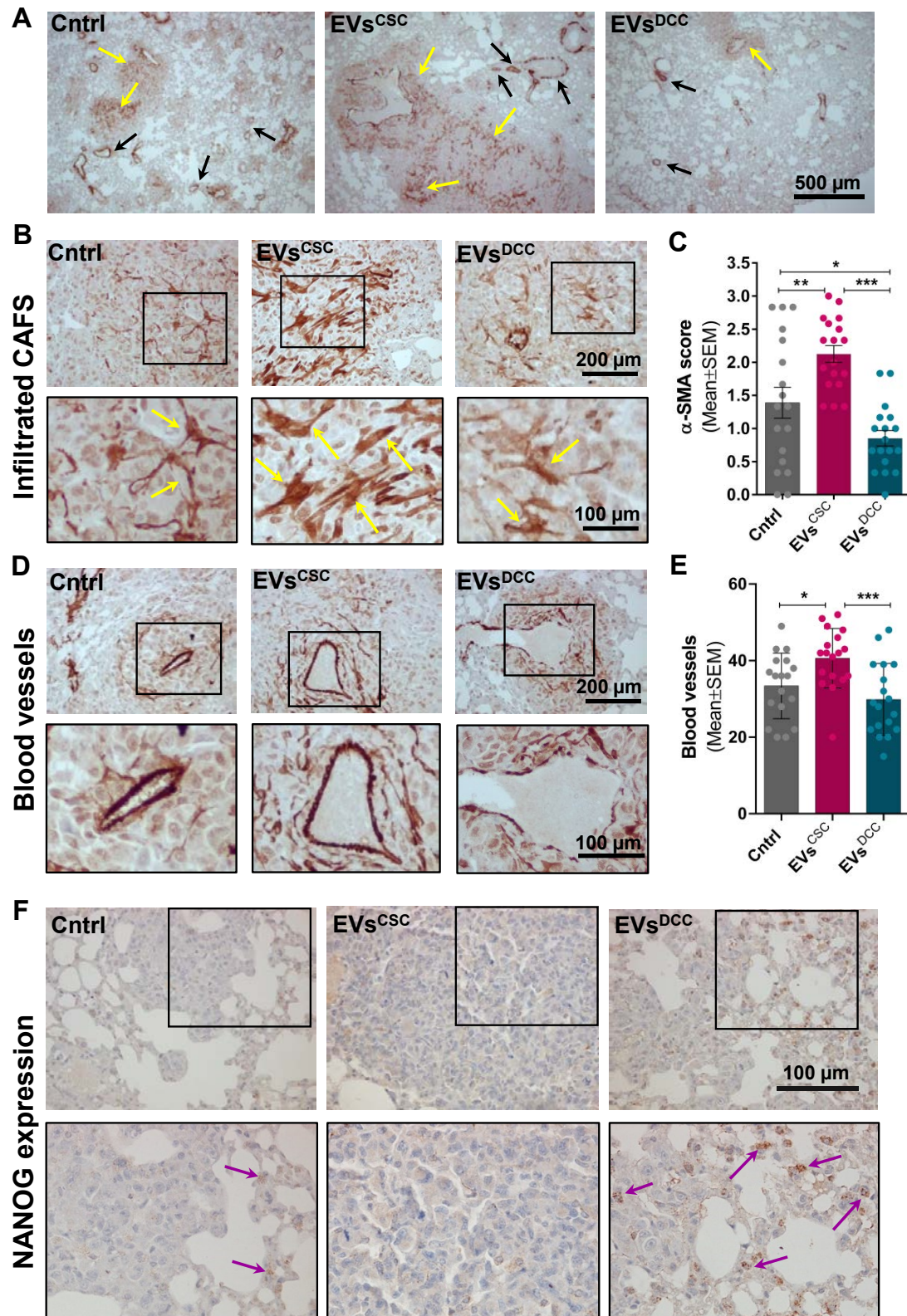


Figure 34. EVs^{CSC} increase the incidence of CAFs and triggers angiogenesis in lungs. **(A)** Low magnification images showing α-SMA staining on MDA-MB-231 lung metastases of mice

educated with EVs^{CSC}, EVs^{DCC} and untreated controls. Yellow arrows indicate fibroblasts infiltrations; black arrows indicate blood vessels. **(B)** Detail of infiltrating CAFs in lungs tissue sections from the distinct mouse groups. Yellow arrows indicate cells with fibroblast-like morphology. **(C)** Semi-quantitative determination of α -SMA immunostaining in lung metastases. Lung sections were analyzed and labeling scores qualitatively attributed, values ranging from 0 (0 % covered area); to 3 (100 % covered area). **(D)** Detail of BV in lungs tissue sections of indicated mice groups. Insets show BV at higher magnification. **(E)** Quantification of BV in lung metastases. **(F)** NANOG immunostaining in control and EVs pre-treated animals, at low (top row) and high magnifications (bottom row), arrows indicate examples of NANOG positive staining.

DISCUSSION

DISCUSSION

TNBC is considered to be the most aggressive breast cancer subtype²⁰⁻²². Indeed, TNBC tumors usually display high grades of intra-tumoral heterogeneity, a factor that challenges therapy^{30,31}. Our results bring out how TNBC intra-tumor heterogeneity significantly impacts on different signaling pathways governed by EVs. Interestingly, we exposed the unique effect of specific EVs^{CSC} and EVs^{DCC} subsets on cancer cells plasticity regulation and metastatic niches conditioning, including fibroblasts activation and angiogenic modulation. More precisely, we addressed that these EVs exert opposed signaling stimuli in tumor cell plasticity regulation, acting as either repressors or activators of stem cell states, respectively. Moreover, they displayed markedly different activities in heterotypic cell communication. EVs^{DCC} could indirectly influence the tumor cell de-differentiation towards CSC states by the stimulation of a cytokine secretory CAFs phenotype while EVs^{CSC} triggered the activation of a distinct and specific myofibroblastic CAF subpopulation, facilitating local invasion and tumor growth. Accordingly, EVs^{CSC} also displayed pro-angiogenic potential and postulated as principal activators of niche modulation enabling metastatic growth. At the same time, EVs^{DCC} emerged as key modulators of metastatic niche resident cells to guide metastatic cells plasticity towards CSC phenotypes.

1 *ALDH1A1:tdTOMATO* REPORTER EFFICIENTLY TAGS CSC-LIKE POPULATIONS IN BREAST CANCER

Intra-tumor heterogeneity poses a significant burden on patients' prognosis and response to therapy^{19,23,27,30,31}. Specifically, CSCs are a crucial subpopulation within tumors with significant roles attributed in tumor initiation, progression, therapy resistance, recurrence and metastasis^{43,45,47,53,76,131,384}. Thereby, the study of CSC requires reliable experimental models to effectively identify and characterize CSCs.

Here we used the CSC model previously generated and validated by our research group in MCF-7 and MDA-MB-231 cell lines to tag and characterize breast CSC-like cells. This strategy is based on the stable transfection of a CSC reporter vector in which the expression of the tdTomato fluorescent protein is under the control of the specific CSC promoter *ALDH1A1*^{378,379}. In this sense, multiple studies have described that *ALDH1A1* upregulation is tightly associated with breast CSC phenotypes^{55,159}. In the present work, we generated equivalent CSC *in vitro* models for HCC1806 and 4T1 cell lines and further validated the CSC-like properties for the already established cell lines. Particularly, we showed that upregulation of *ALDH1A1* is enough to efficiently tag cancer cells that display *in vitro* CSC like features among four different breast cancer cell lines: MDA-MB-231, MCF-7, HCC1806 and 4T1. Specifically, tdTomato+ cells exhibited an upregulation of pluripotency associated genes such as *Nanog* and *Oct-4* when compared to tdTomato- cells. Moreover, isolated CSC-like cells also displayed higher invasive capabilities than tdTomato- cells.

In the case of MDA-MB-231 *ALDH1A1:tdTomato* we further validated the model by assessing additional functional capabilities of CSCs. In this regard, we observed that MDA-MB-231 tdTomato+ cells were able to lead the invasive front together with CAFs in 3D invasion setups, according to reports stating that CSCs are enriched at the invasive/metastatic front of tumors and lead tumor invasion³⁸². Additionally, we found that the stemness reporter NANOG was also upregulated in lung MDA-MB-231 metastatic tumors that were injected with tdTomato+ cells in comparison to the ones formed by metastatic tdTomato- cells.

Indeed, we also validated the tumorigenic phenotype of HCC1806 CSC-like cells. Our results showed HCC1806 tdTomato+ cells were able to form tumors in xenografts more efficiently than their tdTomato- cells counterparts, highlighting the tumorigenicity ability of HCC1806 CSC.

Finally, we also generated a syngeneic TNBC CSC model employing the mouse 4T1 mammary cell line, which has been described to accurately resemble TNBC human models³⁸⁵. Preliminary characterization of the 4T1 *ALDH1A1:tdTomato* cells exhibited stemness related features, namely, upregulation of stem genes, enhanced invasion and SFE% associated to tdTomato fluorescence. These data indicated that *ALDH1A1* reporter represents a suitable CSC marker to tag CSC in murine TNBC cell lines too. Remarkably, this established CSC syngeneic model would allow the design of future studies aimed to unveil the interplay between CSC and tumor immunity under a more physiological approach.

Collectively, our results reinforce previous work carried out by the group and evidence the capacity of the *ALDH1A1:tdTomato* expression cassette to efficiently tag CSC-like subpopulations from heterogeneous breast cancer cell lines. In addition, this CSC model represents an adequate research tool to broaden the insights on the CSC physiology. In turn, this knowledge could guide to further specific therapeutic strategies, aimed to impair the activity of this singular population.

2 CSC AND DCC DYNAMIC EQUILIBRIUM

The initial CSC model theory postulated that tumor hierarchies are sustained by rare self-renewing CSCs whereas the bulk of the tumor is composed of DCC, which are capable only of transient proliferation and therefore do not contribute to long-term growth⁵¹. However, the fact that the CSC phenotype is a dynamic state rather than a defined cell population with unchanging features has been extensively demonstrated during the past years^{165,166,171,386,387}. Although the study of non-static systems is still technically challenging, the emergence of new techniques able to study single cell phenotypes and cell state transitions through reporter cell lines can help to understand cells dynamic behaviors. In this scenario, our CSC model can be a useful tool to gain an in-depth knowledge about heterogeneity and plasticity of CSC phenotypes.

Interestingly, in our hands all the panel of breast cancer cell lines analyzed showed a remarkable interconversion *in vitro* between CSC-like and DCC-like states upon isolation, sustaining that CSC and DCC are plastic entities. MDA-MB-231, MCF-7 and HCC1806 isolated CSCs tended to differentiate into DCC, monitored by the loss of red fluorescence, reaching a cell line specific equilibrium in the ratio of tdTomato+ and tdTomato- cells after certain passages. This differentiation was confirmed by the decrease in the expression of typical stemness markers after several passages. On the contrary, isolated MDA-MB-231, MCF-7 and HCC1806 DCCs tended to increase the expression of CSC related markers over time. In this case, new tdTomato+ cells appeared in isolated DCC cultures. Those results suggested that on one hand, isolated and cultured CSCs

differentiated into DCC reaching a final steady state with a stable CSC population rate characteristic for each cancer cell line. On the other hand, when DCCs were plated alone, CSCs appeared after a few days in culture to regenerate the CSC population.

The above-described results support the notion of cancer cells plasticity but also bolster the concept of tumor phenotypic equilibrium. In this sense, our findings concur with Gupta's *in vitro* experiments on breast cancer cell lines, who showed that the proportion of each phenotype after isolation will tend to a certain constant regardless of the initial population states¹⁷⁴. Accordingly, we observed that isolated CSC tend to reach a steady proportion over time. Moreover, and in agreement with present work, experimental studies with cell lines from other cancer types, namely, colon cancer cell lines, also showed that the CSCs and DCC proportions converged to a determined ratio with time^{175,176}.

3 EVS DICTATE CANCER CELLS PLASTICITY

As described above, tumors can maintain a phenotypic equilibrium that sustains CSC and DCC proportions for functional redundancy, exhibiting homeostatic regulation at each population level. This notion suggests the presence of exhaustive feedback-controls directing the different growth rates among CSC and DCC to maintain the equilibrium. In this regard, mathematical modeling has been employed to explain the differences in the division rates of CSC and DCC for better understanding the complex dynamics and interactions of tumor cell populations³⁸⁸⁻³⁹⁰. However, experiments intended to elucidate the biological nature of this homeostatic regulation remained to be addressed. In this regard, intercellular communication mediated by EVs has been proved crucial in the regulation of multiple pathological processes during tumor growth, maintenance and spread, pointing at EVs as promising candidates in driving tumor cells plasticity processes^{279,391,392}. However, in the TNBC context, whose tumors are composed by heterogeneous CSC and DCC populations, EVs-mediated communication studies have been often biased due to insufficient information regarding the specific cancer cell state of such EVs factories.

3.1 EVs^{CSC} AND EVs^{DCC} PRESENT DISTINCT FUNCTIONAL CARGO

In the present work we aimed to independently study CSC and DCC secreted EVs. Using the MDA-MB-231 *ALDH1A1:tdTomato* cell model we succeed in the isolation and characterization of two unique EVs subpopulations: (i) EVs^{DCC}, secreted from the MDA-MB-231 with a minimal presence of CSCs and (ii) EVs^{CSC}, produced by MDA-MB-231 highly enriched in CSCs.

Our results showed both types of EVs as essentially identical entities regarding their morphometric properties, namely particle size and shape. In addition, no significant differences were observed in terms of cell internalization capacity in either tumor cells or stromal cells, specifically in CCD19 lung fibroblast cells. The same similarity was displayed for EVs protein marker expression but remarkably, EVs contents between EVs^{CSC} and EVs^{DCC} varied to some extent in compliance to the differentiation state of the secreting cells, at least in their protein cargo. Specifically, pluripotency transcription factors NANOG and OCT-4 and CSC related proteins such as ALDH1A1 and CD44 were found to be enriched in EVs^{CSC} fraction compared to EVs^{DCC}. Such differences suggested the possibility for EVs^{CSC} and EVs^{DCC} of delivering distinctively signaling cues and therefore displaying specific roles in intercellular communication.

3.2 EVs^{CSC} AND EVs^{DCC} EXERTED A CONFRONTED REGULATION OF DCC/CSC DYNAMIC EQUILIBRIUM

One of the processes in which differential EVs regulation can play an important role is the control of tumor cells plasticity, previously discussed. According to the results obtained in our MDA-MB-231 *ALDH1A1:tdTomato* model after depletion of either CSCs or DDCs, tumor cells tend to recover a specific cell state equilibrium. Nevertheless, how this cell state transition is driven remain to be fully understood. Due to the absence of external stimuli after cell depletion it was plausible to think of newly synthesized EVs as potential candidates to trigger and regulate this process. Thus, in an attempt to decipher the role of EVs in maintaining cancer cells equilibrium through cell plasticity we challenged the parental MDA-MB-231 cell line with exceeding amounts of either EVs^{DCC} or EVs^{CSC}. Under these circumstances, EVs^{DCC} pulsed the conversion of cancer cells towards a CSC-like phenotype, assessed by an increase in the expression of stem markers like *ALDH1A1*, *Nanog* and *Oct-4* coupled to a significantly higher invasive potential in 2D and 3D models. Note that MDA-MB-231 cells with CSC-like phenotype rendered higher invasive potential in 2D models. In addition, the CSC subpopulation was also responsible, together with CAFs, of leading invasive strands in 3D models. Interestingly, EVs^{CSC} exerted the opposite effect, as the parental cell line exposed to EVs^{CSC} showed a decrease in the expression of stemness reporters and a reduced invasive potential in 2D and 3D models. In this sense, a reduced invasive potential was previously associated with DCC phenotype. Remarkably, and in agreement with our previous findings with the MDA-MB-231 cell line, we also found a tendency of HCC1806 isolated EVs^{CSC} to promote cancer cells differentiation together with an activation of CSC-like phenotypes in parental MCF-7 cell line exposed to EVs^{DCC}.

In the same line, when parental MDA-MB-231 cells were pretreated with either EVs^{CSC} or EVs^{DCC} and then i.v. injected in a mouse lung metastatic model, differences in the stemness state of the cells growing in the lungs were found. Cells pre-treated with EVs^{DCC} showed an increase in the expression of NANOG stemness reporter, while minor expression was found in metastatic cells pre-treated with EVs^{CSC}. Altogether those results indicated that exceeding amounts of EVs^{DCC} prompted parental cancer cell line to acquire a CSC-like phenotype while the same amounts of EVs^{CSC} would promote DCC-like phenotypes.

Our work indicated that EVs^{CSC}/EVs^{DCC} balance may be responsible for controlling cell state transitions *in vitro*. Remarkably, this opposed regulation fitted into the theoretical model proposed by Olmeda and collaborators¹⁷⁷, who have recently postulated that cancer cells plasticity towards stem phenotypes is directed by an unknown activator of tumor cells dedifferentiation. According to their model, this activator would be triggered when the CSC population in tumors approached 0. Framing our results into this rationale, the activator of cell dedifferentiation would be the EVs^{DCC}. Thus, in an equilibrium state EVs^{DCC} action would be counteracted by EVs^{CSC} but when the ratio of EVs^{DCC}/EVs^{CSC} abnormally raises, due to either the depletion of CSC cell subpopulation or by the artificial addition of EVs^{DCC}, EVs^{CSC} could no longer neutralize EVs^{DCC} action and tumor cells would undergo a dedifferentiation process in order to reestablish the equilibrium. On the contrary, when the ratio EVs^{CSC}/EVs^{DCC} is increased, CSCs would tend to differentiate to recover the equilibrium. Still, the molecular actors' and signaling cascades involved in this process require further study.

4 CANCER EVS ORIGIN IMPACT ON STROMAL CELLS RESPONSE

Our results demonstrated how tumor EVs^{CSC} and EVs^{DCC} oppositely regulate recipient cancer cells plasticity. However, it is largely documented that cancer cells are also strongly influenced by other cells within the TME, which create a favorable physical and molecular signaling environment that ensures tumor progression. More precisely, tumor derived EVs can activate normal fibroblasts, as main elements of tumor stroma, to acquire malignant CAF phenotypes that act either as cancer cells plasticity regulators or as pro-invasive elements with significant incidence in disease progression²⁹³⁻³⁰⁰. Moreover, the ability of tumor-derived EVs to sustain angiogenesis by promoting communication between cancer cells and endothelial cells has been also widely described³¹⁰⁻³¹³.

4.1 EVs^{DCC} ACTIVATE SECRETORY CAFs

In this scenario, we wondered whether CAFs may also be involved in CSC/DCC equilibrium regulation by distinct EVs stimulation. Interestingly, lung fibroblasts treated with EVs^{DCC} activated the secretion of pro-stemness cytokines IL-6 and IL-8 while EVs^{CSC} did not show this effect or even reduced the secretion of IL-6. Besides, when we added CM from EVs^{DCC}-treated fibroblasts on parental MDA-MB-231 cells we confirmed an induction of tumor cell dedifferentiation. This process was monitored by an increase of the stem gene expression profile along with higher levels of tdTomato reporter protein. In addition, an increase of cell resistance to chemotherapeutic drugs such as PTX, was also detected. Of note, drug resistance is a hallmark of CSC phenotypes^{129,229}. Conversely, CM produced by fibroblast educated with EVs^{CSC} displayed no significant differences in comparison to the control. This behavior is in accordance with EVs mediated cell plasticity regulation discussed above. However, in this case, EVs^{DCC} would exert an indirect effect on tumor cell dedifferentiation by the induction of cytokine secretion from CAFs. These cytokines in turn would provoke a positive stimuli cascade towards CSCs state transition.

The capacity of CAFs to regulate tumor plasticity through secretion of cytokines has also been extensively examined^{199,393,394}. According to our results, IL-6 and IL-8 outstands among the numerous cytokines described to have a role in CSCs maintenance due to their implication along diverse types of cancers^{219,395,396}, specially in breast cancer^{106,108,397}. Essentially, these cytokines are described to operate via activation of STAT3 and NF- κ B signaling pathways, inducing the expression of stem genes and the subsequent transition of tumor cells towards CSC-like states^{102,112,118,121}. In this regard, Su et al recently described a subpopulation of fibroblasts responsible of providing a constant source of paracrine IL-6 and IL-8 that maintained a feedback loop sustaining CSC stemness via NF- κ B pathway activation in breast cancer²⁰⁸. Specifically, our results reinforce previous studies that suggest that IL-6 and IL-8 neutralization might appear as promising therapeutic target as it would reverse resistance to conventional cancer therapy by impairing CSC maintenance.

Additionally, in spite of numerous studies have pointed the ability of cells from TME in modulating CSC phenotypes, this work shows for the first time that it is the EVs^{DCC} fraction from tumor secreted EVs the responsible of educating stromal cells towards pro-CSC CAFs. Our results reinforce the idea of the tumor behaving as a homeostatic entity that maintains sophisticated regulation mechanisms to control CSC and DCC proportions. In this scenario, the EVs^{DCC}/EVs^{CSC} balance not only affects DCC/CSC plasticity self-regulation but also induces stromal cells to guide the equilibrium towards the appropriate phenotype. The fact that only an excess of EVs^{DCC}

induced fibroblasts to secrete high amounts of pro-stemness cytokines to replenish CSC populations highlights the sophisticated feedback control present at population level of each tumor component.

4.2 EVs^{CSC} ACTIVATE α -SMA+ CAFs

Tumor derived EVs can activate fibroblasts in the TME to physically drive tumor progression and metastasis^{269,278–280} 294. Particularly, myofibroblastic CAFs capable of generating ECM tracks to guide cancer cells largely influence tumor local invasion^{301–309}. When studying the effect of EVs^{CSC} and EVs^{DCC} in promoting relevant CAFs phenotypes, we observed that breast and lung fibroblasts cultured with EVs^{CSC} displayed enhanced ECM remodeling activity. These cells rendered more and longer invasive strands into the surrounding 3D matrix than those educated with EVs^{DCC}. Moreover, we found that only EVs^{CSC} fraction clearly promoted the expression of α -SMA protein, the universal myofibroblastic CAFs activation marker, in recipient lung fibroblasts *in vitro* and *in vivo*. Additionally, a higher presence of α -SMA was also observed in primary tumors exclusively generated from MDA-MB-231 CSC-like cells, in which EVs^{CSC} would be predominant, in comparison to tumors originated by DCC. These data further support the specific role of EVs^{CSC} in the activation of invasive CAFs, which represents a trait largely associated with myofibroblastic CAFs phenotypes.

4.3 EVs^{CSC} AND EVs^{DCC} DICTATE CAFs FUNCTIONAL HETEROGENEITY

Importantly, our findings reveal that EVs^{DCC} and EVs^{CSC} promote different CAFs phenotypes in fibroblasts. These findings concur with recent studies highlighting CAFs heterogeneity among different tumor types^{208,398,399}. These reports documented the co-existence of CAFs sustaining cancer cells invasion (myoCAF) with CAFs subsets displaying an inflammatory pro-CSC phenotype (iCAF). Interestingly, it has been recently described that while CD10⁺GPR77⁺ CAFs promote tumor formation and chemoresistance, by providing a survival niche for BCSC through the secretion of IL-6 and IL-8, other tumor CAFs exhibited a myofibroblastic phenotype based on α -SMA expression²⁰⁸. Similarly, two CAF subpopulations with different levels of α -SMA have been identified in pancreatic tumors, with one being myofibroblastic and the other one pro-inflammatory. Of note, those tumors also showed α -SMA⁺ CAF heterogeneity, including some subsets of iCAFs, α -SMA^{low}IL-6^{high} and others with myoCAF profile, α -SMA^{high}IL-6^{low}⁴⁰⁰.

Up to date the mechanisms driving specific activation of certain CAF phenotypes are not clarified. However, here we present evidence that CAF heterogeneous activation may be governed by distinct subpopulations of tumor EVs. Based on our results, we could conclude that EVs^{CSC}

activate myoCAFs while EVs^{DCC} trigger iCAFs. In this sense, deeper studies focused on the bidirectional crosstalk between CSC, DCC and CAFs are needed to further unveil the molecular mechanisms driving CAFs heterogeneity in tumors. We anticipate that the fine identification of biological cargo present in each specific EVs subset will pave the way to impair the downstream signaling cascades leading to distinct CAFs activation.

4.4 EVs^{CSC} TRIGGER ANGIOGENESIS

Similar to CAFs activation, tumor derived EVs effect on endothelial cells has been also widely described^{310,401}. Specifically, tumor EVs can promote neovascularization via EC remodeling. When we studied possible differences in the angiogenic effect of both EVs subsets we found that EVs^{CSC} promoted new tubules formation in recipient EC more efficiently than EVs^{DCC}. Although increasing number of studies have reported the capacity of EVs to actively regulate the tumor-associated angiogenic programs here we identify CSC derived EVs as key mediator of this process.

5 EVS AND METASTATIC NICHE CONDITIONING

It has been previously reported that tumor EVs can prepare a favorable microenvironment for tumor metastasis by inducing changes in pre-metastatic niches resident cells that would favor metastatic cells engraftment^{351,367,368,375,402}. Our biodistribution studies data showed a marked lung tropism for both types of EVs upon intravenous administration. This biodistribution profile was in accordance with previous reports on EVs derived from TNBC cells which showed a tendency to accumulate into their primary metastatic sites directed by the integrin expression onto the EVs surface³⁷⁵. However, differences between EVs^{CSC} and EVs^{DCC} were observed in ITG α 6 expression, slightly influencing the amounts of tumor EVs in the lung. EVs^{DCC} targeted the mice lung more efficiently than EVs^{CSC}. Remarkably, and despite EVs^{CSC} presented less lung tropism than EVs^{DCC}, significant effects in the pre-metastatic niche conditioning due to EVs^{CSC} action were found.

5.1 EVs^{CSC} BOOST METASTATIC CELLS ENGRAFTMENT BY REMODELING PRE-METASTATIC NICHE RESIDENT STROMAL CELLS

Our experiments revealed remarkable differences in the effect of EVs *in vivo* conditioning in metastatic cells engraftment. We found that mice pre-conditioning with EVs^{CSC} increased the extent of the macrometastasis burden in the lungs, indicating that EVs^{CSC} strongly promoted the

dissemination of malignant cells into the lungs by creating a tumor cell growth supportive niche. The creation of a remodeled metastasis-promoting receptive niche induced by EVs^{CSC} conditioning was assessed by the examination of lungs CAFs activation and the presence of new blood vessels in lung metastatic areas. Consequently, EVs^{CSC} conditioned animals showed higher presence of α -SMA+ CAFs and more blood vessels in lungs than EVs^{DCC} conditioned group. These data supported previous results showing EVs^{CSC} as potent activators of breast and lung α -SMA+ myoCAF*s in vitro* and *in vivo*, with enhanced ECM remodeling and 3D invasion abilities. Moreover, the increased blood vessel number found in mice lung metastasis previously conditioned with EVs^{CSC} was also in agreement with our previous data revealing a higher angiogenic potential of EVs^{CSC} *in vitro*. Altogether these results suggest that EVs secreted by CSC-like cells trigger niche conditioning at the metastatic sites through resident fibroblasts and endothelial cells activation. Those results concur with previous studies addressing the impact of tumor derived EVs on the formation of the lungs pre-metastatic niche. Of note, and despite the role of tumor derived EVs in pre-metastatic niche conditioning has been largely described, few specific studies using CSC derived EVs have been developed in order to unveil the contribution of each tumor EVs subset in pre-metastatic conditioning. However, supporting our data some reports using EVs isolated from particularly malignant cells, e.g. drug resistant tumor cells, often associated with CSCs-like phenotypes, have shown higher metastatic potential than the ones from the parental cell lines⁴⁰³. Additionally, other studies with renal tumor models have investigated the roles of CSCs-derived EVs in tumor metastasis, concluding that EVs shed by renal CSCs greatly enhanced the lung metastasis of renal cancer cells in mice^{361,404}. In summary, EVs^{CSC} role in the pre-metastatic cascade appears as a determinant target that requires further investigation.

5.2 EVs^{DCC} CREATE A CSC SUPPORTIVE METASTATIC NICHE

When exploring the effect of EVs^{DCC} in metastasis derived from the metastatic niche conditioning we found that those EVs produced a negligible response in terms of metastatic burden, stimulation of resident fibroblast towards α -SMA positive CAFs or stimulation of new blood vessels formation. Nevertheless, when we explored EVs^{DCC} impact on the pre-metastatic niche in terms of the promotion of CSC-like phenotype, we found that EVs^{DCC} conditioning in mice seemed to activate the expression of the CSC marker NANOG in metastatic cells. These results reinforced previous *in vitro* findings and suggested that EVs^{DCC} would educate resident fibroblasts to promote IL-6 and IL-8 signaling in pre-metastatic niches. Thereby, their downstream signaling cascades would promote the conversion of arriving metastatic cells towards CSC-like phenotypes. However, more research is needed to fully address this effect *in vivo* (**Figure 35B**).

6 OVERVIEW AND PERSPECTIVES

Conventional anti-cancer therapies preferentially target the proliferative bulk tumor cells, while quiescent and therapy resistant CSCs tend to persist after treatment and finally drive tumor relapse. With the more extensive and in-depth research on EVs, researchers have gradually realized that EVs secreted by CSCs would play a relevant role in tumor progression. However, few studies have focused on the precise study of CSC derived EVs subpopulations. This thesis characterizes this unique EVs subset and elucidates how CSC secreted EVs provoke necessary changes in primary tumor TME and resident stromal cells at the PMN that result crucial for tumor growth and metastatic dissemination. Importantly, our results suggest that therapies targeting CSC populations or designed to specifically impair CSC EVs secretion, thus suppressing the crosstalk with the TME, may achieve clinical success. However, this clinical success would only be attainable if both CSC and DCC are targeted, since CSC/DCC dynamic cell plasticity increases the phenotypic heterogeneity of tumors, augmenting the complexity of the mechanisms underlying carcinogenesis, metastasis and its treatment. In this sense, if CSC were removed from tumors in a hypothetical clinical situation, DCC secreted EVs could rapidly trigger cancer cells dedifferentiation towards CSC phenotypes to restore the missing CSC population. In this scenario, an integrative understanding of cell-to-cell communication via EVs in tumor progression will conduct us towards the design of innovative approaches such as blocking cellular plasticity bidirectionality to finally overcome therapy resistance mechanisms. Indeed, tumor plasticity should be studied as a collective phenomenon, including the extrinsic mechanisms driven by cells from the TME that also play key roles in regulating cellular plasticity.

This thesis unveils new insights on how TNBC tumors create a EV-mediated communication network with the components of the tumor microenvironment that becomes crucial to drive many steps of tumor development and progression. Based on these findings, therapeutic benefits would be achieved in terms of the inhibition of the crosstalk mediated by EVs^{CSC} and EVs^{DCC} with stromal cells or by directly impairing the secretion of both EVs^{CSC} and EVs^{DCC}. Unfortunately, although the therapeutic potential is clear, the targets remain elusive as we still lack of sufficient information about which molecular signals drive EV biogenesis and/or regulates oncogenic cargo in cancer cells. Furthermore, we are still far from understanding which mechanisms driving cancer EV biogenesis are significantly different from physiological EVs biogenesis that could allow intervention without disturbing physiological processes. Thus, it seems more reasonable to focus on the study of the specific cargo of cancer cells EVs that trigger numerous pathological signaling pathways in the TME in order to unveil future therapeutic targets. Specifically, further

studies exploring the specific molecular cargo of different tumor secreted EVs^{CSC} and EVs^{DCC} would open a window to the design more efficient therapeutic strategies addressing the mechanisms supporting tumor survival.

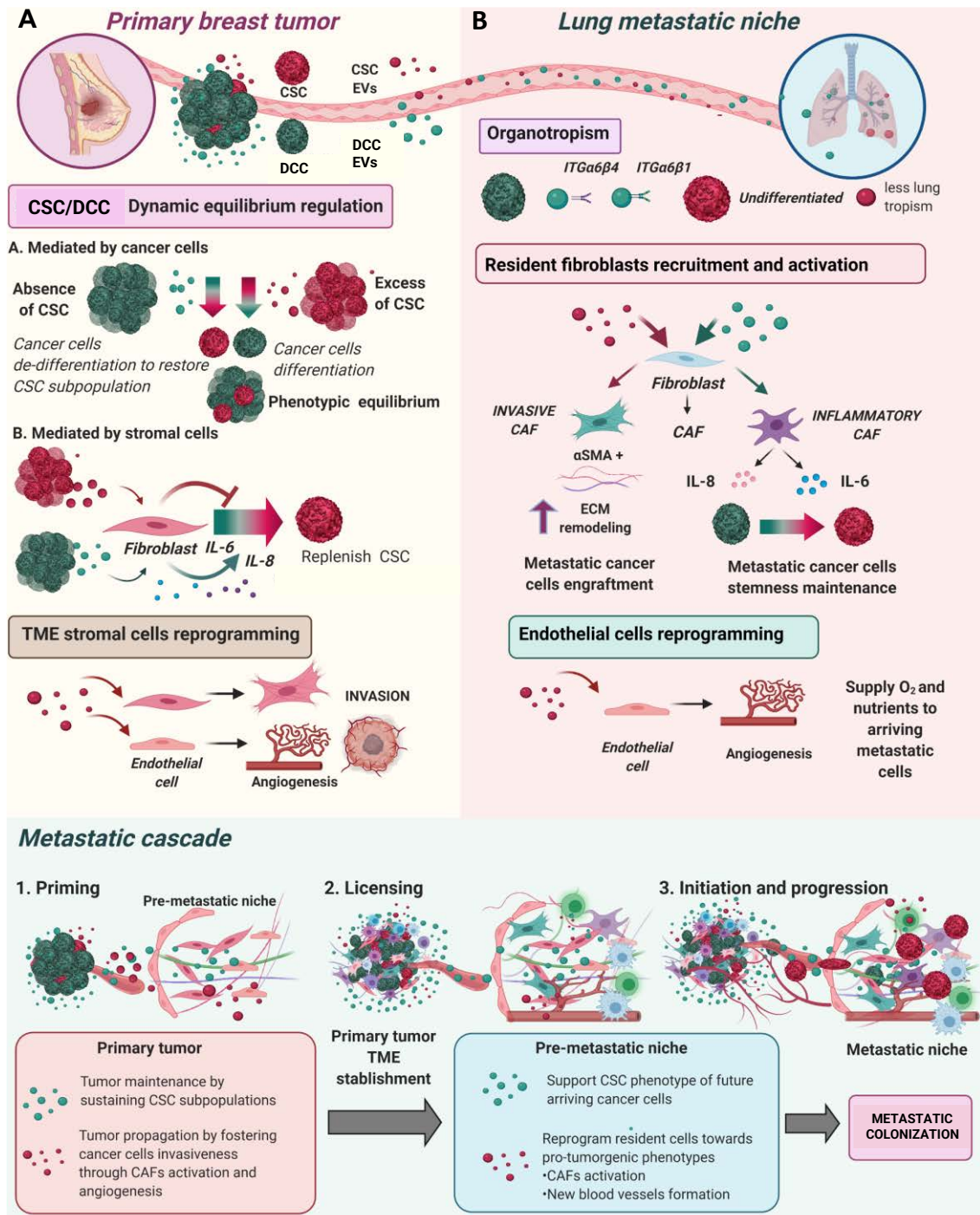


Figure 35. EVs^{CSC} and EVs^{DCC} role in tumor maintenance and metastatic progression. (A) Primary breast tumors are composed by heterogeneous CSC and DCC subpopulations in equilibrium between both cell states. Tumor secreted EVs regulate this phenotypic equilibrium by inducing cancer cells differentiation or de-differentiation depending on tumor requirements. While an excess of EVs^{CSC} triggers cancer cells differentiation, EVs^{DCC} induce the opposite effect, enhancing

tumor cells de-differentiation to restore CSC/DCC balance. EVs^{DCC} also induce stromal cells like fibroblasts to restore missing CSC subpopulations through IL-6 and IL-8 signaling whereas EVs^{CSC} promote CAFs activation and angiogenesis. **(B)** Primary tumor secreted CSC and DCC derived EVs travel through the blood circulation and reach the pre-metastatic lung niche. EVs^{CSC} impact on lung resident cells by inducing resident fibroblasts remodeling towards myoCAF phenotypes and transforming resident EC to trigger angiogenesis. EVs^{DCC} induce resident stromal cells to secrete pro-stemness factors (iCAFs) to ensure the stem phenotype of future metastatic arriving cells.

CONCLUSIONS

CONCLUSIONS

1. ***ALDH1A1:tdTomato* reporter vector allows the identification and isolation of CSC-like subpopulations from heterogeneous breast cancer cell lines** providing a useful tool for the study of this cell subpopulation.
2. **Breast cancer cells show high grades of cellular plasticity**, displaying bi-directional interconversion between CSC and DCC states. These cell state transitions are determined by the CSC/DCC ratio and tend to an equilibrium over time.
3. **EVs^{CSC} and EVs^{DCC} present marked differences in their stemness related protein cargo.**
4. **EVs^{CSC}/ EVs^{DCC} stimulation emerges as a key regulation mechanism of CSC/DCC equilibrium as they oppositely exert cancer cells plasticity.** While the absence of EVs^{CSC} and an abnormal increase of EVs^{DCC} signaling triggers cancer cells de-differentiation to replenish missing CSC population, EVs^{CSC} overstimulation leads to the induction of cancer cells differentiation.
5. **EVs^{DCC} activate CAFs inflammatory (iCAFs) populations with enhanced cytokines secretory phenotype.** CAFs activated by EVs^{DCC} upregulate the secretion of cytokines IL-6 and IL-8, which in turn **induce the de-differentiation of cancer cells** towards CSC-like phenotypes. EVs^{CSC} do not show this effect, which unveils that EVs signaling to stromal cells also mediates CSC/DCC equilibrium.
6. **EVs^{CSC} activate α -SMA+ CAFs subpopulations (myoCAFs) that display enhanced ECM remodeling abilities and higher invasive potential in 3D models. EVs^{CSC} also display angiogenic potential.**
7. **EVs^{CSC} *in vivo* conditioning leads to the formation of supportive metastatic niches** through the activation of resident fibroblasts and endothelial cells **that sustain efficient metastatic cells engraftment.** EVs^{DCC} *in vivo* conditioning induces metastatic niche resident cells to sustain CSC phenotype of arriving metastatic cancer cells.

BIBLIOGRAPHY

BIBLIOGRAPHY

1. Sung, H. *et al.* Global Cancer Statistics 2020: GLOBOCAN Estimates of Incidence and Mortality Worldwide for 36 Cancers in 185 Countries. *CA: A Cancer Journal for Clinicians* (2021) doi:10.3322/caac.21660.
2. Waks, A. G. & Winer, E. P. Breast Cancer Treatment: A Review. *JAMA - Journal of the American Medical Association* **321**, 288–300 (2019).
3. Harbeck, N. *et al.* Breast cancer. *Nature Reviews Disease Primers* vol. 5 (2019).
4. Ferlay, J. *et al.* Estimating the global cancer incidence and mortality in 2018: GLOBOCAN sources and methods. *International Journal of Cancer* **144**, 1941–1953 (2019).
5. Koren, S. & Bentires-Alj, M. Breast Tumor Heterogeneity: Source of Fitness, Hurdle for Therapy. *Molecular Cell* **60**, 537–546 (2015).
6. Zardavas, D., Irrthum, A., Swanton, C. & Piccart, M. Clinical management of breast cancer heterogeneity. *Nature Reviews Clinical Oncology* (2015) doi:10.1038/nrclinonc.2015.73.
7. Turashvili, G. & Brogi, E. Tumor heterogeneity in breast cancer. *Frontiers in Medicine* **4**, (2017).
8. Turashvili, G. & Brogi, E. Tumor heterogeneity in breast cancer. *Frontiers in Medicine* (2017) doi:10.3389/fmed.2017.00227.
9. Osborne, C. K., Yochmowitz, M. G., Knight, W. A. & McGuire, W. L. The value of estrogen and progesterone receptors in the treatment of breast cancer. *Cancer* (1980) doi:10.1002/1097-0142(19801215)46:12+<2884::AID-CNCR2820461429>3.0.CO;2-U.
10. Fitzgibbons, P. L., Murphy, D. A., Hammond, M. E. H., Allred, D. C. & Valenstein, P. N. Recommendations for validating estrogen and progesterone receptor immunohistochemistry assays. *Archives of Pathology and Laboratory Medicine* (2010) doi:10.1043/1543-2165-134.6.930.
11. Wolff, A. C. *et al.* Human epidermal growth factor receptor 2 testing in breast cancer: American society of clinical oncology/college of American pathologists clinical practice guideline focused update. *Journal of Clinical Oncology* (2018) doi:10.1200/JCO.2018.77.8738.
12. Kittaneh, M., Montero, A. J. & Glück, S. Molecular Profiling for Breast Cancer: A Comprehensive Review. *Biomarkers in Cancer* (2013) doi:10.4137/bic.s9455.
13. Eroles, P., Bosch, A., Alejandro Pérez-Fidalgo, J. & Lluch, A. Molecular biology in breast cancer: Intrinsic subtypes and signaling pathways. *Cancer Treatment Reviews* (2012) doi:10.1016/j.ctrv.2011.11.005.
14. Prat, A. *et al.* Clinical implications of the intrinsic molecular subtypes of breast cancer. *Breast* (2015) doi:10.1016/j.breast.2015.07.008.
15. Abe, O. *et al.* Relevance of breast cancer hormone receptors and other factors to the efficacy of adjuvant tamoxifen: Patient-level meta-analysis of randomised trials. *The Lancet* (2011) doi:10.1016/S0140-6736(11)60993-8.

16. Mitri, Z., Constantine, T. & O'Regan, R. The HER2 Receptor in Breast Cancer: Pathophysiology, Clinical Use, and New Advances in Therapy. *Chemotherapy Research and Practice* (2012) doi:10.1155/2012/743193.
17. Fisher, B. *et al.* Tamoxifen for prevention of breast cancer: Report of the National Surgical Adjuvant Breast and Bowel Project P-1 study. *Journal of the National Cancer Institute* (1998) doi:10.1093/jnci/90.18.1371.
18. Piccart-Gebhart, M. J. *et al.* Trastuzumab after Adjuvant Chemotherapy in HER2-Positive Breast Cancer. *New England Journal of Medicine* (2005) doi:10.1056/nejmoa052306.
19. Bianchini, G., Balko, J. M., Mayer, I. A., Sanders, M. E. & Gianni, L. Triple-negative breast cancer: Challenges and opportunities of a heterogeneous disease. *Nature Reviews Clinical Oncology* **13**, 674–690 (2016).
20. Lee, K. L., Kuo, Y. C., Ho, Y. S. & Huang, Y. H. Triple-negative breast cancer: Current understanding and future therapeutic breakthrough targeting cancer stemness. *Cancers* **11**, (2019).
21. Azim, H. A., Ghosn, M., Oualla, K. & Kassem, L. Personalized treatment in metastatic triple-negative breast cancer: The outlook in 2020. *Breast Journal* **26**, 69–80 (2020).
22. McCann, K. E., Hurvitz, S. A. & McAndrew, N. Advances in Targeted Therapies for Triple-Negative Breast Cancer. *Drugs* **79**, 1217–1230 (2019).
23. Zhang, M. & Rosen, J. M. Developmental Insights into Breast Cancer Intratumoral Heterogeneity. *Trends in Cancer* (2015) doi:10.1016/j.trecan.2015.10.005.
24. Yeo, S. K. & Guan, J. L. Breast Cancer: Multiple Subtypes within a Tumor? *Trends in Cancer* (2017) doi:10.1016/j.trecan.2017.09.001.
25. Dagogo-Jack, I. & Shaw, A. T. Tumour heterogeneity and resistance to cancer therapies. *Nature Reviews Clinical Oncology* (2018) doi:10.1038/nrclinonc.2017.166.
26. Bedard, P. L., Hansen, A. R., Ratain, M. J. & Siu, L. L. Tumour heterogeneity in the clinic. *Nature* (2013) doi:10.1038/nature12627.
27. Ramón y Cajal, S. *et al.* Clinical implications of intratumor heterogeneity: challenges and opportunities. *Journal of Molecular Medicine* **98**, 161–177 (2020).
28. Lee, G. & R Hall, R. Cancer Stem Cells: Cellular Plasticity, Niche, and its Clinical Relevance. *Journal of Stem Cell Research & Therapy* **06**, (2016).
29. Skibinski, A. & Kuperwasser, C. The origin of breast tumor heterogeneity. *Oncogene* (2015) doi:10.1038/onc.2014.475.
30. Pece, S. *et al.* Biological and Molecular Heterogeneity of Breast Cancers Correlates with Their Cancer Stem Cell Content. *Cell* (2010) doi:10.1016/j.cell.2009.12.007.
31. Januškevičienė, I. & Petrikaitė, V. Heterogeneity of breast cancer: The importance of interaction between different tumor cell populations. *Life Sciences* **239**, 117009 (2019).
32. van Neerven, S. M., Tieken, M., Vermeulen, L. & Bijlsma, M. F. Bidirectional interconversion of stem and non-stem cancer cell populations: A reassessment of theoretical models for tumor heterogeneity. *Molecular and Cellular Oncology* **3**, 1–9 (2016).

33. Campbell, L. L. & Polyak, K. Breast tumor heterogeneity: Cancer stem cells or clonal evolution? *Cell Cycle* (2007) doi:10.4161/cc.6.19.4914.
34. Shackleton, M., Quintana, E., Fearon, E. R. & Morrison, S. J. Heterogeneity in Cancer: Cancer Stem Cells versus Clonal Evolution. *Cell* (2009) doi:10.1016/j.cell.2009.08.017.
35. Nowell, P. C. The clonal evolution of tumor cell populations. *Science* (1976) doi:10.1126/science.959840.
36. Merlo, L. M. F., Pepper, J. W., Reid, B. J. & Maley, C. C. Cancer as an evolutionary and ecological process. *Nature Reviews Cancer* (2006) doi:10.1038/nrc2013.
37. Janiszewska, M. & Polyak, K. Clonal evolution in cancer: A tale of twisted twines. *Cell Stem Cell* (2015) doi:10.1016/j.stem.2014.12.011.
38. Shackleton, M., Quintana, E., Fearon, E. R. & Morrison, S. J. Heterogeneity in Cancer: Cancer Stem Cells versus Clonal Evolution. *Cell* **138**, 822–829 (2009).
39. Reya, T., Morrison, S. J., Clarke, M. F. & Weissman, I. L. Stem cells, cancer, and cancer stem cells. *Nature* (2001) doi:10.1038/35102167.
40. Wagers, A. J. & Weissman, I. L. Plasticity of adult stem cells. *Cell* (2004) doi:10.1016/S0092-8674(04)00208-9.
41. Kreso, A. & Dick, J. E. Evolution of the cancer stem cell model. *Cell Stem Cell* (2014) doi:10.1016/j.stem.2014.02.006.
42. Dick, J. E. Stem cell concepts renew cancer research. *Blood* (2008) doi:10.1182/blood-2008-08-077941.
43. Owens, T. W. & Naylor, M. J. Breast cancer stem cells. *Frontiers in Physiology* vol. 4 AUG (2013).
44. Zhou, J. *et al.* Stem cells and cellular origins of breast cancer: Updates in the rationale, controversies, and therapeutic implications. *Frontiers in Oncology* **9**, 1–12 (2019).
45. Butti, R., Gunasekaran, V. P., Kumar, T. V. S., Banerjee, P. & Kundu, G. C. Breast cancer stem cells: Biology and therapeutic implications. *International Journal of Biochemistry and Cell Biology* **107**, 38–52 (2019).
46. Feng, Y. *et al.* Breast cancer development and progression: Risk factors, cancer stem cells, signaling pathways, genomics, and molecular pathogenesis. *Genes and Diseases* (2018) doi:10.1016/j.gendis.2018.05.001.
47. Dittmer, J. Breast cancer stem cells: Features, key drivers and treatment options. *Seminars in Cancer Biology* (2018) doi:10.1016/j.semcancer.2018.07.007.
48. Abbaszadegan, M. R. *et al.* Isolation, identification, and characterization of cancer stem cells: A review. *Journal of Cellular Physiology* (2017) doi:10.1002/jcp.25759.
49. Akbarzadeh, M. *et al.* Current approaches in identification and isolation of cancer stem cells. *Journal of Cellular Physiology* **234**, 14759–14772 (2019).
50. Frandsen, T. L., Holst-Hansen, C. & Br nner, N. Tumorigenicity Assays. in *Encyclopedia of Life Sciences* (2001). doi:10.1038/npg.els.0002608.
51. Chumsri, S. & Burger, A. M. Cancer stem cells. in *Perspectives in Stem Cell Research* (2011). doi:10.5604/17322693.1009706.

52. Tirino, V. *et al.* Cancer stem cells in solid tumors: An overview and new approaches for their isolation and characterization. *FASEB Journal* (2013) doi:10.1096/fj.12-218222.
53. Fillmore, C. M. & Kuperwasser, C. Human breast cancer cell lines contain stem-like cells that self-renew, give rise to phenotypically diverse progeny and survive chemotherapy. *Breast Cancer Research* (2008) doi:10.1186/bcr1982.
54. Al-Hajj, M., Wicha, M. S., Benito-Hernandez, A., Morrison, S. J. & Clarke, M. F. Prospective identification of tumorigenic breast cancer cells. *Proceedings of the National Academy of Sciences of the United States of America* (2003) doi:10.1073/pnas.0530291100.
55. Ginestier, C. *et al.* ALDH1 Is a Marker of Normal and Malignant Human Mammary Stem Cells and a Predictor of Poor Clinical Outcome. *Cell Stem Cell* (2007) doi:10.1016/j.stem.2007.08.014.
56. Croker, A. K. *et al.* High aldehyde dehydrogenase and expression of cancer stem cell markers selects for breast cancer cells with enhanced malignant and metastatic ability. *Journal of Cellular and Molecular Medicine* (2009) doi:10.1111/j.1582-4934.2008.00455.x.
57. Ponti, D. *et al.* Isolation and in vitro propagation of tumorigenic breast cancer cells with stem/progenitor cell properties. *Cancer Research* (2005) doi:10.1158/0008-5472.CAN-05-0626.
58. Senbanjo, L. T. & Chellaiah, M. A. CD44: A multifunctional cell surface adhesion receptor is a regulator of progression and metastasis of cancer cells. *Frontiers in Cell and Developmental Biology* (2017) doi:10.3389/fcell.2017.00018.
59. Kristiansen, G. *et al.* CD24 Expression Is a New Prognostic Marker in Breast Cancer. *Clinical Cancer Research* (2003).
60. Tomita, H., Tanaka, K., Tanaka, T. & Hara, A. Aldehyde dehydrogenase 1A1 in stem cells and cancer. *Oncotarget* (2016) doi:10.18632/oncotarget.6920.
61. Vasiliou, V., Pappa, A. & Petersen, D. R. Role of aldehyde dehydrogenases in endogenous and xenobiotic metabolism. *Chemico-Biological Interactions* (2000) doi:10.1016/S0009-2797(00)00211-8.
62. Clark, D. W. & Palle, K. Aldehyde dehydrogenases in cancer stem cells: Potential as therapeutic targets. *Annals of Translational Medicine* (2016) doi:10.21037/atm.2016.11.82.
63. Januchowski, R., Wojtowicz, K. & Zabel, M. The role of aldehyde dehydrogenase (ALDH) in cancer drug resistance. *Biomedicine and Pharmacotherapy* (2013) doi:10.1016/j.biopha.2013.04.005.
64. Mele, L., Liccardo, D. & Tirino, V. Evaluation and isolation of cancer stem cells using ALDH activity assay. in *Methods in Molecular Biology* (2018). doi:10.1007/978-1-4939-7401-6_4.
65. Paoli, P., Giannoni, E. & Chiarugi, P. Anoikis molecular pathways and its role in cancer progression. *Biochimica et Biophysica Acta - Molecular Cell Research* (2013) doi:10.1016/j.bbamcr.2013.06.026.
66. Yousefnia, S., Ghaedi, K., Seyed Forootan, F. & Nasr Esfahani, M. H. Characterization of the stemness potency of mammospheres

- isolated from the breast cancer cell lines. *Tumor Biology* (2019) doi:10.1177/1010428319869101.
67. Grimshaw, M. J. *et al.* Mammosphere culture of metastatic breast cancer cells enriches for tumorigenic breast cancer cells. *Breast Cancer Research* (2008) doi:10.1186/bcr2106.
68. Laranjo, M. *et al.* Mammospheres of hormonal receptor positive breast cancer diverge to triple-negative phenotype. *Breast* (2018) doi:10.1016/j.breast.2017.11.009.
69. Manuel Iglesias, J. *et al.* Mammosphere Formation in Breast Carcinoma Cell Lines Depends upon Expression of E-cadherin. *PLoS ONE* (2013) doi:10.1371/journal.pone.0077281.
70. Lombardo, Y., de Giorgio, A., Coombes, C. R., Stebbing, J. & Castellano, L. Mammosphere formation assay from human breast cancer tissues and cell lines. *Journal of Visualized Experiments* (2015) doi:10.3791/52671.
71. Rajendran, V. & Jain, M. V. In vitro tumorigenic assay: colony forming assay for cancer stem cells. in *Methods in Molecular Biology* (2018). doi:10.1007/978-1-4939-7401-6_8.
72. Franken, N. A. P., Rodermond, H. M., Stap, J., Haveman, J. & van Bree, C. Clonogenic assay of cells in vitro. *Nature Protocols* (2006) doi:10.1038/nprot.2006.339.
73. Golebiewska, A., Brons, N. H. C., Bjerkvig, R. & Niclou, S. P. Critical appraisal of the side population assay in stem cell and cancer stem cell research. *Cell Stem Cell* (2011) doi:10.1016/j.stem.2011.01.007.
74. Hadnagy, A., Gaboury, L., Beaulieu, R. & Balicki, D. SP analysis may be used to identify cancer stem cell populations. *Experimental Cell Research* (2006) doi:10.1016/j.yexcr.2006.08.030.
75. Boesch, M., Wolf, D. & Sopper, S. Optimized stem cell detection using the dyecycle-triggered side population phenotype. *Stem Cells International* (2016) doi:10.1155/2016/1652389.
76. Yousefnia, S. *et al.* Mechanistic Pathways of Malignancy in Breast Cancer Stem Cells. *Frontiers in Oncology* (2020) doi:10.3389/fonc.2020.00452.
77. Bray, S. J. Notch signalling in context. *Nature Reviews Molecular Cell Biology* (2016) doi:10.1038/nrm.2016.94.
78. Dontu, G. *et al.* Role of Notch signaling in cell-fate determination of human mammary stem/progenitor cells. *Breast Cancer Research* (2004) doi:10.1186/bcr920.
79. Farnie, G. & Clarke, R. B. Mammary stem cells and breast cancer - Role of notch signalling. *Stem Cell Reviews* (2007) doi:10.1007/s12015-007-0023-5.
80. Wang, Z., Li, Y., Banerjee, S. & Sarkar, F. H. Emerging role of Notch in stem cells and cancer. *Cancer Letters* (2009) doi:10.1016/j.canlet.2008.09.030.
81. D'Angelo, R. C. *et al.* Notch reporter activity in breast cancer cell lines identifies a subset of cells with stem cell activity. *Molecular Cancer Therapeutics* (2015) doi:10.1158/1535-7163.MCT-14-0228.
82. Harrison, H. *et al.* Regulation of breast cancer stem cell activity by signaling through the Notch4 receptor. *Cancer Research*

- (2010) doi:10.1158/0008-5472.CAN-09-1681.
83. Briscoe, J. & Théron, P. P. The mechanisms of Hedgehog signalling and its roles in development and disease. *Nature Reviews Molecular Cell Biology* (2013) doi:10.1038/nrm3598.
84. Liu, S. *et al.* Hedgehog signaling and Bmi-1 regulate self-renewal of normal and malignant human mammary stem cells. *Cancer Research* (2006) doi:10.1158/0008-5472.CAN-06-0054.
85. Tao, Y., Mao, J., Zhang, Q. & Li, L. Overexpression of Hedgehog signaling molecules and its involvement in triple-negative breast cancer. *Oncology Letters* (2011) doi:10.3892/ol.2011.357.
86. Katoh, M. & Katoh, M. WNT signaling pathway and stem cell signaling network. *Clinical Cancer Research* (2007) doi:10.1158/1078-0432.CCR-06-2316.
87. MacDonald, B. T., Tamai, K. & He, X. Wnt/ β -Catenin Signaling: Components, Mechanisms, and Diseases. *Developmental Cell* (2009) doi:10.1016/j.devcel.2009.06.016.
88. Fodde, R. & Brabletz, T. Wnt/ β -catenin signaling in cancer stemness and malignant behavior. *Current Opinion in Cell Biology* (2007) doi:10.1016/j.ceb.2007.02.007.
89. Cleary, A. S., Leonard, T. L., Gestl, S. A. & Gunther, E. J. Tumour cell heterogeneity maintained by cooperating subclones in Wnt-driven mammary cancers. *Nature* (2014) doi:10.1038/nature13187.
90. Monteiro, J. *et al.* Cancer stemness in Wnt-driven mammary tumorigenesis. *Carcinogenesis* (2014) doi:10.1093/carcin/bgt279.
91. King, T. D., Suto, M. J. & Li, Y. The wnt/ β -catenin signaling pathway: A potential therapeutic target in the treatment of triple negative breast cancer. *Journal of Cellular Biochemistry* (2012) doi:10.1002/jcb.23350.
92. Pohl, S. G. *et al.* Wnt signaling in triple-negative breast cancer. *Oncogenesis* (2017) doi:10.1038/oncsis.2017.14.
93. Dey, N. *et al.* Wnt signaling in triple negative breast cancer is associated with metastasis. *BMC Cancer* (2013) doi:10.1186/1471-2407-13-537.
94. Yang, L. *et al.* Targeting cancer stem cell pathways for cancer therapy. *Signal Transduction and Targeted Therapy* vol. 5 (2020).
95. Leis, O. *et al.* Sox2 expression in breast tumours and activation in breast cancer stem cells. *Oncogene* (2012) doi:10.1038/onc.2011.338.
96. Santaliz-Ruiz, L. E., Xie, X., Old, M., Teknos, T. N. & Pan, Q. Emerging role of nanog in tumorigenesis and cancer stem cells. *International Journal of Cancer* (2014) doi:10.1002/ijc.28690.
97. Yu, F. *et al.* Kruppel-like factor 4 (KLF4) is required for maintenance of breast cancer stem cells and for cell migration and invasion. *Oncogene* (2011) doi:10.1038/onc.2010.591.
98. Huber, M. A. *et al.* NF- κ B is essential for epithelial-mesenchymal transition and metastasis in a model of breast cancer progression. *Journal of Clinical Investigation* (2004) doi:10.1172/JCI200421358.
99. Shostak, K. & Chariot, A. NF- κ B, stem cells and breast cancer: The links get stronger.

- Breast Cancer Research* (2011)
doi:10.1186/bcr2886.
100. Yamamoto, M. *et al.* Epigenetic alteration of the NF- κ B-inducing kinase (NIK) gene is involved in enhanced NIK expression in basal-like breast cancer. *Cancer Science* (2010)
doi:10.1111/j.1349-7006.2010.01685.x.
101. Yamamoto, M. *et al.* NF- κ B non-cell-autonomously regulates cancer stem cell populations in the basal-like breast cancer subtype. *Nature Communications* (2013)
doi:10.1038/ncomms3299.
102. Hartman, Z. C. *et al.* Growth of triple-negative breast cancer cells relies upon coordinate autocrine expression of the proinflammatory cytokines IL-6 and IL-8. *Cancer Research* **73**, (2013).
103. Korkaya, H., Liu, S. & Wicha, M. S. Regulation of cancer stem cells by cytokine networks: Attacking cancer's inflammatory roots. *Clinical Cancer Research* (2011)
doi:10.1158/1078-0432.CCR-10-2743.
104. Jia, D. *et al.* An autocrine inflammatory forward-feedback loop after chemotherapy withdrawal facilitates the repopulation of drug-resistant breast cancer cells. *Cell death & disease* (2017)
doi:10.1038/cddis.2017.319.
105. Ortiz-Montero, P., Londoño-Vallejo, A. & Vernet, J. P. Senescence-associated IL-6 and IL-8 cytokines induce a self- and cross-reinforced senescence/inflammatory milieu strengthening tumorigenic capabilities in the MCF-7 breast cancer cell line. *Cell Communication and Signaling* (2017)
doi:10.1186/s12964-017-0172-3.
106. Iliopoulos, D., Hirsch, H. A., Wang, G. & Struhl, K. Inducible formation of breast cancer stem cells and their dynamic equilibrium with non-stem cancer cells via IL6 secretion. *Proceedings of the National Academy of Sciences of the United States of America* (2011)
doi:10.1073/pnas.1018898108.
107. Liu, S. *et al.* Breast cancer stem cells are regulated by mesenchymal stem cells through cytokine networks. *Cancer Research* (2011)
doi:10.1158/0008-5472.CAN-10-0538.
108. Korkaya, H. *et al.* Activation of an IL6 Inflammatory Loop Mediates Trastuzumab Resistance in HER2+ Breast Cancer by Expanding the Cancer Stem Cell Population. *Molecular Cell* (2012) doi:10.1016/j.molcel.2012.06.014.
109. Hunter, C. A. & Jones, S. A. IL-6 as a key-stone cytokine in health and disease. *Nature Immunology* (2015) doi:10.1038/ni.3153.
110. Masjedi, A. *et al.* The significant role of interleukin-6 and its signaling pathway in the immunopathogenesis and treatment of breast cancer. *Biomedicine and Pharmacotherapy* (2018) doi:10.1016/j.biopha.2018.09.177.
111. Heinrich, P. C. *et al.* Principles of interleukin (IL)-6-type cytokine signalling and its regulation. *Biochemical Journal* (2003)
doi:10.1042/BJ20030407.
112. Kim, S. Y. *et al.* Role of the IL-6-JAK1-STAT3-Oct-4 pathway in the conversion of non-stem cancer cells into cancer stem-like cells. *Cellular Signalling* (2013)
doi:10.1016/j.cellsig.2013.01.007.
113. Marotta, L. L. C. *et al.* The JAK2/STAT3 signaling pathway is required for growth of CD44 +CD24- stem cell-like breast cancer

- cells in human tumors. *Journal of Clinical Investigation* (2011) doi:10.1172/JCI44745.
114. Xie, K. Interleukin-8 and human cancer biology. *Cytokine and Growth Factor Reviews* (2001) doi:10.1016/S1359-6101(01)00016-8.
115. Alfaro, C. *et al.* Interleukin-8 in cancer pathogenesis, treatment and follow-up. *Cancer Treatment Reviews* (2017) doi:10.1016/j.ctrv.2017.08.004.
116. Liu, Q. *et al.* The CXCL8-CXCR1/2 pathways in cancer. *Cytokine and Growth Factor Reviews* (2016) doi:10.1016/j.cytogfr.2016.08.002.
117. Jain, R. K. & Carmeliet, P. SnapShot: Tumor angiogenesis. *Cell* (2012) doi:10.1016/j.cell.2012.05.025.
118. Weis, S. M. & Cheresh, D. A. Tumor angiogenesis: Molecular pathways and therapeutic targets. *Nature Medicine* (2011) doi:10.1038/nm.2537.
119. Kong, L. *et al.* Overexpression of SDF-1 activates the NF- κ B pathway to induce epithelial to mesenchymal transition and cancer stem cell-like phenotypes of breast cancer cells. *International Journal of Oncology* (2016) doi:10.3892/ijo.2016.3343.
120. Wang, Y., Li, C., Li, Y. & Zhu, Z. Involvement of breast cancer stem cells in tumor angiogenesis. *Oncology Letters* (2017) doi:10.3892/ol.2017.7238.
121. Zhou, W., Wang, G. & Guo, S. Regulation of angiogenesis via Notch signaling in breast cancer and cancer stem cells. *Biochimica et Biophysica Acta - Reviews on Cancer* (2013) doi:10.1016/j.bbcan.2013.10.003.
122. Kim, H., Lin, Q., Glazer, P. M. & Yun, Z. The hypoxic tumor microenvironment in vivo selects the cancer stem cell fate of breast cancer cells. *Breast Cancer Research* (2018) doi:10.1186/s13058-018-0944-8.
123. Semenza, G. L. Hypoxia-inducible factors: coupling glucose metabolism and redox regulation with induction of the breast cancer stem cell phenotype. *The EMBO Journal* (2017) doi:10.15252/embj.201695204.
124. Keith, B. & Simon, M. C. Hypoxia-Inducible Factors, Stem Cells, and Cancer. *Cell* (2007) doi:10.1016/j.cell.2007.04.019.
125. Xiang, L. & Semenza, G. L. Hypoxia-inducible factors promote breast cancer stem cell specification and maintenance in response to hypoxia or cytotoxic chemotherapy. in *Advances in Cancer Research* (2019). doi:10.1016/bs.acr.2018.11.001.
126. Samanta, D., Gilkesa, D. M., Chaturvedia, P., Xiang, L. & Semenza, G. L. Hypoxia-inducible factors are required for chemotherapy resistance of breast cancer stem cells. *Proceedings of the National Academy of Sciences of the United States of America* (2014) doi:10.1073/pnas.1421438111.
127. Semenza, G. L. The hypoxic tumor microenvironment: A driving force for breast cancer progression. *Biochimica et Biophysica Acta - Molecular Cell Research* (2016) doi:10.1016/j.bbamcr.2015.05.036.
128. Semenza, G. L. Regulation of the breast cancer stem cell phenotype by hypoxia-inducible factors. *Clinical Science* (2015) doi:10.1042/CS20150451.
129. Dean, M., Fojo, T. & Bates, S. Tumour stem cells and drug resistance. *Nature Reviews Cancer* (2005) doi:10.1038/nrc1590.

130. Doyle, L. A. & Ross, D. D. Multidrug resistance mediated by the breast cancer resistance protein BCRP (ABCG2). *Oncogene* (2003) doi:10.1038/sj.onc.1206938.
131. L., Q., P., O. & I., H. Therapeutic resistance and stemness in mitotically quiescent human breast cancer cells. *Breast Cancer Research and Treatment* (2018).
132. Quayle, L. A., Ottewell, P. D. & Holen, I. Chemotherapy resistance and stemness in mitotically quiescent human breast cancer cells identified by fluorescent dye retention. *Clinical and Experimental Metastasis* (2018) doi:10.1007/s10585-018-9946-2.
133. Ross, A. A. Minimal residual disease in solid tumor malignancies: A review. *Journal of Hematotherapy and Stem Cell Research* (1998) doi:10.1089/scd.1.1998.7.9.
134. Ghiaur, G., Gerber, J. & Jones, R. J. Concise review: Cancer stem cells and minimal residual disease. *Stem Cells* (2012) doi:10.1002/stem.769.
135. Ignatiadis, M. & Reinholz, M. Minimal residual disease and circulating tumor cells in breast cancer. *Breast Cancer Research* (2011) doi:10.1186/bcr2906.
136. Dey, P., Rathod, M. & De, A. Targeting stem cells in the realm of drug-resistant breast cancer. *Breast Cancer: Targets and Therapy* **11**, 115–135 (2019).
137. Chiang, A. C. & Massagué, J. Molecular Basis of Metastasis. *New England Journal of Medicine* (2008) doi:10.1056/nejmra0805239.
138. Chaffer, C. L. & Weinberg, R. A. A perspective on cancer cell metastasis. *Science* (2011) doi:10.1126/science.1203543.
139. Gupta, G. P. & Massagué, J. Cancer Metastasis: Building a Framework. *Cell* (2006) doi:10.1016/j.cell.2006.11.001.
140. Weigelt, B., Peterse, J. L. & Van't Veer, L. J. Breast cancer metastasis: Markers and models. *Nature Reviews Cancer* (2005) doi:10.1038/nrc1670.
141. Jolly, M. K., Ware, K. E., Gilja, S., Somarelli, J. A. & Levine, H. EMT and MET: necessary or permissive for metastasis? *Molecular Oncology* (2017) doi:10.1002/1878-0261.12083.
142. Brabletz, T. EMT and MET in Metastasis: Where Are the Cancer Stem Cells? *Cancer Cell* (2012) doi:10.1016/j.ccr.2012.11.009.
143. Krebs, A. M. *et al.* The EMT-activator Zeb1 is a key factor for cell plasticity and promotes metastasis in pancreatic cancer. *Nature Cell Biology* (2017) doi:10.1038/ncb3513.
144. Yilmaz, M. & Christofori, G. EMT, the cytoskeleton, and cancer cell invasion. *Cancer and Metastasis Reviews* (2009) doi:10.1007/s10555-008-9169-0.
145. Brabletz, T., Kalluri, R., Nieto, M. A. & Weinberg, R. A. EMT in cancer. *Nature Reviews Cancer* (2018) doi:10.1038/nrc.2017.118.
146. Thiery, J. P., Acloque, H., Huang, R. Y. J. & Nieto, M. A. Epithelial-Mesenchymal Transitions in Development and Disease. *Cell* (2009) doi:10.1016/j.cell.2009.11.007.
147. Papadaki, M. A. *et al.* Circulating tumor cells with stemness and epithelial-to-mesenchymal transition features are chemoresistant and predictive of poor outcome in metastatic breast cancer. *Molecular Cancer Therapeutics* (2019) doi:10.1158/1535-7163.MCT-18-0584.

148. Morel, A. P. *et al.* Generation of breast cancer stem cells through epithelial-mesenchymal transition. *PLoS ONE* (2008) doi:10.1371/journal.pone.0002888.
149. Mani, S. A. *et al.* The Epithelial-Mesenchymal Transition Generates Cells with Properties of Stem Cells. *Cell* (2008) doi:10.1016/j.cell.2008.03.027.
150. Wilson, M. M., Weinberg, R. A., Lees, J. A. & Guen, V. J. Emerging Mechanisms by which EMT Programs Control Stemness. *Trends in Cancer* (2020) doi:10.1016/j.trecan.2020.03.011.
151. Velasco-Velázquez, M. A., Popov, V. M., Lisanti, M. P. & Pestell, R. G. The role of breast cancer stem cells in metastasis and therapeutic implications. *American Journal of Pathology* (2011) doi:10.1016/j.ajpath.2011.03.005.
152. Toloudi, M., Apostolou, P., Chatziioannou, M. & Papasotiriou, I. Correlation between cancer stem cells and circulating tumor cells and their value. *Case Reports in Oncology* (2011) doi:10.1159/000324403.
153. Tinhofer, I., Saki, M., Niehr, F., Keilholz, U. & Budach, V. Cancer stem cell characteristics of circulating tumor cells. *International Journal of Radiation Biology* (2014) doi:10.3109/09553002.2014.886798.
154. Balic, M. *et al.* Most early disseminated cancer cells detected in bone marrow of breast cancer patients have a putative breast cancer stem cell phenotype. *Clinical Cancer Research* (2006) doi:10.1158/1078-0432.CCR-06-0169.
155. Fanelli, G. N., Naccarato, A. G. & Scatena, C. Recent Advances in Cancer Plasticity: Cellular Mechanisms, Surveillance Strategies, and Therapeutic Optimization. *Frontiers in Oncology* **10**, 1–10 (2020).
156. Honeth, G. *et al.* The CD44+/CD24- phenotype is enriched in basal-like breast tumors. *Breast Cancer Research* (2008) doi:10.1186/bcr2108.
157. Wang, H. *et al.* CD44+/CD24- phenotype predicts a poor prognosis in triple-negative breast cancer. *Oncology Letters* (2017) doi:10.3892/ol.2017.6959.
158. Ma, F. *et al.* Enriched CD44+/CD24- population drives the aggressive phenotypes presented in triple-negative breast cancer (TNBC). *Cancer Letters* (2014) doi:10.1016/j.canlet.2014.06.022.
159. Li, W. *et al.* Unraveling the roles of CD44/CD24 and ALDH1 as cancer stem cell markers in tumorigenesis and metastasis. *Scientific Reports* (2017) doi:10.1038/s41598-017-14364-2.
160. Park, S. Y., Choi, J. H. & Nam, J. S. Targeting cancer stem cells in triple-negative breast cancer. *Cancers* (2019) doi:10.3390/cancers11070965.
161. Li, C. W. *et al.* Eradication of Triple-Negative Breast Cancer Cells by Targeting Glycosylated PD-L1. *Cancer Cell* (2018) doi:10.1016/j.ccell.2018.01.009.
162. Zomer, A. *et al.* Brief report: Intravital imaging of cancer stem cell plasticity in mammary tumors. *Stem Cells* **31**, 602–606 (2013).
163. Smigiel, J. M. *et al.* Cellular plasticity and metastasis in breast cancer: a pre- and post-malignant problem. *Journal of Cancer Metastasis and Treatment* **2019**, (2019).

164. Marjanovic, N. D., Weinberg, R. A. & Chaffer, C. L. Cell plasticity and heterogeneity in cancer. *Clinical Chemistry* (2013) doi:10.1373/clinchem.2012.184655.
165. Saxena, K., Murali, R., Kumar Jolly, M. & Nair, R. Cancer Stem Cell plasticity-a deadly deal. (2019) doi:10.20944/preprints201912.0388.v1.
166. Batlle, E. & Clevers, H. Cancer stem cells revisited. *Nature Publishing Group* **23**, (2017).
167. Capp, J. P. Cancer stem cells: From historical roots to a new perspective. *Journal of Oncology* vol. 2019 (2019).
168. Wang, W. *et al.* Dynamics between cancer cell subpopulations reveals a model coordinating with both hierarchical and stochastic concepts. *PLoS ONE* **9**, (2014).
169. Li, Y. & Lathera, J. Cancer stem cells: Distinct entities or dynamically regulated phenotypes? *Cancer Research* (2012) doi:10.1158/0008-5472.CAN-11-3070.
170. Yang, G. *et al.* Dynamic equilibrium between cancer stem cells and non-stem cancer cells in human SW620 and MCF-7 cancer cell populations. *British Journal of Cancer* **106**, 1512–1519 (2012).
171. Shimokawa, M. *et al.* Visualization and targeting of LGR5 + human colon cancer stem cells. *Nature* **545**, (2017).
172. Vermeulen, L. *et al.* Wnt activity defines colon cancer stem cells and is regulated by the microenvironment. *Nature Cell Biology* **12**, (2010).
173. Cabrera, M. C. Cancer stem cell plasticity and tumor hierarchy. *World Journal of Stem Cells* **7**, 27 (2015).
174. Gupta, P. B. *et al.* Stochastic state transitions give rise to phenotypic equilibrium in populations of cancer cells. *Cell* **146**, 633–644 (2011).
175. Jiang, D., Wang, Y. & Zhou, D. Phenotypic equilibrium as probabilistic convergence in multi-phenotype cell population dynamics. 1–12 (2017) doi:10.1371/journal.pone.0170916.
176. Zhou, D., Wu, D., Li, Z., Qian, M. & Zhang, M. Q. Population dynamics of cancer cells with cell state conversions. *Quantitative Biology* (2013) doi:10.1007/s40484-013-0014-2.
177. Olmeda, F. & Amar, M. Ben. Clonal pattern dynamics in tumor : the concept of cancer stem cells. *Scientific Reports* 1–18 (2019) doi:10.1038/s41598-019-51575-1.
178. Mittal, S., Brown, N. J. & Holen, I. The breast tumor microenvironment: role in cancer development, progression and response to therapy. *Expert Review of Molecular Diagnostics* vol. 18 (2018).
179. Whiteside, T. L. The tumor microenvironment and its role in promoting tumor growth. *Oncogene* (2008) doi:10.1038/onc.2008.271.
180. Anderson, N. M. & Simon, M. C. The tumor microenvironment. *Current Biology* (2020) doi:10.1016/j.cub.2020.06.081.
181. Burgos-Panadero, R. *et al.* The tumour microenvironment as an integrated framework to understand cancer biology. *Cancer Letters* (2019) doi:10.1016/j.canlet.2019.07.010.
182. Plaks, V., Kong, N. & Werb, Z. The cancer stem cell niche: How essential is the niche in

- regulating stemness of tumor cells? *Cell Stem Cell* vol. 16 225–238 (2015).
183. Iliopoulos, D., Hirsch, H. A., Wang, G. & Struhl, K. Inducible formation of breast cancer stem cells and their dynamic equilibrium with non-stem cancer cells via IL6 secretion. **108**, 1397–1402 (2011).
184. Korkaya, H., Liu, S. & Wicha, M. S. Breast cancer stem cells, cytokine networks, and the tumor microenvironment. *Journal of Clinical Investigation* (2011) doi:10.1172/JCI57099.
185. Xie, G. *et al.* IL-6-induced epithelial-mesenchymal transition promotes the generation of breast cancer stem-like cells analogous to mammosphere cultures. *International Journal of Oncology* (2012) doi:10.3892/ijo.2011.1275.
186. Kalluri, R. & Zeisberg, M. Fibroblasts in cancer. *Nature Reviews Cancer* (2006) doi:10.1038/nrc1877.
187. Kalluri, R. The biology and function of fibroblasts in cancer. *Nature Reviews Cancer* (2016) doi:10.1038/nrc.2016.73.
188. Bhowmick, N. A., Neilson, E. G. & Moses, H. L. Stromal fibroblasts in cancer initiation and progression. *Nature* (2004) doi:10.1038/nature03096.
189. Pein, M. *et al.* Metastasis-initiating cells induce and exploit a fibroblast niche to fuel malignant colonization of the lungs. *Nature Communications* (2020) doi:10.1038/s41467-020-15188-x.
190. Räsänen, K. & Vaheri, A. Activation of fibroblasts in cancer stroma. *Experimental Cell Research* (2010) doi:10.1016/j.yexcr.2010.04.032.
191. Mishra, P. J. *et al.* Carcinoma-associated fibroblast-like differentiation of human mesenchymal stem cells. *Cancer Research* (2008) doi:10.1158/0008-5472.CAN-08-0943.
192. Kalluri, R. The biology and function of fibroblasts in cancer. *Nature Publishing Group* doi:10.1038/nrc.2016.73.
193. Naito, Y. *et al.* Cancer extracellular vesicles contribute to stromal heterogeneity by inducing chemokines in cancer-associated fibroblasts. *Oncogene* 5566–5579 (2019) doi:10.1038/s41388-019-0832-4.
194. Huang, T., Guan, X. & Fu, L. Therapeutic targeting of the crosstalk between cancer-associated fibroblasts and cancer stem cells. **9**, 1889–1904 (2019).
195. Su, S. *et al.* CD10+GPR77+ Cancer-Associated Fibroblasts Promote Cancer Formation and Chemoresistance by Sustaining Cancer Stemness. *Cell* **172**, 841-856.e16 (2018).
196. Pelon, F. *et al.* Cancer-associated fibroblast heterogeneity in axillary lymph nodes drives metastases in breast cancer through complementary mechanisms. *Nature Communications* **11**, (2020).
197. Monteran, L. & Erez, N. The dark side of fibroblasts: Cancer-associated fibroblasts as mediators of immunosuppression in the tumor microenvironment. *Frontiers in Immunology* vol. 10 (2019).
198. Fiori, M. E. *et al.* Cancer-associated fibroblasts as abettors of tumor progression at the crossroads of EMT and therapy resistance. *Molecular Cancer* (2019) doi:10.1186/s12943-019-0994-2.

199. Chen, W. J. *et al.* Cancer-associated fibroblasts regulate the plasticity of lung cancer stemness via paracrine signalling. *Nature Communications* (2014) doi:10.1038/ncomms4472.
200. Erez, N., Truitt, M., Olson, P. & Hanahan, D. Cancer-Associated Fibroblasts Are Activated in Incipient Neoplasia to Orchestrate Tumor-Promoting Inflammation in an NF- κ B-Dependent Manner. *Cancer Cell* (2010) doi:10.1016/j.ccr.2009.12.041.
201. Buchsbaum, R. J. & Oh, S. Y. Breast cancer-associated fibroblasts: Where we are and where we need to go. *Cancers* **8**, 1–19 (2016).
202. Kessenbrock, K., Plaks, V. & Werb, Z. Matrix Metalloproteinases: Regulators of the Tumor Microenvironment. *Cell* (2010) doi:10.1016/j.cell.2010.03.015.
203. Chan, T. S., Shaked, Y. & Tsai, K. K. Targeting the Interplay Between Cancer Fibroblasts, Mesenchymal Stem Cells, and Cancer Stem Cells in Desmoplastic Cancers. *Frontiers in Oncology* vol. 9 (2019).
204. Costa, A. *et al.* Fibroblast Heterogeneity and Immunosuppressive Environment in Human Breast Cancer. *Cancer Cell* **33**, 463-479.e10 (2018).
205. Rudnick, J. A. *et al.* Functional heterogeneity of breast fibroblasts is defined by a prostaglandin secretory phenotype that promotes expansion of cancer-stem like cells. *PLoS ONE* (2011) doi:10.1371/journal.pone.0024605.
206. Goetz, J. G. *et al.* Biomechanical remodeling of the microenvironment by stromal caveolin-1 favors tumor invasion and metastasis. *Cell* (2011) doi:10.1016/j.cell.2011.05.040.
207. Tsuyada, A. *et al.* CCL2 mediates cross-talk between cancer cells and stromal fibroblasts that regulates breast cancer stem cells. *Cancer Research* (2012) doi:10.1158/0008-5472.CAN-11-3567.
208. Su, S. *et al.* CD10+GPR77+ Cancer-Associated Fibroblasts Promote Cancer Formation and Chemoresistance by Sustaining Cancer Stemness. *Cell* **172**, 841-856.e16 (2018).
209. Cazet, A. S. *et al.* Targeting stromal remodeling and cancer stem cell plasticity overcomes chemoresistance in triple negative breast cancer. *Nature Communications* (2018) doi:10.1038/s41467-018-05220-6.
210. Xu, H. *et al.* Tumor-derived mesenchymal-stem-cell-secreted IL-6 enhances resistance to cisplatin via the STAT3 pathway in breast cancer. *Oncology Letters* (2018) doi:10.3892/ol.2018.8463.
211. Galland, S. & Stamenkovic, I. Mesenchymal stromal cells in cancer: a review of their immunomodulatory functions and dual effects on tumor progression. *Journal of Pathology* (2020) doi:10.1002/path.5357.
212. Singh, J. K., Simões, B. M., Howell, S. J., Farnie, G. & Clarke, R. B. Recent advances reveal IL-8 signaling as a potential key to targeting breast cancer stem cells. *Breast Cancer Research* (2013) doi:10.1186/bcr3436.
213. Cuiffo, B. G. *et al.* MSC-regulated microRNAs converge on the transcription factor FOXP2 and promote breast cancer metastasis. *Cell Stem Cell* (2014) doi:10.1016/j.stem.2014.10.001.
214. Deshmukh, S. K. *et al.* Inflammation, immunosuppressive microenvironment and breast cancer: opportunities for cancer

- prevention and therapy. *Annals of Translational Medicine* (2019) doi:10.21037/atm.2019.09.68.
215. Peterko, A. C. *et al.* PD-L1 and HSP-70 molecules are part of immunosuppressive environment in the deep layer of the lymphocyte predominant breast cancer (LPBC). *European Journal of Cancer* (2020) doi:10.1016/S0959-8049(20)30576-1.
216. Annaratone, L. *et al.* The Multifaceted Nature of Tumor Microenvironment in Breast Carcinomas. *Pathobiology* (2020) doi:10.1159/000507055.
217. Ugel, S., De Sanctis, F., Mandruzzato, S. & Bronte, V. Tumor-induced myeloid deviation: When myeloid-derived suppressor cells meet tumor-Associated macrophages. *Journal of Clinical Investigation* (2015) doi:10.1172/JCI80006.
218. Cui, T. X. *et al.* Myeloid-derived suppressor cells enhance stemness of cancer cells by inducing microRNA101 and suppressing the corepressor CTBP2. *Immunity* (2013) doi:10.1016/j.immuni.2013.08.025.
219. Peng, D. *et al.* Myeloid-derived suppressor cells endow stem-like qualities to breast cancer cells through IL6/STAT3 and NO/NOTCH cross-talk signaling. *Cancer Research* (2016) doi:10.1158/0008-5472.CAN-15-2528.
220. Chen, J., Imanaka, N., Chen, J. & Griffin, J. D. Hypoxia potentiates Notch signaling in breast cancer leading to decreased E-cadherin expression and increased cell migration and invasion. *British Journal of Cancer* (2010) doi:10.1038/sj.bjc.6605486.
221. Lan, J. *et al.* Hypoxia-inducible factor 1-dependent expression of adenosine receptor 2B promotes breast cancer stem cell enrichment. *Proceedings of the National Academy of Sciences of the United States of America* (2018) doi:10.1073/pnas.1809695115.
222. Kim, H., Lin, Q. & Yun, Z. BRCA1 regulates the cancer stem cell fate of breast cancer cells in the context of hypoxia and histone deacetylase inhibitors. *Scientific Reports* (2019) doi:10.1038/s41598-019-46210-y.
223. Sun, X. *et al.* Hypoxia-mediated cancer stem cell resistance and targeted therapy. *Bio-medicine and Pharmacotherapy* **130**, 110623 (2020).
224. Najafi, M. *et al.* Hypoxia in solid tumors: a key promoter of cancer stem cell (CSC) resistance. *Journal of Cancer Research and Clinical Oncology* (2020) doi:10.1007/s00432-019-03080-1.
225. Yang, D. *et al.* Oxidized ATM promotes breast cancer stem cell enrichment through energy metabolism reprogram-mediated acetyl-CoA accumulation. *Cell Death and Disease* (2020) doi:10.1038/s41419-020-2714-7.
226. Kim, H., Lin, Q. & Yun, Z. The hypoxic tumor microenvironment in vivo selects tumor cells with increased survival against genotoxic stresses. *Cancer Letters* **431**, 142–149 (2018).
227. Tanei, T. *et al.* Association of breast cancer stem cells identified by aldehyde dehydrogenase 1 expression with resistance to sequential paclitaxel and epirubicin-based chemotherapy for breast cancers. *Clinical Cancer Research* (2009) doi:10.1158/1078-0432.CCR-08-1479.
228. Li, X. *et al.* Intrinsic resistance of tumorigenic breast cancer cells to chemotherapy.

- Journal of the National Cancer Institute* (2008) doi:10.1093/jnci/djn123.
229. Phi, L. T. H. *et al.* Cancer stem cells (CSCs) in drug resistance and their therapeutic implications in cancer treatment. *Stem Cells International* (2018) doi:10.1155/2018/5416923.
230. Jia, D. *et al.* Cardamonin reduces chemotherapy-enriched breast cancer stem-like cells in vitro and in vivo. *Oncotarget* (2016) doi:10.18632/ONCOTARGET.5819.
231. Lagadec, C., Vlashi, E., Della Donna, L., Dekmezian, C. & Pajonk, F. Radiation-induced reprogramming of breast cancer cells. *Stem Cells* (2012) doi:10.1002/stem.1058.
232. Zhang, S. *et al.* Inhibition of chemotherapy resistant breast cancer stem cells by a ROR1 specific antibody. *Proceedings of the National Academy of Sciences of the United States of America* (2019) doi:10.1073/pnas.1816262116.
233. Sun, Z., Wang, L., Dong, L. & Wang, X. Emerging role of exosome signalling in maintaining cancer stem cell dynamic equilibrium. *Journal of Cellular and Molecular Medicine* (2018) doi:10.1111/jcmm.13676.
234. Pai, A., Tanouchi, Y., Collins, C. H. & You, L. Engineering multicellular systems by cell-cell communication. *Current Opinion in Biotechnology* (2009) doi:10.1016/j.copbio.2009.08.006.
235. Mittelbrunn, M. & Sánchez-Madrid, F. Intercellular communication: Diverse structures for exchange of genetic information. *Nature Reviews Molecular Cell Biology* (2012) doi:10.1038/nrm3335.
236. Maas, S. L. N., Breakefield, X. O. & Weaver, A. M. Extracellular Vesicles: Unique Intercellular Delivery Vehicles. *Trends in Cell Biology* **27**, 172–188 (2017).
237. Desrochers, L. M., Antonyak, M. A. & Cerione, R. A. Extracellular Vesicles: Satellites of Information Transfer in Cancer and Stem Cell Biology. *Developmental Cell* (2016) doi:10.1016/j.devcel.2016.04.019.
238. Yáñez-Mó, M. *et al.* Biological properties of extracellular vesicles and their physiological functions. *Journal of Extracellular Vesicles* (2015) doi:10.3402/jev.v4.27066.
239. Van Niel, G., D'Angelo, G. & Raposo, G. Shedding light on the cell biology of extracellular vesicles. *Nature Reviews Molecular Cell Biology* (2018) doi:10.1038/nrm.2017.125.
240. Iraci, N., Leonardi, T., Gessler, F., Vega, B. & Pluchino, S. Focus on extracellular vesicles: Physiological role and signalling properties of extracellular membrane vesicles. *International Journal of Molecular Sciences* (2016) doi:10.3390/ijms17020171.
241. György, B. *et al.* Membrane vesicles, current state-of-the-art: Emerging role of extracellular vesicles. *Cellular and Molecular Life Sciences* (2011) doi:10.1007/s00018-011-0689-3.
242. Willms, E. *et al.* Cells release subpopulations of exosomes with distinct molecular and biological properties. *Scientific Reports* (2016) doi:10.1038/srep22519.
243. Yoon, Y. J., Kim, O. Y. & Ghossein, Y. S. Extracellular vesicles as emerging intercellular communicasomes. *BMB Reports* (2014) doi:10.5483/BMBRep.2014.47.10.164.

244. Zaborowski, M. P., Balaj, L., Breakefield, X. O. & Lai, C. P. Extracellular Vesicles: Composition, Biological Relevance, and Methods of Study. *BioScience* (2015) doi:10.1093/biosci/biv084.
245. Skotland, T., Sagini, K., Sandvig, K. & Llorente, A. An emerging focus on lipids in extracellular vesicles. *Advanced Drug Delivery Reviews* (2020) doi:10.1016/j.addr.2020.03.002.
246. Wen, S. W. *et al.* Breast Cancer-Derived Exosomes Reflect the Cell-of-Origin Phenotype. *Proteomics* **19**, (2019).
247. Abels, E. R. & Breakefield, X. O. Introduction to Extracellular Vesicles: Biogenesis, RNA Cargo Selection, Content, Release, and Uptake. *Cellular and Molecular Neurobiology* (2016) doi:10.1007/s10571-016-0366-z.
248. Mathieu, M., Martin-Jaular, L., Lavieu, G. & Théry, C. Specificities of secretion and uptake of exosomes and other extracellular vesicles for cell-to-cell communication. *Nature Cell Biology* **21**, 9–17 (2019).
249. Tkach, M. & Théry, C. Communication by Extracellular Vesicles: Where We Are and Where We Need to Go. *Cell* (2016) doi:10.1016/j.cell.2016.01.043.
250. O'Donoghue, E. J. & Krachler, A. M. Mechanisms of outer membrane vesicle entry into host cells. *Cellular Microbiology* (2016) doi:10.1111/cmi.12655.
251. Théry, C. *et al.* Minimal information for studies of extracellular vesicles 2018 (MISEV2018): a position statement of the International Society for Extracellular Vesicles and update of the MISEV2014 guidelines. *Journal of Extracellular Vesicles* (2018) doi:10.1080/20013078.2018.1535750.
252. Wang, H. X. & Gires, O. Tumor-derived extracellular vesicles in breast cancer: From bench to bedside. *Cancer Letters* **460**, 54–64 (2019).
253. Kalluri, R. & LeBleu, V. S. The biology, function, and biomedical applications of exosomes. *Science* **367**, (2020).
254. Hanson, P. I. & Cashikar, A. Multivesicular body morphogenesis. *Annual Review of Cell and Developmental Biology* (2012) doi:10.1146/annurev-cellbio-092910-154152.
255. Trajkovic, K. *et al.* Ceramide triggers budding of exosome vesicles into multivesicular endosomes. *Science* (2008) doi:10.1126/science.1153124.
256. Henne, W. M., Buchkovich, N. J. & Emr, S. D. The ESCRT Pathway. *Developmental Cell* (2011) doi:10.1016/j.devcel.2011.05.015.
257. Wollert, T. & Hurley, J. H. Molecular mechanism of multivesicular body biogenesis by ESCRT complexes. *Nature* (2010) doi:10.1038/nature08849.
258. Stuffers, S., Sem Wegner, C., Stenmark, H. & Brech, A. Multivesicular endosome biogenesis in the absence of ESCRTs. *Traffic* (2009) doi:10.1111/j.1600-0854.2009.00920.x.
259. Schmidt, O. & Teis, D. The ESCRT machinery. *Current Biology* (2012) doi:10.1016/j.cub.2012.01.028.
260. Babst, M. MVB vesicle formation: ESCRT-dependent, ESCRT-independent and everything in between. *Current Opinion in Cell Biology* (2011) doi:10.1016/j.ceb.2011.04.008.
261. Andreu, Z. & Yáñez-Mó, M. Tetraspanins in extracellular vesicle formation and function.

- Frontiers in Immunology* (2014)
doi:10.3389/fimmu.2014.00442.
262. Rana, S. & Zöller, M. Exosome target cell selection and the importance of exosomal tetraspanins: A hypothesis. *Biochemical Society Transactions* (2011)
doi:10.1042/BST0390559.
263. Mathieu, M., Martin-Jaular, L., Lavie, G. & Théry, C. Specificities of secretion and uptake of exosomes and other extracellular vesicles for cell-to-cell communication. *Nature Cell Biology* (2019)
doi:10.1038/s41556-018-0250-9.
264. Jeppesen, D. K. *et al.* Reassessment of Exosome Composition. *Cell* (2019)
doi:10.1016/j.cell.2019.02.029.
265. Pathan, M. *et al.* Vesiclepedia 2019: A compendium of RNA, proteins, lipids and metabolites in extracellular vesicles. *Nucleic Acids Research* (2019) doi:10.1093/nar/gky1029.
266. Keerthikumar, S. *et al.* ExoCarta: A Web-Based Compendium of Exosomal Cargo. *Journal of Molecular Biology* (2016)
doi:10.1016/j.jmb.2015.09.019.
267. Choi, D. S., Kim, D. K., Kim, Y. K. & Gho, Y. S. Proteomics, transcriptomics and lipidomics of exosomes and ectosomes. *Proteomics* (2013) doi:10.1002/pmic.201200329.
268. Bernard, V., Ling, J. & Maitra, A. Heterogeneity of tumor exosomes - role in precision medicine. in *Diagnostic and Therapeutic Applications of Exosomes in Cancer* (2018).
doi:10.1016/B978-0-12-812774-2.00004-3.
269. Green, T. M., Alpaugh, M. L., Barsky, S. H., Rappa, G. & Lorico, A. Breast cancer-derived extracellular vesicles: Characterization and contribution to the metastatic phenotype. *BioMed Research International* **2015**, (2015).
270. Cocucci, E., Racchetti, G. & Meldolesi, J. Shedding microvesicles: artefacts no more. *Trends in Cell Biology* (2009)
doi:10.1016/j.tcb.2008.11.003.
271. Muralidharan-Chari, V., Clancy, J. W., Sedgwick, A. & D'Souza-Schorey, C. Microvesicles: Mediators of extracellular communication during cancer progression. *Journal of Cell Science* (2010) doi:10.1242/jcs.064386.
272. Raposo, G. & Stoorvogel, W. Extracellular vesicles: Exosomes, microvesicles, and friends. *Journal of Cell Biology* **200**, 373–383 (2013).
273. Gould, S. J. Exosomes and Microvesicles. in *Encyclopedia of Biological Chemistry: Second Edition* (2013). doi:10.1016/B978-0-12-378630-2.00426-6.
274. Balaj, L. *et al.* Tumour microvesicles contain retrotransposon elements and amplified oncogene sequences. *Nature Communications* (2011) doi:10.1038/ncomms1180.
275. Shao, H. *et al.* Protein typing of circulating microvesicles allows real-time monitoring of glioblastoma therapy. *Nature Medicine* (2012) doi:10.1038/nm.2994.
276. Camussi, G., Deregibus, M. C., Bruno, S., Cantaluppi, V. & Biancone, L. Exosomes/microvesicles as a mechanism of cell-to-cell communication. *Kidney International* (2010)
doi:10.1038/ki.2010.278.
277. Atkin-Smith, G. K. *et al.* A novel mechanism of generating extracellular vesicles during apoptosis via a beads-on-a-string membrane structure. *Nature Communications* (2015) doi:10.1038/ncomms8439.

278. Becker, A. *et al.* Extracellular Vesicles in Cancer: Cell-to-Cell Mediators of Metastasis. *Cancer Cell* vol. 30 836–848 (2016).
279. Maia, J. *et al.* Exosome-Based Cell-Cell Communication in the Tumor Microenvironment. *6*, 1–19 (2018).
280. Wendler, F., Stamp, G. W. & Giamas, G. Tumor–Stromal Cell Communication: Small Vesicles Signal Big Changes. *Trends in Cancer* **2**, 326–329 (2016).
281. Xu, R. *et al.* Extracellular vesicles in cancer — implications for future improvements in cancer care. *Nature Reviews Clinical Oncology* (2018) doi:10.1038/s41571-018-0036-9.
282. Minciacchi, V. R., Freeman, M. R. & Di Vizio, D. Extracellular Vesicles in Cancer: Exosomes, Microvesicles and the Emerging Role of Large Oncosomes. *Seminars in Cell and Developmental Biology* (2015) doi:10.1016/j.semcd.2015.02.010.
283. Kosaka, N., Yoshioka, Y., Fujita, Y. & Ochiya, T. Versatile roles of extracellular vesicles in cancer. *Journal of Clinical Investigation* (2016) doi:10.1172/JCI81130.
284. Bebelman, M. P., Smit, M. J., Pegtel, D. M. & Baglio, S. R. Biogenesis and function of extracellular vesicles in cancer. *Pharmacology and Therapeutics* (2018) doi:10.1016/j.pharmthera.2018.02.013.
285. Théry, C. Cancer: Diagnosis by extracellular vesicles. *Nature* (2015) doi:10.1038/nature14626.
286. Al-Nedawi, K. *et al.* Intercellular transfer of the oncogenic receptor EGFRvIII by microvesicles derived from tumour cells. *Nature Cell Biology* (2008) doi:10.1038/ncb1725.
287. Zeng, A. L. *et al.* Tumour exosomes from cells harbouring PTPRZ1-MET fusion contribute to a malignant phenotype and temozolomide chemoresistance in glioblastoma. *Oncogene* (2017) doi:10.1038/onc.2017.134.
288. Cesi, G. *et al.* A new ALK isoform transported by extracellular vesicles confers drug resistance to melanoma cells. *Molecular Cancer* (2018) doi:10.1186/s12943-018-0886-x.
289. Kalra, H. *et al.* Extracellular vesicles containing oncogenic mutant β -catenin activate Wnt signalling pathway in the recipient cells. *Journal of Extracellular Vesicles* (2019) doi:10.1080/20013078.2019.1690217.
290. Goh, C. Y. *et al.* Exosomes in triple negative breast cancer: Garbage disposals or Trojan horses? *Cancer Letters* vol. 473 90–97 (2020).
291. Chen, W. xian *et al.* Exosomes from docetaxel-resistant breast cancer cells alter chemosensitivity by delivering microRNAs. *Tumor Biology* (2014) doi:10.1007/s13277-014-2242-0.
292. O'Brien, K. *et al.* Exosomes from triple-negative breast cancer cells can transfer phenotypic traits representing their cells of origin to secondary cells. *European Journal of Cancer* (2013) doi:10.1016/j.ejca.2013.01.017.
293. Ji, Q. *et al.* Primary tumors release ITGBL1-rich extracellular vesicles to promote distal metastatic tumor growth through fibroblast-niche formation. *Nature Communications* **11**, (2020).
294. Webber, J. P. *et al.* Differentiation of tumour-promoting stromal myofibroblasts by

- cancer exosomes. *Oncogene* (2015) doi:10.1038/onc.2013.560.
295. Chowdhury, R. *et al.* Cancer exosomes trigger mesenchymal stem cell differentiation into pro-angiogenic and pro-invasive myofibroblasts. *Oncotarget* (2015) doi:10.18632/oncotarget.2711.
296. Cho, J. A., Park, H., Lim, E. H. & Lee, K. W. Exosomes from breast cancer cells can convert adipose tissue-derived mesenchymal stem cells into myofibroblast-like cells. *International Journal of Oncology* (2012) doi:10.3892/ijo.2011.1193.
297. Li, K., Liu, T., Chen, J., Ni, H. & Li, W. Survivin in breast cancer-derived exosomes activates fibroblasts by up-regulating SOD1, whose feedback promotes cancer proliferation and metastasis. *Journal of Biological Chemistry* **295**, 13737–13752 (2020).
298. Gong, C. *et al.* miR-21 induces myofibroblast differentiation and promotes the malignant progression of breast phyllodes tumors. *Cancer Research* (2014) doi:10.1158/0008-5472.CAN-14-0125.
299. Baroni, S. *et al.* Exosome-mediated delivery of miR-9 induces cancer-Associated fibroblast-like properties in human breast fibroblasts. *Cell Death and Disease* (2016) doi:10.1038/cddis.2016.224.
300. Valcz, G. *et al.* Perspective: bidirectional exosomal transport between cancer stem cells and their fibroblast-rich microenvironment during metastasis formation. *npj Breast Cancer* vol. 4 (2018).
301. Orimo, A. *et al.* Stromal fibroblasts present in invasive human breast carcinomas promote tumor growth and angiogenesis through elevated SDF-1/CXCL12 secretion. *Cell* (2005) doi:10.1016/j.cell.2005.02.034.
302. Benyahia, Z. *et al.* Stromal fibroblasts present in breast carcinomas promote tumor growth and angiogenesis through adrenomedullin secretion. *Oncotarget* (2017) doi:10.18632/oncotarget.14999.
303. Suh, J., Kim, D.-H. & Surh, Y.-J. Abstract 4096: Fibroblast growth factor-2-derived from cancer-associated fibroblasts stimulates proliferation and migration of human breast cancer cells. in (2016). doi:10.1158/1538-7445.am2016-4096.
304. Attieh, Y. & Vignjevic, D. M. The hallmarks of CAFs in cancer invasion. *European Journal of Cell Biology* (2016) doi:10.1016/j.ejcb.2016.07.004.
305. Attieh, Y. *et al.* Cancer-associated fibroblasts lead tumor invasion through integrin- β 3-dependent fibronectin asse. *Journal of Cell Biology* (2017) doi:10.1083/jcb.201702033.
306. Gaggioli, C. *et al.* Fibroblast-led collective invasion of carcinoma cells with differing roles for RhoGTPases in leading and following cells. *Nature Cell Biology* (2007) doi:10.1038/ncb1658.
307. Calvo, F. *et al.* Mechanotransduction and YAP-dependent matrix remodelling is required for the generation and maintenance of cancer-associated fibroblasts. *Nature Cell Biology* (2013) doi:10.1038/ncb2756.
308. Glentis, A. *et al.* Cancer-associated fibroblasts induce metalloprotease-independent cancer cell invasion of the basement membrane. *Nature Communications* (2017) doi:10.1038/s41467-017-00985-8.

309. Yang, X., Li, Y., Zou, L. & Zhu, Z. Role of exosomes in crosstalk between cancer-associated fibroblasts and cancer cells. *Frontiers in Oncology* **9**, 1–6 (2019).
310. Ludwig, N. & Whiteside, T. L. Potential roles of tumor-derived exosomes in angiogenesis. *Expert Opinion on Therapeutic Targets* (2018) doi:10.1080/14728222.2018.1464141.
311. Ahmadi, M. & Rezaie, J. Tumor cells derived-exosomes as angiogenic agents: Possible therapeutic implications. *Journal of Translational Medicine* (2020) doi:10.1186/s12967-020-02426-5.
312. King, H. W., Michael, M. Z. & Gleadle, J. M. Hypoxic enhancement of exosome release by breast cancer cells. *BMC Cancer* (2012) doi:10.1186/1471-2407-12-421.
313. Kosaka, N. *et al.* Neutral sphingomyelinase 2 (nSMase2)-dependent exosomal transfer of angiogenic micrornas regulate cancer cell metastasis. *Journal of Biological Chemistry* (2013) doi:10.1074/jbc.M112.446831.
314. Ozawa, P. M. M. *et al.* Extracellular vesicles from triple-negative breast cancer cells promote proliferation and drug resistance in non-tumorigenic breast cells. *Breast Cancer Research and Treatment* (2018) doi:10.1007/s10549-018-4925-5.
315. Wang, B. *et al.* Cisplatin-resistant MDA-MB-231 Cell-derived Exosomes Increase the Resistance of Recipient Cells in an Exosomal miR-423-5p-dependent Manner. *Current Drug Metabolism* (2019) doi:10.2174/1389200220666190819151946.
316. Mao, L. *et al.* Exosomes decrease sensitivity of breast cancer cells to adriamycin by delivering microRNAs. *Tumor Biology* (2016) doi:10.1007/s13277-015-4402-2.
317. Sharma, A. Chemoresistance in cancer cells: Exosomes as potential regulators of therapeutic tumor heterogeneity. *Nanomedicine* (2017) doi:10.2217/nnm-2017-0184.
318. Lv, M. meng *et al.* Exosomes mediate drug resistance transfer in MCF-7 breast cancer cells and a probable mechanism is delivery of P-glycoprotein. *Tumor Biology* (2014) doi:10.1007/s13277-014-2377-z.
319. Boelens, M. C. *et al.* Exosome transfer from stromal to breast cancer cells regulates therapy resistance pathways. *Cell* (2014) doi:10.1016/j.cell.2014.09.051.
320. Adem, B., Vieira, P. F. & Melo, S. A. Decoding the Biology of Exosomes in Metastasis. *Trends in Cancer* **6**, 20–30 (2020).
321. Wang, S. E. Extracellular vesicles and metastasis. *Cold Spring Harbor Perspectives in Medicine* (2020) doi:10.1101/cshperspect.a037275.
322. Yamaguchi, H., Wyckoff, J. & Condeelis, J. Cell migration in tumors. *Current Opinion in Cell Biology* (2005) doi:10.1016/j.ceb.2005.08.002.
323. Bonnans, C., Chou, J. & Werb, Z. Remodeling the extracellular matrix in development and disease. *Nature Reviews Molecular Cell Biology* (2014) doi:10.1038/nrm3904.
324. Mu, W., Rana, S. & Zöller, M. Host matrix modulation by tumor exosomes promotes motility and invasiveness. *Neoplasia (United States)* (2013) doi:10.1593/neo.13786.
325. Nawaz, M. *et al.* Extracellular Vesicles and Matrix Remodeling Enzymes: The Emerging Roles in Extracellular Matrix Remodeling,

- Progression of Diseases and Tissue Repair. *Cells* (2018) doi:10.3390/cells7100167.
326. Galindo-Hernandez, O., Serna-Marquez, N., Castillo-Sanchez, R. & Salazar, E. P. Extracellular vesicles from MDA-MB-231 breast cancer cells stimulated with linoleic acid promote an EMT-like process in MCF10A cells. *Prostaglandins Leukotrienes and Essential Fatty Acids* (2014) doi:10.1016/j.plefa.2014.09.002.
327. Erdogan, B. *et al.* Cancer-associated fibroblasts promote directional cancer cell migration by aligning fibronectin. *Journal of Cell Biology* (2017) doi:10.1083/jcb.201704053.
328. Greening, D. W. *et al.* Emerging roles of exosomes during epithelial-mesenchymal transition and cancer progression. *Seminars in Cell and Developmental Biology* (2015) doi:10.1016/j.semcdb.2015.02.008.
329. Kim, H. *et al.* The Emerging Roles of Exosomes as EMT Regulators in Cancer. *Cells* (2020) doi:10.3390/cells9040861.
330. Zomer, A. *et al.* In vivo imaging reveals extracellular vesicle-mediated phenocopying of metastatic behavior. *Cell* (2015) doi:10.1016/j.cell.2015.04.042.
331. Aga, M. *et al.* Exosomal HIF1 α supports invasive potential of nasopharyngeal carcinoma-associated LMP1-positive exosomes. *Oncogene* (2014) doi:10.1038/onc.2014.66.
332. Franzen, C. A. *et al.* Urothelial cells undergo epithelial-to-mesenchymal transition after exposure to muscle invasive bladder cancer exosomes. *Oncogenesis* (2015) doi:10.1038/oncsis.2015.21.
333. Jeppesen, D. K. *et al.* Quantitative proteomics of fractionated membrane and lumen exosome proteins from isogenic metastatic and nonmetastatic bladder cancer cells reveal differential expression of EMT factors. *Proteomics* (2014) doi:10.1002/pmic.201300452.
334. Luga, V. *et al.* Exosomes mediate stromal mobilization of autocrine Wnt-PCP signaling in breast cancer cell migration. *Cell* (2012) doi:10.1016/j.cell.2012.11.024.
335. Galindo-Hernandez, O. *et al.* Extracellular vesicles from women with breast cancer promote an epithelial-mesenchymal transition-like process in mammary epithelial cells MCF10A. *Tumor Biology* (2015) doi:10.1007/s13277-015-3711-9.
336. Fidler, I. J. The pathogenesis of cancer metastasis: The “seed and soil” hypothesis revisited. *Nature Reviews Cancer* (2003) doi:10.1038/nrc1098.
337. Peget, S. The Distribution of Secondary Growths in Cancer of the Breast. *The Lancet* (1888).
338. Kaplan, R. N. *et al.* VEGFR1-positive haematopoietic bone marrow progenitors initiate the pre-metastatic niche. *Nature* (2005) doi:10.1038/nature04186.
339. Psaila, B. & Lyden, D. The metastatic niche: Adapting the foreign soil. *Nature Reviews Cancer* (2009) doi:10.1038/nrc2621.
340. Celià-Terrassa, T. & Kang, Y. Metastatic niche functions and therapeutic opportunities. *Nature Cell Biology* vol. 20 868–877 (2018).
341. Liu, Y. & Cao, X. Characteristics and Significance of the Pre-metastatic Niche. *Cancer Cell* (2016) doi:10.1016/j.ccell.2016.09.011.

342. Guo, Y. *et al.* Effects of exosomes on pre-metastatic niche formation in tumors. *Molecular Cancer* **18**, 1–11 (2019).
343. Lobb, R. J., Lima, L. G. & Möller, A. Exosomes: Key mediators of metastasis and pre-metastatic niche formation. *Seminars in Cell and Developmental Biology* (2017) doi:10.1016/j.semcdb.2017.01.004.
344. Kramer, R. H. & Nicolson, G. L. Interactions of tumor cells with vascular endothelial cell monolayers: A model for metastatic invasion. *Proceedings of the National Academy of Sciences of the United States of America* (1979) doi:10.1073/pnas.76.11.5704.
345. Mensah, S. A. *et al.* Metastatic cancer cell attachment to endothelium is promoted by endothelial glycocalyx sialic acid degradation. *AIChE Journal* (2019) doi:10.1002/aic.16634.
346. Mierke, C. T. Role of the Endothelium during Tumor Cell Metastasis: Is the Endothelium a Barrier or a Promoter for Cell Invasion and Metastasis? *Journal of Biophysics* (2008) doi:10.1155/2008/183516.
347. Mierke, C. T. Cancer cells regulate biomechanical properties of human microvascular endothelial cells. *Journal of Biological Chemistry* (2011) doi:10.1074/jbc.M111.256172.
348. Mierke, C. T. Cancer metastasis and biomechanics of the endothelium. in *Mechanobiology of the Endothelium* (2015). doi:10.1201/b18060.
349. García-Román, J. & Zentella-Dehesa, A. Vascular permeability changes involved in tumor metastasis. *Cancer Letters* (2013) doi:10.1016/j.canlet.2013.03.005.
350. Hoshino, A. *et al.* Tumour exosome integrins determine organotropic metastasis. *Nature* **527**, 329–335 (2015).
351. Peinado, H. *et al.* Melanoma exosomes educate bone marrow progenitor cells toward a pro-metastatic phenotype through MET. *Nature Medicine* (2012) doi:10.1038/nm.2753.
352. Di Modica, M. *et al.* Breast cancer-secreted miR-939 downregulates VE-cadherin and destroys the barrier function of endothelial monolayers. *Cancer Letters* (2017) doi:10.1016/j.canlet.2016.09.013.
353. Tominaga, N. *et al.* Brain metastatic cancer cells release microRNA-181c-containing extracellular vesicles capable of destructing blood-brain barrier. *Nature Communications* (2015) doi:10.1038/ncomms7716.
354. Zhou, W. *et al.* Cancer-Secreted miR-105 destroys vascular endothelial barriers to promote metastasis. *Cancer Cell* (2014) doi:10.1016/j.ccr.2014.03.007.
355. Bielenberg, D. R. & Zetter, B. R. The Contribution of Angiogenesis to the Process of Metastasis. *Cancer Journal (United States)* (2015) doi:10.1097/PPO.000000000000138.
356. Feng, W., Dean, D. C., Hornicek, F. J., Shi, H. & Duan, Z. Exosomes promote pre-metastatic niche formation in ovarian cancer. *Molecular Cancer* (2019) doi:10.1186/s12943-019-1049-4.
357. Tang, M. K. S. *et al.* Soluble E-cadherin promotes tumor angiogenesis and localizes to exosome surface. *Nature Communications* (2018) doi:10.1038/s41467-018-04695-7.

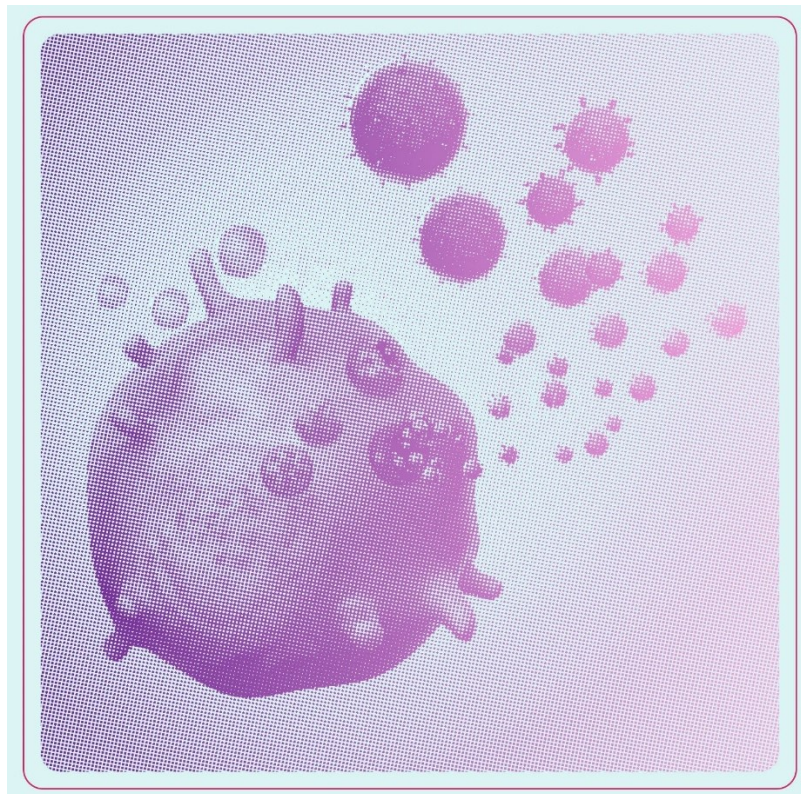
358. Gupta, G. P. *et al.* Mediators of vascular remodelling co-opted for sequential steps in lung metastasis. *Nature* (2007) doi:10.1038/nature05760.
359. Horie, K. *et al.* Exosomes expressing carbonic anhydrase 9 promote angiogenesis. *Biochemical and Biophysical Research Communications* (2017) doi:10.1016/j.bbrc.2017.08.107.
360. Pasquier, J. *et al.* Microparticles mediated cross-talk between tumoral and endothelial cells promote the constitution of a pro-metastatic vascular niche through Arf6 up regulation. *Cancer Microenvironment* (2014) doi:10.1007/s12307-013-0142-2.
361. Grange, C. *et al.* Microvesicles released from human renal cancer stem cells stimulate angiogenesis and formation of lung premetastatic niche. *Cancer Research* (2011) doi:10.1158/0008-5472.CAN-11-0241.
362. Zeng, Z. *et al.* Cancer-derived exosomal miR-25-3p promotes pre-metastatic niche formation by inducing vascular permeability and angiogenesis. *Nature Communications* (2018) doi:10.1038/s41467-018-07810-w.
363. Chow, A. *et al.* Macrophage immunomodulation by breast cancer-derived exosomes requires Toll-like receptor 2-mediated activation of NF- κ B. *Scientific Reports* (2014) doi:10.1038/srep05750.
364. Ludwig, S. *et al.* Suppression of lymphocyte functions by plasma exosomes correlates with disease activity in patients with head and neck cancer. *Clinical Cancer Research* (2017) doi:10.1158/1078-0432.CCR-16-2819.
365. Czernek, L. & Döchler, M. Functions of Cancer-Derived Extracellular Vesicles in Immunosuppression. *Archivum Immunologiae et Therapiae Experimentalis* (2017) doi:10.1007/s00005-016-0453-3.
366. Chen, G. *et al.* Exosomal PD-L1 contributes to immunosuppression and is associated with anti-PD-1 response. *Nature* (2018) doi:10.1038/s41586-018-0392-8.
367. Costa-Silva, B. *et al.* Pancreatic cancer exosomes initiate pre-metastatic niche formation in the liver. *Nature Cell Biology* (2015) doi:10.1038/ncb3169.
368. Peinado, H. *et al.* Pre-metastatic niches: Organ-specific homes for metastases. *Nature Reviews Cancer* (2017) doi:10.1038/nrc.2017.6.
369. Liu, Y. *et al.* Tumor Exosomal RNAs Promote Lung Pre-metastatic Niche Formation by Activating Alveolar Epithelial TLR3 to Recruit Neutrophils. *Cancer Cell* (2016) doi:10.1016/j.ccell.2016.06.021.
370. Novo, D. *et al.* Mutant p53s generate pro-invasive niches by influencing exosome podocalyxin levels. *Nature Communications* (2018) doi:10.1038/s41467-018-07339-y.
371. Yokoi, A. *et al.* Malignant extracellular vesicles carrying MMP1 mRNA facilitate peritoneal dissemination in ovarian cancer. *Nature Communications* (2017) doi:10.1038/ncomms14470.
372. Zhang, H. *et al.* CD44 splice isoform switching determines breast cancer stem cell state. *Genes and Development* **33**, 166–179 (2019).
373. La Shu, S. *et al.* Metabolic reprogramming of stromal fibroblasts by melanoma exosome microRNA favours a pre-metastatic

- microenvironment. *Scientific Reports* (2018) doi:10.1038/s41598-018-31323-7.
374. Yamamura, Y. *et al.* Akt-girdin signaling in cancer-associated fibroblasts contributes to tumor progression. *Cancer Research* (2015) doi:10.1158/0008-5472.CAN-14-1317.
375. Hoshino, A. *et al.* Tumour exosome integrins determine organotropic metastasis. *Nature* (2015) doi:10.1038/nature15756.
376. Fang, T. *et al.* Tumor-derived exosomal miR-1247-3p induces cancer-associated fibroblast activation to foster lung metastasis of liver cancer. *Nature Communications* **9**, (2018).
377. Morancho, A. *et al.* Cerebral ischaemia and matrix metalloproteinase-9 modulate the angiogenic function of early and late out-growth endothelial progenitor cells. *Journal of Cellular and Molecular Medicine* **17**, (2013).
378. Gener, P. *et al.* Pivotal role of AKT2 during dynamic phenotypic change of breast cancer stem cells. *Cancers* **11**, 1–18 (2019).
379. Gener, P. *et al.* Fluorescent CSC models evidence that targeted nanomedicines improve treatment sensitivity of breast and colon cancer stem cells. *Nanomedicine: Nanotechnology, Biology, and Medicine* (2015) doi:10.1016/j.nano.2015.07.009.
380. Labernadie, A. *et al.* A mechanically active heterotypic E-cadherin/N-cadherin adhesion enables fibroblasts to drive cancer cell invasion. *Nature Cell Biology* (2017) doi:10.1038/ncb3478.
381. Seras-Franzoso, J. *et al.* Extracellular vesicles from recombinant cell factories improve the activity and efficacy of enzymes defective in lysosomal storage disorders. *Journal of Extracellular Vesicles* **10**, (2021).
382. Yoshida, G. J. The heterogeneity of cancer stem-like cells at the invasive front. *Cancer Cell International* **17**, 1–5 (2017).
383. Public Health England. MDA-MB-231 Cell Line Profile. *European Collection of Authenticated Cell Cultures* (2020).
384. O’Conor, C. J., Chen, T., González, I., Cao, D. & Peng, Y. Cancer stem cells in triple-negative breast cancer: A potential target and prognostic marker. *Biomarkers in Medicine* **12**, 813–820 (2018).
385. DuPré, S. A., Redelman, D. & Hunter, K. W. The mouse mammary carcinoma 4T1: Characterization of the cellular landscape of primary tumours and metastatic tumour foci. *International Journal of Experimental Pathology* **88**, (2007).
386. Fumagalli, A. *et al.* Plasticity of Lgr5-Negative Cancer Cells Drives Metastasis in Colorectal Cancer. *Cell stem cell* **26**, 569-578.e7 (2020).
387. Wahl, G. M. & Spike, B. T. Cell state plasticity, stem cells, EMT, and the generation of intra-tumoral heterogeneity. *npj Breast Cancer* vol. 3 (2017).
388. Liu, X. *et al.* Nonlinear growth kinetics of breast cancer stem cells: Implications for cancer stem cell targeted therapy. *Scientific Reports* **3**, (2013).
389. Lander, A. D., Gokoffski, K. K., Wan, F. Y. M., Nie, Q. & Calof, A. L. Cell lineages and the logic of proliferative control. *PLoS Biology* **7**, (2009).
390. Deleyrolle, L. P. *et al.* Determination of somatic and cancer stem cell self-renewing

- symmetric division rate using sphere assays. *PLoS ONE* **6**, (2011).
391. Yamauchi, T. & Moroishi, T. The Yin and Yang of tumour-derived extracellular vesicles in tumour immunity. *Journal of Biochemistry* (2021) doi:10.1093/jb/mvaa132.
392. Wang, X. *et al.* The roles of extracellular vesicles in the development, microenvironment, anticancer drug resistance, and therapy of head and neck squamous cell carcinoma. *Journal of Experimental and Clinical Cancer Research* vol. 40 (2021).
393. Kolář, M. *et al.* Upregulation of IL-6, IL-8 and CXCL-1 production in dermal fibroblasts by normal/malignant epithelial cells in vitro: Immunohistochemical and transcriptomic analyses. *Biology of the Cell* **104**, 738–751 (2012).
394. van der Zee, M. *et al.* IL6/JAK1/STAT3 Signaling Blockade in Endometrial Cancer Affects the ALDHhi/CD126+ Stem-like Component and Reduces Tumor Burden. *Cancer research* **75**, 3608–22 (2015).
395. Chen, L. *et al.* The IL-8/CXCR1 axis is associated with cancer stem cell-like properties and correlates with clinical prognosis in human pancreatic cancer cases. *Scientific Reports* (2014) doi:10.1038/srep05911.
396. van der Zee, M. *et al.* IL6/JAK1/STAT3 Signaling Blockade in Endometrial Cancer Affects the ALDHhi/CD126+ Stem-like Component and Reduces Tumor Burden. *Cancer research* **75**, 3608–22 (2015).
397. Singh, J. K. *et al.* Targeting CXCR1/2 significantly reduces breast cancer stem cell activity and increases the efficacy of inhibiting HER2 via HER2-dependent and independent mechanisms. *Clinical Cancer Research* (2013) doi:10.1158/1078-0432.CCR-12-1063.
398. Costa, A. *et al.* Fibroblast Heterogeneity and Immunosuppressive Environment in Human Breast Cancer. *Cancer cell* **33**, 463-479.e10 (2018).
399. Pelon, F. *et al.* Cancer-associated fibroblast heterogeneity in axillary lymph nodes drives metastases in breast cancer through complementary mechanisms. *Nature Communications* **11**, (2020).
400. Öhlund, D. *et al.* Distinct populations of inflammatory fibroblasts and myofibroblasts in pancreatic cancer. *The Journal of experimental medicine* (2017) doi:10.1084/jem.20162024.
401. Song, W. Biomedicine & Pharmacotherapy Tumor-derived extracellular vesicles in angiogenesis. *Biomedicine & Pharmacotherapy* **102**, 1203–1208 (2018).
402. Fang, T. *et al.* Tumor-derived exosomal miR-1247-3p induces cancer-associated fibroblast activation to foster lung metastasis of liver cancer. *Nature Communications* (2018) doi:10.1038/s41467-017-02583-0.
403. Keklikoglou, I. *et al.* Chemotherapy elicits pro-metastatic extracellular vesicles in breast cancer models. *Nature Cell Biology* **21**, (2019).
404. Wang, L. *et al.* CD103-positive CSC exosome promotes EMT of clear cell renal cell carcinoma: Role of remote MiR-19b-3p. *Molecular Cancer* **18**, 1–15 (2019).

CHAPTER II

*Study of the interplay between Cancer Stem Cells
Extracellular Vesicles and the Tumor Immune
Microenvironment in Head and Neck Squamous Cell
Carcinoma*



LIST OF FIGURES

Figure 1. HNSCC incidence among men.....	150
Figure 2. The Tumor Immune Microenvironment (TIME) in HNSCC.....	156
Figure 3. Effect of tumor derived EVs in TIME modulation towards immunosuppression	158
Figure 4. <i>hPGK:CD63-eGFP</i> lentivector.	163
Figure 5. <i>ALDH1A1:CD63-eGFP</i> lentivector.....	163
Figure 6. <i>SRE:CD63-eGFP</i> lentivector.....	163
Figure 7. <i>ALDH1A1:SrtA</i> lentivector.....	163
Figure 8. <i>SS-mSca-LPETGG: mCMV-PGK:CD63-eGFP</i> lentivector.....	164
Figure 9. #50 Vector map.....	164
Figure 10. #51 Vector map.....	165
Figure 11. #54 Vector map.....	165
Figure 12. Schematic representation of inter-cellular labeling reaction.....	166
Figure 13. mEER CSC models generation.....	176
Figure 14. mEER CSC model validation	177
Figure 15. MOC2 CSC model validation.....	178
Figure 16. mEER <i>ALDH1A1:CD63-eGFP</i> and mEER <i>SRE:CD63-eGFP</i> models <i>in vivo</i> experiment illustrative design.....	179
Figure 17. Overlaid dot plot representation of analyzed cell populations present in tumors from mice bearing genetically modified mEER cells studied by FACs.....	180
Figure 18. <i>In vivo</i> released mEER EVs ^{CSC} target MHC-II- Mac (M2) and PD-1+ T cells in the TIME	182
Figure 19. mEER <i>ALDH1A1:SrtA</i> <i>in vivo</i> model experiment illustrative design.....	183
Figure 20. mEER <i>ALDH1A1:StrA</i> overlaid dot plot representation.....	183
Figure 21. <i>ALDH1:SrtA</i> CSC <i>in vivo</i> model increases tEVs ^{CSC} -cell labelling sensitivity and reveals a predominant specific interaction between tEVs ^{CSC} , MHC-II- Macrophages and PD-1 + T cells in the TME.....	185
Figure 22. Representative IF images of tumor sections carrying mEER <i>PGK:CD63-eGFP</i> cells.....	187
Figure 23. Representative IF images of tumors carrying mEER <i>ALDH1A1:CD63-eGFP</i> cells.....	188
Figure 24. CSC and TAMs show spatial close localization in the TME.....	189

LIST OF TABLES

Table 1. Biological role and functional analysis of the HNSCC CSC markers.....	152
Table 2. Taqman probes references (Thermo Fisher Scientific)	167
Table 3. Taqman probes references (Thermo Fisher Scientific)	168
Table 4. Panel describing the fluorochromes and markers combinations employed for flow cytometry analysis.....	170
Table 5. Surface markers employed for the identification of immune cell populations.	170

The introduction of cancer immunotherapy as an effective treatment option for HNSCC highlights the urgent need to deeper study the tumor-immune interplay. Given the unique roles of CSC in cancer progression, to better understand the forces involved in CSC EVs-immune cell interactions becomes imperative. Here, we aimed to study the endogenous interactions between CSC EVs and immune cell populations in the TME and identify which are the immune cells subsets that preferably bind CSC EVs under pathophysiological settings. For this aim, we developed an efficient experimental model to track endogenous secreted CSC EVs with the advantage peculiarity of the absence of EVs *in vitro* manipulation. To study those interactions, we challenged mice with engineered HSCC tumor cells expressing the EVs pan-marker CD63-eGFP under the control of ALDH1A1 and SRE CSC-specific promoters. Subsequent fluorescence signal in immune cells allowed us to identify immune cell populations which had interacted with CSC EVs. Moreover, in order to increase the sensitivity of the interactions detection, we also employed a recently developed and validated novel strategy to label EV-binding immune cells based on the transpeptidase activity of the bacterial enzyme Sortase A (SrtA). Under this approach, mice were challenged with HSCC tumor cell lines genetically engineered to encode SrtA under the CSC ALDH1A1 promoter. The catalytic nature of SrtA+ CSC EV-bound transmembrane protein reporter system increased the detection sensitivity of CSC EVs-immune cells interactions compared to the CD63-eGFP approach. Furthermore, analysis of mice carrying tumor cells expressing EVs reporters under either constitutive promoter (hPGK) or CSC specific reporter (ALDH1A1) allowed us to statistically test for selective behavior of CSC EVs as compared to bulk tumor EVs in both experimental strategies. Results from our studies reported significant differences between the immune cell subsets that are targeted by bulk total tumor EVs compared to CSC EVs fraction, identifying for the first time that M2 Macrophages represent the main immune cell target for CSC released EVs, suggesting an active communication crosstalk between those cell populations via EVs. Moreover, a close spatial localization of TAMs and CSC was appreciated in tumors, supporting previous studies indicating that TAMs constitute a relevant component of CSC niches. Indeed, a high interaction rate was also found between CSC EVs and PD-1+T cells. Given the profound impact that M2 TAMs have in immunosuppression and tumor progression and the acquired relevance of PD-1/PD-L1 immune checkpoints in HSCC immunotherapy, a deeper investigation of the specific immune modulator biological cargo of CSC EVs will be of crucial interest.

INTRODUCTION

1 HEAD AND NECK SQUAMOUS CELL CARCINOMA

Head and neck squamous cell carcinomas (HNSCCs) develop from the mucosal epithelium in the oral cavity, pharynx and larynx and are the most common malignancies that arise in the head and neck, accounting for approximately 90% of all oral and oropharyngeal cell carcinomas (OCCC). HNSCC is the sixth most common cancer worldwide with over 400,000 new cases and more than 150,000 deaths reported each year. Males are affected significantly more than females, with a ratio ranging from 2:1 to 4:1¹.

HNSCC development has been correlated with exposure to tobacco-derived carcinogens and excessive alcohol consumption and also to infection with oncogenic strains of human papillomavirus (HPV), primarily HPV-16. HNSCCs of the oral cavity and larynx are still primarily associated with tobacco, being referred as HPV-negative HNSCC². The chronic exposure of the upper aerodigestive tract to these carcinogenic factors can result in dysplastic or premalignant lesions in the oropharyngeal mucosa and ultimately result in HNSCC. The relative prevalence of these risk factors contributes to the variations in the observed distribution of HNSCC in different areas of the world (Figure 1)³.

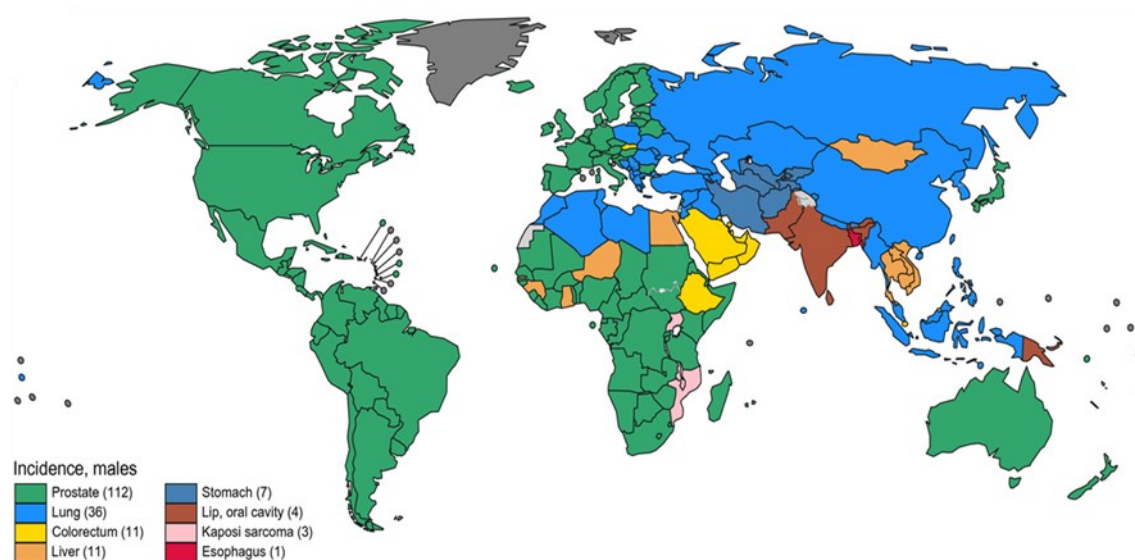


Figure 1. Cancer Incidence in 2020 in Each Country Among Men. Obtained from Globocan 2020⁴.

Advances in HNSCCC traditional treatments (surgery, radiotherapy, chemotherapy) and the introduction of new immunotherapy and combination therapies have only provided a marginal increase of survival as tumor recurrence still occurs in 50% of the patients. Many patients still present incurable advanced-stage disease and lymph node metastasis that ultimately cause their death. Consequently, the 5-year overall survival rate of HNSCC still has not improved³.

2 HNSCC CANCER STEM CELLS

HNSCC display high grades of tumor heterogeneity⁵ and multiple studies have identified CSC-like subpopulations in patients derived tumors as well as in xenografts⁶⁻⁸. Thus, HNSCC high local recurrence rates and therapy resistance are attributed to the presence of CSC within tumors. As in many cancer types, CSCs also play a central role in the pathogenesis, progression and therapy resistance of HNSCC⁶.

2.1 CURRENT APPROACHES TO ISOLATE HNSCC CSC

2.1.1 IDENTIFICATION OF CSC BASED ON BIOLOGICAL MARKERS

Common CSC biological markers are also reported to be expressed on HNSCC CSC. CD44, one of the universal CSC biomarkers, has been employed to identify CSC like cells within HNSCC heterogeneous tumors and cell lines⁹⁻¹¹. Specifically, CD44 variant isoform CD44v3 is highly expressed in CSCs and correlates with HNSCC progression¹². Similarly, ALDH1A1, which is a significant marker for breast CSCs, is also markedly upregulated in HNSCC CSCs⁸⁻¹¹. Furthermore, CD133^{6,7} and the expression of the SMAD Responsive Element (SRE)¹³ have also been used to identify CSC-like populations in HNSCC. Indeed, stem cell transcriptional factors OCT-4, SOX2 and NANOG are also correlated with the CSC phenotype in HNSCC¹⁴⁻¹⁶.

2.1.2 IDENTIFICATION OF CSC BASED ON CSC FUNCTIONAL PROPERTIES

The properties of CSCs, responsible for tumor progression and recurrence, can also be employed for their selective isolation. HNSCC CSCs are capable of growing under anchorage-independent conditions thus, CSCs can be successfully enriched from primary HNSCC samples or cell lines using the sphere forming assay¹⁷. Moreover, SP assay can also identify tumor cell subpopulations with higher in vitro clonogenicity, invasiveness and tumorigenicity compared to non-SP in HNSCC^{18,19}.

<i>CSC Marker</i>	<i>Biological Function</i>	<i>Detection Method</i>	<i>Functional Validation</i>
CD44 ²⁰	Cell surface protein: Receptor for hyaluronic acid, cell-cell and cell-matrix contacts, migration	Flow cytometry, Immunohisto- /Immunocytochemistry	Serial transplantation, xenograft assay
CD133 ²¹	Cell surface protein: possible role in membrane organization	Flow cytometry, Immunohisto- /Immunocytochemistry	Xenograft tumor formation assay
Aldehyde dehydrogenase (ALDH) ²²	Intracellular enzyme oxidizing aldehydes: detoxification, retinoic acid production	Aldefluor assay	Xenotransplantation, Sphere formation assay, (Matrigel/Transwell-invasion assay, Colony formation after irradiation)
Side population (SP) ²³	ABC transporter-mediated efflux of endogenous and exogenous substances	DNA dye (Hoechst 33342) exclusion assay	Xenograft assay, Serial sphere formation assay, (Matrigel invasion assay, Cell viability after chemotherapeutic drugs)

Table 1. Biological role and functional analysis of the HNSCC CSC markers. Based on ²⁴.

2.2 CSC DRIVE TUMORIGENESIS, METASTATIC SPREAD AND DRUG RESISTANCE IN HNSCC

HNSCC CSC subpopulations exhibit unique malignant intrinsic characteristics and play key roles in tumor initiation, growth and metastasis^{6,24}. Numerous studies have demonstrated the ability of CSC to drive tumorigenesis in HNSCC mice models²⁵. For example, HNSCC ALDH1+CD44+ cancer cells present higher tumorigenicity due to the upregulation of SOX2 by aberrantly activated PI3K/mTOR signaling¹⁶.

Moreover, HNSCC CSC have been demonstrated to be highly implied in metastasis disease⁶. Metastasis is a major therapeutic problem for HNSCC and the presence of lymph node metastasis is a strong predictor of therapeutic failure². Experimental data for HNSCC suggest a partial overlap of EMT and CSC signatures and HNSCC cells expressing CSC markers also show increased EMT and higher abilities for cell migration^{7,26,27}. Accordingly, the expression of a group of typical EMT transcription factors correlate with reduced OS of HNSCC patients^{27,28}.

Besides, HNSCC are also believed to drive therapy resistance and tumor relapse²⁴. *In vitro* assays show that when HNSCC CSCs are irradiated or exposed to chemotherapy they are 10 times more resistant to apoptosis than DCC²⁹. Accordingly, CSC markers expression levels can predict patient overall survival and local recurrence, and are correlated with radiotherapy response^{30,31}.

Interestingly, HNSCC CSCs also exhibit singular properties to avoid immune detection and eradication³². Recently, a number of studies have shown that CSCs contribute to the generation of an immunosuppressive, pro-tumorigenic immune milieu³²⁻³⁷.

3 THE TUMOR IMMUNE MICROENVIRONMENT IN HNSCC

The host immune system can recognize and eliminate neoplastic cells in a phenomenon known as immunosurveillance. According to this concept, the immune system constantly recognizes and destroys emerging malignant cells before they can develop into detectable tumors^{38,39}. To escape the control of the immune system, tumor cells develop multiple strategies that make them unrecognizable by immune cells or that efficiently suppress the immune response⁴⁰.

HNSCC is characterized to be one of the most immunosuppressive human tumors. In general, HNSCC tumors present a high infiltration of immune cells and it is well recognized that the

tumor immune microenvironment (TIME) plays an important regulatory role in tumor development, metastasis, and therapy failure⁴¹.

3.1 COMPONENTS OF HNSCC TUMORS IMMUNE MICROENVIRONMENT

The HNSCC TIME consists of tumour-infiltrating lymphocytes (TILs); including T cells, B cells and natural killer (NK) cells, and myeloid lineage cells (including macrophages, neutrophils, myeloid dendritic cells (MDC) and myeloid-derived suppressor cells (MDSCs))⁴². Both innate (eg, NK cells) and adaptive (eg, CD8+ T cells) immune cells play a crucial role in immune surveillance and controlling tumor growth. On the other hand, some subsets of immune cells (eg, MDSCs and macrophages) act as immunosuppressors and promote tumor growth⁴¹⁻⁴³. HNSCC tumours evade immune surveillance by a number of different mechanisms. In this regard, tumors often evade the host's immune surveillance by suppressing anti-tumor cells function or by activating and expanding immunosuppressive cell populations⁴⁴.

3.1.1 ANTITUMOR IMMUNE CELLS

3.1.1.1 T CELLS

T cells are lymphocytes that comprise a crucial component of the adaptive immune system and are categorized into CD4+ and CD8+ T cells. TILs display anti-tumor immunity. TILs directly kill tumor cells via producing perforin/ granzymes or by secreting cytokines with anti-tumor activity that are also involved in the recruitment of other immune cells with cytotoxic antitumor abilities⁴⁵. However, HNSCC tumors usually present dysfunctional TILs, which exhibit decreased cytokine production and proliferation ability and lack of cytotoxic functions⁴⁶. TILs have been studied to become exhausted and dysfunctional in HNSCCs by multiple mechanisms. Specifically, those exhausted TILs are characterized by the upregulation of several checkpoint markers, such as Programmed Cell Death 1 (PD-1)⁴¹. The PD-1/PD-L1 pathway is regarded as a key immunosuppressive mechanism operating in HNSCC⁴⁷. The PD-1 receptor is an immune checkpoint present in immune cells that limits their anti-tumor activity when it binds to its ligand PD-L1. PD-1 signaling in CD8+ T cells directly inhibits effector T-cell functions, including proliferation, survival, cytokine production and cytotoxicity^{46,47}. HNSCCs express increased levels of PD-L1 on their surface⁴⁸⁻⁵¹ causing a direct effect on the functions of T cells as well as promoting their apoptosis. Thus, PD-L1 presence on the surface of HNSCC tumor cells drives immunosuppression and contributes to tumor immune escape⁴⁷. Consequently, immunotherapies based on the use of antibodies targeting this immune checkpoint have arisen as innovative treatment alternatives for HNSCC tumors^{52,53}.

3.1.1.2 NATURAL KILLER CELLS

NK cells are one of the most representative anti-tumor immune cells as NK cells eliminate cancer cells through secretion of immunomodulatory cytokines. NK cells can recognize cancer cells that escape detection by cytotoxic T cells⁵⁴. In HNSCC, NK cells directly kill cancer cells by cytoplasmic granule release, FasL or TNF-related apoptosis-inducing ligand (TRAIL) and antibody-dependent cellular cytotoxicity (ADCC)⁴⁷⁴. However, HNSCC tumors usually inhibit NK cell activity⁵⁶. In HNSCC patients, NK cells have been shown to be functionally impaired and preferentially targeted for apoptosis^{57,58}.

3.1.1.3 MYELOID DENDRITIC CELLS

MDCs comprise the most important antigen-presenting cells (APCs) with a high capacity to initiate anti-tumor adaptive immune responses⁵⁹. Several factors in the TME have been implicated in the downregulation of MDCs function, which subsequently inhibits T cell activation⁴¹. HNSCC patients have reported lower numbers of MDCs compared to healthy controls, and low densities of MDCs have been associated with poor prognosis^{60,61}.

3.1.2 IMMUNOSUPPRESSIVE CELLS

3.1.2.1 TUMOR ASSOCIATED MACROPHAGES

Macrophages (Mac) are monocyte-derived innate immune cells that play an essential role in the maintenance of tissue homeostasis, the control of pathogens, and the overall surveillance of tissue changes. According to their mechanisms of activation and subsequent roles in the polarization of the immune response, macrophages are divided into two main phenotypes⁶². Inflammatory M1 macrophages (M1 Mac) are activated by interferon (IFN)- γ and are involved in antitumoral helper T (Th)1 immune responses. Anti-inflammatory M2 macrophages (M2 Mac), which are alternatively activated by IL-4, IL-10, IL-13, and/or prostaglandin E2, are associated with protumoral Th2 immune responses^{62,63}.

Tumor-associated macrophages (TAMs) are common in HNSCCs and they generally show the tumor-promoting M2 phenotype that is associated with the production of the immunosuppressive cytokines IL-10 and TGF- β and the inhibition of M1 cytotoxic activity^{64,65}. These TAMs have been also associated with angiogenesis, local tumor progression, therapy resistance and metastasis⁶⁶⁻⁶⁸. Consequently, high levels of TAMs presenting M2 phenotype in HNSCC tumors is correlated with lymph node metastasis and poor prognosis^{64,68-70}.

3.1.2.2 MYELOID-DERIVED SUPPRESSOR CELLS

MDSCs form a heterogeneous population of immature myeloid cells that are precursors of granulocytes, monocytes, and DC⁷¹. Pathological MDSC accumulation is associated with chronic inflammation and cancer progression, and MDSCs are known to exhibit significant immunosuppressive and protumor functions⁷¹⁻⁷³. Various factors in the immunosuppressive TME induce the accumulation of MDSCs, which in turn alter tumor-infiltrating T cells and produce soluble factors that support tumor growth and invasion⁷³. Therefore, high density of MDSCs in HNSCC patients has been associated with poor survival⁷⁴.

3.1.2.3 REGULATORY T CELLS

Regulatory T (Treg) cells are a subpopulation of CD4+ T cells that prevent autoimmunity and are involved in the HNSCC immunosuppressive TME as they regulate tumor progression by lowering anti-tumor immunity. Tregs secrete a variety of immunosuppressive cytokines, such as IL-10, IL-33 and TGF- β , further promoting HNSCC TIME suppression by causing effector T cells dysfunction and by inhibiting the action of DCs, NK cells, and B cells⁷⁵. In patients with HNSCCs, Tregs are increased in peripheral blood and the most representative subtype among T cells infiltrating the tumor, resulting in an immunosuppressed state^{76,77}.

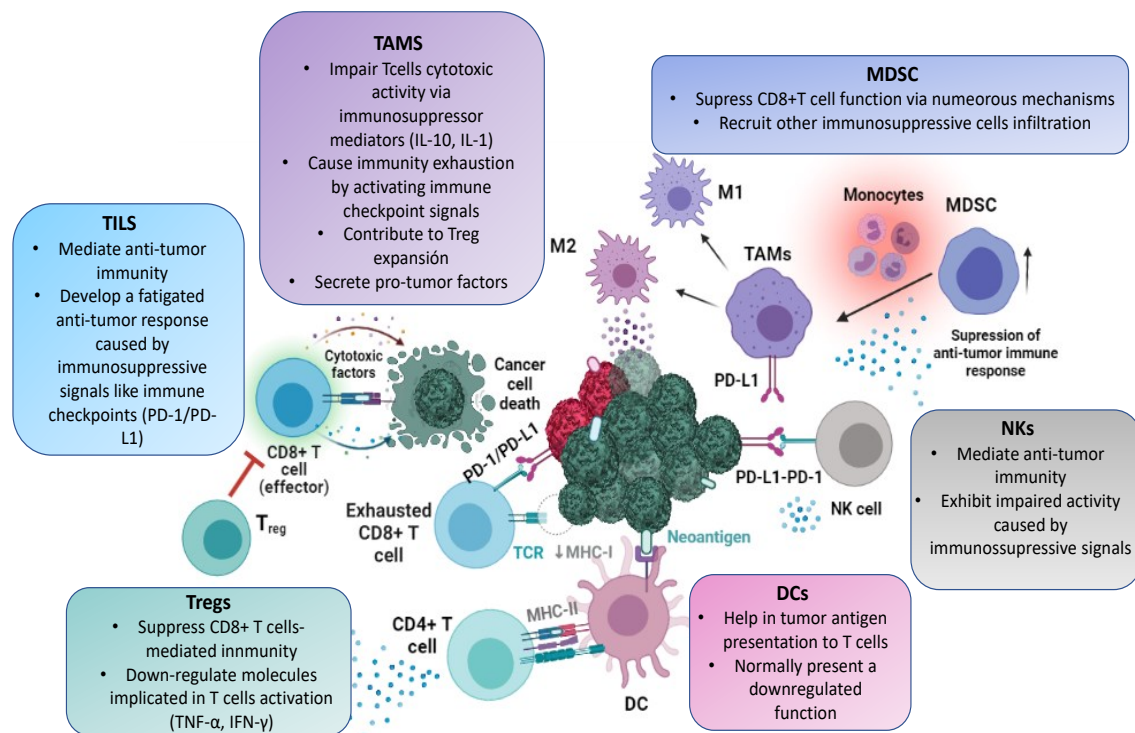


Figure 2. The Tumor Immune Microenvironment in HNSCC ^{41,42,53,78}.

4 THE INTERACTION BETWEEN CSC AND IMMUNE CELLS

CSCs importantly modulate HNSCC TIME. CSC can modulate T cells, TAMs and MDSC activity towards immunosuppressive pathways^{32–37}. Importantly, those immune cells can also acquire the abilities for sustaining CSC stemness and its survival^{37,79–81}.

For example, HNSCC CD44+ CSCs are less immunogenic and present higher expression of PD-L1 than CD44- DCC. Thus, CD44+ CSCs can mediate immunosuppression by inhibiting the activity of CD8+T cell through PD-1/PD-L1 pathway. Additionally, CD44+ cells suppress Th1 responses and enhance Tregs and MDSCs responses⁸².

Recently, the critical role of CSC on driving TAMs immunosuppressive phenotypes in HNSCC has been addressed. Indeed, TAMs are considered be essential for building the CSCs niche microenvironment, thereby forming a signaling loop to promote cancer progression⁸³.

Thus, CSCs play a critical role in establishing an immunosuppressive network. This complex communication network between tumor and immune cells operates through various secreted cytokines and chemokines^{37,84}. Notably, those interactions could be also be mediated by tumor released EVs⁸⁵.

5 EXTRACELLULAR VESICLES IN THE HNSCC TIME

Emerging evidence has shown that tumors can interfere with host immunity by secreting EVs and the role of EVs in cancer immunity has been extensively described^{86–90}. Tumor derived EVs can affect the proliferation, apoptosis, cytokine production and reprogramming of both innate and adaptive immune cells by transducing different signals thus modifying anti-cancer immune response impairing effector cells activity and creating an immunosuppressive microenvironment^{91–97}.

As many other cancer types, HNSCC tumor cells release EVs containing immunoregulatory factors that play important roles in regulating the TIME of HNSCC^{98–100}. The immunological activities of EVs are related to many aspects of immune regulation, including antigen presentation, immune activation, immune surveillance, and immune suppression⁹⁸. HNSCC secreted EVs mediate immune suppression through directly/indirectly inhibiting the functions of T cells and NK cells and promoting the activity of immune suppressor cells, including TAMs, MDSCs and Tregs¹⁰¹. For example, HNSCC-derived EVs carrying NK receptor G2 (NKG2D) ligands contribute to evading immunity by lowering the cytotoxicity of NK cells¹⁰². Furthermore, EVs derived from HNSCC not only inhibit the activation and proliferation of anti-tumor T cells but also prevent

their differentiation and promote their conversion to Tregs and MDSCs^{102,103}. Similarly, macrophages educated by HNSCC tumor EVs activated immunosuppressive signaling pathways and promoted the proliferation, migration, and invasion of tumor cells^{104,105}.

In summary, tumor EVs have an important immunomodulation role in the primary niche, which favors tumor growth and supports metastasis by suppressing the immune system response¹⁰⁶.

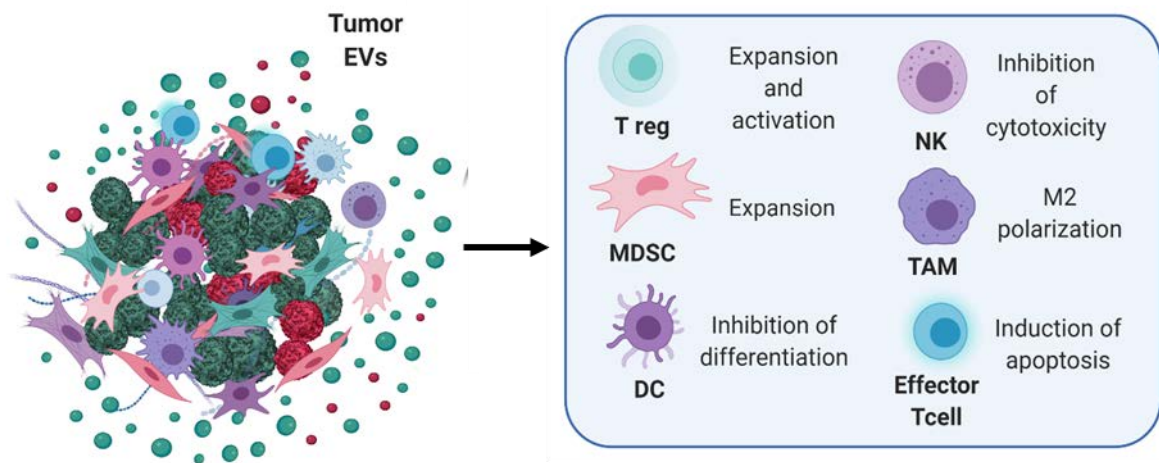


Figure 3. Effect of tumor derived EVs in TIME modulation towards immunosuppression^{86-88,90}.

HYPOTHESIS AND OBJECTIVES

HYPOTHESIS AND OBJECTIVES

HNSCC present high local recurrence rates and therapy resistance that can be attributed to the presence of CSC within tumors⁶. CSC exhibit unique malignant intrinsic characteristics and are believed to drive therapy resistance and tumor relapse, as they can survive and dynamically adapt to changing and unfavorable environmental conditions¹⁰⁷⁻¹¹². Indeed, CSCs also exhibit singular properties to avoid immune detection and eradication³². Recently, a number of studies have shown that CSCs contribute to the generation of an immunosuppressive, pro-tumorigenic immune milieu by regulating the activity of various immune cells in the tumor microenvironment (TME)^{113,114}.

Emerging evidence has shown that tumors can interfere with host immunity by secreting EVs⁸⁶⁻⁹⁰. Tumor derived EVs can affect the proliferation, apoptosis, cytokine production and reprogramming of both innate and adaptive immune cells by transducing different signals thus modifying anti-cancer immune response impairing the effector cells activity and creating an immunosuppressive microenvironment⁹¹⁻⁹⁷. However, whether CSC-derived EVs have a role in modulating tumor-infiltrating immune cells is still unclear.

The introduction of cancer immunotherapy as an effective treatment option for HNSCC highlights the urgent need to deeper study the tumor-immune interplay⁵². Given the unique roles of CSC in cancer progression, to better understand the forces involved in CSC EVs-immune cell interactions becomes imperative. Here, we aimed to study the endogenous interactions between CSC EVs and immune cell populations in the TME.

Hypothesis

CSC derived EVs play a key role in modulating tumors-infiltrating immune cells activity

To test this hypothesis the following objectives were established

Objectives:

1. Generate and validate HNSCC cell models tagging total tumor EVs and CSC derived EVs in order to identify specific EVs subsets from heterogeneous cell populations.
2. Generate HNSCC *in vivo* models allowing the physiological tracking of total tumor endogenous secreted EVs and CSC derived EVs.
3. Study the specific *in vivo* interactions between total tumor cells and CSC derived EVs with tumor infiltrating immune cells subsets.
4. Assess CSC and immune cell subsets localization in tumors.

MATERIALS AND METHODS

MATERIALS AND METHODS

1 LENTIVIRAL VECTORS

- Lentiviral (LV) transfer plasmids coding for CD63-eGFP and dLNGFR **dLNGFR:mCMV-PGK:CD63-eGFP (#7)** was cloned as previously described¹¹⁵ and used to tag tumor total secreted EVs, as EVs marker CD63-eGFP expression is subjected to the regulation of the *phosphoglycerate Kinase (PGK)* constitutive promoter.



Figure 4. *hPGK:CD63-eGFP* lentivector¹¹⁶.

- LV transfer plasmids coding for **ALDH1A1:CD63-eGFP (#50)** and **SRE:CD63-eGFP (#51)** expression cassettes were designed at home and cloned by Genewiz. Those LV were used to tag CSC derived EVs as CD63-eGFP expression is subjected to the regulation of CSC specific promoters *ALDH1A1* and *SRE*.



Figure 5. *ALDH1A1:CD63-eGFP* lentivector.



Figure 6. *SRE:CD63-eGFP* lentivector.

- LV transfer plasmid coding for **ALDH1A1:SrtA (#54)** was designed at home and cloned by Genewiz. This plasmid was used to engineer CSC EVs to display a membrane-bound form of Sortase A (SrtA), a bacterial transpeptidase that can catalyze the transfer of reporter molecules on the surface of EV-binding cells, under the expression of *ALDH1A1* CSC promoter



Figure 7. *ALDH1A1:SrtA* lentivector.

- LV transfer plasmid coding for ***SS-mSca-LPETGG: mCMV-PGK:CD63-eGFP (#46)*** was designed at home and cloned by Genewiz. This plasmid was used to tag tumor total secreted EVs (same strategy as #7) and also to detect EVs-SrtA interactions with recipient cell surfaces based on the mSCARLET (mSCA) red fluorescence coupled to the enzyme substrate reaction (*SS-mSca-LPETGG*).



Figure 8. *SS-mSca-LPETGG: mCMV-PGK:CD63-eGFP* lentivector.

Detailed maps of plasmids used to clone the lentivectors employed to tag CSC EVs are presented below:

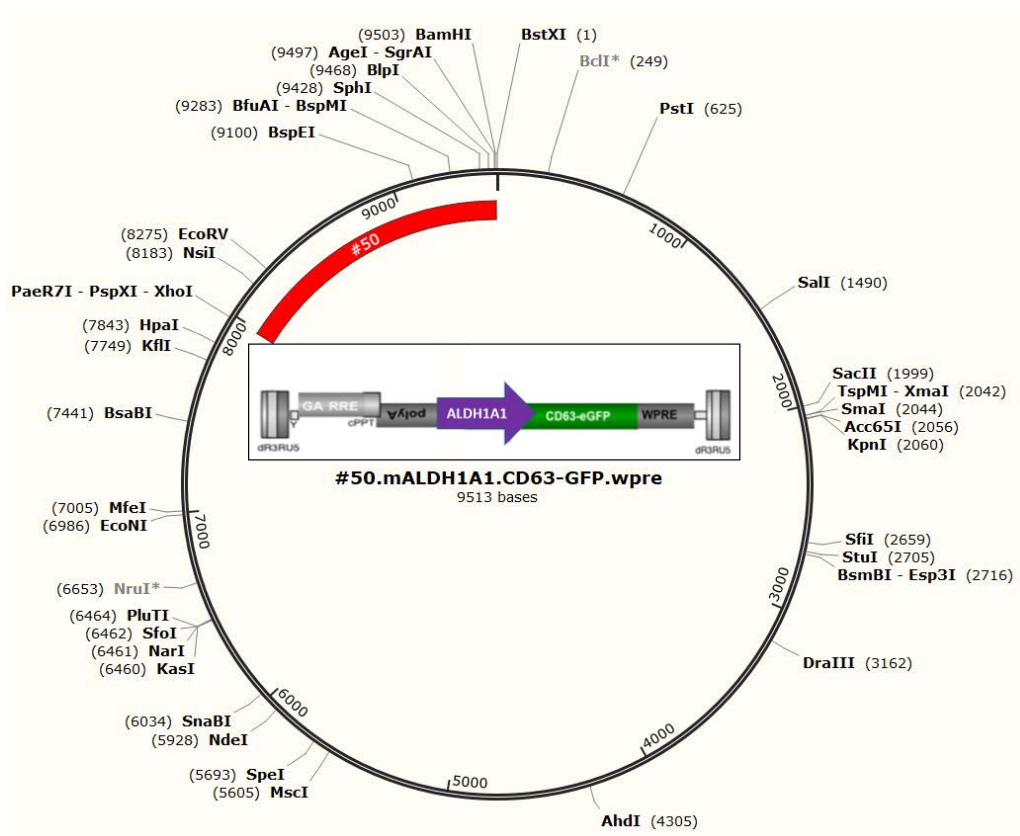


Figure 9. #50 Vector map.

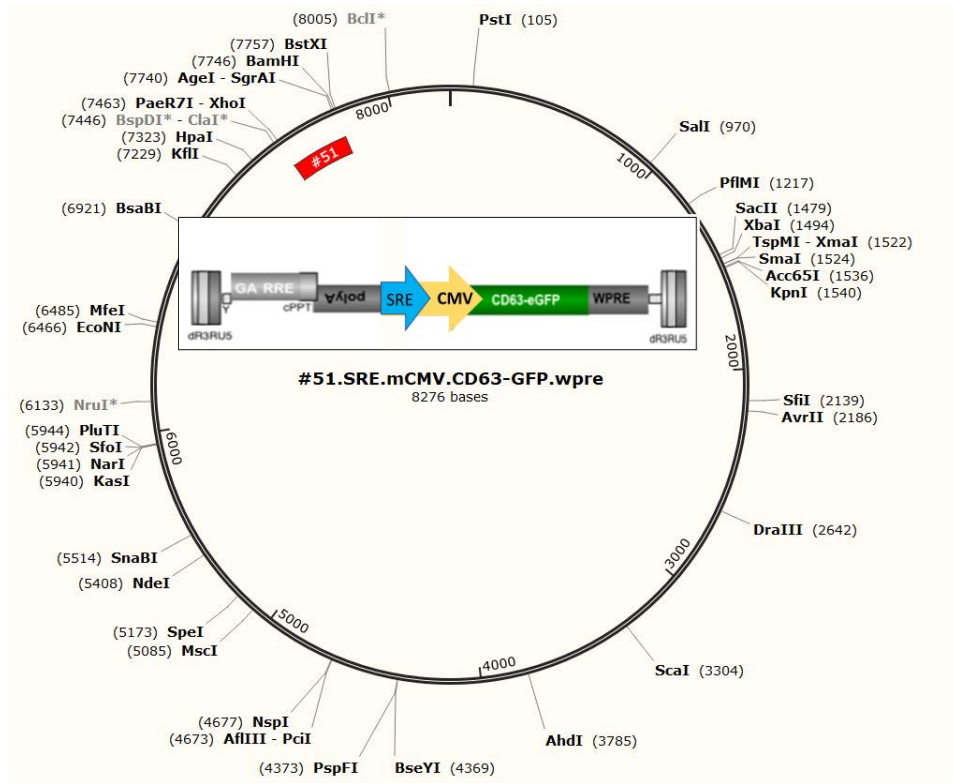


Figure 10. #51 Vector map.

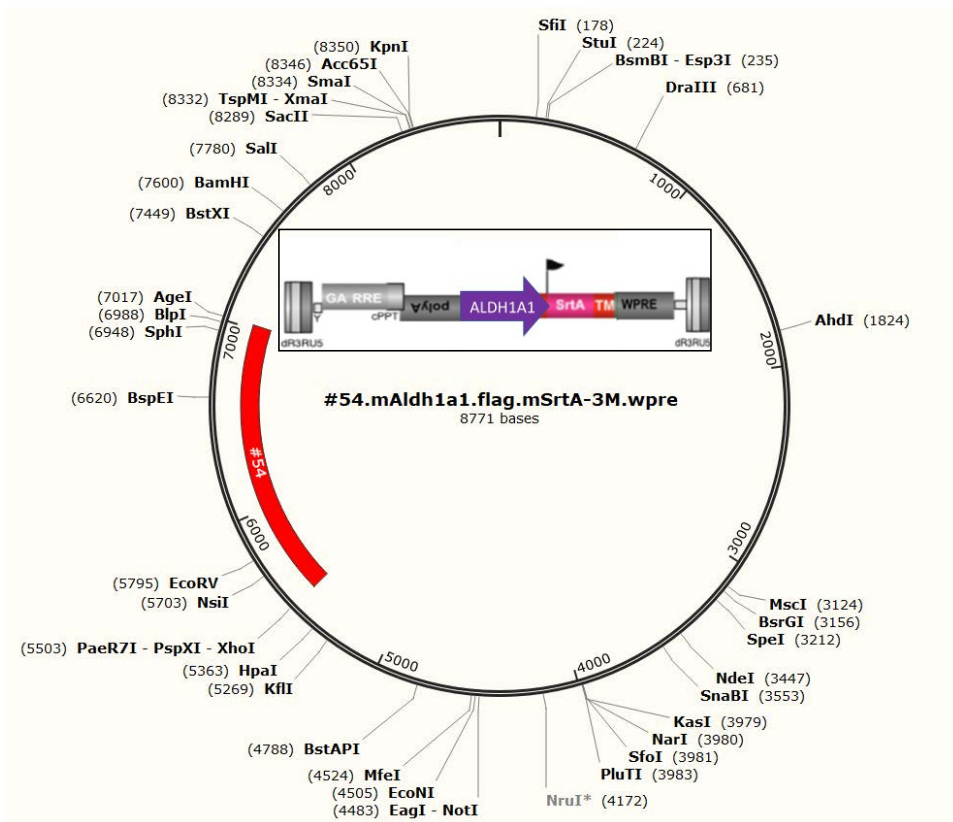


Figure 11. #54 Vector map.

The strategy employed to detect EVs-cells interactions based on SrtA experimental approach is fully detailed in¹¹⁶. Briefly, SrtA-expressing CSC EVs (#54) and SrtA-negative target cells (immune cells) are found mixed together in tumors. In the presence of the SrtA biotinylated substrate peptide (encoded by #46), when SrtA⁺ EVs come in close contact with other cells, SrtA covalently links the substrate peptide to membrane proteins of a nearby target cell. (i.e., cell-to-cell surface labeling). A brief scheme of the process is summarized in **Figure 12**.

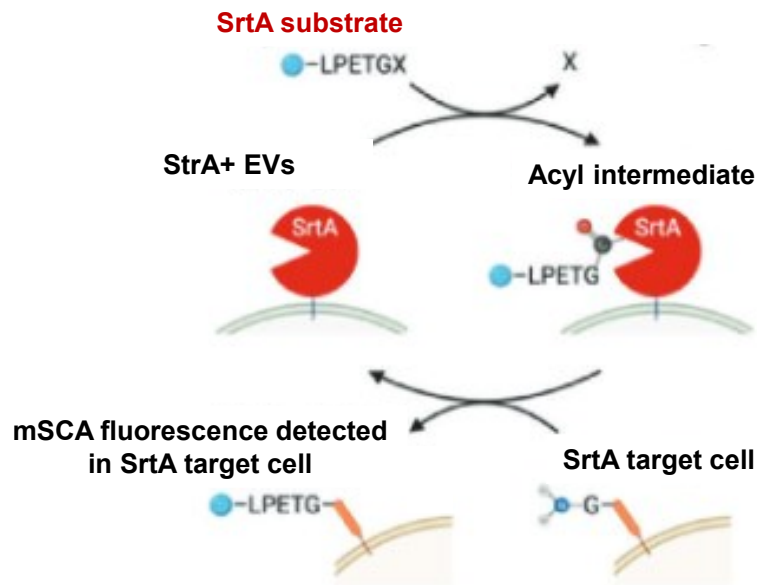


Figure 12. Schematic representation of inter-cellular labeling reaction.

2 CELL LINES AND CULTURE CONDITIONS

2.1 PARENTAL CELL LINES

Murine oral squamous cell carcinoma (OSCC) cell lines **MOC2** (a chemical carcinogenesis model) and **mEER** (a Ras-dependent, HPV16-E6/E7-dependent model) were obtained from Kerafast, Inc, and Dr. Varner (UCSD), respectively. Both cell lines were routinely maintained in IMDM/DMEM/F12 (50:25:25) supplemented with 5% fetal bovine serum (FBS), 2 mM L-Glutamine, 1x Pen/Strep solution, Hydrocortisone (25ug/uL), Cholera Toxin (0.25µg/µl), Transferrin (25µg/µl), Insulin (10µg/µl), Tri-Iodo-Thyronine (0.2µg/µl), E.G.F. (10 µg/mL).

All cell cultures were propagated at 37°C and 5% CO₂ in a humidified incubator.

2.2 ENGINEERED CELL LINES

In order to fluorescently label total tumor secreted EVs (tEVs^{total}) **mEER dLNGFR:mCMV-PGK:CD63-eGFP** (Green fluorescent protein) cell line was generated as previously reported by our group¹¹⁵.

Lentiviral (LV) transfer plasmids coding for *ALDH1A1:CD63-eGFP*, *SRE:CD63-eGFP*, *ALDH1A1:SrtA* and *SS-mSca-LPETGG: mCMV-PGK:CD63-eGFP* were propagated in *Escherichia coli* DH5 α . Maxiprep was performed with Endo-free Macherey-Nagel kit. Unconcentrated lentiviral vectors were generated as previously reported by our group¹¹⁵.

To generate engineered cells lines expressing CSC derived EVs (EVs^{CSC}) fluorescent reporters MOC2 and mEER cells were seeded at a concentration of 10⁵ cells per well in a 6-well plate and transduced with previously described LV vector supernatants (1:1 ratio with complete media) *ALDH1A1:CD63-eGFP*, *SRE:CD63-eGFP* and *ALDH1A1:SrtA* in the presence of 1 μ g/ml polybrene (Millipore).

For the simultaneous *in vivo* detection of both tEVs^{total} and tEVs^{CSC} mEER cell line was double transduced with *SS-mSca-LPETGG: mCMV-PGK:CD63-eGFP* and *ALDH1A1:SrtA* LV vectors in the presence of 1 μ g/ml polybrene (Millipore).

Generated engineered cell lines were cultured under the same conditions than the ones described for the parental cell lines and propagated at 37°C and 5% CO₂ in a humidified incubator.

3 IN VITRO ASSAYS

3.1 LV COPY NUMBER ASSAY

To assess the copy number of LV vectors present in engineered cells total DNA was extracted from genetically modified 200,000 mEER and MOC2 *ALDH1A1:CD63-eGFP* and *SRE:CD63-eGFP* cell lines using QIAamp DNA Micro Kit (Qiagen). LV sequence was detected using a custom TaqMan method (Thermo Fisher Scientific) on RRE sequence in a Vii7 PCR system. TaqMan probes for reference genes *ActinB*, *GusB* and *HPRT-1* were purchased from ThermoFisher (**Table 2**). One copy per genome standard was used, as previously described¹¹⁵.

Gene	TaqMan Probe Reference
GusB	Mm01197698_m1
Actin	Mm02619580_g1
HPRT-1	Mm03024075_m1

Table 2. Taqman probes references (Thermo Fisher Scientific)

3.2 FLUORESCENCE-ACTIVATED CELL SORTING (FACS)

FACS was used to sort CSC subpopulations from heterogeneous mEER and MOC cell lines. For cell sorting, a starting amount of 5×10^6 cells were used. mEER and MOC2 *ALDH1A1:CD63-eGFP* and *SRE:CD63-eGFP* cells were detached and resuspended in previously described supplemented IMDM/DMEM/F12 medium. 7AAD (1 $\mu\text{g}/\text{mL}$, Life Technologies) was used for vital staining (Biolegend). Cells were sorted according to GFP expression in a FACS Aria cell sorter (BD Biosciences, CA, USA). GFP+ and GFP- sorted cells were collected in complete medium and used for subsequent experiments.

3.3 STEM GENE PROFILE VALIDATION

Total RNA was extracted from 300,000 mEER and MOC2 (flow-sorted as *ALDH1A1:CD63-eGFP+/-* and *SRE:CD63-eGFP+/-* cells) using the RNeasy Mini Kit (Qiagen) and the RNA obtained was reverse transcribed using a High Capacity cDNA Reverse Transcription Kit (Thermo Fisher Scientific) according to the manufacturer's instructions. The cDNA reverse transcription product was amplified with specific probes by qPCR using TaqMan method (Thermo Fisher Scientific). Specific probes used for the reaction are specified in **Table 1**. The reaction was performed in triplicate on a Vii7 Real time PCR system (Applied Biosystems). Relative normalized quantities (NRQ) of mRNA expression were calculated using the comparative Ct method ($2^{-\Delta\Delta\text{Ct}}$) with two reference genes (GAPDH and Actin) used as endogenous controls.

Gene	TaqMan Probe Reference
ALDH1A1	Mm00657317_m1
Oct-4	Mm03053917_g1
Sox-2	Mm03053810_s1
Nanog	Mm02019550_s1
CD133	Mm00477121_m1
Actin	Mm02619580_g1
GAPDH	Mm99999915_g1

Table 3 Taqman probes references (Thermo Fisher Scientific)

3.4 OROSPHERE FORMATION ASSAY

Either 5000 mEER or MOC *ALDH1A1:CD63-eGFP+* and *ALDH1A1:CD63-eGFP-* cells/well were seeded in 2ml in 6-well ultra-low attachment plates (Corning) in StemXVivo Serum-Free Tumorsphere Media (R&D Systems). Cells were cultured for 10 to 14 days, and orosphere formation was assessed in each well using fluorescence microscopy.

4 ANIMAL EXPERIMENTATION

Six to eight week old C57BL/6J mice were purchased from Charles River Laboratories and housed under conventional conditions and provided with food and water ad libitum. Animal care was handled in accordance with the Guide for the Care and Use of Laboratory Animals of the Oregon Health & Science University (OHSU) and covered by OHSU Institutional Animal Care and Use Committee (IACUC).

For tumor challenge, parental mEER cells (control) and genetically modified mEER *dLNGFR:mCMV-PGK:CD63-eGFP*, mEER *ALDH1A1:CD63-eGFP*, mEER *SRE:CD63-eGFP*, mEER *SS-mSca-LPETGG:mCMV-PGK:CD63-eGFP*, mEER *ALDH1A1:SrtA* and mEER *SS-mSca-LPETGG:mCMV-PGK:CD63-eGFP plus ALDH1A1:SrtA* cells were intradermally injected (1×10^6 in 50 μ l of PBS) in the flank of six to eight week old C57BL/6J mice. After 12 days mice were euthanized and tumors collected, divided in two sections and processed either for flow cytometry or embedded in OCT compound for IF imaging analysis.

5 FLOW CYTOMETRY

Tumors were mechanically dissociated into single cell suspensions as previously described¹¹⁵. Cell suspensions were labeled with conjugated antibodies (Biolegend, BD or eBiosciences) and 7AAD (Sigma) also as described in¹¹⁶.

Fluorochromes employed were the following: eGFP, Bv421, Bv510, Bv605, Bv785, PE, PD, PerCP, PC7, APC, A700, AC7. The panel used for flow analysis is detailed in **Table 4**.

	Bv421	Bv510	Bv605	Bv785	FITC	PE	PD	PerCP	PC7	APC	A700	AC7
Filters	450/50	505LP 515/20	595LP 605/30	750LP 780/60	505LP 525/50	582/15	600LP 610/20	635LP 670/14	750LP 780/40	670/30	685LP 730/45	750LP 780/60
Laser	405	405	405	405	488	561	561	488	561	640	640	640
Voltage	400	450	525	517	400	450	550	602	550	490		447
Marker	31	Live	11c	11b	GFP	PD1	SCA	II	45	F4/80	3	B220

Table 4. Panel describing the fluorochromes and markers combinations employed for flow cytometry analysis.

The strategy employed to identify immune cells of interest is detailed in **Table 5**.

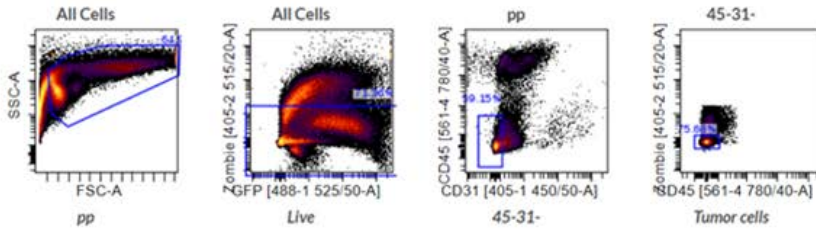
Cell population	Surface markers
Tumor cells	7AAD– CD45– CD31– GFP+
Endothelial cells	7AAD– CD45– CD31+
B cells	7AAD– CD45+ B220+
Macrophages MHC-II+	7AAD– CD45+ CD11b+ F4/80+ II+
Macrophages MHC-II-	7AAD– CD45+ CD11b+ F4/80+ II-
Inflammatory monocytes	7AAD– CD45+ CD11b+ CD11c+
Resident monocytes	7AAD– CD45+ CD11b+ CD11c-
Neutrophils	7AAD– CD45+ F4/80- CD11c- SSChii
Dendritic cells	7AAD– CD45+ CD11c+ F4/80– II+
PD-1 + T cells	7AAD– CD45+ F4/80- B220- CD3+ PD-1+
PD-1 - T cells	7AAD– CD45+ F4/80- B220- CD3+ PD-1-

Table 5. Surface markers employed for the identification of different immune cell populations.

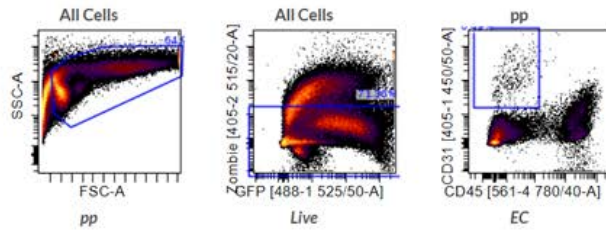
5.1.1 GATING STRATEGY

The complete gating strategy employed to identify each cell population in experimental tumors cell suspensions is detailed below.

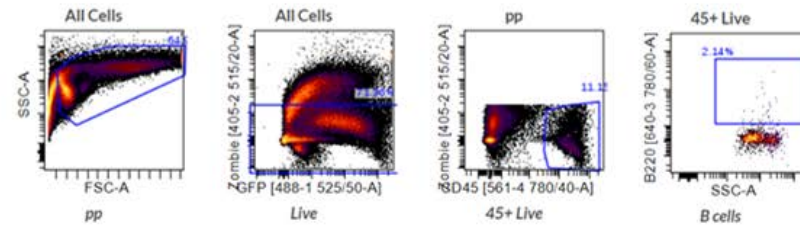
Tumor cells



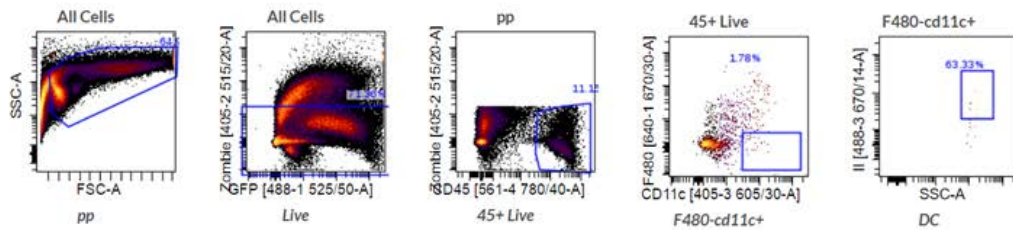
EC



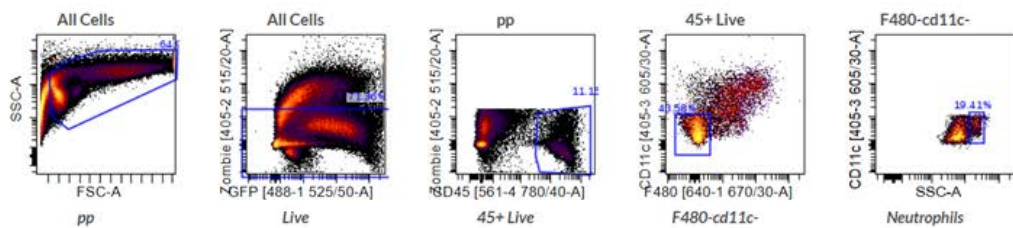
B cells



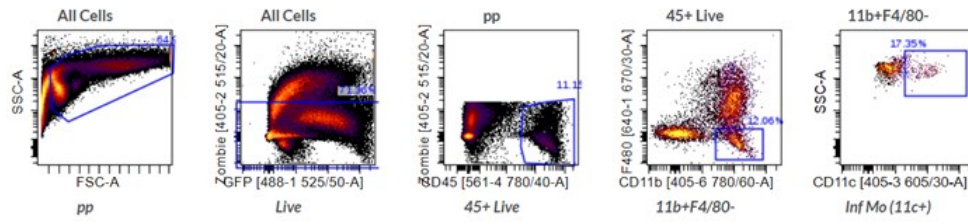
DC



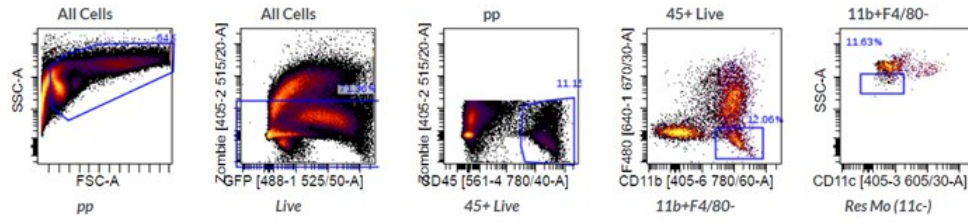
Neutrophils



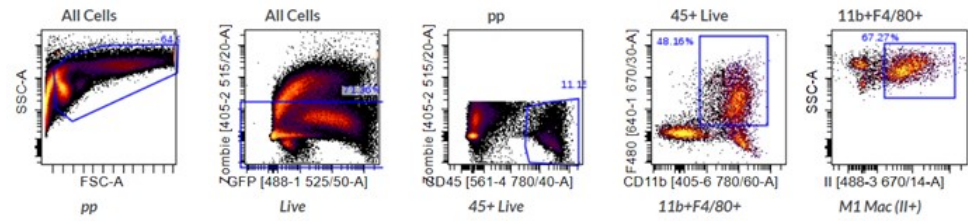
Inf Mo (11c+)



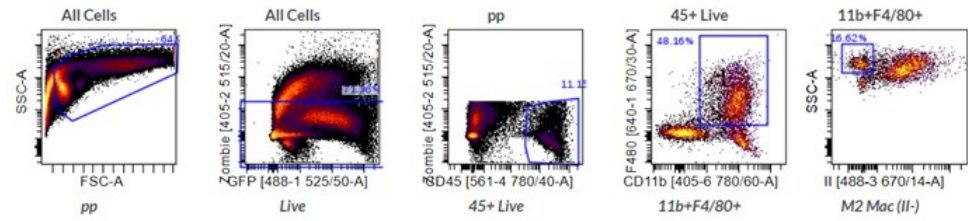
Res Mo (11c-)



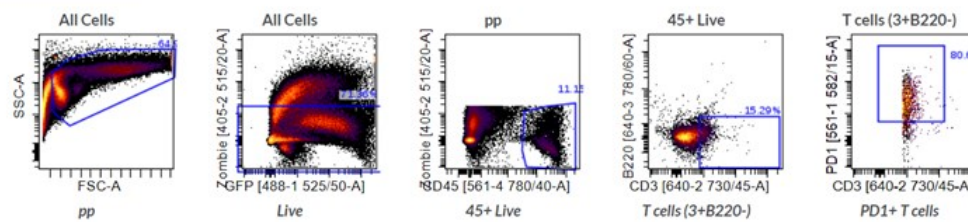
M1 Mac (II+)



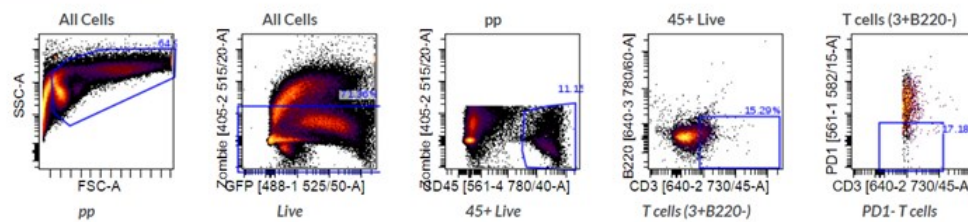
M2 Mac (II-)



PD1+ T cells



PD1- T cells



6 TUMORS IF IMAGING

5-10 μm thick OCT microsections from experimental tumors were mounted on glass slides for immunofluorescent labeling. Briefly, after 15' fixation in PFA 4%, samples were washed in PBS-Tween 0.3% and primary antibodies, anti-rabbit eGFP (1:200, Abcam) GFP anti-CD45 Biotin (1:200, Biolegend) and anti-F4/80 Alexafluor-647 (1:200, Biolegend) were supplemented in PBS/BSA 3 % (w/v) and incubated ON at 4°C. Samples were further washed 3 times in PBS-Tween 0.3% before the addition of secondary antibody. Goat Anti-rabbit Alexa Fluor488 1:1000 and Streptavidin 1:500 were added and incubated 1h at RT. Slides were then washed and mounted with mounting media ProLong for visualization. Tumors were imaged using a Spinning Disk Confocal microscope (Yokogawa CSU-X1 on Zeiss Axio Observer).

7 CARTOONS

All the cartoons employed in the schemes and figures presented in this thesis were manually created with Biorender.com online application.

8 STATISTICAL ANALYSIS

Bar graphs display mean value \pm SEM. 2-way ANOVA Sidak's test or non-parametric Tukey's test were employed for multiple mean comparisons. The significance threshold was established at $p < 0.05$, and significance levels were schematically assigned *($0.01 \leq p < 0.05$), **($0.001 \leq p < 0.01$), ***($0.0001 \leq p$), ****($0.00001 \leq p$). All the analyses and graphs were performed using GraphPad Prism 6 software (GraphPad, San Diego).

RESULTS

RESULTS

1 GENETIC LABELING OF CSC DERIVED EVs

Tumor secreted EVs (tEVs) represent prominent regulators of the immune response in cancer^{106,117}. CSC secreted EVs (tEVs^{CSC}) are a subset of tEVs whose immune modulatory activity is still unknown. In order to start investigating whether tEVs^{CSC} have a role in shaping immune cell activity in the TME, we genetically modified the EV producing cell lines to label tEVs^{CSC} with fluorescent proteins. This approach allowed us to avoid any bias in EV composition due to *in vitro* isolation. In particular, we genetically engineered murine oral squamous cell carcinoma (OSCC) cell lines to express the vesicular membrane-associated protein CD63, fused with enhanced green fluorescence protein (CD63-eGFP)¹¹⁵ under the control of a CSC-specific promoter. We tested two different CSC-specific promoters, *ALDH1A1* and *SRE*^{13,118–121}. As reference controls, we labeled the whole population of tEVs^{total} (including tEVs^{CSC}) by expressing the CD63-eGFP fusion protein under a constitutive promoter (*hPGK*). We worked on two different OSCC cell lines, a Ras-dependent, HPV16-E6/E7-dependent model (mEER) and a chemical carcinogenesis model (MOC2).

1.1 MEER EVs^{CSC-GFP+} IN VITRO MODEL VALIDATION

In order to assess if our experimental approach efficiently labeled CSC subpopulations, we performed *in vitro* imaging of engineered mEER cells. Note that CD63-GFP reporter would label cells membrane on two distinct setups: constitutively and under the regulation of CSC specific promoters. As expected, the constitutive reporter (PGK:CD63-eGFP) showed green fluorescence in virtually all mEER tumor cells (**Figure 13A**). On the other hand, much less green fluorescent cells were observed in both mEER cells carrying the vectors *ALDH1A1:CD63-eGFP* (**Figure 13B**) and *SRE:CD63-eGFP* (**Figure 13C**). In order to confirm that the observed differential expression of the tEVs reporter CD63-eGFP was due to the restricted expression of the *ALDH1A1* and *SRE* promoters among CSCs (and not because of low transduction efficiency), a LV copy number assay was performed. These analyses indicated that mEER *SRE:CD63-eGFP* cells carried on average 30 LV copies per cell (CpC), and that 5 CpC were detected in mEER *ALDH1A1:CD63-eGFP* cells, indicating full transduction of the tumor cell population (**Figure 13D**).

Flow cytometry analysis revealed that although eGFP fluorescence was detected in a high percentage of modified mEER *ALDH1A1:CD63-eGFP* and *SRE:CD63-eGFP* cells because of basal expression of the promoters, only less to the 10% of the tumor cell population presented high levels of eGFP fluorescence. This data indicated that brightest eGFP⁺ cells presented high levels of expression of the stemness promoters and may constitute the CSC population (**Figure 15E**).

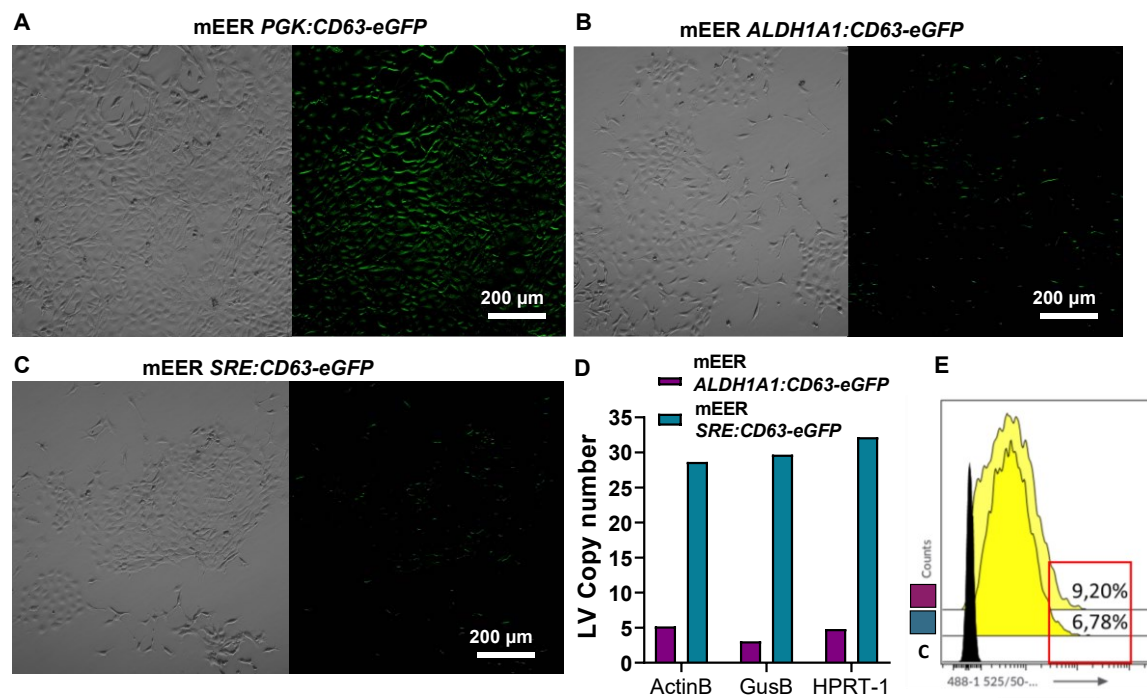


Figure 13. mEER CSC models generation. (A) Representative confocal microscopy images of cultured mEER cells stably transduced with *PGK:CD63-eGFP* reporter. (B, C) Representative confocal microscopy images of mEER *ALDH1A1:CD63-eGFP* cells and *SRE:CD63-eGFP* cells in culture. (D) LV copy number present in genetically modified *ALDH1A1:CD63-eGFP* and *SRE:CD63-eGFP* mEER cells assessed by PCR. (E) eGFP fluorescence presented by mEER modified cells analyzed by flow cytometry analysis. % of brightest eGFP fluorescent cells that represented the CSC subpopulation are indicated.

Accordingly, engineered cells were then flow sorted based on the levels of eGFP fluorescence and the stemness nature of the eGFP⁺ brightest cells was evaluated. RT-qPCR assay revealed that both mEER *ALDH1A1:CD63-GFP⁺* and mEER *SRE:CD63-eGFP⁺* cells showed significantly higher expression levels of the stemness marker *Nanog* when compared to *GFP⁻* cells (**Figure 14A**). Additionally, flow sorted mEER *ALDH1A1:CD63-GFP⁺* cells efficiently formed orospheres when cultured in serum-free LA conditions (**Figure 14B**) while *GFP⁻* cells were not able to form orospheres but showed small cellular aggregations (data not shown). Furthermore, gene expression analysis revealed that mEER *ALDH1A1:CD63-eGFP⁺* orospheres expressed significant

higher levels of the stemness markers *ALDH1A1*, *Nanog*, *Oct-4*, *CD-133* and *Sox-2* than unsorted mEER *ALDH1A1:CD63-eGFP* cells cultured in attachment conditions (**Figure 14C**).

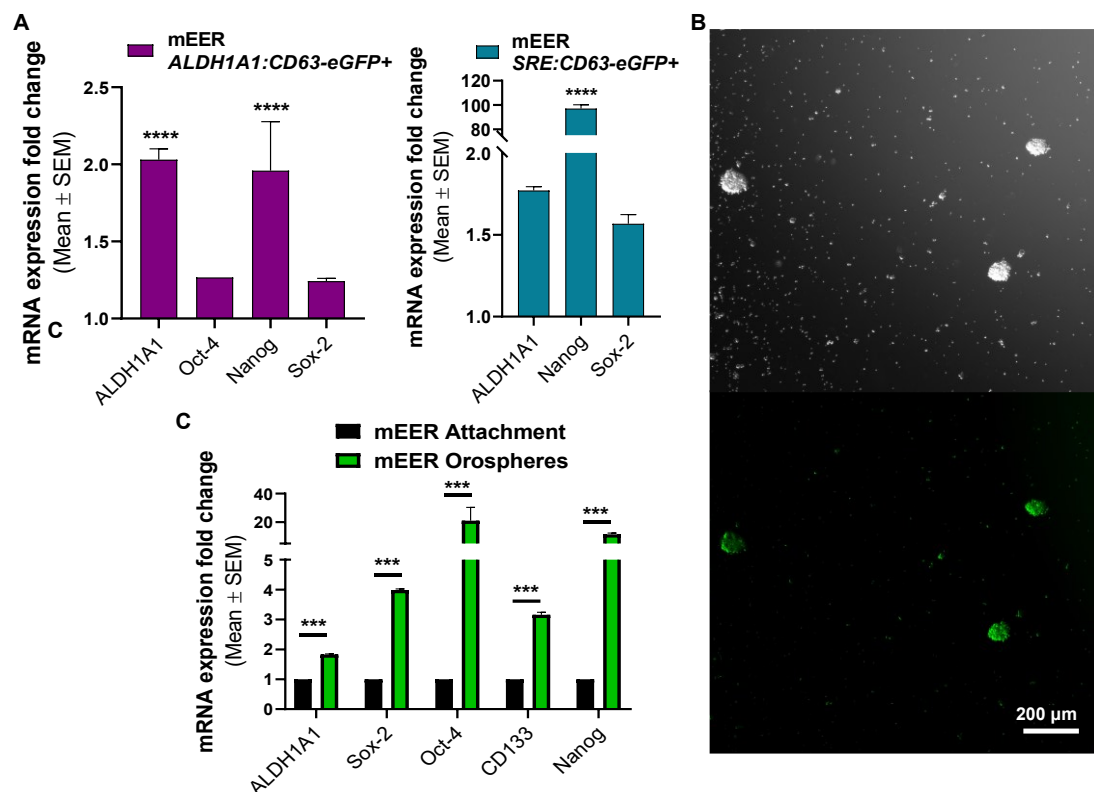


Figure 14. mEER CSC model validation. (A) Relative increase in stemness gene expression of flow sorted brightest mEER eGFP + cells compared to eGFP- cells analyzed by RT-qPCR. **(B)** Representative microscopy images of flow sorted mEER *ALDH1A1:CD63-eGFP+* orospheres growing in 3D tumorspheres specific medium. **(C)** Stemness gene expression signature of mEER *ALDH1A1:CD63-eGFP+* orospheres compared to mEER cells growing in attachment conditions assessed by RT-qPCR.

Altogether, these data confirmed the ability of *ALDH1A1:CD63-eGFP* and *SRE:CD63-eGFP* expression cassettes to restrict expression of the tEVs reporter within CSC-enriched subpopulations in the heterogeneous mEER cancer cell line.

1.2 MOC2 EVs^{CSC-GFP+} *IN VITRO* MODEL VALIDATION

We further aimed to assess if our experimental approach efficiently labeled MOC2 CSC subpopulations. To this end, we performed *in vitro* imaging of engineered MOC2 *ALDH1A1:CD63-eGFP* and *SRE:CD63-eGFP* cells. We observed the presence of few eGFP+ cells within the cell cultures (**Figure 15A, B**). Then, engineered cells were flow sorted based on the levels of eGFP fluorescence and the stemness nature of the eGFP+ brightest cells was evaluated by qPCR

analysis. Expectedly, MOC2 *ALDH1A1:CD63-eGFP*⁺ and MOC2 *SRE:CD63-eGFP*⁺ cells showed significantly greater expression of the stemness markers *ALDH1A1* and *Oct-4* than *GFP*⁻ cells (**Figure 15C**). Indeed, similar to mEER model, MOC2 *ALDH1A1:CD63-eGFP*⁺ cells formed bigger cell clusters than *GFP*⁻ cells when cultured in LA conditions (**Figure 15D**). Collectively, this data suggested that our designed expression cassettes could restrict the expression of the tEV reporter within CSC-like cells in MOC2 cell line.

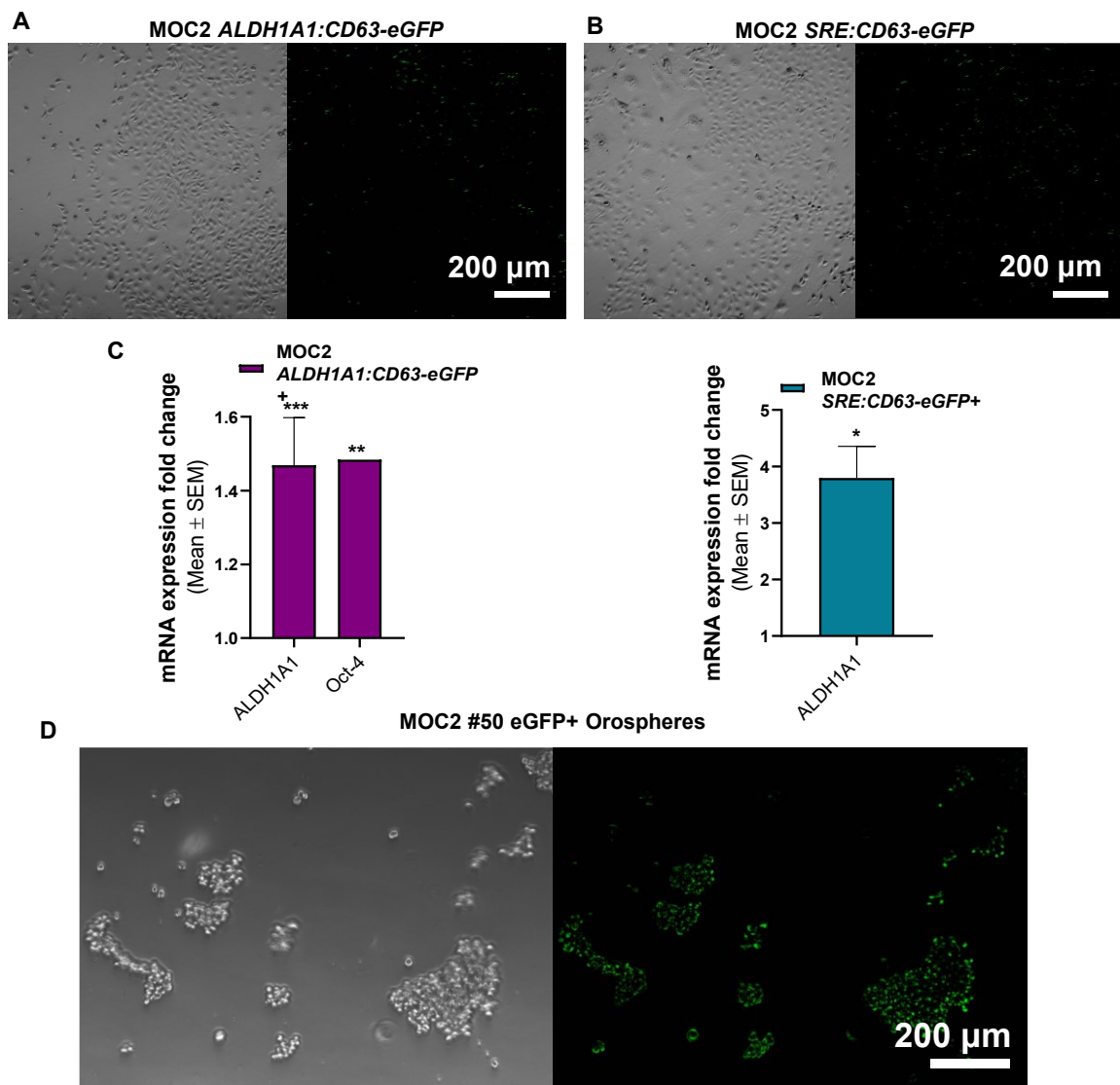


Figure 15. MOC2 CSC model validation. (A, B) Representative confocal microscopy images of cultured MOC2 *ALDH1A1:CD63-GFP* cells and *SRE:CD63-GFP* cells in culture. (C) Relative increase in stemness gene expression of flow sorted MOC2 GFP⁺ cells compared to GFP⁻ cells analyzed by RT-qPCR. (D) Representative images of flow sorted MOC2 *ALDH1A1:CD63-GFP*⁺ cells growing in 3D tumorsphere specific medium.

2 *IN VIVO* STUDY OF THE EVs^{CSC} - IMMUNE CELLS INTERPLAY

2.1 EVs^{CSC} REPORTERS REVEAL A SPECIFIC HIGH INTERACTION RATE BETWEEN EVs^{CSC}, MHC-II- MAC AND PD-1+ T CELLS IN THE TIME

We and others have previously investigated the interactions that occur in the TME between tEVs and immune cells^{88,115}. However, whether tEVs^{CSC} possess a distinct tropism toward tumor infiltrating immune cells is still unknown. In order to test if tEVs^{CSC} preferentially interact with specific immune cell subsets, we challenged mice with mEER tumor cells carrying the *ALDH1A1:CD63-eGFP* or the *SRE:CD63-eGFP* expression cassettes. As control, we used mice bearing mEER tumor cells carrying the *PGK:CD63-eGFP* expression cassette. Experiment design is detailed in **Figure 16**.

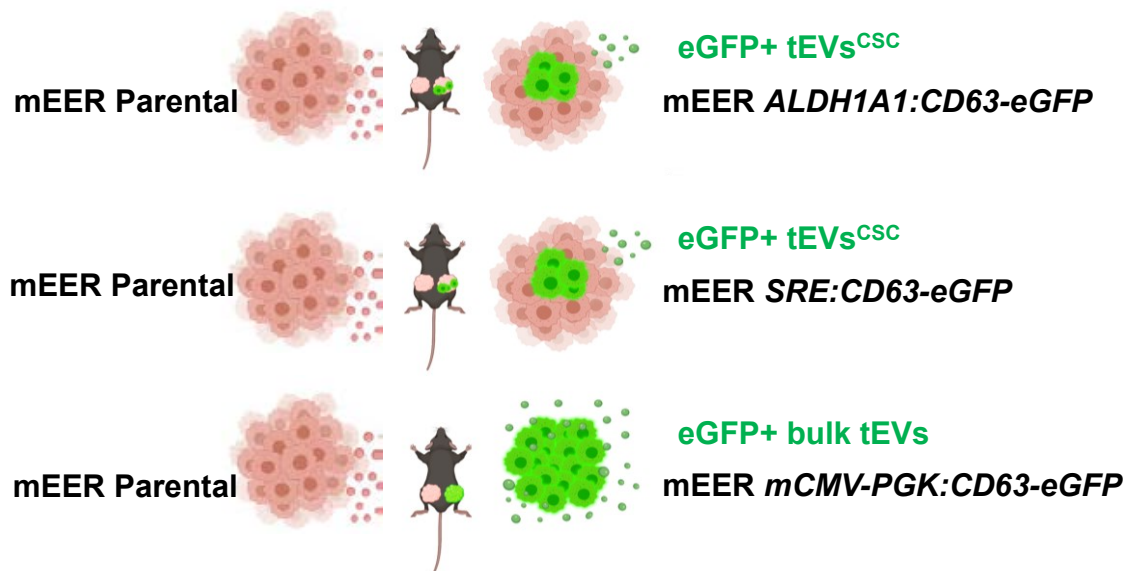


Figure 16. mEER *ALDH1A1:CD63-eGFP* and mEER *SRE:CD63-eGFP* models *in vivo* experiment illustrative design.

Flow cytometry-based analysis revealed the presence of different levels of CD45⁺ CD63-eGFP⁺ cells among groups (**Figure 17**).

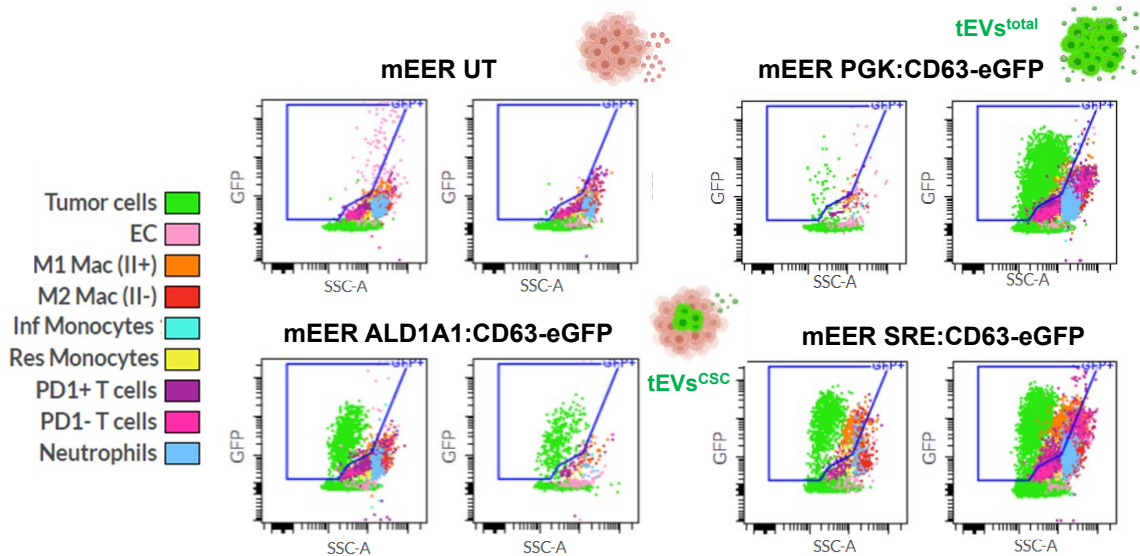


Figure 17. Overlaid dot plot representation of analyzed cell populations present in tumors from mice bearing genetically modified mEER cells studied by FACS. Two representative dot plots are displayed per group and CD63-eGFP+ gate is indicated in each case.

We then wondered if differences in tEVs^{total} and tEVs^{CSC} tropism exist within functional subsets of CD45+ cells. Specifically, F4/80+ Mac MHCII+ (M1) and II- (M2), inflammatory and resident monocytes (Mo), PD-1+ and PD-1- T cells and Neutrophils (Neu) immune subpopulations were analyzed. Other immune cells assessed were found in negligible numbers and discarded from the analysis and included DC (gated as CD45+, F480-, 11c+, II+) and B cells (CD45+, B220+). In tumors formed by mEER cells constitutively expressing CD63-eGFP, immune subsets CD45+ CD63-eGFP+ were detected as follows: MHC-II+ Mac (41.03%), inflammatory Mo (Inf Mo) (21,51%) and Neu (11,11%) (**Figure 18A**). When we analyzed tumors expressing either of the tEVs^{CSC} reporters, we observed an increased fraction of CD63-eGFP+ MHC-II- Mac among CD45+ CD63-eGFP+ cells in tEVs^{CSC}, particularly, 35.01%, average between *ALDH1A1:CD63-eGFP* and *SRE:CD63-eGFP* in comparison to 7.70% in *PGK:CD63-eGFP* tumors. Interestingly, we observed an enrichment in the interactions between mEER tEVs^{CSC} and PD-1+T cells (14,38%), as compared to tEVs^{total} (4.49%), mainly at the expense of tEVs-Mo interactions (**Figure 18B**). We observed statistically significant differences between the percentage of CD63-eGFP+ MHC-II+ Mac infiltrating tumors constitutively expressing the tEV^{total} reporter (87,35%) and those present in tumors carrying tEVs^{CSC} reporters (10,5%), indicating that MHC-II+ Mac predominantly uptake non-CSC tEVs. Statistical differences were also found between SRE tumors carrying tEVs^{total} and tEVs^{CSC} reporters on CD63-eGFP+ EC, Inf Mo, Res Mo and Neu, indicating a low rate

of interaction between tEVs^{CSC} and those immune subsets. On the other hand, the percentage of CD63-eGFP+ MHC-II⁻ Mac did not significantly change, suggesting that MHC-II⁻ Mac predominantly uptake tEVs^{CSC} (**Figure 18C**). When we analyzed monocyte subsets, we observed a significant decrease in the percentage of CD63-eGFP+ monocytes from both inflammatory and resident subsets, indicating that monocytes predominantly uptake non-CSC tEVs (**Figure 18C**). By labeling T cells with the activation marker PD-1, we observed that the percentage of CD63-eGFP+ PD-1+ T cells did not significantly change between tumors constitutively expressing the tEV reporter (9,6%) and those present in tumors carrying CSC reporters (6%), suggesting that, similarly to MHC-II⁻ Mac, also PD-1+ T cells predominantly uptake tEVs^{CSC} (**Figure 18C**). To highlight these differences, we calculated a tEVs^{CSC} specificity index by dividing the percentage of CD45+ CD63-eGFP+ immune cells for each subset in the tEVs^{CSC} groups by the percentage of the corresponding subsets from the tEVs group. We observed that the tEVs^{CSC} specificity index was 0.89 for MHC-II⁻ Mac and 0.63 for PD-1+ T cells, whereas all other tested subsets were below 0.21 (**Figure 18D**). Altogether, these data suggest that tEVs^{CSC} possess a preferential tropism towards MHC-II⁻ Mac and PD-1+ T cells.

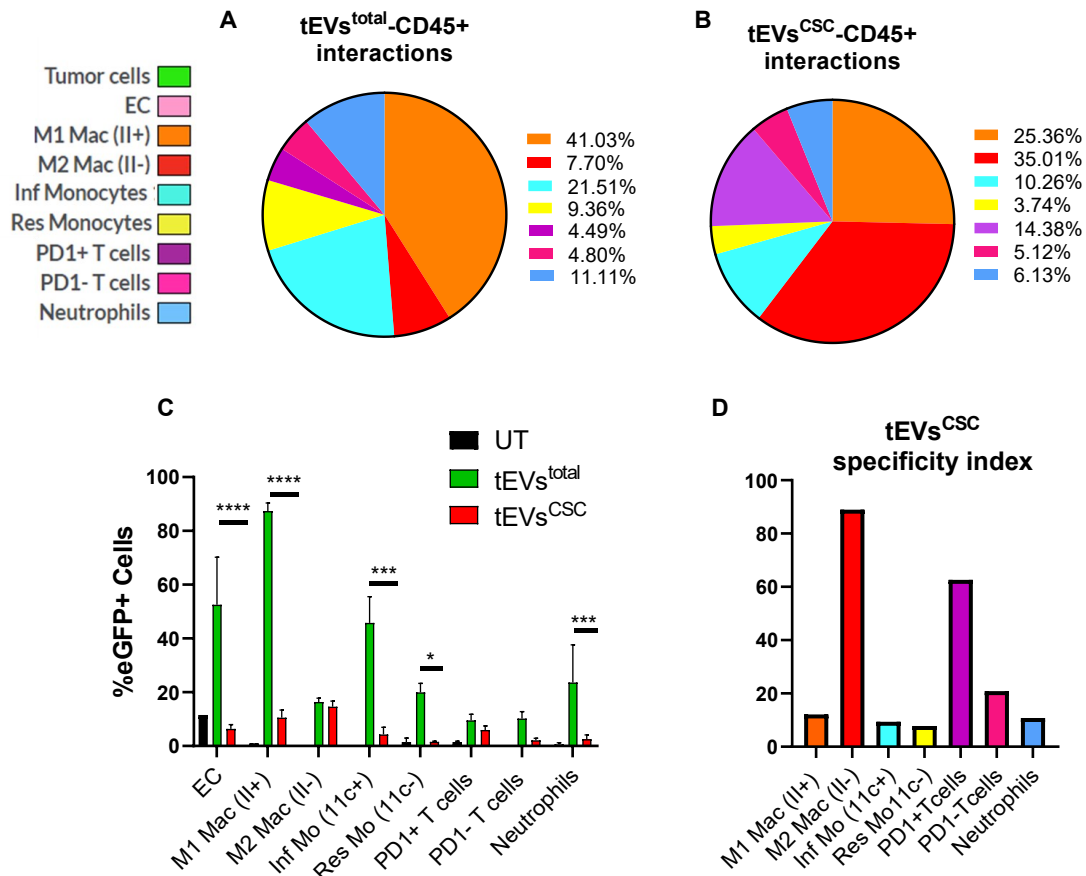


Figure 18. *In vivo* released mEER EVs^{CSC} target MHC-II- Mac (M2) and PD-1+ T cells in the TME. **(A)** Representative graph of the % of specific tEVs^{total-eGFP+}-CD45⁺ immune cell subsets interactions. **(B)** Same representation for the % of specific tEVs^{CSC-eGFP+}-CD45⁺ interactions. **(C)** Summary graph presenting the % of immune cell subsets presenting CD63-eGFP⁺ fluorescence in unlabeled EVs tumors (UT), tEVs^{total-eGFP+} labeled tumors and tEVs^{CSC-eGFP+} labeled tumors. **(D)** Calculated index of the % from tumors 100% tEVs^{total}-immune cell subsets interactions that correspond to specific tEVs^{CSC}-immune cell subsets interactions.

Furthermore, we next aimed to increase the specificity of detection of the tEVs^{CSC}-immune cells interactions by using a sensitive and stringent tagging strategy recently developed and validated by our group¹¹⁶. This strategy consisted in the engineering of EV producing cells to display a membrane-bound form of SrtA onto tEVs^{CSC}. SrtA is a bacterial transpeptidase that catalyzes the transfer of a peptide substrate on the surface of EV-binding cells rendering a fluorescent signal (**Figure 12, M&M**). Thereby, mEER tumor cells were modified to express the SrtA enzyme on their membrane under the regulation of the *ALDH1A1* promoter. Of note, these cells also expressed both, the *CD63-GFP* construct and the *SS-mSca-LPETGG* SrtA peptide substrate. Such setup allowed us to detect in the same tumor the eGFP fluorescence in CD45⁺ cells derived from CD45⁺-EVs^{total-eGFP+} interactions together with the mSCA fluorescence derived from the specific binding of EVs^{CSC-SrtA+} to specific CD45⁺ subsets. Under this premise, mice

were challenged with the above described modified mEER tumor cells. Indeed, another two groups of mice were injected with mEER tumor cells engineered to express either the *ALDH1A1:StrA* construct without the SrtA substrate or the *PGK:CD63-eGFP* construct and the *SS-mSca-LPETGG* substrate without the SrtA to later establish the negative controls for the background of both the eGFP and the mSCA fluorescence, respectively. Detailed scheme of the experiment design is presented in **Figure 19**.

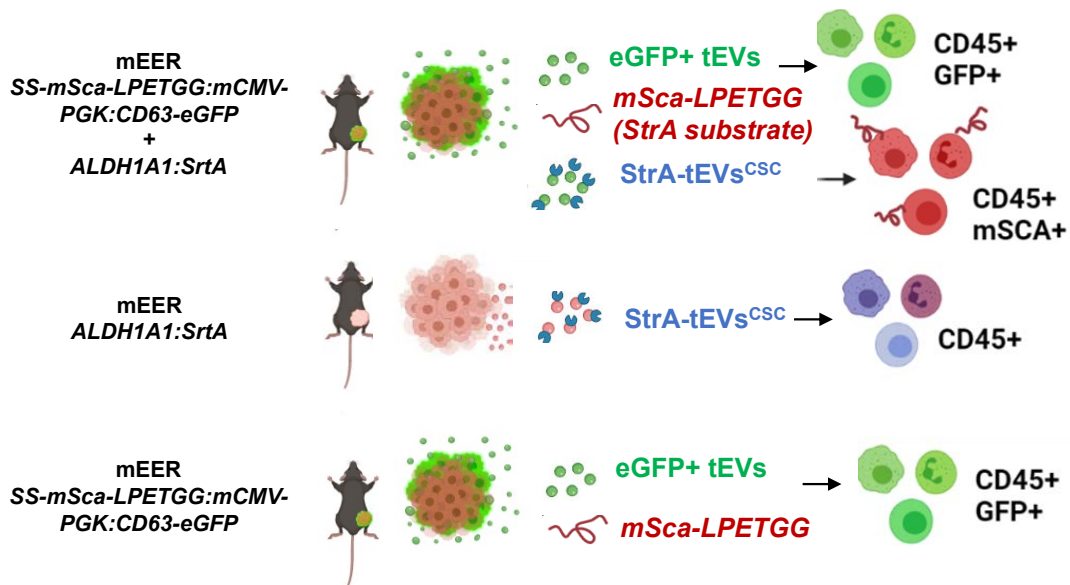


Figure 19. mEER ALDH1A1:SrtA *in vivo* model experiment illustrative design.

Expectedly, flow cytometry analysis of tumors revealed differences in the % of CD63-eGFP+ and mSCA+ cells between groups (**Figure 20**).

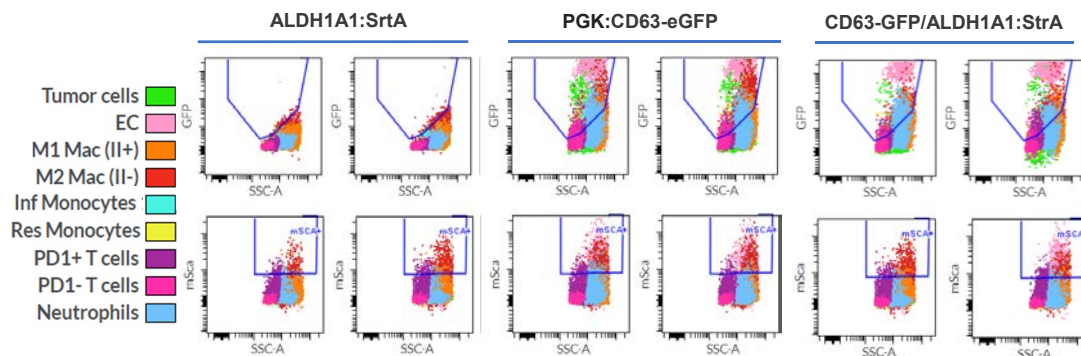


Figure 20. mEER ALDH1A1:StrA overlaid dot plot representation. Different cell populations present in tumors from mice bearing genetically modified mEER cells. 4 dot plots per group are represented.

Tumors' flow cytometry deeper analysis revealed proportions of each CD45+ immune cell subset presenting CD63-eGFP+ fluorescence because of EVs^{total} labeling, resulting the MHC-II+ Mac the 30,59% of total CD45+ CD63-eGFP+ cells, followed by Neu (18,75%) and inflammatory Mo

(16,02%) (**Figure 21A**). When same tumors were analyzed for mSCA+ fluorescence we found that the highest fraction of CD45+ mSCA+ cells corresponded to MHC-II- Mac, indicating that tEVs^{CSC} – MHC-II- Mac interaction corresponded to the 35,56% of total EVs^{CSC}-CD45+ interactions, followed by MHC-II+ Mac (24,94%). Interestingly, PD-1+ T cells represented the other subpopulation presenting high levels of mSCA fluorescence (15,02% of total CD45+ mSCA+ cells) while CD63-eGFP+ PD-1+ T cells only accounted for the 8,84% of total CD45+eGFP+ cells (**Figure 21B**). Expectedly, the % of immune cell subsets presenting CD63-eGFP fluorescence was higher than the % of cells showing mSCA fluorescence, as tEVs^{CSC-StrA+} were supposed to be a minor fraction of the tEVs^{total-eGFP+} (**Figure 21C**). Peculiarly, significant differences were found between the % of CD63-eGFP+ cells and the % of mSCA+ cells in the same cell subsets than in our previous experiment (EC, MHC-II+ M1 Mac, Inf Mo, Res Mo, Neu). Of note, PD-1- T cells were statistically significant in this experiment (**Figure 21C**). Interestingly, no statistically relevant differences were found among MHC-II- Mac or PD-1 + cells suggesting that those immune subpopulations were responsible for the predominant uptake of tEVs^{CSC}. These results also indicated that tumor tEVs^{total} targeted different immune cell subsets when compared to tEVs^{CSC} (**Figure 21C**). tEVs^{CSC} specificity index obtained to elucidate the real % of interactions between tEVs^{CSC}-CD45+ cells among all tEVs^{total}-CD45+ cells interactions resulted specifically increased for MHC-II- Mac (0,63) and PD-1+T cell subpopulation (0,44), while this index remained lower than 0,23 for the rest of the immune cell subsets (**Figure 21D**). Finally, when the specificity index from both experiments were studied together (**Figure 18D and Figure 21D**), significant differences were found between MHC-II- M2 Mac index (0,76) and the rest of the immune subsets, which index remained lower than 0,17. Of note, PD-1 + T cells tEVs^{CSC} interaction index was also remarkably high (0,53) (**Figure 21E**). Those data indicated that from all the interactions that take place between tumor cells and MHC-II- Mac and PD-1+ T cells in the TME via tumor secreted EVs, around the 76% and the 53% correspond to tEVs^{CSC} mediated interactions, respectively. Those results suggested an active interplay between CSC, MHC-II- Mac and PD-1+T cells via EVs.

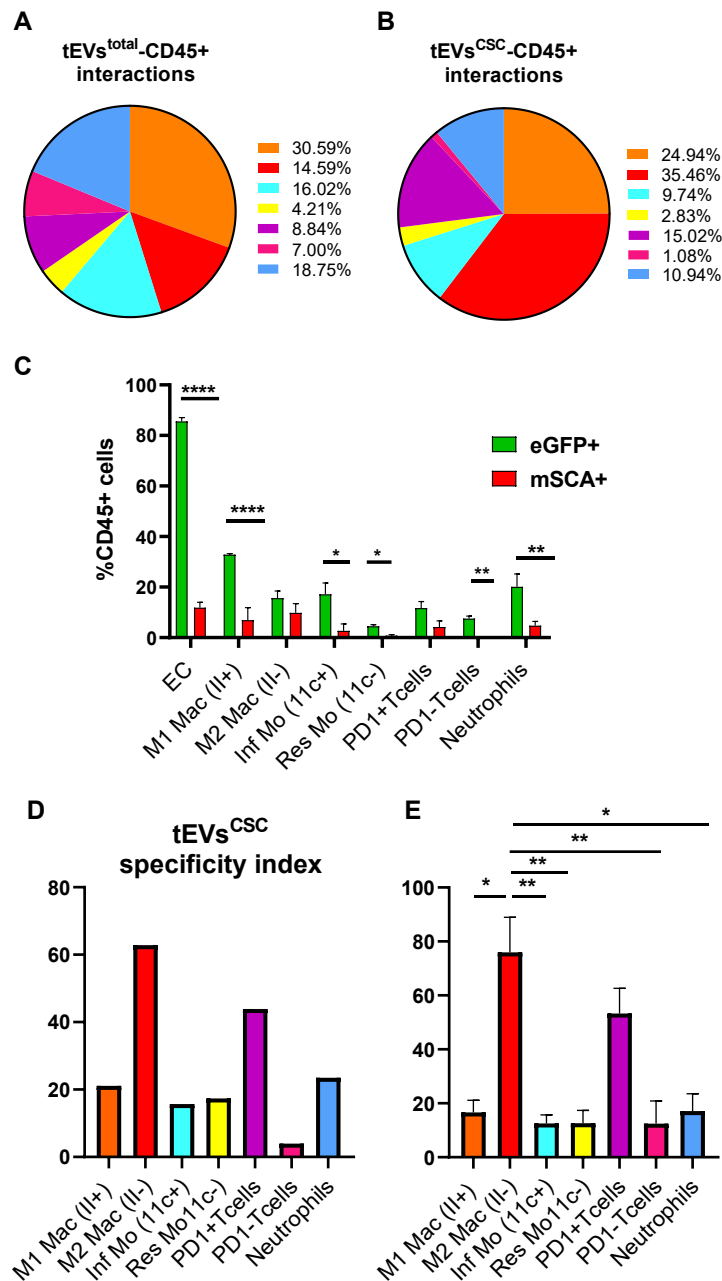


Figure 21. ALDH1:SrtA CSC *in vivo* model reveals a predominant specific interaction between $tEVs^{CSC}$, MHC-II- Mac and PD-1+ T cells in the TME. (A) Representative graphs showing the % of specific $tEVs^{total-CD45+}$ immune cell subsets interactions respect to all $tEVs^{total-CD45+}$ interactions. **(B)** Identification of the % of specific $tEVs^{CSC-CD45+}$ immune cell subsets interactions respect to all $tEVs^{CSC-CD45+}$ interactions. **(C)** Summary graph presenting the % of immune cell subsets presenting CD63-eGFP+ and mSCA+ fluorescence in tumors carrying modified mEER *ALDH1A1:StrA/PGK:CD63-eGFP* tumor cells **(D)** Calculated index of the % from tumors 100% $tEVs^{total-}$ immune cell subsets interactions that correspond to specific $tEVs^{CSC-}$ immune cell subsets interactions. **(E)** Graph presenting the mean value of specificity index for both experiments.

3 CSC AND TAMs SHOW SPATIAL CLOSE LOCALIZATION IN THE TME

TAMs are crucial regulators of cancer cells in TME. They are highly plastic cells that can be re-programmed by signals found within TME acquiring key roles in tumor cells progression, immune evasion and immunosuppression¹²². Our flow cytometry data highlighted an important CSC–TAMs communication via EVs. To further study this phenomenon, IF for α -CD45 and α -F4/80 was performed in mice OCT preserved tumors sections carrying either tumor cells genetically modified with *PGK:CD63-eGFP* reporter or tumor cells engineered to express *ALDH1A1:CD63-eGFP*. Confocal microscopy images showed a clear eGFP+ signal in all tumor cells carrying the constitutive *PGK:CD63-eGFP* reporter (**Figure 22**) whereas few eGFP+ cells were found in tumors with *ALDH1A1:CD63-eGFP* engineered tumor cells, being those eGFP+ cells identified as CSC (**Figure 23**). Additionally, a clear signal of CD45+ cells surrounding and actively infiltrating the tumors was found in all cases. We found that among CD45+ cells a high % corresponded to F4/80+ cells, which were identified as TAMs. Although TAMs were mainly aggregated forming a layer surrounding the tumor borders, they were also found infiltrating some intra-tumor areas in close contact with GFP+ tumor cells (**Figure 22 and 23**). Singularly, an adjacent localization of TAMs and CSC was observed (**Figure 23**).

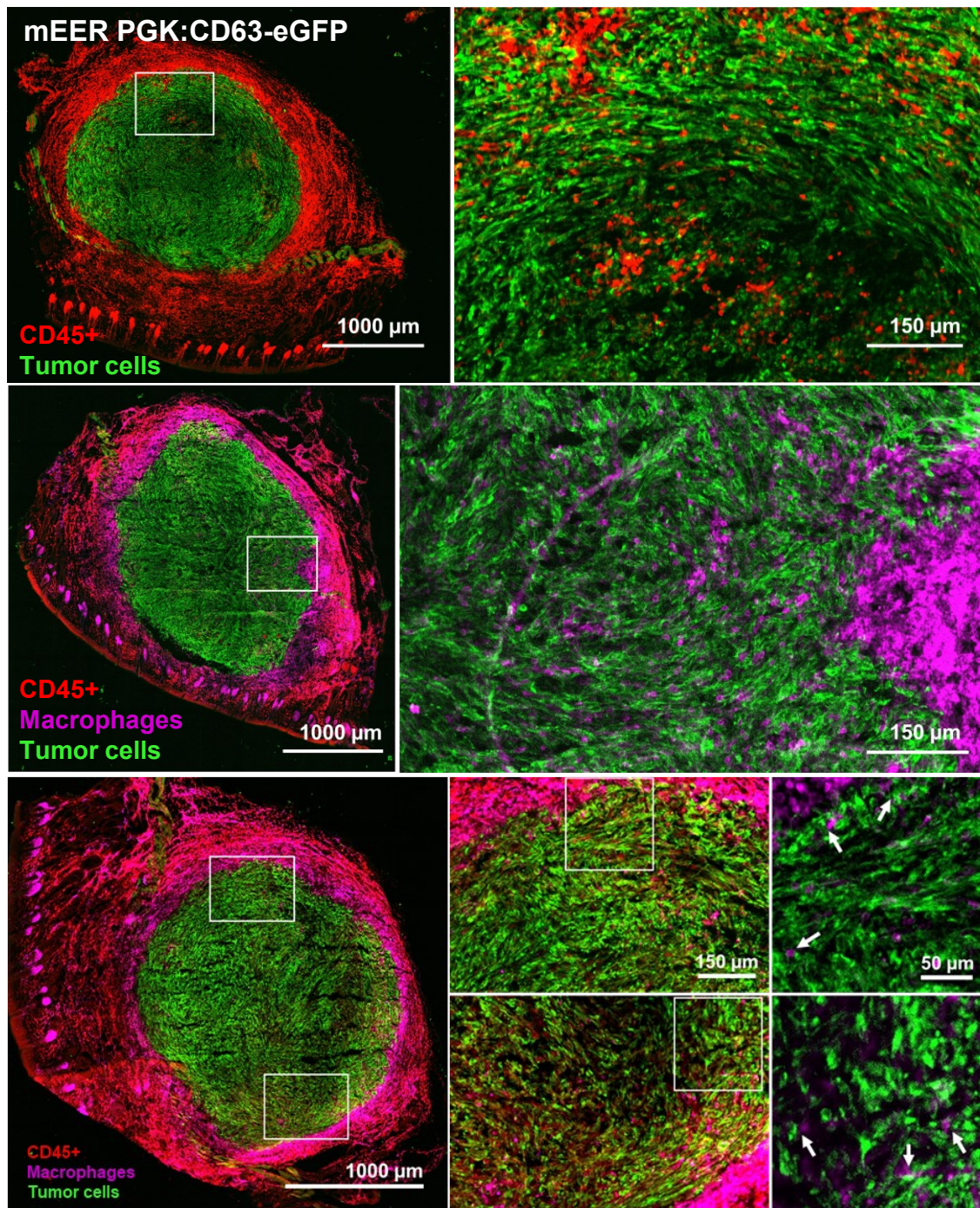


Figure 22. Representative IF images of tumor sections carrying mEER *PGK:CD63-eGFP* tumor cells. Arrows indicate F4/80+ Mac.

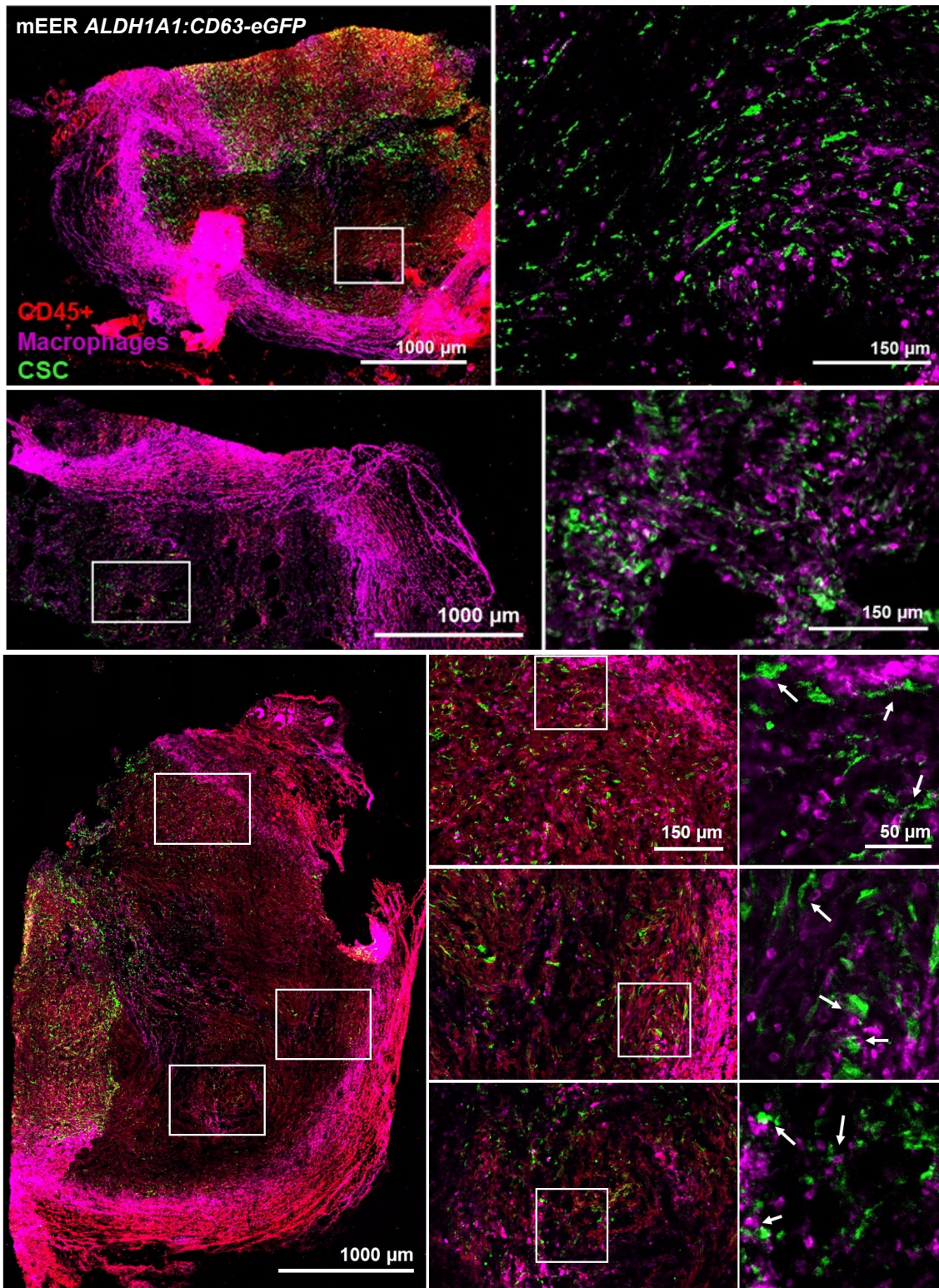


Figure 23. Representative IF images of tumors carrying mEER *ALDH1A1:CD63-eGFP* tumor cells. Arrows in the insets indicate TAMs-CSC interactions.

We next measured the distance between total tumor cells and TAMs and CSC and TAMs in random tumor sections. Results showed that distance between CSC and TAMs was significantly smaller than the distance between total tumor cells and TAMs (**Figure 24**). These results supported the hypothesis of a close interaction between CSC and TAMs in the TME.

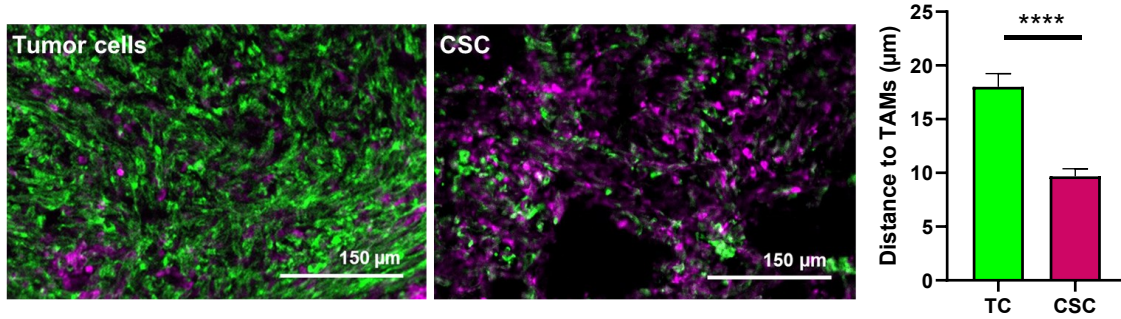


Figure 24. CSC and TAMs show spatial close localization in the TME. Graph showing the distance in μm between CSC and bulk tumor cells with TAMs.

DISCUSSION

DISCUSSION

Tumor released EVs are key modulators of tumor immunity¹¹⁷. However, previous studies have usually disregarded the phenotypic state of tumor secreting EVs. Given the importance of CSC in cancer biology¹¹², this study presents a novel strategy to effectively track CSC secreted EVs in the TME under physiological conditions. Here we specifically focused on the *in vivo* study of the interplay between CSC secreted EVs and infiltrating tumor immune cell populations, reporting for the first time specific interactions of CSC EVs fraction with the immune tumor stroma.

1 GENETIC LABELING OF CSC DERIVED EVS

In this thesis we aimed to study the endogenous interactions between CSC EVs and immune cell populations in the TME and identify which are the immune cells subsets that preferably bind CSC EVs under pathophysiological settings. For this aim, we developed an efficient experimental model to track endogenous secreted CSC EVs.

ALDH1A1 expression has been reported to be upregulated in many solid tumor types. In addition, SRE has recently emerged as a new CSC reporter in HNSCC. Based on this, and given that the CD63-eGFP construct has been described to efficiently label tumor derived EVs, we engineered HNSCC tumor cells to express the EVs pan-marker CD63-eGFP under the control of *ALDH1A1* and *SRE* CSC-specific promoters. This strategy allowed us to efficiently separate two tumor subpopulations based on their membrane CD63-eGFP fluorescence. When the stemness profile of CD63-eGFP+ cells was analyzed, we found that these cells displayed CSC features summarized as a greater expression of pluripotency associated genes and an increased sphere formation capacity compared to the eGFP-cell subpopulation.

Thereby, this strategy allowed to develop a cancer cell line model in which the EVs reporter would be subjected to the restricted expression on the CSC subpopulation, allowing the *in vivo* tracking of those EVs subset and the study of the EVs^{CSC}-immune cell interactions. Of note, our developed experimental approach to specifically track CSC secreted EVs can be useful for the design of multiple studies investigating the *in vivo* interactions not only between CSC EVs and immune cells but also with multiple stromal cells present in the TME and in metastatic niches. Indeed, we remark that this strategy possesses the advantage of avoiding any EVs *in vitro* manipulation, mimicking more efficiently a physiological scenario.

2 STUDY OF THE *IN VIVO* INTERACTIONS BETWEEN CSC AND IMMUNE CELLS VIA EVs

To study tumor CSC derived EVs-immune cells interactions, we challenged mice with engineered HSCC tumor cells expressing the EVs pan-marker CD63-eGFP under the control of *ALDH1A1* and *SRE* CSC-specific promoters. In parallel, we also injected mice with HNSCC tumor cells expressing EVs CD63-eGFP+ reporter under a constitutive promoter (*hPGK*). Subsequent fluorescence signal in immune cells allowed us to identify immune cell populations which had interacted with either CSC derived EVs or total tumor derived EVs, respectively. Moreover, we also employed a recently developed and validated strategy to label EVs-binding immune cells based on the transpeptidase activity of the bacterial enzyme SrtA¹¹⁶. Under this approach, mice were challenged with HNSCC tumor cell lines genetically engineered to encode SrtA under the CSC validated *ALDH1A1* promoter. Furthermore, analysis of mice carrying tumor cells expressing both EVs reporters under either constitutive promoter (*hPGK*) or CSC specific reporter (*ALDH1A1*) allowed us to statistically test for selective behavior of CSC EVs as compared to bulk tumor EVs.

Interestingly, results from our studies reported significant differences between the immune cell subsets that are targeted by bulk total tumor EVs compared to CSC EVs fraction, identifying for the first time that MHC-II- M2 Mac and PD-1+ T cells represent the main immune cell target for CSC released EVs, suggesting an active communication crosstalk between these cell populations via EVs. Moreover, a close spatial localization of TAMs and CSC was appreciated in tumors, supporting previous studies indicating that TAMs constitute a relevant component of CSC niches.

2.1 EVs^{CSC} AND MACROPHAGES INTERPLAY

Among all the immune cell subsets studied, we identified Mac as the immune cell type with the highest percentage of interaction rate with both total tEVs^{total} and tEVs^{CSC}. These results could be expected, as TAMs constitute the most abundant population of tumor-infiltrating immune cells in TME¹²³. Mac are extremely plastic cells and are known to exhibit a spectrum of polarization phenotypes. In the extremes of these polarized phenotypes M1 and M2 macrophages are found. While MHC-II+ M1 Mac are believed to constitute critical effectors of innate host defense displaying anti-tumor activity, MHC-II- M2 polarized Mac are regarded as promoters of tumor development^{122,124}. TAMs are usually educated by environmental factors to present a M2 state, becoming crucial contributors of the immunosuppressive niche by exerting

an inhibitory effect on the cytotoxic function of tumor-killing immune cells^{125,126}. Accordingly, the presence of M2 Mac within primary tumors has been correlated with a poor prognosis for many types of cancer^{125,127,128}.

Here we reported clear differences between the interaction rates of M1 and M2 Mac with each EVs fraction. Although numerous studies have addressed the ability of tumor derived EVs to polarize TAMs towards pro-tumorigenic M2 phenotypes^{129–132}, our data revealed that not total tumor derived EVs, but CSC fraction secreted EVs directly targeted M2 Mac subpopulations. Our first approach, in which EVs^{CSC} were targeted with the CD63-eGFP construct, described significant differences between the M1 and M2 populations interacting with tEVs^{total} compared to specific EVs^{CSC}. While tEVs^{total} mainly interacted with M1 Mac, EVs^{CSC} preferably targeted M2 Mac. Accordingly, the experimental EVs-SrtA-reporter approach confirmed a specific high interaction rate between M2 Mac and EVs^{CSC}.

Accumulating evidence supports the idea of an active crosstalk between M2 Mac and CSC. Recent reports indicated that CSC promote M2 Mac phenotypes that in turn become closely involved in the maintenance of CSC niches³⁷. In agreement to this, we found that TAMs localize in the vicinity of CSC in tumors. CSC reside in specific niches in which stromal cells surrounding them secrete a variety of biological factors that sustain their stemness biology. The CSC niche is particularly important in the maintenance of CSC self-renewal, repopulation potential, and tumor initiation^{133,134}. Interestingly, our data revealed that TAMs constitute a relevant component of CSC niches, supporting the high interaction rate observed between CSC and TAMs. Accordingly, the relevance of TAMs in CSC biology is reinforced by a growing list of TAM-derived factors implicated in the maintenance of CSC stemness in different types of cancer^{37,79,135,136}. Recent studies in different cancer types have elucidated that CSC create a paracrine loop that induce M2 Mac polarization towards an immunosuppressive phenotype, which in turn promote and support CSC aggressive phenotype^{79–81,137}. Moreover, M2 Mac have been also described to be responsible of therapy resistance by promoting the CSC phenotype and thus the chemoresistance of cancer cells through the IL-6/STAT3 pathway^{138–141}. However, these studies have not established a direct role of CSC EVs in mediating this communication network with TAMs. In this regard, our findings provide evidence implicating CSC secreted EVs as signal transducers in CSC-M2 Mac interactions. Understanding this communication loop, essential for tumor progression and therapy resistance, would pave the way for the development of new therapies targeting the disruption of CSC-TAMs EVs mediated crosstalk. Such therapies would have the potential to improve immunosuppression and response to therapy.

2.2 EVs^{CSC} AND PD-1+ T CELLS INTERPLAY

Together with TAMs, PD-1+T cells were the immune subset that presented high interaction rates with EVs^{CSC}. The PD-1/PD-L1 pathway is regarded as a key immunosuppressive mechanism operating in HNSCC^{48–50,53}. The PD-1 receptor is an immune checkpoint present in immune cells that limits their anti-tumor activity when it binds to its ligand PD-L1. PD-L1 occurrence on the surface of tumor cells drives immune suppression and contributes to tumor immune escape. PD-1 signaling in CD8+ T cells directly inhibits effector T-cell functions, including proliferation, survival, cytokine production and cytotoxicity⁴⁶. Tumor EVs can also present PD-L1 on their surface, playing critical immunosuppressive roles when binding to PD-1+T cells^{142,143}. Specifically, circulating PD-L1^{high} exosomes in HNSCC patients' plasma but not soluble PD-L1 levels have been associated with disease progression¹⁴⁴. Our study reveals that EVs^{CSC} closely interact with PD-1+T cell populations subsets, suggesting the presence of PD-L1 ligand in EVs^{CSC} fraction. This strategy could result an important mechanism by which EVs^{CSC} may operate immunosuppression by targeting PD-1+T cells. Thus, it would be interesting to study if PD-L1 is enriched in EVs^{CSC}, as PD-L1 may be produced at high enough levels that could compete with this immune check-point inhibitor antibodies finally affecting to immune-therapy response.

3 OVERVIEW AND PERSPECTIVES

HNSCC tumors are characterized to be highly immunosuppressive⁴². HNSCC present high local recurrence rates and therapy resistance that can be attributed to the presence of CSC within tumors. Indeed, CSCs also exhibit singular properties to avoid immune detection and eradication³². Emerging evidence has shown that tumors can interfere with host immunity by secreting EVs¹¹⁷. Tumor derived EVs can affect the proliferation, apoptosis, cytokine production and reprogramming of both innate and adaptive immune cells by transducing different signals thus modifying anti-cancer immune response impairing the effector cells activity and creating an immunosuppressive microenvironment^{91–97}.

Our findings elucidate that CSC secreted EVs could arise as key immunosuppression mediators by promoting M2 Mac expansion and impairing anti-tumor T cells activity. Given the profound impact that M2 TAMs have in immunosuppression and tumor progression and the acquired relevance of PD-1/PD-L1 immune checkpoints in HNSCC immunotherapy, a deeper investigation of the specific immune modulator biological cargo of EVs^{CSC} will be of crucial interest. In

this sense, further studies elucidating the immune perturbations driven by CSC released EVs in those immune subsets are required.

In summary, deeper study of the specific immune-modulators present in EVs^{CSC} is needed to specifically target their immunosuppressive signals. We anticipate that future research focused on the immunomodulation orchestrated by EVs^{CSC} will open a new window for the development of therapeutic strategies to improve current immunotherapy approaches.

CONCLUSIONS

CONCLUSIONS

1. *ALDH1A1:CD63-eGFP*, *SRE:CD63-eGFP* and *ALDH1A1:SrtA* expression cassettes allow the efficient tracking of CSC derived EVs inter-cellular interactions *in vivo*.
2. CSC EVs preferably interact with MHC-II- M2 Macrophages and PD-1+ T cells in the TIME.
3. CSC localize in the vicinity of TAMs within the TIME

BIBLIOGRAPHY

BIBLIOGRAPHY

1. Sung, H. *et al.* Global Cancer Statistics 2020: GLOBOCAN Estimates of Incidence and Mortality Worldwide for 36 Cancers in 185 Countries. *CA: A Cancer Journal for Clinicians* (2021) doi:10.3322/caac.21660.
2. Johnson, D. E. *et al.* Head and neck squamous cell carcinoma. *Nature Reviews Disease Primers* (2020) doi:10.1038/s41572-020-00224-3.
3. Johnson, D. E. *et al.* Head and neck squamous cell carcinoma. *Nature Reviews Disease Primers* (2020) doi:10.1038/s41572-020-00224-3.
4. Sung, H. *et al.* Global Cancer Statistics 2020: GLOBOCAN Estimates of Incidence and Mortality Worldwide for 36 Cancers in 185 Countries. *CA: A Cancer Journal for Clinicians* (2021) doi:10.3322/caac.21660.
5. Mroz, E. A. & Rocco, J. W. Intra-tumor heterogeneity in head and neck cancer and its clinical implications. *World Journal of Otorhinolaryngology-Head and Neck Surgery* **2**, (2016).
6. Chinn, S. B. *et al.* Cancer stem cells: Mediators of tumorigenesis and metastasis in head and neck squamous cell carcinoma. *Head and Neck* **37**, (2015).
7. Biddle, A. *et al.* Cancer stem cells in squamous cell carcinoma switch between two distinct phenotypes that are preferentially migratory or proliferative. *Cancer Research* **71**, (2011).
8. de Jong, M. C. *et al.* CD44 expression predicts local recurrence after radiotherapy in larynx cancer. *Clinical Cancer Research* **16**, (2010).
9. Prince, M. E. *et al.* Identification of a subpopulation of cells with cancer stem cell properties in head and neck squamous cell carcinoma. *Proceedings of the National Academy of Sciences of the United States of America* (2007) doi:10.1073/pnas.0610117104.
10. Roy, S. *et al.* Inhibition of CD44 sensitizes cisplatin-resistance and affects Wnt/ β -catenin signaling in HNSCC cells. *International Journal of Biological Macromolecules* (2020) doi:10.1016/j.ijbiomac.2020.01.131.
11. Gomez, K. E. *et al.* Cancer cell CD44 mediates macrophage/ monocyte-driven regulation of head and neck cancer stem cells. *Cancer Research* (2020) doi:10.1158/0008-5472.CAN-20-1079.
12. Bourguignon, L. Y. W., Earle, C. & Shiina, M. Activation of matrix Hyaluronan-Mediated CD44 signaling, epigenetic regulation and chemoresistance in head and neck cancer stem cells. *International Journal of Molecular Sciences* vol. 18 (2017).
13. Oshimori, N., Oristian, D. & Fuchs, E. TGF- β Promotes Heterogeneity and Drug Resistance in Squamous Cell Carcinoma. *Cell* **160**, 963–976 (2015).
14. Chiou, S. H. *et al.* Positive correlations of Oct-4 and Nanog in oral cancer stem-like cells and high-grade oral squamous cell carcinoma. *Clinical Cancer Research* **14**, (2008).
15. Koo, B. S. *et al.* Oct4 is a critical regulator of stemness in head and neck squamous carcinoma cells. *Oncogene* **34**, (2015).
16. Keysar, S. B. *et al.* Regulation of head and neck squamous cancer stem cells by PI3K and SOX2. *Journal of the National Cancer Institute* **109**, (2017).
17. Lim, Y. C. *et al.* Cancer stem cell traits in squamospheres derived from primary head and neck squamous cell carcinomas. *Oral Oncology* **47**, (2011).
18. Tabor, M. H. *et al.* Head and neck cancer stem cells: The side population. *Laryngoscope* **121**, (2011).
19. Loebinger, M. R. *et al.* Squamous cell cancers contain a side population of stem-like cells that are made chemosensitive by ABC transporter blockade. *British Journal of Cancer* **98**, (2008).
20. Prince, M. E. *et al.* Identification of a subpopulation of cells with cancer stem cell properties in head and neck squamous cell carcinoma. *Proceedings of the National Academy of Sciences of the United States of America* (2007) doi:10.1073/pnas.0610117104.
21. Wei, X. D. *et al.* In vivo investigation of CD133 as a putative marker of cancer stem cells in hep-2 cell line. *Head and Neck* (2009) doi:10.1002/hed.20935.

22. Chen, Y. C. *et al.* Aldehyde dehydrogenase 1 is a putative marker for cancer stem cells in head and neck squamous cancer. *Biochemical and Biophysical Research Communications* (2009) doi:10.1016/j.bbrc.2009.05.048.
23. Song, J., Chang, I., Chen, Z., Kang, M. & Wang, C. Y. Characterization of side populations in HNSCC: Highly invasive, chemo-resistant and abnormal Wnt signaling. *PLoS ONE* **5**, (2010).
24. Peitzsch, C., Nathansen, J., Schniewind, S. I., Schwarz, F. & Dubrovskaya, A. Cancer stem cells in head and neck squamous cell carcinoma: Identification, characterization and clinical implications. *Cancers* **11**, (2019).
25. Lee, S. H. *et al.* Wnt/ β -catenin signalling maintains self-renewal and tumorigenicity of head and neck squamous cell carcinoma stem-like cells by activating Oct4. *Journal of Pathology* **234**, (2014).
26. Biddle, A., Gammon, L., Liang, X., Costea, D. E. & Mackenzie, I. C. Phenotypic Plasticity Determines Cancer Stem Cell Therapeutic Resistance in Oral Squamous Cell Carcinoma. *EBioMedicine* **4**, (2016).
27. Mendelsohn, A. H. *et al.* Snail as a novel marker for regional metastasis in head and neck squamous cell carcinoma. *American Journal of Otolaryngology - Head and Neck Medicine and Surgery* **33**, (2012).
28. Häyry, V. *et al.* Bmi-1 expression predicts prognosis in squamous cell carcinoma of the tongue. *British Journal of Cancer* **102**, (2010).
29. Harper, L. J., Piper, K., Common, J., Fortune, F. & Mackenzie, I. C. Stem cell patterns in cell lines derived from head and neck squamous cell carcinoma. *Journal of Oral Pathology and Medicine* **36**, (2007).
30. Motegi, A. *et al.* Impact of Expression of CD44, a Cancer Stem Cell Marker, on the Treatment Outcomes of Intensity Modulated Radiation Therapy in Patients with Oropharyngeal Squamous Cell Carcinoma. *International Journal of Radiation Oncology Biology Physics* **94**, (2016).
31. Näsman, A. *et al.* Absent/weak CD44 intensity and positive human papillomavirus (HPV) status in oropharyngeal squamous cell carcinoma indicates a very high survival. *Cancer Medicine* **2**, (2013).
32. Müller, L. *et al.* Bidirectional Crosstalk Between Cancer Stem Cells and Immune Cell Subsets. *Frontiers in Immunology* (2020) doi:10.3389/fimmu.2020.00140.
33. Clara, J. A., Monge, C., Yang, Y. & Takebe, N. Targeting signalling pathways and the immune microenvironment of cancer stem cells — a clinical update. *Nature Reviews Clinical Oncology* (2020) doi:10.1038/s41571-019-0293-2.
34. Wang, G. *et al.* Tumor microenvironment in head and neck squamous cell carcinoma: Functions and regulatory mechanisms. *Cancer Letters* (2021) doi:10.1016/j.canlet.2021.03.009.
35. Lee, Y. *et al.* Cd44+ cells in head and neck squamous cell carcinoma suppress t-cell-mediated immunity by selective constitutive and inducible expression of PD-L1. *Clinical Cancer Research* (2016) doi:10.1158/1078-0432.CCR-15-2665.
36. Chikamatsu, K., Takahashi, G., Sakakura, K., Ferrone, S. & Masuyama, K. Immunoregulatory properties of CD44+ cancer stem-like cells in squamous cell carcinoma of the head and neck. *Head and Neck* (2011) doi:10.1002/hed.21420.
37. Chen, P., Hsu, W. H., Han, J., Xia, Y. & DePinho, R. A. Cancer Stemness Meets Immunity: From Mechanism to Therapy. *Cell Reports* (2021) doi:10.1016/j.celrep.2020.108597.
38. Zitvogel, L., Tesniere, A. & Kroemer, G. Cancer despite immunosurveillance: Immunoselection and immunosubversion. *Nature Reviews Immunology* vol. 6 (2006).
39. Vesely, M. D., Kershaw, M. H., Schreiber, R. D. & Smyth, M. J. Natural innate and adaptive immunity to cancer. *Annual Review of Immunology* **29**, (2011).
40. Dunn, G. P., Bruce, A. T., Ikeda, H., Old, L. J. & Schreiber, R. D. Cancer immunoediting: From immunosurveillance to tumor escape. *Nature Immunology* vol. 3 (2002).
41. Qin, Y., Zheng, X., Gao, W., Wang, B. & Wu, Y. Tumor microenvironment and immune-related therapies of head and neck squamous cell carcinoma. *Molecular Therapy - Oncolytics* vol. 20 (2021).
42. Chen, S. M. Y. *et al.* Tumor immune microenvironment in head and neck cancers. *Molecular Carcinogenesis* **59**, 766–774 (2020).
43. Binnewies, M. *et al.* Understanding the tumor immune microenvironment (TIME)

- for effective therapy. *Nature Medicine* **24**, (2018).
44. Fialová, A., Koucký, V., Hajdušková, M., Hladíková, K. & Špíšek, R. Immunological Network in Head and Neck Squamous Cell Carcinoma—A Prognostic Tool Beyond HPV Status. *Frontiers in Oncology* vol. 10 (2020).
 45. Lin, B. *et al.* Tumor-infiltrating lymphocytes: Warriors fight against tumors powerfully. *Biomedicine and Pharmacotherapy* vol. 132 (2020).
 46. Bai, J. *et al.* Regulation of PD-1/PD-L1 pathway and resistance to PD-1/PDL1 blockade. *Oncotarget* vol. 8 (2017).
 47. Veigas, F. *et al.* Immune checkpoint pathways in head and neck squamous cell carcinoma. *Cancers* vol. 13 (2021).
 48. Schneider, S. *et al.* PD-1 and PD-L1 expression in HNSCC primary cancer and related lymph node metastasis – impact on clinical outcome. *Histopathology* **73**, (2018).
 49. Zheng, A. *et al.* PD-L1 promotes head and neck squamous cell carcinoma cell growth through mTOR signaling. *Oncology Reports* **41**, (2019).
 50. Mattox, A. K. *et al.* PD-1 expression in head and neck squamous cell carcinomas derives primarily from functionally anergic CD4+ TILs in the presence of PD-L1+ TAMs. *Cancer Research* **77**, (2017).
 51. Koutsodontis, G. *et al.* PDL1-expressing circulating tumor cells (CTCs) in head and neck squamous cell carcinoma (HNSCC). *Journal of Clinical Oncology* **33**, (2015).
 52. Moskovitz, J., Moy, J. & Ferris, R. L. Immunotherapy for Head and Neck Squamous Cell Carcinoma. *Current Oncology Reports* vol. 20 (2018).
 53. Mei, Z., Huang, J., Qiao, B. & Lam, A. K. yin. Immune checkpoint pathways in immunotherapy for head and neck squamous cell carcinoma. *International Journal of Oral Science* vol. 12 (2020).
 54. Trinchieri, G. Biology of Natural Killer Cells. *Advances in Immunology* **47**, (1989).
 55. Friedman, J. *et al.* Direct and antibody-dependent cell-mediated cytotoxicity of head and neck squamous cell carcinoma cells by high-affinity natural killer cells. *Oral Oncology* **90**, (2019).
 56. Terrén, I., Orrantia, A., Vitallé, J., Zenarruabeitia, O. & Borrego, F. NK cell metabolism and tumor microenvironment. *Frontiers in Immunology* vol. 10 (2019).
 57. Klöß, S. *et al.* Increased sMICA and TGFβ1 levels in HNSCC patients impair NKG2D-dependent functionality of activated NK cells. *Oncolimmunology* **4**, (2015).
 58. Bauernhofer, T., Kuss, I., Henderson, B., Baum, A. S. & Whiteside, T. L. Preferential apoptosis of CD56dim natural killer cell subset in patients with cancer. *European Journal of Immunology* vol. 33 (2003).
 59. Fu, C. & Jiang, A. Dendritic Cells and CD8 T Cell Immunity in Tumor Microenvironment. *Frontiers in immunology* vol. 9 (2018).
 60. Reichert, T. E., Scheuer, C., Day, R., Wagner, W. & Whiteside, T. L. The number of intratumoral dendritic cells and ζ-chain expression in T cells as prognostic and survival biomarkers in patients with oral carcinoma. *Cancer* **91**, (2001).
 61. Goldman, S. A. *et al.* Peritumoral CD1a-positive dendritic cells are associated with improved survival in patients with tongue carcinoma. *Archives of Otolaryngology - Head and Neck Surgery* **124**, (1998).
 62. Gordon, S. Alternative activation of macrophages. *Nature Reviews Immunology* vol. 3 (2003).
 63. Italiani, P. & Boraschi, D. From monocytes to M1/M2 macrophages: Phenotypical vs. functional differentiation. *Frontiers in Immunology* vol. 5 (2014).
 64. Petruzzi, M. N. M. R., Cherubini, K., Salum, F. G. & de Figueiredo, M. A. Z. Role of tumour-associated macrophages in oral squamous cells carcinoma progression: An update on current knowledge. *Diagnostic Pathology* vol. 12 (2017).
 65. Mantovani, A., Sozzani, S., Locati, M., Allavena, P. & Sica, A. Macrophage polarization: Tumor-associated macrophages as a paradigm for polarized M2 mononuclear phagocytes. *Trends in Immunology* vol. 23 (2002).
 66. Fu, E. *et al.* M2 macrophages reduce the radiosensitivity of head and neck cancer by releasing HB-EGF. *Oncology Reports* **44**, (2020).
 67. Gao, L. *et al.* Tumor associated macrophages induce epithelial to mesenchymal transition via the EGFR/ERK1/2 pathway in head

- and neck squamous cell carcinoma. *Oncology Reports* **40**, (2018).
68. Kumar, A. T. *et al.* Prognostic Significance of Tumor-Associated Macrophage Content in Head and Neck Squamous Cell Carcinoma: A Meta-Analysis. *Frontiers in Oncology* **9**, (2019).
69. He, K. F. *et al.* CD163+ tumor-associated macrophages correlated with poor prognosis and cancer stem cells in oral squamous cell carcinoma. *BioMed Research International* **2014**, (2014).
70. Costa, N. L. *et al.* Tumor-associated macrophages and the profile of inflammatory cytokines in oral squamous cell carcinoma. *Oral Oncology* **49**, (2013).
71. Ostrand-Rosenberg, S. & Sinha, P. Myeloid-Derived Suppressor Cells: Linking Inflammation and Cancer. *The Journal of Immunology* **182**, (2009).
72. Law, A. M. K., Valdes-Mora, F. & Gallego-Ortega, D. Myeloid-Derived Suppressor Cells as a Therapeutic Target for Cancer. *Cells* vol. 9 (2020).
73. Umansky, V., Blattner, C., Gebhardt, C. & Utikal, J. The role of myeloid-derived suppressor cells (MDSC) in cancer progression. *Vaccines* vol. 4 (2016).
74. Lang, S. *et al.* Clinical relevance and suppressive capacity of human myeloid-derived suppressor cell subsets. *Clinical Cancer Research* **24**, (2018).
75. Vignali, D. A. A., Collison, L. W. & Workman, C. J. How regulatory T cells work. *Nature Reviews Immunology* vol. 8 (2008).
76. Alhamarneh, O., Amarnath, S. M. P., Stafford, N. D. & Greenman, J. Regulatory T cells: What role do they play in antitumor immunity in patients with head and neck cancer? *Head and Neck* vol. 30 (2008).
77. Ohue, Y. & Nishikawa, H. Regulatory T (Treg) cells in cancer: Can Treg cells be a new therapeutic target? *Cancer Science* vol. 110 (2019).
78. Wang, G. *et al.* Tumor microenvironment in head and neck squamous cell carcinoma: Functions and regulatory mechanisms. *Cancer Letters* (2021) doi:10.1016/j.canlet.2021.03.009.
79. Li, X. *et al.* CXCL12/CXCR4 pathway orchestrates CSC-like properties by CAF recruited tumor associated macrophage in OSCC. *Experimental Cell Research* (2019) doi:10.1016/j.yexcr.2019.03.013.
80. Nusblat, L. M., Carroll, M. J. & Roth, C. M. Crosstalk between M2 macrophages and glioma stem cells. *Cellular Oncology* (2017) doi:10.1007/s13402-017-0337-5.
81. Tao, W. *et al.* Dual Role of WISP1 in maintaining glioma stem cells and tumor-supportive macrophages in glioblastoma. *Nature Communications* (2020) doi:10.1038/s41467-020-16827-z.
82. Chikamatsu, K., Takahashi, G., Sakakura, K., Ferrone, S. & Masuyama, K. Immunoregulatory properties of CD44+ cancer stem-like cells in squamous cell carcinoma of the head and neck. *Head and Neck* (2011) doi:10.1002/hed.21420.
83. Taniguchi, S. *et al.* Tumor-initiating cells establish an IL-33–TGF- β niche signaling loop to promote cancer progression. *Science* **369**, (2020).
84. Celià-Terrassa, T. & Kang, Y. Metastatic niche functions and therapeutic opportunities. *Nature Cell Biology* vol. 20 868–877 (2018).
85. Xie, F. *et al.* Extracellular Vesicles in Cancer Immune Microenvironment and Cancer Immunotherapy. *Advanced Science* (2019) doi:10.1002/adv.201901779.
86. Marar, C., Starich, B. & Wirtz, D. Extracellular vesicles in immunomodulation and tumor progression. *Nature Immunology* (2021) doi:10.1038/s41590-021-00899-0.
87. Czernek, L. & Döchler, M. Functions of Cancer-Derived Extracellular Vesicles in Immunosuppression. *Archivum Immunologiae et Therapiae Experimentalis* (2017) doi:10.1007/s00005-016-0453-3.
88. Robbins, P. D. & Morelli, A. E. Regulation of immune responses by extracellular vesicles. *Nature Reviews Immunology* (2014) doi:10.1038/nri3622.
89. Mittal, S., Gupta, P., Chaluvally-Raghavan, P. & Pradeep, S. Emerging role of extracellular vesicles in immune regulation and cancer progression. *Cancers* (2020) doi:10.3390/cancers12123563.
90. Xie, F. *et al.* Extracellular Vesicles in Cancer Immune Microenvironment and Cancer Immunotherapy. *Advanced Science* (2019) doi:10.1002/adv.201901779.

91. Raimondo, S., Pucci, M., Alessandro, R. & Fontana, S. Extracellular vesicles and tumor-immune escape: Biological functions and clinical perspectives. *International Journal of Molecular Sciences* **21**, (2020).
92. Zhou, X. *et al.* The function and clinical application of extracellular vesicles in innate immune regulation. *Cellular and Molecular Immunology* (2020) doi:10.1038/s41423-020-0391-1.
93. Srivastava, A., Rathore, S., Munshi, A. & Ramesh, R. Extracellular Vesicles in Oncology: from Immune Suppression to Immunotherapy. *AAPS Journal* (2021) doi:10.1208/s12248-021-00554-4.
94. Wieckowski, E. U. *et al.* Tumor-Derived Microvesicles Promote Regulatory T Cell Expansion and Induce Apoptosis in Tumor-Reactive Activated CD8 + T Lymphocytes. *The Journal of Immunology* (2009) doi:10.4049/jimmunol.0900970.
95. Chen, X. *et al.* Exosomes derived from hypoxic epithelial ovarian cancer cells deliver microRNAs to macrophages and elicit a tumor-promoted phenotype. *Cancer Letters* (2018) doi:10.1016/j.canlet.2018.08.001.
96. Cooks, T. *et al.* Mutant p53 cancers reprogram macrophages to tumor supporting macrophages via exosomal miR-1246. *Nature Communications* (2018) doi:10.1038/s41467-018-03224-w.
97. Mittal, S., Gupta, P., Chaluvally-Raghavan, P. & Pradeep, S. Emerging role of extracellular vesicles in immune regulation and cancer progression. *Cancers* (2020) doi:10.3390/cancers12123563.
98. Taylor, D. D. & Gercel-Taylor, C. Exosomes/microvesicles: mediators of cancer-associated immunosuppressive microenvironments. *Seminars in immunopathology* (2011) doi:10.1007/s00281-010-0234-8.
99. Ludwig, S. *et al.* Exosomes as immune regulators in head and neck cancer. *HNO* vol. 68 (2020).
100. Xiao, C. *et al.* Exosomes in Head and Neck Squamous Cell Carcinoma. *Frontiers in Oncology* vol. 9 (2019).
101. Wang, X. *et al.* The roles of extracellular vesicles in the development, microenvironment, anticancer drug resistance, and therapy of head and neck squamous cell carcinoma. *Journal of Experimental and Clinical Cancer Research* vol. 40 (2021).
102. Whiteside, T. L. Immune modulation of T-cell and NK (natural killer) cell activities by TEXs (tumour-derived exosomes). in *Biochemical Society Transactions* vol. 41 (2013).
103. Hong, C. S., Funk, S., Muller, L., Boyiadzis, M. & Whiteside, T. L. Isolation of biologically active and morphologically intact exosomes from plasma of patients with cancer. *Journal of Extracellular Vesicles* **5**, (2016).
104. Chen, W., Xiao, M., Zhang, J. & Chen, W. M1-like tumor-associated macrophages activated by exosome-transferred THBS1 promote malignant migration in oral squamous cell carcinoma. *Journal of Experimental and Clinical Cancer Research* **37**, (2018).
105. Bellmunt, À. M., López-Puerto, L., Lorente, J. & Closa, D. Involvement of extracellular vesicles in the macrophage-tumor cell communication in head and neck squamous cell carcinoma. *PLoS ONE* **14**, (2019).
106. Raimondo, S., Pucci, M., Alessandro, R. & Fontana, S. Extracellular vesicles and tumor-immune escape: Biological functions and clinical perspectives. *International Journal of Molecular Sciences* **21**, (2020).
107. Reya, T., Morrison, S. J., Clarke, M. F. & Weissman, I. L. Stem cells, cancer, and cancer stem cells. *Nature* (2001) doi:10.1038/35102167.
108. Capp, J. P. Cancer stem cells: From historical roots to a new perspective. *Journal of Oncology* vol. 2019 (2019).
109. Kreso, A. & Dick, J. E. Evolution of the cancer stem cell model. *Cell Stem Cell* (2014) doi:10.1016/j.stem.2014.02.006.
110. Saxena, K., Murali, R., Kumar Jolly, M. & Nair, R. Cancer Stem Cell plasticity-a deadly deal. (2019) doi:10.20944/preprints201912.0388.v1.
111. Gilormini, M. *et al.* Isolation and characterization of a head and neck squamous cell carcinoma subpopulation having stem cell characteristics. *Journal of Visualized Experiments* (2016) doi:10.3791/53958.
112. Batlle, E. & Clevers, H. Cancer stem cells revisited. *Nature Publishing Group* **23**, (2017).
113. Müller, L. *et al.* Bidirectional Crosstalk Between Cancer Stem Cells and Immune Cell Subsets. *Frontiers in Immunology* (2020) doi:10.3389/fimmu.2020.00140.

114. Clara, J. A., Monge, C., Yang, Y. & Takebe, N. Targeting signalling pathways and the immune microenvironment of cancer stem cells — a clinical update. *Nature Reviews Clinical Oncology* (2020) doi:10.1038/s41571-019-0293-2.
115. Pucci, F. *et al.* SCS macrophages suppress melanoma by restricting tumor-derived vesicle-B cell interactions. *Science* (2016) doi:10.1126/science.aaf1328.
116. Hamilton, N., Claudio, N. M., Armstrong, R. J. & Pucci, F. Cell Surface Labeling by Engineered Extracellular Vesicles. *Advanced Bio-systems* **4**, (2020).
117. Marar, C., Starich, B. & Wirtz, D. Extracellular vesicles in immunomodulation and tumor progression. *Nature Immunology* (2021) doi:10.1038/s41590-021-00899-0.
118. Chen, Y. C. *et al.* Aldehyde dehydrogenase 1 is a putative marker for cancer stem cells in head and neck squamous cancer. *Biochemical and Biophysical Research Communications* (2009) doi:10.1016/j.bbrc.2009.05.048.
119. Chen, Y. W. *et al.* Cucurbitacin I suppressed stem-like property and enhanced radiation-induced apoptosis in head and neck squamous carcinoma-derived CD44 +ALDH1+ cells. *Molecular Cancer Therapeutics* (2010) doi:10.1158/1535-7163.MCT-10-0504.
120. Qian, X. *et al.* ALDH1-positive cancer stem-like cells are enriched in nodal metastases of oropharyngeal squamous cell carcinoma independent of HPV status. *Oncology Reports* (2013) doi:10.3892/or.2013.2340.
121. Clay, M. R. *et al.* Single-marker identification of head and neck squamous cell carcinoma cancer stem cells with aldehyde dehydrogenase. *Head and Neck* (2010) doi:10.1002/hed.21315.
122. Pan, Y., Yu, Y., Wang, X. & Zhang, T. Tumor-Associated Macrophages in Tumor Immunity. *Frontiers in Immunology* (2020) doi:10.3389/fimmu.2020.583084.
123. Baig, M. S. *et al.* Tumor-derived exosomes in the regulation of macrophage polarization. *Inflammation Research* (2020) doi:10.1007/s00011-020-01318-0.
124. Zhou, J. *et al.* Tumor-Associated Macrophages: Recent Insights and Therapies. *Frontiers in Oncology* (2020) doi:10.3389/fonc.2020.00188.
125. Pollard, R. & W., J. Tumor-associated macrophages : from mechanisms to therapy. *Immunity*. (2015) doi:10.1016/j.immuni.2014.06.010.Tumor-associated.
126. Colegio, O. R. *et al.* Functional polarization of tumour-associated macrophages by tumour-derived lactic acid. *Nature* (2014) doi:10.1038/nature13490.
127. Park, I. H. *et al.* Tumor-derived induces expression on immunosuppressive NK cells in triple-negative breast cancer. **8**, 32722–32730 (2017).
128. Franklin, R. A. *et al.* The cellular and molecular origin of tumor-associated macrophages. *Science* (2014) doi:10.1126/science.1252510.
129. Zhou, Z. *et al.* CCL18 secreted from M2 macrophages promotes migration and invasion via the PI3K/Akt pathway in gallbladder cancer. *Cellular Oncology* (2019) doi:10.1007/s13402-018-0410-8.
130. Cai, J., Qiao, B., Gao, N., Lin, N. & He, W. Oral squamous cell carcinoma-derived exosomes promote M2 subtype macrophage polarization mediated by exosome-enclosed miR-29a-3p. *American Journal of Physiology - Cell Physiology* (2019) doi:10.1152/ajpcell.00366.2018.
131. Li, L. *et al.* Exosomes derived from hypoxic oral squamous cell carcinoma cells deliver miR-21 to normoxic cells to elicit a prometastatic phenotype. *Cancer Research* (2016) doi:10.1158/0008-5472.CAN-15-1625.
132. Ito, A. *et al.* Extracellular vesicles shed from gastric cancer mediate protumor macrophage differentiation. *BMC Cancer* (2021) doi:10.1186/s12885-021-07816-6.
133. Plaks, V., Kong, N. & Werb, Z. The cancer stem cell niche: How essential is the niche in regulating stemness of tumor cells? *Cell Stem Cell* vol. 16 225–238 (2015).
134. Lee, G. & R Hall, R. Cancer Stem Cells: Cellular Plasticity, Niche, and its Clinical Relevance. *Journal of Stem Cell Research & Therapy* **06**, (2016).
135. Lu, H. *et al.* A breast cancer stem cell niche supported by juxtacrine signalling from monocytes and macrophages. *Nature Cell Biology* (2014) doi:10.1038/ncb3041.
136. Mitchem, J. B. *et al.* Targeting tumor-infiltrating macrophages decreases tumor-initiating cells, relieves immunosuppression,

- and improves chemotherapeutic responses. *Cancer Research* (2013) doi:10.1158/0008-5472.CAN-12-2731.
137. Raghavan, S., Mehta, P., Xie, Y., Lei, Y. L. & Mehta, G. Ovarian cancer stem cells and macrophages reciprocally interact through the WNT pathway to promote pro-tumoral and malignant phenotypes in 3D engineered microenvironments. *Journal for Immunotherapy of Cancer* (2019) doi:10.1186/s40425-019-0666-1.
138. Kong, L. *et al.* Deletion of interleukin-6 in monocytes/macrophages suppresses the initiation of hepatocellular carcinoma in mice. *Journal of Experimental and Clinical Cancer Research* (2016) doi:10.1186/s13046-016-0412-1.
139. Xu, X., Ye, J., Huang, C., Yan, Y. & Li, J. M2 macrophage-derived IL6 mediates resistance of breast cancer cells to hedgehog inhibition. *Toxicology and Applied Pharmacology* (2019) doi:10.1016/j.taap.2018.12.013.
140. Yin, Y. *et al.* The immune-microenvironment confers chemoresistance of colorectal cancer through macrophage-derived IL6. *Clinical Cancer Research* (2017) doi:10.1158/1078-0432.CCR-17-1283.
141. Zhu, X. *et al.* IL-6R/STAT3/miR-204 feedback loop contributes to cisplatin resistance of epithelial ovarian cancer cells. *Oncotarget* (2017) doi:10.18632/oncotarget.16610.
142. Poggio, M. *et al.* Suppression of Exosomal PD-L1 Induces Systemic Anti-tumor Immunity and Memory. *Cell* (2019) doi:10.1016/j.cell.2019.02.016.
143. Chen, G. *et al.* Exosomal PD-L1 contributes to immunosuppression and is associated with anti-PD-1 response. *Nature* (2018) doi:10.1038/s41586-018-0392-8.
144. Theodoraki, M. N., Yerneni, S. S., Hoffmann, T. K., Gooding, W. E. & Whiteside, T. L. Clinical significance of PD-L1 β exosomes in plasma of head and neck cancer patients. *Clinical Cancer Research* (2018) doi:10.1158/1078-0432.CCR-17-2664.

Article 1. (Submitted to *Advanced Science*)

Cancer stem cell state defines extracellular vesicle activity in triple negative breast cancer

Patricia González-Callejo, Petra Gener, Zamira V. Díaz-Riascos, Sefora Conti, Patricia Cámara-Sánchez, Roger Riera, Sandra Mancilla, Miguel García-Gabilondo, Vicente Peg, Diego Arango, Anna Rosell, Anna Labernadie, Xavier Trepas, Lorenzo Albertazzi, Simó Schwartz Jr, Joaquin Seras-Franzoso*, Ibane Abasolo*

P. Gonzalez-Callejo, Dr. P. Gener, Dr. Z.V. Díaz-Riascos, P. Cámara-Sánchez, S. Mancilla, Dr. S. Schwartz Jr*, Dr. J. Seras-Franzoso* and Dr. I. Abasolo.

Drug Delivery & Targeting, CIBBIM-Nanomedicine, Vall d'Hebron Institut de Recerca (VHIR), Universitat Autònoma de Barcelona (UAB), P/ de la Vall d'Hebron, 119-129, Barcelona, 08035, Spain. Networking Research Center on Bioengineering, Biomaterials and Nanomedicine (CIBER-BBN), P/ de la Vall d'Hebron, 119-129, Barcelona, 08035, Spain

E-mail: Joaquin.Seras@vhir.org and Simo.Schwartz@vhir.org

Dr. Z.V. Díaz-Riascos, P. Cámara-Sánchez, S. Mancilla and Dr. I. Abasolo.

Functional Validation & Preclinical Research (FVPR), CIBBIM-Nanomedicine, Vall d'Hebron Institut de Recerca (VHIR), Universitat Autònoma de Barcelona (UAB), P/ de la Vall d'Hebron, 119-129, Barcelona, 08035, Spain.

S. Conti, Dr. A. Labernadie, Dr. X. Trepas

Integrative Cell and Tissue Dynamics Group, Institute for Bioengineering of Catalonia C/Baldiri Reixac 15-21, Helix Building, (IBEC), Barcelona, 08028, Spain.

R. Riera and Dr. L. Albertazzi

Nanoscopy for Nanomedicine Group, Institute for Bioengineering of Catalonia (IBEC), C/Baldiri Reixac 15-21, Helix Building, Barcelona, 08028, Spain.

M. García-Gabilondo and Dr. A. Rosell.

Neurovascular Research Laboratory, Vall d'Hebron Institut de Recerca (VHIR), Universitat Autònoma de Barcelona (UAB), P/ de la Vall d'Hebron, 119-129, Barcelona, 08035, Spain.

Dr. V. Peg

Department of Pathology, Vall d'Hebron University Hospital, Universitat Autònoma de Barcelona (UAB), P/ de la Vall d'Hebron, 119-129, Barcelona, 08035, Spain.

Spanish Biomedical Research Network Centre in Oncology (CIBERONC), P/ de la Vall d'Hebron, 119-129, Barcelona, 08035, Spain.

Dr. D. Arango

Biomedical Research in Digestive Tract Tumors, CIBBIM-Nanomedicine, Vall d'Hebron Research Institute (VHIR), Universitat Autònoma de Barcelona (UAB), P/ de la Vall d'Hebron, 119-129, Barcelona, 08035, Spain

Dr. L. Albertazzi

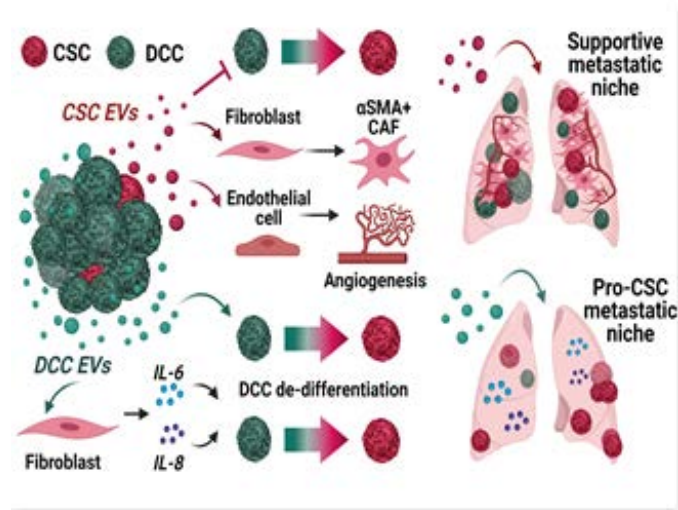
Department of Biomedical Engineering, Institute for Complex Molecular Systems (ICMS), Eindhoven University of Technology, De Zaale, Eindhoven, 5612AJ, Netherlands

Abstract

Intra-tumor phenotypic heterogeneity is the result of a dynamic equilibrium between cancer stem cells (CSC) and differentiated cancer cells (DCC). Extracellular vesicles (EVs) released by both cancer cell subpopulations are known to play a relevant role in the inter-cellular communication and disease progression. However, the particular contribution of EVs secreted by either CSC or DCC (EVs^{CSC} and EVs^{DCC}) to tumor plasticity remains elusive.

Herein we describe how EVs^{CSC} and EVs^{DCC} subpopulations differentially interact with CSC, DCC and cancer associated fibroblasts (CAFs) to control cancer cell phenotype within tumors and to condition distant organs for hosting metastatic cells. In detail, EVs^{CSC} and EVs^{DCC} obtained from triple negative breast cancer models exert opposite roles in tumor cell plasticity. EVs^{CSC} promote cancer cells differentiation whilst EVs^{DCC} induce tumor cell transition towards CSC-like states in two complementary ways. Directly by EV^{DCC} interaction with cancer cells and via triggering IL-6/IL-8 signaling from EV^{DCC} activated fibroblasts. Remarkably, only EVs^{CSC} produce the *in vitro* and *in vivo* activation of myofibroblastic CAFs subpopulations, promoting angiogenesis and increasing the invasiveness of cancer cells. Indeed, exogenously administered EVs^{CSC} prompt the formation of receptive lung metastatic niches supporting macrometastasis growth whilst EVs^{DCC} induce the secretion of pro-stem signals in the niche.

Table of contents



Cancer Stem Cell (CSC) derived EVs inhibit tumor cell dedifferentiation and promote activation of invasive cancer associated fibroblasts and angiogenesis in the metastatic niche. Conversely, EVs from Differentiated Cancer Cell (DCC), promotes tumor cell dedifferentiation and activation of IL-6 and IL-8 secretory fibroblasts.

1. Introduction

Triple-negative breast cancer (TNBC) is a group of particularly aggressive and invasive breast cancer subtypes representing nearly 15% of all breast tumors^[1,2]. At the molecular level, TNBC is characterized by the lack of expression of therapeutic targets such as estrogen receptor alpha (ER α), progesterone receptor (PR) and epidermal growth factor 2 receptor (HER2). Besides, TNBC tumors are markedly heterogeneous and cancer cells within them co-exist in distinct phenotypic states^[3]. Particularly, cancer stem cells (CSCs) are often over-represented in TNBCs and have been associated with the higher chemotherapy resistance, metastatic spread and tumor recurrence rates observed in TNBC patients^[4-6]. In this regard, much research has been focused on targeting these CSC to develop effective therapies for TNBC^[7,8]. However, CSCs removal has shown minimal clinical impact. Probably, due to the fact that cancer cell hierarchies within the tumor have been proven much more plastic than previously anticipated^[9-11].

Classical models of tumor maintenance and progression attributed to CSC the role of delivering differentiated cancer cells (DCC)^[12]. However, there is a growing body of evidence supporting phenotypic bidirectional transitions in tumor cells *in vitro* and *in vivo*^[13-15]. On the one hand, DCC have been proven to gain stem properties under certain circumstances e.g. nutrient deprivation, reduced cell anchorage and presence of chemotherapeutic compounds^[9,10,16]. On the other hand, breast cancer cell lines depleted from their CSC fraction have shown to restore this subpopulation, revealing an idiosyncratic equilibrium among cancer cell subpopulations at multiple phenotypic states^[17]. This phenomena has been proposed to arise through de novo occurrence of CSC-like cells from DCC, suggesting the existence of mechanisms finely controlling the cell state balance within tumor cells^[17]. Multiple external and internal signals, produced by CSCs, DCCs, cancer associated fibroblasts (CAFs), immune cells or mesenchymal cells in the tumor microenvironment (TME), have been shown to regulate CSC self-renewal and differentiation processes, as well as the maintenance of CSC/DCC equilibrium^[18-21]. Such signals comprise small molecules like growth factors, hormones, metabolites and cytokines but also supramolecular entities such as extracellular vesicles (EVs)^[22,23]. EVs constitute a heterogeneous group of nano-sized membrane vesicles enabling the exchange of proteins, lipids and nucleic acids between cells^[24]. In TNBC, EVs secretion has been proven crucial for tumor maintenance and metastatic propagation, both processes intimately related to the occurrence of CSCs^[25-27].

Importantly, EVs influence can stretch to distal regions, impacting on the pre-conditioning of the metastatic sites^[28-30]. Particularly interesting is the role of cancer cell derived EVs in fibroblast regulation. In this regard, EVs have been shown to upregulate NF- κ B signaling pathway driving fibroblasts transition to CAFs^[29]. These activated populations of fibroblasts have been described significantly supporting tumor progression and metastasis^[30,31]. A number of CAFs subtypes have been shown to display, either a direct effect on tumor local invasion e.g. extracellular matrix (ECM) remodeling capacity, or indirectly intervene as mediators of TME signaling, leading to immunosuppression events and fostering CSC phenotypes^[19,32,33]. Altogether, the role of cancer cell

derived EVs in CAFs, culminates in the generation of a receptive pre-metastatic niche, capable of homing circulating cancer cells and supporting their growth. Noteworthy, in spite of tumor EVs relevance in cancer progression and considering that EVs' composition has been proven largely determined by the cell source^[34], the study of EVs' contribution to cancer pathophysiology has generally disregarded the phenotypic state of the EVs-secreting cancer cells.

Here, we aimed to evaluate the role of EVs isolated from cancer cells at distinct differentiation states (CSC vs. DCC) in TNBC progression. EVs were harvested from DCC and cancer cells with stem-like phenotype, distinctively tagged with red fluorescent reporter that allowed their recognition and isolation^[15,35]. We observed substantial differences in the cargo of EVs isolated from CSC and DCC of MDA-MB-231 cells, respectively. Interestingly, the impact of these EVs on cellular plasticity, fibroblasts activation and pro-angiogenic triggering was also unique *in vitro* and *in vivo*. Thus, the co-existence of cancer cells at distinct phenotypic states (e.g. CSC, DCC) within TNBC, seems to be a determinant factor defining the role of cancer cell derived EVs on the diverse facets of tumor maintenance and propagation.

2. Results

2.1. Set up and validation of MDA-MB-231 *in vitro* model for CSC and DCC EVs isolation.

CSC and DCC cell subpopulations were obtained by fluorescence-activated cell sorting (FACS) from the MDA-MB-231 ALDH1A1:tdTomato model, previously described by our group^[15]. These cells are stably transfected with a vector expressing tdTomato fluorescent protein under the control of the ALDH1A1 promoter, thus identifying the population of ALDH1A1 expressing CSC, while non-fluorescent cells represent more differentiated cancer cells or DCCs^[15]. As expected, tdTomato + CSCs isolated from MDA-MB-231 ALDH1A1:tdTomato line lost red fluorescence over time^[15] and significantly decreased stemness gene expression after a 5 passages, denoting a tendency to differentiate into DCC (**Figure 1B**). Interestingly, a subpopulation of DCCs, isolated as MDA-MB-231 ALDH1A1:tdTomato- cells, progressively acquired stem features in cell culture as represented by the re-expression of tdTomato and significant increase in stem gene expression over time (**Figure 1C, D**). These results were further validated with an alternative TNBC cell line, namely HCC1806 (**Figure S1**). Prior to EV production MDA-MB-231 CSC and MDA-MB-231 DCC *in vitro* cell propagation was optimized (**Figure S2**). To maintain the stemness features of CSCs (>95% tdTomato+) serum-free stemness media was employed (**Figure S2A**) while DCCs were cultured in presence of a minimal fraction (<2% tdTomato+) of CSCs (**Figure S2B**) to avoid de-differentiation. In these culture conditions MDA-MB-231 CSCs showed significantly higher mRNA levels of prevalent stem gene reporters, *ALDH1A1*, *Nanog* and *Oct-4*, than MDA-MB-231 DCC (**Figure 1E, F**). Besides, phenotypic traits like cancer cell invasion also proved more accentuated for MDA-MB-231 CSC than for their MDA-MB-231 DCC counterpart (**Figure 1G**). HCC1806 CSC had also significantly higher invasiveness in 2D models than DCC cultures (**Figure S1**).

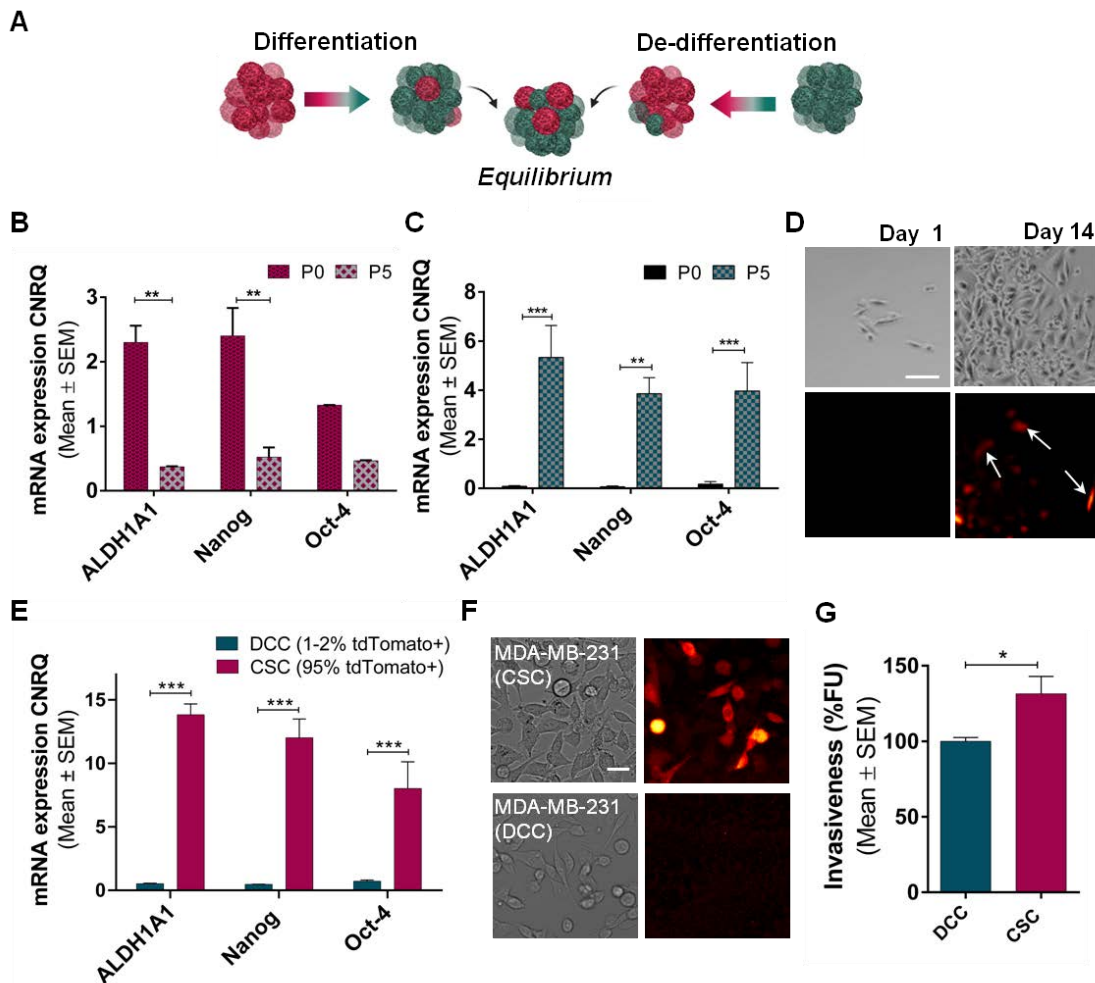


Figure 1. MDA-MB-231 CSC model set up for CSC and DCC EVs isolation. (A) Scheme representing cancer cell state transitions upon isolation of distinct cancer cell subpopulations, namely CSC and DCC. (B) Stemness reporters *ALDH1A1*, *Nanog* and *Oct-4* in MDA-MB-231 tdTomato+ cells analyzed by qPCR after sorting (P0) and after 5 passages in cell culture (P5). (C) Stemness gene expression in MDA-MB-231 tdTomato- cells at P0 and after 5 passages in cell culture (P5). CNRQ stands for Calibrated Normalized Relative Quantity with respect to GAPDH and actin housekeeping genes. (D) MDA-MB-231 tdTomato- cells imaged at day 1 and 14 after sorting, scale bar = 50 μ m. (E, F, G) MDA-MB-231 CSC and DCC cells cultured as detailed in the Material & Methods section. (E) Gene expression of stemness reporters *ALDH1A1*, *Nanog* and *Oct-4* detected by qPCR. (F) Representative images of CSCs and DCCs, scale bar = 25 μ m. (G) 2D laminin invasion assay with CSC and DCC cells. (* $p < 0.05$; ** $p < 0.01$; *** $p < 0.001$).

2.2. EVs protein cargo depends on the CSC-like state of the MDA-MB-231 secreting cells.

EVs secreted from both MDA-MB-231 CSC (EVs^{CSC}) and MDA-MB-231 DCC (EVs^{DCC}) were successfully isolated by charge neutralization-based precipitation. Both types of EVs presented pseudo-spherical morphologies as observed by CryoTEM and STORM imaging (Figure 2A, B) with a size distribution ranging from 100 to 300 nm in diameter. Nanoparticle tracking analysis (NTA) placed the main peak at 145 nm in diameter for both types of vesicles although a minor population of bigger particles could be detected in all samples (Figure 2C). In addition, the presence of typical protein

markers such as CD81, TSG101 and ALIX indicated that isolated EVs were enriched in exosomes (Figure 2D). Low β -tubulin occurrence in EVs samples confirmed them free from significant cell debris contamination. Furthermore, to investigate possible differences in the internalization of EVs derived from CSC and DCC, the uptake of fluorescently labeled EVs^{CSC} and EVs^{DCC} into parental MDA-MB-231 cells and the lung fibroblast cell line CCD19 was assessed. After 6 h of incubation, a similar spotted fluorescent signal pattern was observed in both, tumor cells and fibroblasts, probably corresponding to clusters of EVs being gathered within endosomal vesicles. STORM imaging showed smaller cytoplasmatic structures matching the size of individual EVs (Figure S3). Overall, no differences were observed in the fluorescent signal intensity or distribution, suggesting that EVs entered into recipient cells irrespectively of the differentiation state of the EVs cell source, CSC or DCC (Figure 2E). Additional analysis performed by flow cytometry revealed no differences in the uptake kinetics profile between EVs^{CSC} and EVs^{DCC} by MDA-MB-231 cells (Figure S3). Interestingly, despite similarities in size, shape, cell internalization capacity and even EV-specific protein signature, differences in the stemness related protein cargo were clearly detected. EVs^{CSC} presented higher levels of typical stemness protein markers such as ALDH1A1, CD44, SOX9, NANOG, OCT4, SOX2 and E-cadherin than EVs^{DCC} (Figure 2F, G).

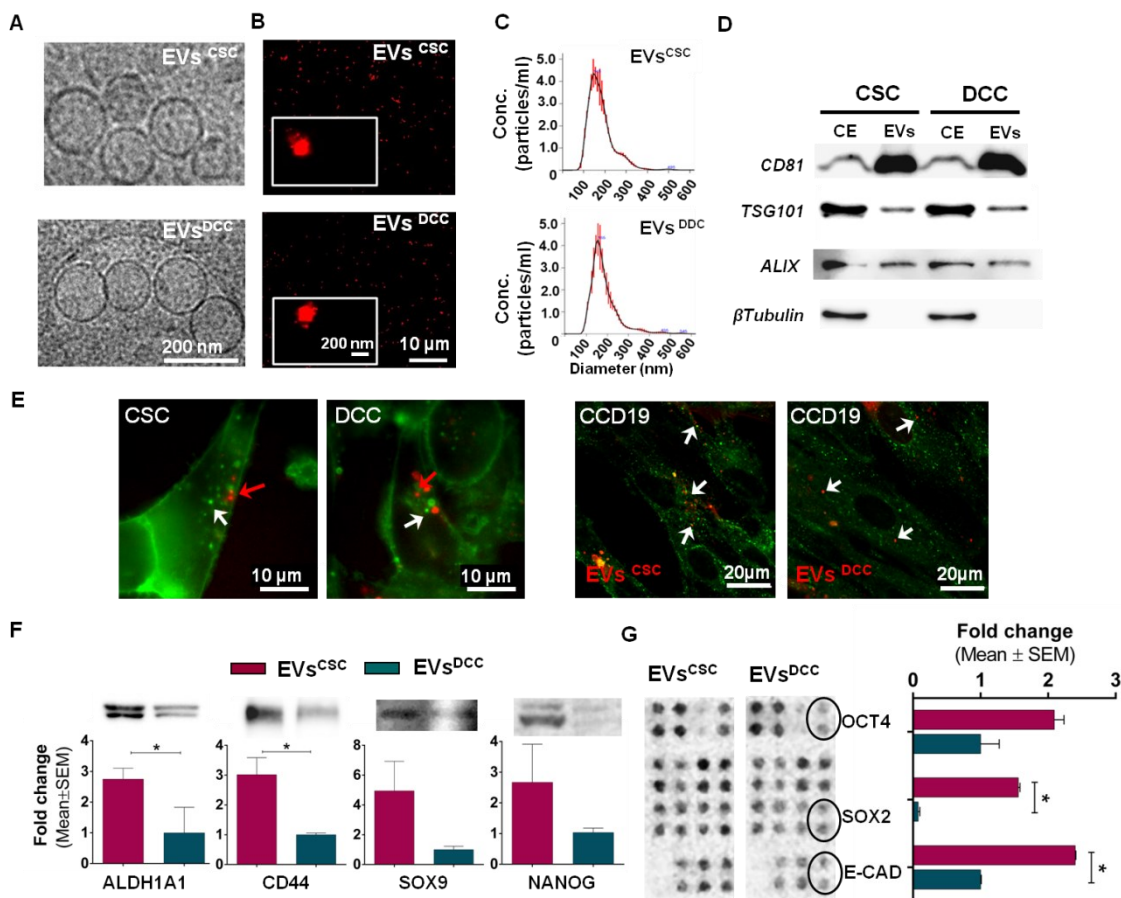


Figure 2. EVs^{CSC} and EVs^{DCC} characterization. (A) CryoTEM imaging of isolated EVs^{CSC} and EVs^{DCC}. (B) Stochastic Optical Resolution Microscopy (STORM) imaging of isolated EVs previously labeled with DiD. (C) Size distribution by nanoparticle tracking analysis (NTA) of EVs^{CSC} and EVs^{DCC}. (D) EVs typical markers, CD81, TSG101 and ALIX and cell lysate control, β -tubulin identified by WB.

20 μg of total protein was loaded per lane and cell extracts (CE) were included as controls. (E) Representative images from fluorescence microscopy of DiD-labeled EVs^{CSC} (red) and DiOC-labeled EVs^{DCC} (green) inside MDA-MB 231 cells (WGA, green), *left panel* and DiD-labeled EVs^{CSC} and EVs^{DCC} (red) in CCD19 cells (Cell Mask, green), *right panel*. Arrows indicate EVs, on the left panel white arrows show DiD-labeled EVs^{CSC} while red arrows indicate DiOC-labeled EVs^{DCC}. On the right panel white arrows show either type of EVs. (F) ALDH1A1, CD44, SOX9 and NANOG protein cargo in EV^{CSC} and EVs^{DCC} examined by Western blot. (G) The relative expression of stem genes was determined using Human Pluripotent Stem Cell Arrays for EV^{CSC} and EVs^{DCC}, revealing differences in OCT4, SOX2 and E-Cadherin protein levels. The complete array is available in (Figure S3F). In F and G quantification of blots are shown as the fold change in the band/dot intensity of EVs^{CSC} / EVs^{DCC}. (* $p < 0.05$).

2.3. EVs^{DCC} direct tumor cells plasticity towards a CSC phenotype *in vitro*.

To explore the influence of EVs^{CSC} and EVs^{DCC} in cell plasticity regulation we overstimulated the parental MDA-MB-231 cell line with either EVs^{CSC} or EVs^{DCC} for 3 days (Figure 3A). Remarkably, gene expression analysis revealed a significant reduction in the stem gene reporters' expression for tumor cells treated with EVs^{CSC}. Specifically, mRNA levels of *ALDH1A1*, *Nanog* and *Oct-4* were reduced >2-fold (Figure 3A). Of note, HCC1806 breast cancer cells treated with EVs^{CSC} also decreased stem gene expression levels (Figure S4B). Interestingly, EVs^{DCC} exerted the opposite effect, increasing the relative expression of *ALDH1A1*, *Nanog* and *Oct-4* >50% (Figure 3A).

Next, the impact of EVs on cell invasiveness was studied using a 2D invasion assay with cells previously incubated with either EVs^{CSC} or EVs^{DCC}. MDA-MB-231 parental cells conditioned with EVs^{CSC} displayed 4- fold lower invasion capacity ($p = 0.013$; Figure 3B). In the case of cells treated with EVs^{DCC}, a noticeable higher number of invasive cells was observed in MDA-MB-231 treated with EVs^{DCC} in comparison to EVs^{CSC} treated samples, but differences in cell invasiveness were not statistically significant when compared to the untreated control (Figure 3B).

On the basis of a recent study, showing that mechanically active heterotypic adhesions between CAFs and cancer cells enable cooperative tumor invasion^[36], we used multifactorial 3D invasion models to study the influence of EVs on cancer invasiveness in a more complex scenario. In this model, spheroids composed by CAFs and cancer cells form invasive cell strands as they degrade an artificial extracellular matrix, consisting in a combination of Matrigel® plus collagen (Figure 3D). The impact of EVs was analyzed by pre-incubation of parental MDA-MB-231 cells, with either EVs^{CSC} or EVs^{DCC} prior to cancer cells mixing with breast CAFs. Confocal imaging of the resulting spheroids showed that EVs^{DCC} pre-treated cancer cells produced significantly higher numbers of invasive strands than the untreated cells ($p = 0.0476$), being the mean score for strand spread = 2.73 ± 0.10 and 2.1 ± 0.15 respectively (Figure 3D). Conversely, EVs^{CSC} treated cells formed less invasive strands when compared to both untreated and EVs^{DCC} conditioned cells ($p = 0.0063$ and $p < 0.0001$, respectively), with the mean strand spread score dropping to 1.16 ± 0.10 (Figure 3D). Altogether our results suggested that EVs secreted by the same cell source at distant differentiation cell states exert an opposed regulation of cancer cell plasticity mechanistically enabling self-control of the process (Figure 3D).

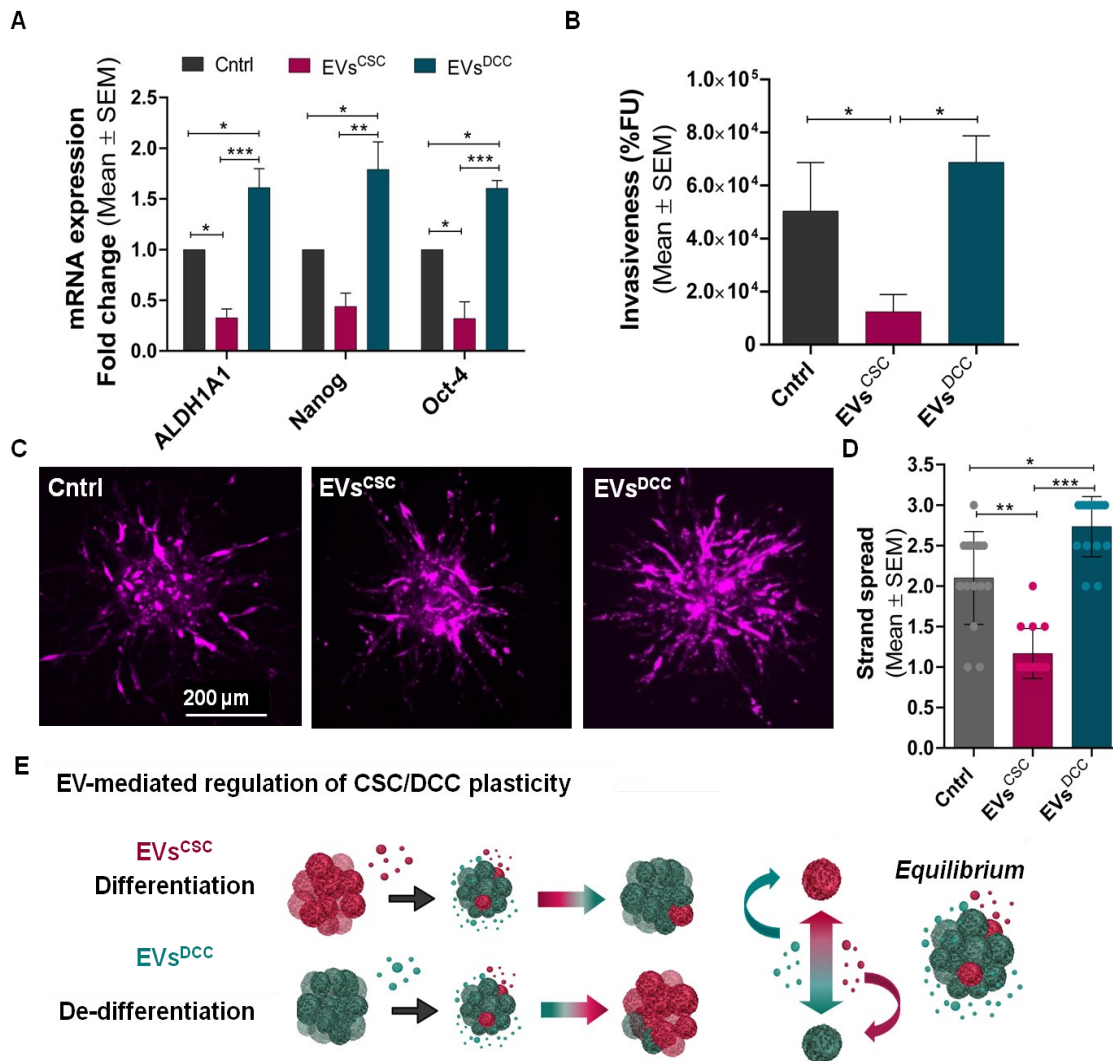


Figure 3. EVs^{CSC} and EVs^{DCC} control tumor cells plasticity *in vitro*. (A) Relative stem gene expression (qPCR) of MDA-MB-231 cells treated with either EVs^{CSC} or EVs^{DCC} for 3 days. (B) 2D laminin invasion assay with MDA-MB-231 cells previously pre-treated with EVs^{CSC} or EVs^{DCC}. (C) Representative images of 3D invasion model of spheroids, embedded in Matrigel® plus collagen, formed by MDA-MB-231 previously reprogrammed with EVs^{CSC} and EVs^{DCC}, in purple cells stained with CellTracker™. (D) Qualitative score of 3D invasion images according to spread of invasive strands. (* $p < 0.05$; ** $p < 0.01$; *** $p < 0.001$) (Further images are available in **Figure S4**). (E) Scheme summarizing EV action in MDA-MB-231 cell line depending on the EV producing cell state.

2.4. EVs^{DCC} impact cancer cells plasticity towards CSC via fibroblasts stimulation of cytokine secretion *in vitro*.

To investigate how cancer cells interact with a fibroblast-rich TME and how the TME feedback modulates cancer cell plasticity, we further explored the EV-mediated communication between fibroblasts, CSC and DCC. To this end, CCD19 fibroblasts were incubated with either EVs^{CSC} or EVs^{DCC}, washed to remove EVs and allowed to secrete bioactive factors. CCD19 conditioned media (CM) were collected for cytokine analysis and further employed to challenge MDA-MB-231 cells. In addition, CCD19 cells were also subjected to gene expression analysis (scheme displayed in **Figure 4A**).

Cytokine arrays were used to assess expression changes in CCD19 CM and showed that EVs^{DCC} triggered the secretion of cytokines IL-8, IL-6 and CXCL1. Specifically, IL-8 and IL-6 levels increased 61.5- and 2.7-fold, respectively, when compared to untreated controls. Treatment of CCD19 cells with EVs^{DCC}, also induced the release of CXCL1, which was undetectable in the control CM. Conversely, incubation of CCD19 cells with EVs^{CSC} caused a decrease in IL-6 secretion compared to untreated cells (**Figure 4B**). These results were further confirmed by, IL-6 and IL-8 gene expression analysis on CCD19 cells exposed to EVs. EVs^{DCC} promoted higher mRNA levels of *IL-6* and *IL-8*, 6.4- and 100-fold, respectively, while EV^{CSC} induced much milder increases (1.4-fold for *IL-6* and 4.3-fold for *IL-8*) (**Figure 4C**).

Furthermore, the response of MDA-MB-231 cells was also analyzed when challenged with either EVs^{CSC}-CM or EVs^{DCC}-CM, obtained from CCD19 fibroblasts (scheme displayed in **Figure 4A**). MDA-MB-231 cells cultured in EVs^{DCC}-CM showed a remarkable boost in the expression of *ALDH1A1*, *Nanog* and *Oct-4*, with 3.6 ± 0.7 ; 5.54 ± 0.4 and 4.6 ± 0.4 times higher expressions than the untreated control, respectively (**Figure 4D**). Of note, EVs^{CSC}-CM did not display any relevant effect on the stemness gene expression profile of MDA-MB-231 cells (**Figure 4D**). Moreover, when supplementing MDA-MB-231 cell cultures with recombinant IL-8 and IL-6, the two main cytokines upregulated by EVs^{DCC} in CCD19 cells, the expression of stemness related genes was also raised. Specifically, IL-6 significantly increased the expression of *ALDH1A1*, *Nanog* and *ABCG1* while IL-8 exerted a substantial upregulating effect on *Nanog* (**Figure 4E**). In agreement with the previous results, MDA-MB-231 ALDH:tdTomato cells cultured with EVs^{DCC}-CM displayed a higher number of tdTomato+ cells, as a result of the activation of the ALDH1A1 promoter (**Figure 4F**).

To further study the EVs^{DCC} - TME mediated drift of MDA-MB-231 cells towards a stem-like state, we investigated resistance to a reference chemotherapeutic drug such as paclitaxel (PTX). Note that drug resistance is a major hallmark for CSCs. We observed that MDA-MB-231 parental cells supplemented with EVs^{DCC}-CM were more resistant to PTX, showing a significant increase in cell viability (14.14%) at 0.04 μ M PTX when compared to control cells and to MDA-MB-231 cells cultured in EVs^{CSC}-CM (14.76%) (**Figure 4G**). Remarkably, MDA-MB-231 cells incubated with EVs^{CSC}-CM did not show any difference in cell viability in comparison to the control (**Figure 4G**).

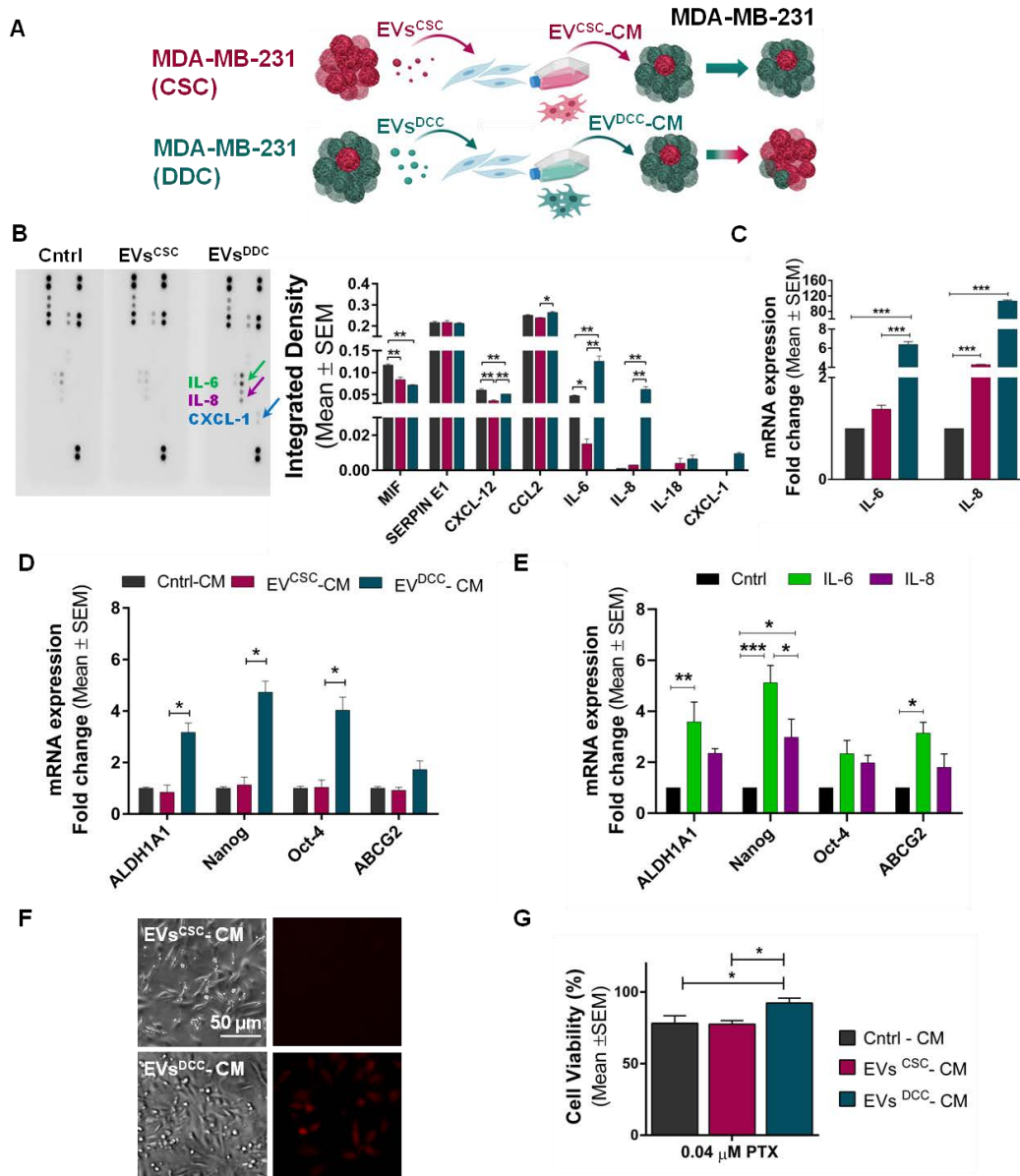


Figure 4. EVs^{DCC} regulate cancer cells plasticity through stromal fibroblasts. (A) Scheme of the experimental approach, CCD19 fibroblasts were educated with either MDA-MB-231 EVs^{CSC} or EVs^{DCC} and CCD19 conditioned media (CM) were collected for analysis and further supplemented to MDA-MB-231 parental cells. (B) Total Human Profiler Cytokine array performed in CCD19 CM and densitometric quantification of the obtained signal. (C) Gene expression of IL-6 and IL-8 in CCD19 cells conditioned with MDA-MB-231 EVs^{CSC} or EVs^{DCC} by qPCR. (D) Effect of CCD19 CM obtained after treatment with MDA-MB-231 EVs^{CSC} or EVs^{DCC} in parental MDA-MB-231 stemness gene expression by qPCR. (E) Gene expression in MDA-MB-231 cells treated with 20 ng/mL of recombinant IL-8 or IL-6 by qPCR. (F) Representative images of tdTomato⁺ cells in MDA-MB-231 ALDH1A1:tdTomato cells after treatment with CCD19-CM. (G) MTT cell viability assay of MDA-MB-231 cells incubation with CCD19 CM and different concentrations of PTX (**p* < 0.05; ***p* < 0.01; ****p* < 0.001).

2.5. EVs^{CSC} induce the activation of lung and breast fibroblasts in 3D invasion models and trigger angiogenesis *in vitro*

Once we established that EVs^{DCC} triggered a cytokine secretory phenotype in human fibroblasts we explored whether other functional capabilities were also affected by cancer cell derived EVs.

To this end, we first performed 3D invasion assays using spheroids formed by either human CAFs of invasive ductal breast carcinoma (CAF_s IDC) or CCD19 lung fibroblasts, previously treated with EVs^{CSC} and EVs^{DCC} for 48 h. The 3D invasive capacity of fibroblasts was monitored by recording the number and length of strands branched from spheroids into the surrounding Matrigel® / collagen matrix. As observed in **Figure 5A, B and C** CAF_s IDC spheroids treated with EVs^{CSC} formed more, 27 ± 1 and longer strands $260.7 \pm 6.7 \mu\text{m}$, than the ones supplemented with the EVs^{DCC} fraction (number of strands 23 ± 1 and length, $238.4 \pm 5.8 \mu\text{m}$). Lung fibroblast spheroids treated with EVs^{CSC} also displayed significantly higher number of strands, 58 ± 3 and longer, $156.8 \pm 3.4 \mu\text{m}$ when compared to untreated spheroids and to EVs^{DCC} treated ones (number, 30 ± 2 ; length, $129.9 \pm 3.9 \mu\text{m}$) (**Figure 5D, E and F**). Supporting these results, α -SMA immunofluorescence of CCD19 lung fibroblasts revealed higher α -SMA levels after treatment with EVs^{CSC} in comparison to EVs^{DCC} treated cells (**Figure S5A**). Note that α -SMA counts as a relevant marker in myofibroblastic fibroblast phenotype activation. Interestingly EVs^{CSC} exhibited a clear enrichment of the α -SMA protein in their payload compared to the EVs^{DCC} (**Figure S5B**).

Additionally, the influence of EVs^{CSC} and EVs^{DCC} on angiogenesis was assessed by challenging endothelial progenitor cells (EPC) with both types of EVs and recording the *in vitro* tube formation capability of endothelial cells. Results showed that EVs^{CSC} significantly enhanced the formation of new tubes in terms of length ($p = 0.0459$), and complexity of the network, as displayed by the relative increase in the number of branching points ($p = 0.0347$) and the number of total loops completed ($p = 0.0176$), in comparison to EPC treated with EVs^{DCC} (**Figure 5G, H, I and J**).

Those results highlighted the unique role of EVs^{CSC} in dictating a functional activation of fibroblasts and in promoting angiogenesis, processes closely related to local tumor spread and to the construction of receptive niches for the cancer cells metastatic growth.

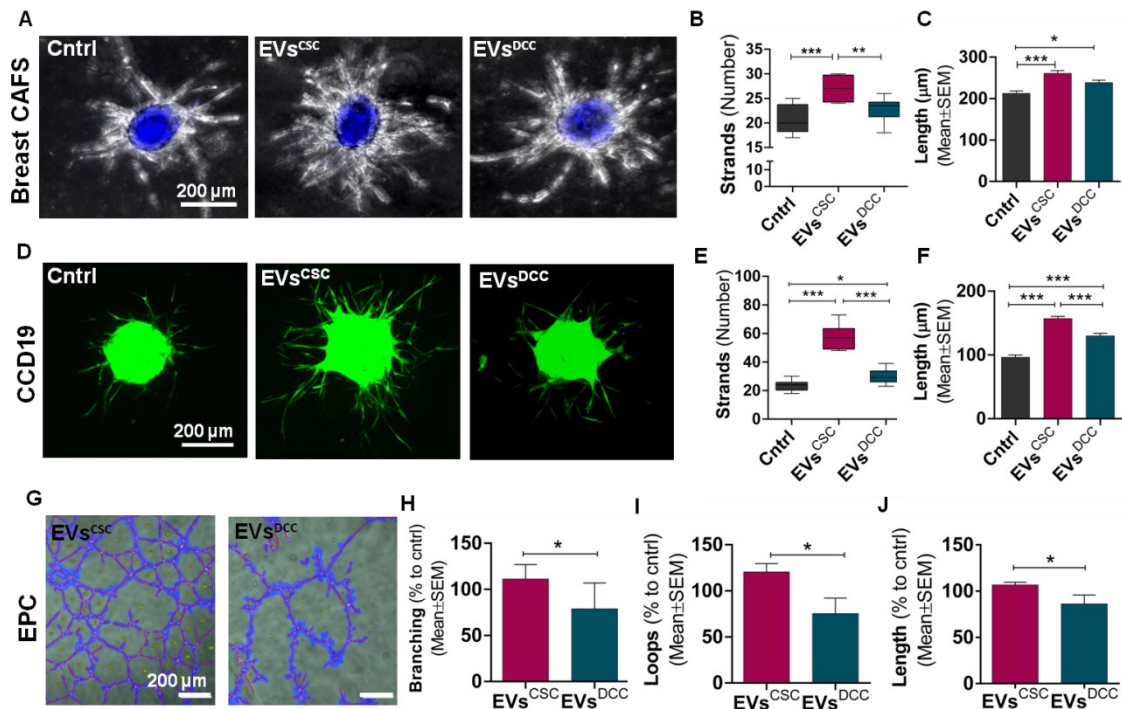


Figure 5. EVs^{CSC} and EVs^{DCC} *in vitro* role in invasion and angiogenesis. (A) Representative Z stack projection images of 3D invasive spheroids of breast CAFs educated with EVs^{CSC} or EVs^{DCC}. Graphs displaying the number (B) and length (C) of invasive strands from breast CAFs spheroids. Box plots corresponding to the representation of the number of strands show the median value as an horizontal line. Bar charts display the mean value as indicated in y axis. (D) Representative Z stack projection images of 3D invasive spheroids lung CCD19 fibroblasts educated with EVs^{CSC} or EVs^{DCC}. Graphs displaying the number (E) and length (F) of invasive strands from CCD19 spheroids represented as described above. (G) Representative images of *in vitro* tube formation assay performed with EPC treated with either EVs^{CSC} or EVs^{DCC}, the number of branching points (H), total loops (I) and tubes length (J) referred to those in non-treated control cells are represented in the graphs. (* $p < 0.05$; ** $p < 0.01$; *** $p < 0.001$).

2.6. EVs^{CSC} boosts lung metastasis *in vivo*

In order to explore whether EVs^{CSC} and EVs^{DCC} also played a different role in the activation of stromal cells *in vivo*, we studied the biodistribution and the lung annidation of EVs derived from MDA-MB-231 cancer cells.

First, the biodistribution profile of DiR labeled EVs was analyzed 24h after intravenous administration. As shown in **Figure 6A** similar EVs *in vivo* distribution patterns were observed for both EVs^{CSC} and EVs^{DCC}, with a major accumulation in lungs, liver and spleen. However, EVs^{DCC} displayed a higher tendency to target the lungs ($p = 0.0153$). Histological analysis confirmed that significantly higher numbers of EVs^{DCC} were able to reach the lung compared to EVs^{CSC}. Specifically, 3.87 ± 1.011 particles per cell were detected in the case of EVs^{DCC} versus the 1.675 ± 0.256 particles per cell observed for EVs^{CSC} (**Figure 6C**). This difference in lung tropism was in accordance with the integrin (ITG) $\alpha 6\beta 1$ expression for both EVs types (**Figure 6B**). The presence of ITG $\alpha 6\beta 1$ heterodimer has been previously

shown important for EVs lung tropism^[37], and although ITG β 1 expression was similar in EVs^{CSC} and EVs^{DCC}, higher amounts of ITG α 6 were clearly displayed on EVs^{DCC}.

After confirming our EVs were able to reach the lungs we proceeded with the functional assessment of pre-metastatic niche conditioning. To this end, two groups of NOD/SCID mice received i.v. administrations of 75 μ g of either EVs^{CSC} or EVs^{DCC} every other day during 5 days. Mice from the control group were administered with equivalent volumes of PBS following the same regimen. Subsequently, luciferase expressing MDA-MB-231 cancer cells were i.v. injected into the tail vein and lung metastasis was evaluated over time (**Figure 6D**). *In vivo* bioluminescence imaging (BLI) showed that mice preconditioned with EVs^{CSC} displayed significantly more BLI signal in the lungs than control mice or those pre-treated with EVs^{DCC} (**Figure 6E**). These results were confirmed by *ex vivo* BLI determination. Accordingly, lungs excised from animals treated with EVs^{CSC} reached $1.50 \pm 0.16 \times 10^8$ ph/s, while lungs from EVs^{DCC} pre-treated mice displayed only $3.62 \pm 1.34 \times 10^7$ ph/s, in the same range than untreated animals, $5.7 \pm 0.51 \times 10^7$ ph/s (**Figure 6F**).

Furthermore, the number of lung metastasis was individually counted in each of the lungs and results revealed a remarkable impact of EVs^{CSC} on the macrometastatic burden (metastatic foci > 2 mm). Precisely, the number of lung macrometastasis per mouse achieved 137 ± 21 for EVs^{CSC} treated group while EVs^{DCC} treated group and untreated animals produced significantly lower numbers 64 ± 24 and 79 ± 19 , respectively. No relevant differences in the micrometastasis count were detected (**Figure 6G**). Additionally, results on lung BLI intensity and macroscopic metastasis counting were confirmed by histopathological evaluation on hematoxylin-eosin sections (**Figure 6H**) and by immunohistochemistry against vimentin (**Figure S6**). Notably, the group injected with EVs^{CSC} presented an almost total coverage of lungs by metastatic lesions.

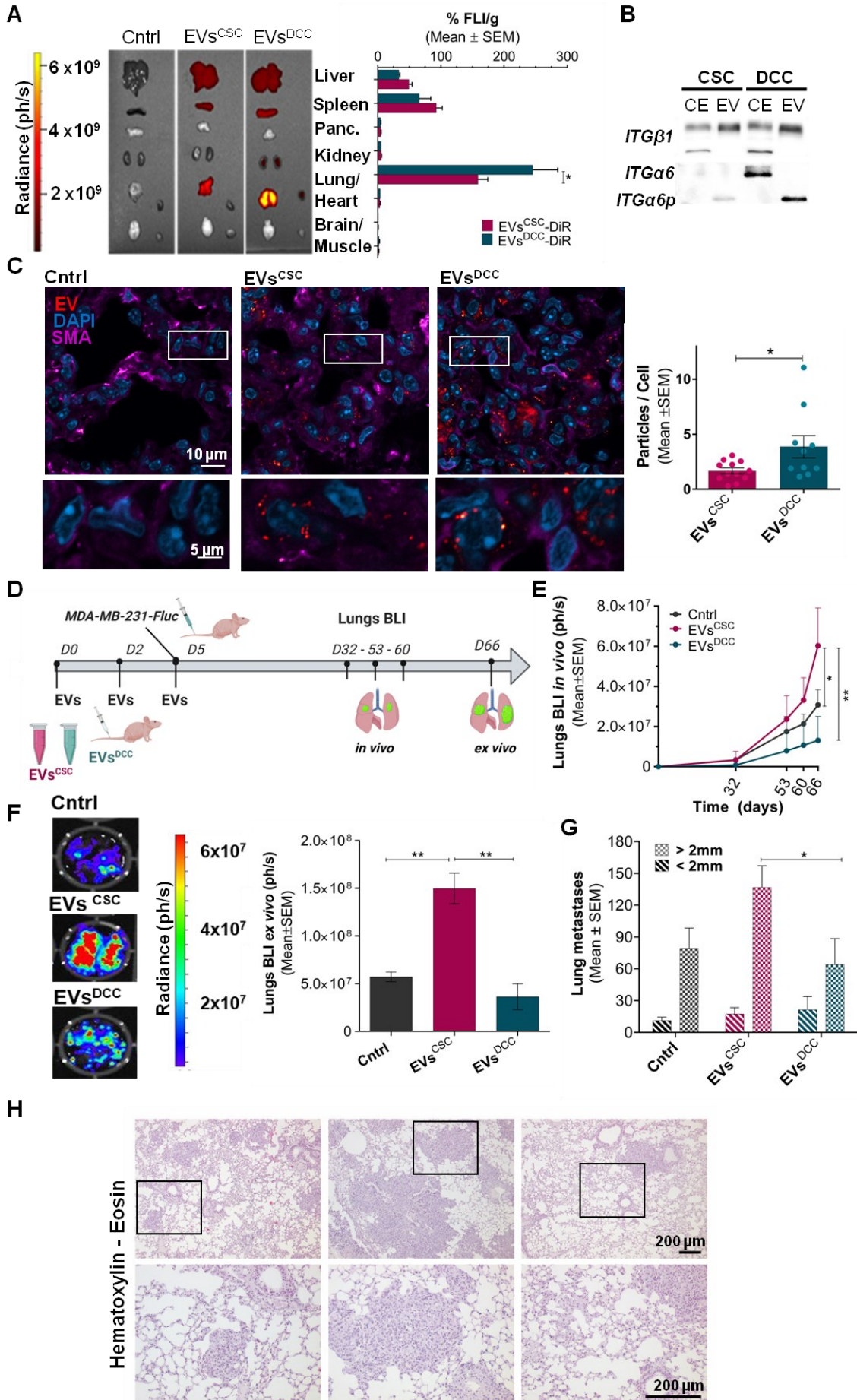


Figure 6. EVs^{CSC} conditioning boosts lung metastasis *in vivo*. (A) FLI analysis of the DiR-labeled EVs after 24h upon tail vein injection of 300 μ g of either EVs^{CSC} or EVs^{DCC}. *Left panels*, representative ex-vivo FLI images of the studied organs for each group. *On the right*, graph displaying ex-vivo FLI values normalized with respect to the untreated controls and represented as % of the total FLI/g. (B) Western blot immunodetection of ITG β 1 and ITG α 6 for cell extracts (CE), EVs^{CSC} and EVs^{DCC}. 20 μ g of total protein was loaded per lane. (C) *On the left*, representative immunofluorescence (IF) images of lung sections 24h after intravenous administration with 300 μ g of DiR-labeled EVs. *On the right*, DiR labeled particle quantification from IF images normalized by cell number for EVs^{CSC} and EVs^{DCC} treated mice (D) Schematic representation of experimental design for the *in vivo* study of MDA-MB-231. EVs^{CSC} and EVs^{DCC} conditioning effect on lung metastasis. (E) Lung metastasis evolution monitored by *in vivo* luciferase-based BLI of mice pre-treated with EVs^{CSC} and EVs^{DCC} and injected with MDA-MB-231 expressing luciferase cells along the time. (F) *On the left*, representative *ex vivo* BLI images of lungs at the end point for each condition. *On the right*, BLI ex-vivo quantification of lungs at the endpoint. (G) Total number of macro and micrometastasis in the lungs manually counted for control, EVs^{CSC} and EVs^{DCC} preconditioned animals. (H) (* $p < 0.05$; ** $p < 0.01$; *** $p < 0.001$).

2.7. EVs^{CSC} increase the number of infiltrating CAFs and triggers angiogenesis in the metastatic niche.

Next, we explored the *in vivo* effect of EVs^{CSC} and EVs^{DCC} on lung stromal cells, namely fibroblasts and vascular endothelial cells. To evaluate the presence of activated fibroblasts derived from EVs education in metastatic lesions, α -SMA immunostaining was performed in lung tissues from animals previously conditioned with either EVs^{CSC} or EVs^{DCC} and subsequently injected with MDA-MB-231 cells (**Figure 7A**). Detail of α -SMA immunostaining of fibroblast like cells can be observed in **Figure 7B**. CAFs in the lungs of animals treated with EVs^{CSC} was evidenced by a higher presence of α -SMA-labeled cells displaying distinctive fibroblast morphologies within the metastatic lesions, mean score for α -SMA staining = 2.125. Control animals and mice conditioned with EVs^{DCC} also showed a clear signal for the α -SMA marker, but with significantly lower scores, (mean scores of 0.85; and 1.38, respectively; **Figure 7C**). Interestingly, the same pattern of CAF infiltration was also observed in orthotopic primary tumors formed by MDA-MB-231 CSCs in comparison to the ones generated from MDA-MB-231 DCCs, being considerably higher the number of α -SMA labeled fibroblasts within MDA-MB-231 CSC tumors (**Figure S5D and E**). α -SMA immunostaining of lung sections from healthy animals administered with EVs^{CSC} was also more intense in comparison to EVs^{DCC}-treated and untreated mice (**Figure S5F**). Additionally, MDA-MB-231 cells pre-treated with EVs^{CSC} or EVs^{DCC} prior to intravenous administration exhibited similar lung metastatic growth irrespective of the EVs type (data not shown). These results suggest that EVs^{CSC} have a stronger effect in lung cells than into the MDA-MB-231 cancer cells injected to generate the experimental metastasis model.

Moreover, α -SMA also tagged vascular endothelial cells, and enabled thus to assess EVs impact on angiogenesis. Blood vessels (b.v) structures, detailed in **Figure 7D**, were counted in random lung sections. Concomitantly with the previous results, lungs from animals injected with EVs^{CSC} exhibited the highest b.v. number (40.61 ± 1.833 b.v./field), compared to EVs^{DCC} injected animals lungs (29.83 ± 2.22 b.v./field) and control animals (33.38 ± 2.02 b.v./field,) (**Figure 7E**).

On the other hand, although no significant *in vivo* effect of EVs^{DCC} was observed in terms of functional TME activation favoring metastatic cells engraftment, we could detect a marked labeling pattern for the NANOG protein (**Figure 7F**). This signal was more intense and widely distributed all over the lung than the one displayed by EVs^{CSC} conditioned mice or untreated animals. NANOG labeling was further validated by the staining of lung metastasis formed after intravenous injections of equivalent amounts of MDA-MB-231 CSC and DCC. As expected, a stronger signal of NANOG protein was observed in MDA-MB-231 CSC derived metastases (**Figure S7**). In agreement with these data, and with previous *in vitro* cell plasticity assays, when MDA-MB-231 cells were pre-incubated *in vitro* with either EVs^{CSC} or EVs^{DCC} prior to intravenous injection in mice, a more marked NANOG labeling was observed in metastases derived from EVs^{DCC} pre-treated MDA-MB-231 cells (**Figure S7**). Altogether these findings suggest a major contribution of EVs^{CSC} to functional activation of the metastatic niche while EVs^{DCC} perform a role as mediators of cancer cell plasticity towards CSC phenotypes.

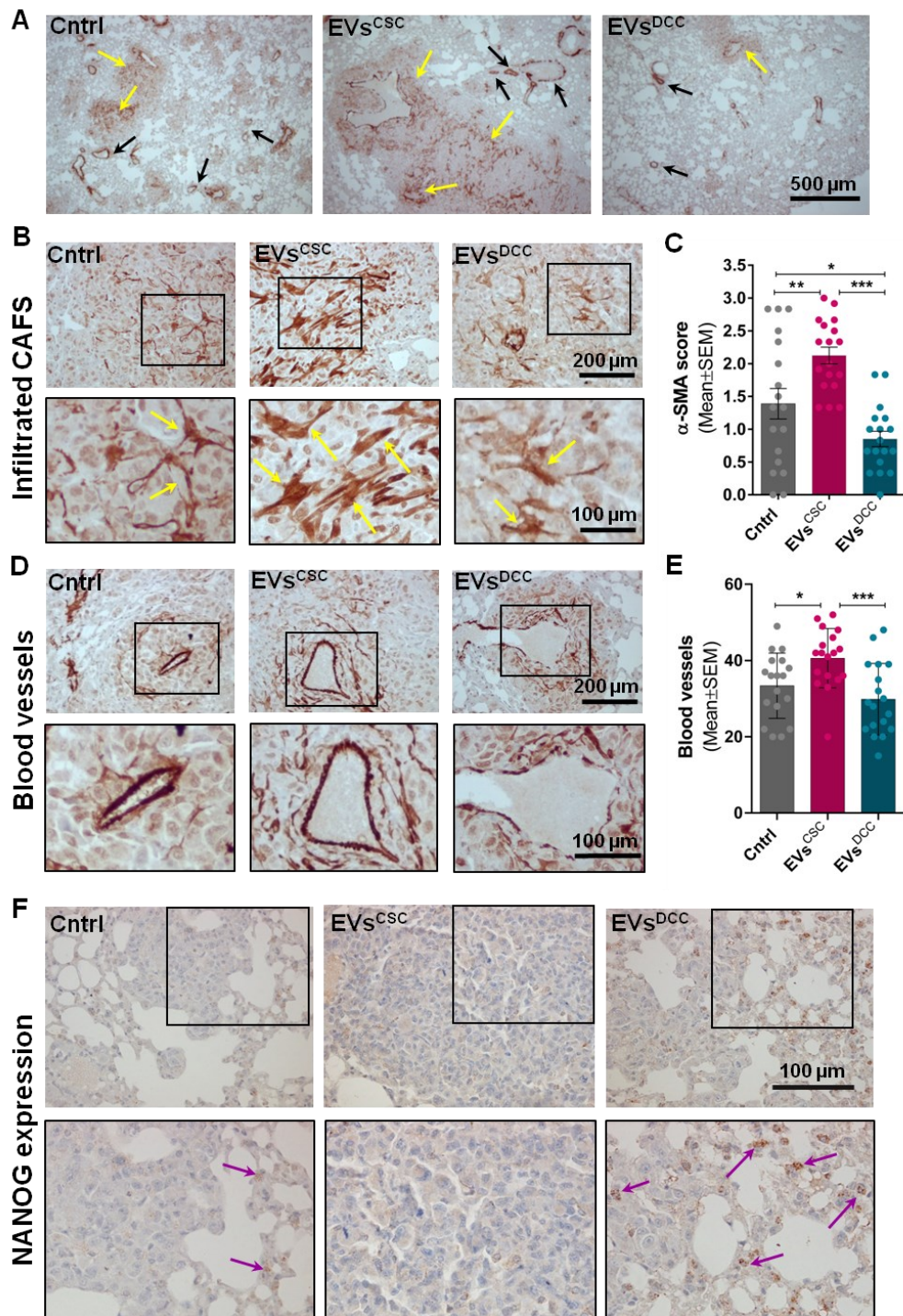


Figure 7. EVs^{CSC} increase the incidence of CAFs and triggers angiogenesis in lungs. (A) Low magnification images showing α -SMA staining on MDA-MB-231 lung metastases of mice educated with EVs^{CSC}, EVs^{DCC} and untreated controls. Yellow arrows indicate fibroblasts infiltrations; black arrows indicate blood vessels. (B) Detail of infiltrating cancer associated fibroblasts (CAFs) in lungs tissue sections from the distinct mouse groups. Yellow arrows indicate cells with fibroblast-like morphology. (C) Semi-quantitative determination of α -SMA immunostaining in lung metastases. Lung sections were analyzed and labeling scores qualitatively attributed, values ranging from 0 (0 % covered area); to 3 (100 % covered area). (D) Detail of blood vessels in lungs tissue sections of indicated mice groups. Insets show blood vessels at higher magnification. (E) Quantification of blood vessels in lung

metastases. (F) NANOG immunostaining in control and EVs pre-treated animals, at low (top row) and high magnifications (bottom row), arrows indicate examples of NANOG positive staining.

3. Discussion

Intercellular communication mediated by EVs has been proved crucial in the regulation of multiple pathological processes during tumor growth, maintenance and spread^[24]. However, in the TNBC context, whose tumors are composed by heterogeneous and highly plastic cell populations, EV-mediated communication studies have been frequently biased due to insufficient information regarding the specific cancer cell state of such EV factories. In the present work we have established an experimental setup consisting in the use of two different breast cancer cell subpopulations isolated from the MDA-MB-231 TNBC cell line that are distant in the stemness axis. This approach allowed us to isolate and characterize two unique EVs subpopulations, EVs^{DCC} isolated from the MDA-MB-231 with a minimal presence of CSCs and EVs^{CSC} produced by MDA-MB-231 highly enriched in CSCs. Our results showed both types of EVs as essentially identical entities regarding their morphometric properties, namely particle size and shape. In addition, no significant differences were observed in terms of cell internalization capacity in either tumor cells or stromal cells, specifically in CCD19 lung fibroblast cells. The same similarity was displayed for EVs protein marker expression but remarkably, EVs contents between EVs^{CSC} and EVs^{DCC} varied to some extent in compliance to the differentiation state of the secreting cells, at least in their protein cargo. Such differences suggested the possibility for EVs^{CSC} and EVs^{DCC} of delivering distinctively signaling cues and therefore displaying specific roles in intercellular communication.

In this regard, one of the processes in which differential EV regulation can play an important role is the control of tumor cells plasticity. According to the results obtained in our MDA-MB-231 model after depletion of either CSCs or DDCs, tumor cells tend to recover a specific cell state equilibrium. This data is in agreement with previous studies hypothesizing cell phenotypic transitions as the mechanism to maintain a balance between CSCs and DCCs among different tumor types^[14,17,38]. Nevertheless, how this cell state transition is driven remain to be fully understood. Due to the absence of external stimuli after cell depletion it was plausible to think of newly synthesized EVs as potential candidates to trigger and regulate this process. Thus, in an attempt to decipher the role of EVs in maintaining cancer cells equilibrium through cell plasticity we challenged the parental MDA-MB-231 cell line with exceeding amounts of either EVs^{DCC} or EVs^{CSC}. Under these circumstances EVs^{DCC} pulsed the conversion of cancer cells towards a stem phenotype, assessed by an increase in the expression of stem markers like *ALDH1A1*, *Nanog* and *Oct-4* coupled to a significantly higher invasive potential in 3D models. Interestingly, EVs^{CSC} exerted the opposite effect after their incubation with the parental cell line. These results indicated that EVs^{CSC}/EVs^{DCC} balance may be responsible for controlling cell state transitions *in vitro*. Remarkably, this opposed regulation fitted into the theoretical model proposed by Olmeda and collaborators^[39], who have recently postulated that cancer cells plasticity towards stem phenotypes is

directed by an unknown activator of tumor cells dedifferentiation. According to their model, this activator would be triggered when the CSC population density in tumors approached 0. Framing our results into this rationale, the activator of cell dedifferentiation would be the EVs^{DCC}. Thus, in an equilibrium state EVs^{DCC} action would be counteracted by EVs^{CSC} but when the ratio of EVs^{DCC}/EVs^{CSC} abnormally raises, due to either the depletion of CSC cell subpopulation or by the artificial addition of EVs^{DCC}, EVs^{CSC} could no longer neutralize EVs^{DCC} action and tumor cells would undergo a dedifferentiation process in order to reestablish the equilibrium. On the contrary, when the ratio EVs^{CSC}/EVs^{DCC} is increased, CSCs would tend to differentiate to recover the equilibrium. Still, the molecular actors' and signaling cascades involved in this process require further study.

Our results demonstrated how EVs^{CSC} and EVs^{DCC} oppositely regulate CSC equilibrium *in vitro*. However, additional signals coming from stromal cells in TME cannot be excluded as they have been widely described to induce cancer cells to acquire stemness traits to maintain CSC niches. In this sense, cross-talk between cancer cells and cells from the TME has been widely investigated. More precisely, multiple studies have shown that tumor derived EVs can activate normal fibroblasts, as main elements of tumor stroma, to acquire malignant CAF phenotypes with significant incidence in disease progression^[29,30]. In turn, the capacity of CAFs to regulate tumor plasticity through secretion of cytokines has also been extensively examined^[40,41]. IL-6 and IL-8 outstands among the numerous cytokines described to have a role in CSCs maintenance due to their implication along diverse types of cancers^[41-43], specially in breast cancer^[38,44,45]. Essentially, these cytokines operate via activation of STAT3 and NF- κ B signaling pathways, inducing the expression of stem genes and the subsequent transition of tumor cells towards CSC-like states. In this regard, Su et al recently described a subpopulation of fibroblasts responsible of providing a constant source of paracrine IL-6 and IL-8 that maintained a feedback loop sustaining CSC stemness via NF- κ B pathway activation in breast cancer^[18]. In this scenario, and considering the previous identification of opposite roles for EVs^{CSC} and EVs^{DCC} in tumor cell plasticity regulation, we wondered whether CAFs may also be involved in CSC/DCC equilibrium regulation by distinct EVs stimulation. Interestingly, lung fibroblasts treated with EVs^{DCC} activated the secretion of pro-stemness cytokines IL-6, IL-8 while EVs^{CSC} did not show this effect or even reduced the secretion of IL-6. Using CM from EVs^{DCC} treated fibroblast on parental MDA-MB-231 cells we confirmed an induction of tumor cell dedifferentiation. This process was monitored by an increase of the stem gene expression profile along with higher levels of tdTomato reporter protein, regulated by the *ALDH1A1* promoter. In addition, an increase of resistance to chemotherapeutic drugs such as PTX was also detected. As expected, CM produced by fibroblast education with EVs^{CSC} displayed no significant differences in comparison to the control. These results seem to agree with cell plasticity regulation discussed above. However, in this case EVs^{DCC} would exert tumor cell dedifferentiation indirectly, by the induction of cytokine secretion from CAFs that in turn would provoke a positive stimuli cascade towards CSCs state transition. Moreover, EVs^{CSC} ability to shift cancer cell

phenotype towards more differentiated states seems to be limited to the direct action of such EVs^{CSC} in the tumor cells irrespective of CAF mediated signaling.

Nevertheless, additional CAFs subsets with distinct functionalities have been identified. Particularly, CAFs capable of generating ECM tracks to guide cancer cells have been shown of importance for ECM remodeling at primary tumor and metastatic sites, largely influencing tumor local invasion^[36,46,47]. When studying the effect of distinct EVs subsets in other relevant CAFs phenotypes, we observed that breast and lung fibroblasts cultured with EVs^{CSC} displayed enhanced remodeling activity of the surrounding 3D matrix rendering more and longer invasive strands than those educated with EVs^{DCC}.

Our results concur with recent studies highlighting CAFs heterogeneity among different tumor types^[18,32,33]. However, up to date the mechanisms driving specific activation of certain CAF phenotypes have been not clarified. Here, we present evidence that CAF heterogeneous activation may be governed by distinct subpopulations of tumor EVs.

It has been previously reported that tumor EVs can prepare a favorable microenvironment for tumor metastasis by inducing changes in pre-metastatic niches resident cells that would favor metastatic cells engraftment^[28,29]. Our data showed a marked lung tropism for both types of EVs upon intravenous administration. This biodistribution profile was in accordance with previous reports on EVs derived from TNBC cells which showed a tendency to accumulate into their primary metastatic sites directed by the integrin expression onto the EVs surface^[30,37]. However, differences were observed in ITG α 6 expression, slightly influencing the amounts of tumor EVs in the lung. EVs^{DCC} targeted the mice lung more efficiently than EVs^{CSC}. This result suggests that the differential capacity of EV subtypes to reach the metastatic site might have a direct impact in the metastatic niche pre-conditioning

In addition, our experiments revealed that EVs^{CSC} conditioning increased the extent of the macrometastasis burden in mice lungs, indicating that EVs^{CSC} strongly promoted the dissemination of malignant cells into the lungs by creating a tumor cell growth supportive niche. Consequently, EVs^{CSC} treated animals showed higher presence of CAFs and more blood vessels in lungs than EVs^{DCC} treated group. These data supported previous *in vitro* results showing EVs^{CSC} as potent activators of breast and lung CAFs 3D invasion. Moreover, higher levels of α -SMA, a marker of myofibroblastic activation, were detected in fibroblasts *in vitro* but also in lungs from healthy animals after EVs^{CSC} administration. Reinforcing EVs^{CSC} mediated activation of invasive CAFs, a higher presence of α -SMA was also observed in primary tumors exclusively generated from MDA-MB-231 CSC-like cells. Increased blood vessel number was also in agreement with higher angiogenic potential of EVs^{CSC} *in vitro*. Of note, no specific studies using CSC derived EVs have been developed in order to unveil the contribution of each tumor EVs subset in pre-metastatic conditioning. However, some reports using EVs isolated from particularly malignant cells, e.g. drug resistant tumor cells, often associated with CSCs-like phenotypes have shown higher metastatic potential than the ones from the parental cell lines^[48]. Altogether these results suggest that EVs secreted by CSC-like cells trigger niche conditioning at the metastatic sites.

Conversely, EVs^{DCC} produced a negligible response in terms of metastatic burden and stimulation of resident fibroblast towards α -SMA positive CAFs, comparable to the values displayed in control samples. Nevertheless, EVs^{DCC} seemed to activate the expression of the stem marker NANOG in pretreated animals as well as in metastases derived from pre-treated MDA-MB-231 cells. These results were in agreement with previous *in vitro* promotion of cancer stem cell phenotypes via the direct action of EVs^{DCC} in tumor cells along with the indirect signaling through IL-6 and IL-8 secretory fibroblasts. This study reveals that while targeting CSC and CSC derived EVs could result in a therapeutic benefit against metastatic dissemination, this approach should consider the action of residual DCC secreted EVs that could rapidly trigger cancer cells de-differentiation towards a stem phenotype restoring tumor growth and aggressiveness. In this sense, a deeper knowledge of tumor cell plasticity regulation and their interactions with TME will help to develop more efficient therapeutic strategies addressing point by point all mechanisms supporting tumor survival.

4. Conclusion

We have identified two distinct subsets of EVs, namely EVs^{CSC} and EVs^{DCC}, according to the stem cell state from their cell source. These EVs exerted opposed signaling stimuli in direct tumor cell plasticity regulation, acting as repressors and activators of stem cell states, respectively. Moreover, they displayed markedly different activities in heterotypic cell communication. EVs^{DCC} could indirectly influence tumor cell dedifferentiation state by the stimulation of a cytokine secretory CAFs phenotype while EVs^{CSC} triggered the activation of a distinct and specific myofibroblastic CAF subpopulation, facilitating local invasion and growth. Accordingly, EVs^{CSC} also displayed proangiogenic potential and postulated as principal activators of niche modulation enabling metastatic growth.

5. Experimental Section/Methods

Cell lines and culture conditions:

Parental cell lines: Human breast MDA-MB-231 cell line, human lung CCD19 were obtained from American Type Culture Collection (ATCC HTB-26TM, CCL-210TM, respectively). Human Cancer Associated Fibroblasts from Invasive Ductal Breast Carcinoma (CAF_s IDC) were isolated from patient tissue samples and immortalized by pBABE-Hygro-HTERT retroviral transfection (Courtesy of Erik Sahai, Francis Crick Institute, UK). MDA-MB-231 was routinely maintained in RPMI 1640 Medium supplemented with 10% fetal bovine serum (FBS), 2 mM L-Glutamine, 1x Non-essential aminoacids, 1x antimycotic-antibiotic solution. CDD19 cells were cultured in DMEM/High Glucose supplemented with 10% FBS, 1x antimycotic-antibiotic solution and 1x Insulin-Transferrin-Selenium (all from Gibco). Outgrowth Endothelial Progenitor Cells (EPCs) were isolated from stroke patients as previously described^[49] and cultured in fibronectin-coated flasks with endothelial growth medium (EGM2, Lonza) supplemented with the factors included in the kit and 10% FBS.

Genetically-modified cell lines: MDA-MB-231 ALDH:tdTomato cell line was generated as *in vitro* CSC-like models from breast MDA-MB-231 cells as previously reported by our group. ^[15,35] MDA-

MDA-MB-231 ALDH:tdTomato cell line stably exhibiting low content of CSC (1-2%), (DCC), was maintained as described for the parental cell line with the addition of blasticidin at 10 µg/mL (Gibco). MDA-MB-231 ALDH:tdTomato displaying a high number (99%) of CSC-like cells (CSC) were cultured in serum-free RPMI 1640 Medium supplemented with 6% glucose, 2 mM L-Glutamine, 1X AA, 4 µg/mL heparin (Sigma-Aldrich), 2 mg/mL BSA (Sigma-Aldrich), 0.02 µg/mL EGF (Sigma-Aldrich), 0.01 µg/mL FGFb (Thermo Fisher Scientific), 10 µg/mL putrescin (Sigma-Aldrich), 0.1 mg/mL apo-transferrin (Sigma-Aldrich), 25 µg/mL insulin (Sigma-Aldrich), 20 µM progesterone (Sigma-Aldrich) to prevent cell differentiation. These cell lines were employed for EVs^{CSC} and EVs^{DCC} production along the study.

MDA-MB-231.Fluc2-C19 cells were routinely cultured as described for the parental cell line with the addition of neomycin at 500 µg/mL.

All cell cultures were propagated at 37°C and 5% CO₂ in a humidified incubator.

CSC isolation:

CSC subpopulations from MDA-MB-231 ALDH:tdTomato were isolated according to their tdTomato expression in a FACS Aria cell sorter (BD Biosciences). Two consecutive sorting rounds were employed for CSCs cell enrichment. tdTomato + cells from the first sorting round were collected and expanded in complete RPMI 1640 medium for re-sorting. Re-sorted tdTomato + cells displayed high extents of CSC-like cells (99%) and were further maintained as described above. tdTomato – sorted cells were also collected and cultured in regular maintenance medium to be used in cell state equilibrium experiments. Representative scheme of cells sorting procedure is detailed in **Figure S2C**.

Purification of EVs^{CSC} and EVs^{DCC}:

Supernatants (SN) coming from MDA-MB-231 CSC and DCC cell cultures, after 48h incubation in EV-depleted medium, were centrifuged at 300 g at 4°C for 10 min in order to remove dead cells. Additional centrifugation steps at increasing centrifugation speed 2,000 g, 10 min 4°C and 10,000 g 20 min 4°C were carried out to eliminate potential sub-cellular debris. Clarified SNs were concentrated through centrifugation at 5,000 g, 15 min, 4°C, using 300,000 KDa VIVAspin devices (Sartorius). The concentration factor varied from 50X to 100X depending on the sample. EVs were then precipitated from concentrated SN by the addition of “Total Exosome Isolation Reagent” (Invitrogen) according to manufacturer’s instructions. Samples were centrifuged at 16,000 g for 1 h at 4°C and pellets containing the EVs resuspended in PBS. Purified EVs were stored at 4°C. Note that prior to every EVs purification batch a qPCR control was performed to assess the maintenance of the stemness expression profile of *ALDH1A1*, *Nanog* and *Oct-4* in CSC and DCC cultured cells.

EVs characterization:

CryoTEM morphometric assessment and particle size distribution and concentration were further studied by Nanoparticle Tracking Analysis (NTA) performed as described by Seras-Franzoso and co-workers^[50].

RNA Extraction and Quantitative Real Time-qPCR (qPCR) :

Total RNA was extracted from 300,000 cells using the RNeasy Micro Kit (Qiagen) and the RNA obtained was reverse transcribed using a High Capacity cDNA Reverse Transcription Kit (Thermo Fisher Scientific) according to the manufacturer's instructions. The cDNA reverse transcription product was amplified with specific primers (**Table S1**) by qPCR using a SYBR Green method (Thermo Fisher Scientific). The reaction was performed in triplicate on a 7500 Real time PCR system (Applied Biosystems). Relative normalized quantities (NRQ) of mRNA expression were calculated using the comparative Ct method ($2^{-\Delta\Delta C_t}$) through Qbase™ software with two reference genes (hGAPDH and hActin) used as endogenous controls.

Cell state equilibrium restoration assay: 500.000 MDA-MB-231 tdTomato+ (CSC) and tdTomato-sorted cells (DCC) were seeded in adherent plates of 10 cm diameter. Total RNA was extracted and used for subsequent qPCR analysis at different passages: after sorting (AS), passage 1 (P1) and passage 5 (P5), to monitor changes in the stem gene expression profile of each cancer cells subpopulation.

MDA-MB-231 CSC and DCC subpopulations stem gene profile validation: Re-sorted tdTomato + CSC and DCC were maintained in cell culture as described above. Total RNA was extracted to further assess the expression of stem reporters in each cell subpopulation by qPCR analysis prior to every purification batch of EVs^{CSC} and EVs^{DCC}.

Effect of EVs^{CSC} and EVs^{DCC} on parental MDA-MB-231 stem gene expression profile: 50,000 MDA-MB-231 parental cells were seeded in 2 mL of complete RPMI medium in 6-well plates. Then, 25 µg/mL of either EVs^{CSC} or EVs^{DCC} were added to each well for 3 consecutive days (150 µg total EVs/well). After 72h in culture, total RNA was extracted and used for subsequent qPCR analysis.

Effect of EVs^{CSC} and EVs^{DCC} on CCD19 IL-6 and IL-8 expression: 50,000 CCD19 cells were seeded in 2 mL of complete DMEM medium in 6-well plates. Then, 25 µg/ml of either EVs^{CSC} or EVs^{DCC}, were added to each well for 3 consecutive days (150 µg total EVs/well). After 72h in culture, total RNA was extracted and used for subsequent qPCR analysis.

Effect of fibroblasts CM on MDA-MB-231 parental cells stem gene expression profile: 2 mL of fibroblasts EVs^{CSC}-CM and EVs^{DCC}-CM were collected (as described above) and added to 6-well plates seeded with 50,000 MDA-MB-231 parental cells. After 48h in culture, 100,000 MDA-MB-231 cells were collected and total RNA was extracted for qPCR analysis. The rest of the collected cells were used for MTT assays.

Effect of IL-6 and IL-8 on stem gene expression profile in parental MDA-MB-231: 20 ng/mL of either recombinant soluble IL-8 or IL-6 (R&D Systems) were added to 50,000 MDA-MB-231 parental cells seeded in 6-well plates. After 48h in culture, total RNA was extracted and qPCR analysis was performed.

Protein extraction and Western blotting:

Cell pellets and EVs samples were lysed with Cell Lytic M reagent (Sigma-Aldrich) containing a protease inhibitor cocktail (Sigma-Aldrich). Proteins in crude lysates were quantified using the bicinchoninic acid assay (BCA) Protein Assay (Pierce Biotechnology). A total of 20 μg of whole-cell lysates were separated by SDS-PAGE and transferred onto PVDF membranes (Merck Millipore). Membranes were blocked in 5% non-fat dry milk (w/v) in TBS buffer, 1 h at RT. Targeted proteins were probed using primary antibodies (**Table S2**), O.N at 4°C. Horseradish peroxidase (HRP)-conjugated secondary antibodies, anti-mouse (P0447, Dako) or anti-rabbit (P0217, Dako), were then added as requested and incubated for 1 h at room temperature. Extensive washing in TBS-Tween (0.05% v/v) was performed between blocking and antibodies incubation steps. Membranes were developed using Immobilon® HRP substrate (Merck Millipore) in a LI-COR Odyssey Fc imaging system. Band intensity on the blots was quantified using the ImageJ NIH software.

EV fluorescent labeling:

DiOC/DiD or DiR (Invitrogen™) were supplemented to EVs^{CSC} and EVs^{DCC} to a concentration of 250 $\mu\text{g}/\text{mL}$ and 500 $\mu\text{g}/\text{mL}$ respectively, for 30 min at 37°C. Samples were then dialyzed (Slide-A-Lyzer™ MINI Dialysis Device, 3.5K MWCO, 0.1 mL, Thermo Scientific) against PBS, O.N. at 4°C.

Confocal microscopy:

MDA-MB-231 cells and CCD19 cells were seeded in an 8 chambered coverglass (Lab-Tek®II, Eppendorf) and incubated 24 h at 37°C and 5% CO₂. Then, 2.5 $\mu\text{g}/\text{mL}$ DiD-labeled EVs^{CSC} and DiOC-labeled EVs^{DCC} were added to MDA-MB-231 CSC or DCC cells and incubated for 12 h while DiD-labeled EVs^{CSC} or EVs^{DCC} were added to CCD19 cells and also incubated for 12 h. Cell medium was removed and cell membranes fluorescently tagged. Samples were fixed in 4% paraformaldehyde (PFA) prior to visualization. Note that, MDA-MB-231 cell membranes were counterstained with 5 $\mu\text{g}/\text{mL}$ WGA-AF488 (Thermo Fischer Scientific), 10 min at 37°C and visualized using Nikon Eclipse Ti microscope (Nikon) with 100X/1.49 NA oil immersion objective. While CCD19 cell membranes were stained with 5 $\mu\text{g}/\text{mL}$ Cell Mask™ (Invitrogen), 10 min at 37°C and image acquisition was carried out in a spectral confocal microscope FV1000 (Olympus) with a PLAPON 40XO objective. Further image processing was performed using ImageJ NIH software in both cases.

2D invasion assay:

50,000 parental MDA-MB-231, MDA-MB-231 CSC and MDA-MB-231 DCC cells were seeded in 6 well plates. Then, 25 $\mu\text{g}/\text{ml}$ of either EVs^{CSC} or EVs^{DCC} were added to parental MDA-MB-231 for 3 consecutive days (150 μg total EVs/well). On the third day, the invasiveness of EVs educated MDA-MB-231 parental cells and MDA-MB-231 CSC and DCC cell subpopulations was assessed using the CytoSelect™ Laminin Cell Invasion Assay Kit (Cell Biolabs). Briefly, inserts were placed in a 24 well plate and cell suspensions containing 1×10^6 cells/mL of MDA-MB-231 CSC and DCC cells and parental MDA-MB-231 cells previously treated with EVs^{CSC} or EVs^{DCC}, added to the insert. After 48 h

incubation, invasive cells were dissociated from the lower side of the membranes, lysed, and quantified using CyQuant® GR Fluorescent Dye (Cell Biolabs).

3D invasion assay:

200,000 parental MDA-MB-231 were seeded in P10 plates and 25 µg/mL of either EVs^{CSC} or EVs^{DCC} were added to growing cells for 3 consecutive days. In parallel, 200,000 CAFs IDC were seeded in a P10 plate. Then, MDA-MB-231 and CAFs IDC cells were trypsinized to single-cell suspension, centrifuge and resuspended with 3 mL of culture medium containing 2 µL of CellTracker™ staining solution. After 30 min of incubation, cells were washed, counted and resuspended to reach a final concentration of 75×10^5 cells/mL. Hence, a cell suspension containing the two cell types at a 1:1 ratio and 0.25% methylcellulose solution in DMEM was prepared and 3D invasion assay was performed as described by Labernadie et al.^[36,51]. Briefly, 20 µL droplets of mixed cells were plated onto the lid of a 10 cm culture dish and allowed to form spheroids in a 37°C, 5% CO₂ incubator O.N. The spheroids were then embedded in a Rat tail collagen type I /Matrigel gel mix at in 24-well glass-bottomed cell culture plates (MatTek) and incubated at 37°C and 5% CO₂ until invasive strands were formed. Sixty hours later, the spheroids were imaged with a spinning disk confocal microscope at a magnification of $\times 10$, $\times 20$ and $\times 40$. Z stack images spanning 100–150 µm were collected and image stacks were analyzed with ImageJ software. Same procedure was used to assess fibroblasts 3D invasive abilities, starting with an initial concentration of 1×10^5 cells/mL of either CCD19 human fibroblasts or CAFs IDC.

Drug resistance assay:

Resistance to Paclitaxel (PTX) of MDA-MB-231 cells previously treated with either EVs^{CSC}-CM and EVs^{DCC}-CM was assessed by MTT assay. 5,000 cells/well were seeded in 96-well plate and incubated for 24h at 37°C, 5% CO₂. 0.04µM of PTX (Teva) was then added to growing cells. Complete medium was used as negative control and 10% DMSO as positive control of cytotoxicity. After 48h of incubation, 0.5 mg/mL 3-(4,5-dimethylthiazol-2-yl)-2,5-diphenyl tetrazolium bromide (MTT) was added to each well. Plates were incubated for an additional 4 h at 37°C and 180 µL of DMSO (Sigma) was added to each well. The absorbance at 590 nm of each well was read on a microplate reader ELx800 (BioTek). Cell viability was calculated using a minimum of 3 biological replicates with 6 technical replicates for each assay.

Cytokine and stem protein arrays:

Cytokine antibody-pair-based assays were performed using human cytokine array kit (R&D Systems, ARY005B) according to the manufacturer's protocol. In brief, 100,000 CCD19 fibroblasts seeded in 6-well plates were cultured alone or treated with either EVs^{CSC} or EVs^{DCC}, 25 µg/mL per day during 3 days. Culture supernatants were next collected (CM) and centrifuged at 13,000 rpm during 10 min to remove cell debris. Array membranes, previously spotted with capture antibodies by the manufacturer, were incubated with 0.5 mL of CM O.N. at 4 °C. Membranes were then washed three times with 50 mL

of washing buffer at RT, incubated with a streptavidin–horseradish peroxidase-coupled antibody (1:2000) for 30 min at RT and revealed using Chemi-Reagent Mix. The immunoblot images were captured and visualized using the LI-COR Odyssey Fc imaging system and dot intensity was measured using ImageJ NIH software. Human pluripotent stem cell antibody array (R&D Systems, ARY010) was performed in accordance with the manufacturer's instructions. Briefly, approximately 500 µg of total-EVs^{CSC} and EVs^{DCC} lysates were incubated with array membranes O.N. at 4 °C. Membranes were then washed and incubated with a streptavidin–horseradish peroxidase-coupled antibody (1:2000) for 30 min at RT and revealed using Chemi-Reagent Mix. The immunoblot images were captured, visualized and processed as described for *Cytokine array* assay.

Tube formation assay:

Capacity to promote vessel-like tube formation was assessed as described elsewhere^[49]. Briefly, human EPCs were resuspended in basal medium without growth factors (EBM2, Lonza) and seeded at 20,000 cells per well in growth factor reduced Matrigel (Corning) following manufacturer's protocol. Note that Matrigel was thawed at 4°C, dispensed in the microslides (Ibidi) and allowed to polymerize at 37°C till producing a uniform semisolid ECM cell-support prior. Immediately after cell seeding cells were treated with either 25µg/ml EVs^{CSC} or EVs^{DCC} suspensions or basal media (as control condition). After O.N. incubation at 37°C and 5% CO₂ images were taken at 4x and analyzed blindly using Wintube online tool. Tube length, branching points and total loops were quantified as relevant features for tube formation capacity. Tubulogenesis parameters of the control condition (basal media) were used as a reference value for the EVs treatments.

In vivo experimentation:

Female NOD.CB17-Prkdcscid/J mice (Charles River, MA, USA) were kept in pathogen-free conditions and used at six weeks of age. Animal care was handled in accordance with the Guide for the Care and Use of Laboratory Animals of the Vall Hebron University Hospital Animal Facility, and the experimental procedures were approved by the Animal Experimentation Ethical Committee at the institution (approval number CEA-OH/9467/2).

Biodistribution assay:

EVs^{CSC} and EVs^{DCC} biodistribution studies were performed by intravenously administration of 300 µg DiR-labeled EVs^{CSC} or EVs^{DCC} through the mouse tail vein. After 24 h, animals were euthanized and *ex vivo* DiR-EVs localization was assessed using in an IVIS® Spectrum equipment for image acquisition and Living Image Software™ to further quantify the fluorescent signal (FLI). FLI was normalized to the weight of the wet tissue and represented as the percentage of total FLI per animal. Lung tissues were collected, embedded in OCT matrix following standard procedures and stored at -80°C till further analysis; see *high resolution confocal microscopy* and *α-SMA immunofluorescent detection in lung sections* (supplementary material).

High Resolution Confocal microscopy: OCT blocks from the biodistribution assay were processed into 5 μm thick sections using a cryostat Leica CM3050. Tissue slices were mounted on microscopy glass slides and fixed in ice-cold methanol, 30 min at -20°C . After fixation samples were immunolabeled against α -SMA and the nuclei were fluorescently dyed with DAPI, as detailed in the supplementary information. Images were acquired in a confocal spectral LSM980 microscope (Zeiss) operating at high resolution, $XY = 120\text{ nm}$ and $Z = 350\text{ nm}$, using the Airy Scan mode and a plan apochromat 63X/1.40 oil objective. 12 random sections with a fluorescence intensity dynamic range of 16 bytes were further quantified using Image J NIH software. Briefly, DiR fluorescent signal was transformed to a binary image in order to identify and count the number of particles per field. DiR labeled particle number was normalized in front of the number of cell nuclei per section.

Lung metastasis mice models:

In order to examine the roles of EVs^{CSC} and EVs^{DCC} in lung metastasis models, 3 total doses of 75 μg of EVs^{CSC} or EVs^{DCC} were intravenously injected into female nude mice through the tail vein every other day. On the 5th day, 1×10^6 firefly luciferase-expressing MDA-MB-231.Fluc2-C19 cells were intravenously injected through the tail vein. After 2 months, lung metastasis were measured and quantified by ex vivo bioluminescent imaging using IVIS Spectrum (PerkinElmer) and lung tissues were recovered for manual macrometastasis and micrometastasis counting and further processed for hematoxylin-eosin staining analysis and evaluation by a trained histopathologist.

Immunohistochemistry:

The presence of α -SMA and NANOG proteins were assessed in paraffin-embedded formalin fixed sections. Slides were incubated with 10% normal goat serum (NGS) in antibody diluent (1% BSA (w/v) in 100 mM Tris buffer) and then primary antibodies were added, O.N at 4°C (see Table S2). Next horseradish peroxidase-conjugated secondary antibody, anti-Mouse or anti-Rabbit, as required, was added to the samples (Dako, EnVision+ System-HRP Labeled Polymer). Finally, the sections were developed with diaminobenzidine (DAB) colorimetric reagent solution (Dako) and counterstained with Harris hematoxylin (Sigma-Aldrich). Extensive washing in PBS/Tween 20, 1% (v/v) was performed before and after antibody incubations steps. Evaluation of α -SMA labeling was used to assess the number of infiltrated CAFs and blood vessels in lung metastatic lesions. 18 random sections in a 4x magnification per mice group were analyzed for each parameter. For CAFs infiltration assessment, total lungs sections area covered by α -SMA positive fibroblasts like cells was qualitatively scored and represented, staining score values ranging from 0 (0 % positive area) to 3 (100 % positive area). Each evaluation was made blindly by 3 independent observers. The number of blood vessels was quantitatively assessed by manually counting the number of α -SMA positive blood vessels in 18 random lung sections per mice group. Subsequent mean score for both parameters was then calculated for each group. NANOG labeling was qualitatively assessed in 3 random sections at 4X, 10X and 20X magnifications. Representative images were displayed.

Statistical analysis:

Bar graphs display mean value \pm standard error of the mean (SEM). Statistical analysis consisted in normality data distribution assessment by Kolmogorov-Smirnov test. If data fitted into a normal distribution, unpaired Student's t-test, for single comparison of means, or one-way ANOVA for multiple comparisons was then applied. Otherwise, non-parametric Mann-Whitney test or Tukey test were employed for single and multiple mean comparisons respectively.

Data represented as Fold Change (FC) were normalized following the $X = \text{Log}(\text{FC})$ function. Columns statistics were then used to assess the mean difference in comparison to a theoretical Log (FC) value equal to 0. The significance threshold was established at $p < 0.05$, and significance levels were schematically assigned $*(0.01 \leq p < 0.05)$, $**(0.001 \leq p < 0.01)$, $*** (0.0001 \leq p)$. All the analyses and graphs were performed using GraphPad Prism 6 software (GraphPad, San Diego).

Supporting Information

Supporting Information is available from the Wiley Online Library or from the author.

Acknowledgements

This study was supported by ISCIII PI20/01474 (co-founded by Fondo Europeo de Desarrollo Regional (FEDER)) granted to S.S.Jr and P.G., the 2017-SGR-638 and -1427 from the Generalitat de Catalunya to S.S.Jr and A.R, respectively, and PENTRI-2 from CIBER-BBN granted to IA. A.L is recipient of Obra Social “La Caixa” Junior Leader Postdoctoral Fellowship, (LCF/BQ/PR18/11640001). J.S-F was awarded with an Asociación Española Contra el Cancer (AECC), (AIO14142112SERA) post-doctoral fellowship.

We are indebted to Unitat of Alta Tecnologia (UAT) at the Vall d’Hebron Research Institute for their assistance in flow cytometry and confocal microscopy procedures. We also thank to “Servei de Microscòpia” at the Universitat Autònoma de Barcelona (UAB) where electron microscopy analysis took place. Additionally, part of physicochemical EVs characterization and all the in vivo studies were performed by the Unique Scientific and Technical Infrastructures (ICTS) “NANBIOSIS”, at the Bioengineering, Biomaterials and Nanomedicine Research Center (CIBER-BBN), specifically NTA analysis was carried out at Unit 6: Biomaterial Processing and Nanostructuring and animal experimentation at Unit 20: in vivo experimental platform (<https://www.nanbiosis.es/platform-units/>). We also thank Dr. Pedro Fuentes and Dr. Marion Martinez for kindly providing ITG β 1 and ITG α 6 antibodies respectively.

Competing interests

V.P. has received fees as consultant, participated in advisory boards or received travel grants from Roche, Sysmex, MSD, AstraZeneca, Bayer and Exact Sciences. The rest of the authors declare no potential conflict of interests.

Received: ((will be filled in by the editorial staff))

Revised: ((will be filled in by the editorial staff))

Published online: ((will be filled in by the editorial staff))

Supporting Information

Cancer stem cell state defines extracellular vesicle activity in triple negative breast cancer

Patricia González-Callejo, Petra Gener, Zamira V. Díaz-Riascos, Sefora Conti, Patricia Cámara-Sánchez, Roger Riera, Sandra Mancilla, Miguel García-Gabilondo, Vicente Peg, Diego Arango, Anna Rosell, Anna Labernadie, Xavier Trepas, Lorenzo Albertazzi, Simó Schwartz Jr, Joaquin Seras-Franzoso*, Ibane Abasolo*

Supporting Methods

HCC1806 CSC model

Model generation: HCC1806 cells were transfected an expression vector delivering tdTomato flouochrome expression under a minimal promoter of ALDH1A1(35) with Lipofectamine 2000 (Thermo Fisher Scientific), and cultured under selective pressure with 10 µg/mL blasticidin for two weeks to ensure that all cells contained the reporter gene. Positive tdTomato cells (tdTomato⁺) were sorted from HCC1806 ALDH1A1:tdTomato cell line by fluorescence-activated cell sorting (FACS) as described for MDA-MB-231 ALDH1A1:tdTomato cells.

Stemness gene expression profile: 500,000 tdTomato⁺ and tdTomato⁻ sorted cells (identified as CSC and DCC, respectively) were sorted from HCC1806 ALDH1A1:tdTomato cell line and total RNA was extracted for qPCR analysis of different stemness markers.

Cell state equilibrium restoration assay: tdTomato⁺ and tdTomato⁻ were sorted by FACS and reseeded in complete RPMI medium. The percentage of tdTomato⁺ within the cell line was monitored after each passage by flow cytometry until it was obtained a tdTomato⁺ stabilized cell subpopulation. Changes in the stemness gene expression profile of each cancer cells subpopulation was monitored over time at different passages (after sorting (AS), at passage1 (P1) and at passage 5 (P5)).

2D Invasion Assay: The invasiveness of each cancer cells subpopulation was assessed using the CytoSelect™ Laminin Cell Invasion Assay Kit (Cell Biolabs). Briefly, inserts were placed in a 24 well plates and cell suspensions containing 1 × 10⁶ cells/mL of HCC1806 tdTomato⁺ and tdTomato⁻ cells were added to each insert. After 48 h incubation, invasive cells were dissociated from the lower side of the membranes, lysed, and quantified using CyQuant® GR Fluorescent Dye (Cell Biolabs).

In vivo growth: Six-week-old female NOD/SCID mice (NOD.CB-17-Prkdcscid/Rj) were obtained from Janvier Laboratories (Le Genest-Saint-Isle, France), housed under specific pathogen-free conditions and provided with food and water ad libitum. 1,000, 10,000 and 100,000 cells of either tdTomato⁺ or tdTomato⁻ cells (n=5) where inoculated orthotopically in mice by intramammary fat pat (i.m.f.p.) inoculation in a 1:1 mixture with Matrigel (Corning). Tumor incidence and growth was monitored up to 4 weeks post-inoculation.

Flow cytometry

DiD labeled EVs^{CSC} or EVs^{DCC} were added to MDA-MB-231 CSC or DCC cell cultures, 2.5 µg EVs/mL, and incubated for 15 min, 4h, 8h and 24h. After incubation cells were treated with trypsin 0.05 % (w/v) (Biological Industries) to detach cells, and neutralized in complete RPMI medium supplemented with DAPI (1 µg/mL final concentration). Cell fluorescence intensity was analyzed in a LSR Fortessa flow cytometer (Beckton Dickinson). Data was further processed using FCS express 4 software (De novo software) and median fluorescence intensity represented. All time points were tested in duplicate.

Stochastic Optical Reconstruction Microscopy (STORM)

Parental MDA-MB-231 cells were seeded in an 8 chambered coverglass and incubated with 2.5 µg/mL DiD labeled EVs (H) or (L) overnight in cell culture conditions. Cell medium was removed and cells were stained with 5 µg/mL WGA-AF488 (Thermo Fischer Scientific) and fixed in 4% PFA. Samples were imaged in STORM buffer (5% w/v glucose, 100 mM cysteamine, 0.5 mg/mL glucose oxidase and 40 µg/mL catalase in PBS) to ensure an adequate photoswitching of the fluorophores. DiD-labeled EVs H and L and MDA-MB-231 cells incubated with DiD-labeled EVs were imaged with a 647nm laser (160 mW) using NIS-Elements software in Nikon Eclipse Ti microscope (Nikon Europe, Amsterdam). The sample was illuminated using a total internal reflection fluorescence (TIRF) alignment for EVs structure imaging or a highly inclined and laminated optical (HILO) alignment for intracellular imaging. The z-level was kept constant by Nikon perfect focus system. Fluorescence was collected by a Nikon 100x, 1.49 NA oil immersion objective and images acquired with a Hamamatsu 19 ORCA-Flash 4.0 camera. For each channel 20,000 frames were acquired and analyzed by fitting a 2D Gaussian function to obtain the localizations of fluorophores. Resulting images were then analyzed with ImageJ.

Immunofluorescence

α-SMA immunofluorescent detection in CCD19 cells: For α-SMA immunofluorescence detection, 15,000 CCD19 cells/well were seeded on 8-well coverslips (Lab-Tek®II, Eppendorf) and treated with either EVs^{CSC} or EVs^{DCC}, 25 µg/mL per day during 3 days. After 72 h of incubation, cells were fixed in 4% PFA for 15 min, permeabilized with 0.1% SDS in PBS for 10 min and blocked in PBS-Tween 0.3% with 5% BSA for 30 min. Samples were then incubated with anti-α-SMA antibody diluted in PBS-Tween 0.3% with 5% BSA O.N. at 4 °C. Cells were washed 3 times in PBS-Tween 0.3% and further incubated with secondary goat antibody anti-mouse conjugated to Alexa Fluor™ 488, 1:1000 (Invitrogen). 30 min at RT in PBS-Tween 0.3% with 5% BSA. Samples were further washed 3 times in PBS-Tween 0.1%. Finally, a drop of antifading mounting medium ProLong (Thermo Fischer Scientific) was added and slides examined using an FV1000 confocal microscope (Olympus) with a 40× objective. Images (at least five random positions per condition) were acquired with identical exposure times and settings. Fluorescence intensity was quantified using Image J NIH software.

α-SMA immunofluorescent detection in lung sections: 5 µm thick OCT microsections from the lungs of animals treated with either EVs^{CSC} or EVs^{DCC}, 300 µg EVs for 24h, were mounted on glass slides for α-SMA immunofluorescent labeling. Briefly, samples were fixed in ice-cold methanol, 30 min at -20°C.

After fixation samples were washed once in PBS followed by 3 washing steps in PBS-Tween 0.3%. Primary antibody, anti- α -SMA (1:500), was supplemented in PBS/BSA 3 % (w/v) and incubated O.N. at 4°C. Samples were further washed 3 times PBS-Tween 0.3% before the addition of secondary antibody. Goat antibody anti-mouse conjugated to Alexa Fluor™ 488, 1:1000 (Invitrogen) was incubated 1h at RT. Then slides were washed again 3 times in PBS-Tween 0.3% and cell nuclei counterstained with DAPI at 1 μ g/mL, 5 min, RT. Finally samples were washed in PBS-Tween 0.3% and a drop of antifading mounting medium ProLong (Thermo Fischer Scientific) added. Images were acquired in a confocal spectral LSM980 microscope (Zeiss) operating at high resolution, XY = 120 nm and Z = 350 nm, using the Airy Scan mode and a plan apochromat 63X/1.40 oil objective. 12 random sections with a fluorescence intensity dynamic range of 16 bytes were further quantified using Image J NIH software. SMA fluorescent signal was normalized in front of the number of cell nuclei per section

In vivo lung metastases of EV-conditioned mouse

Paraffin embedded sections obtained as described in the *immunohistochemistry* section were immune labeled against vimentin. Evaluation of vimentin labeling was determined by the allocation of staining score values from 0 (0 % staining coverage) to 3 (100 % staining coverage) to the individual sections and subsequent mean score calculation of MS for each group. 18 random sections in a 4X magnification per mice group (8 mice/group) were analyzed and total lungs sections area covered by vimentin positive cells was qualitatively scored and represented.

In vivo lung metastases of EV-conditioned MDA-MB-231 cells

To study the effect of EVs^{CSC} and EVs^{DCC} in metastatic capacity of MDA-MB-231 cells, 4×10^6 Luciferase-expressing MDA-MB-231.Fluc2-C19 cells seeded in 20 mL of RPMI complete medium were exposed to 25 μ g/mL of EVs^{CSC} or EVs^{DCC} for 3 consecutive days. Lung tissues were further fixed in Bouin solution and processed for immunohistochemical analysis of NANOG. Non-treated MDA-MB-231.Fluc2-C19 cells were also administered intravenously as control.

In vivo lung metastases of CSC and DCC isolated from MDA-MB-231 cells

1×10^6 cells/mice of either MDA-MB-231.Fluc2-C19. ALDH1:tdTomato⁺ (CSC) or tdTomato⁻ (DCC) cells were intravenously injected into the tail vein of NOD-SCID mice. After 2 months, lungs were excised and processed as described above.

MDA-MB-231 ALDH:tdTomato orthotopic model

A total number of 1,000 cells of either MDA-MB-231.Fluc2-C19. ALDH1:tdTomato⁺ or tdTomato⁻ were orthotopically inoculated into the mice mammary pad (n = 8) in a PBS:Matrigel 1:1 solution. Tumor growth was monitored twice a week by conventional caliper measurements. When tumors reached a volume range between 250–450 mm³, tumors were excised and paraffin embedded for histopathological analysis. Standard trichrome Masson staining and α -SMA immunodetection (as detailed above) were performed in order to visualize infiltrating fibroblasts.

Supporting Figures

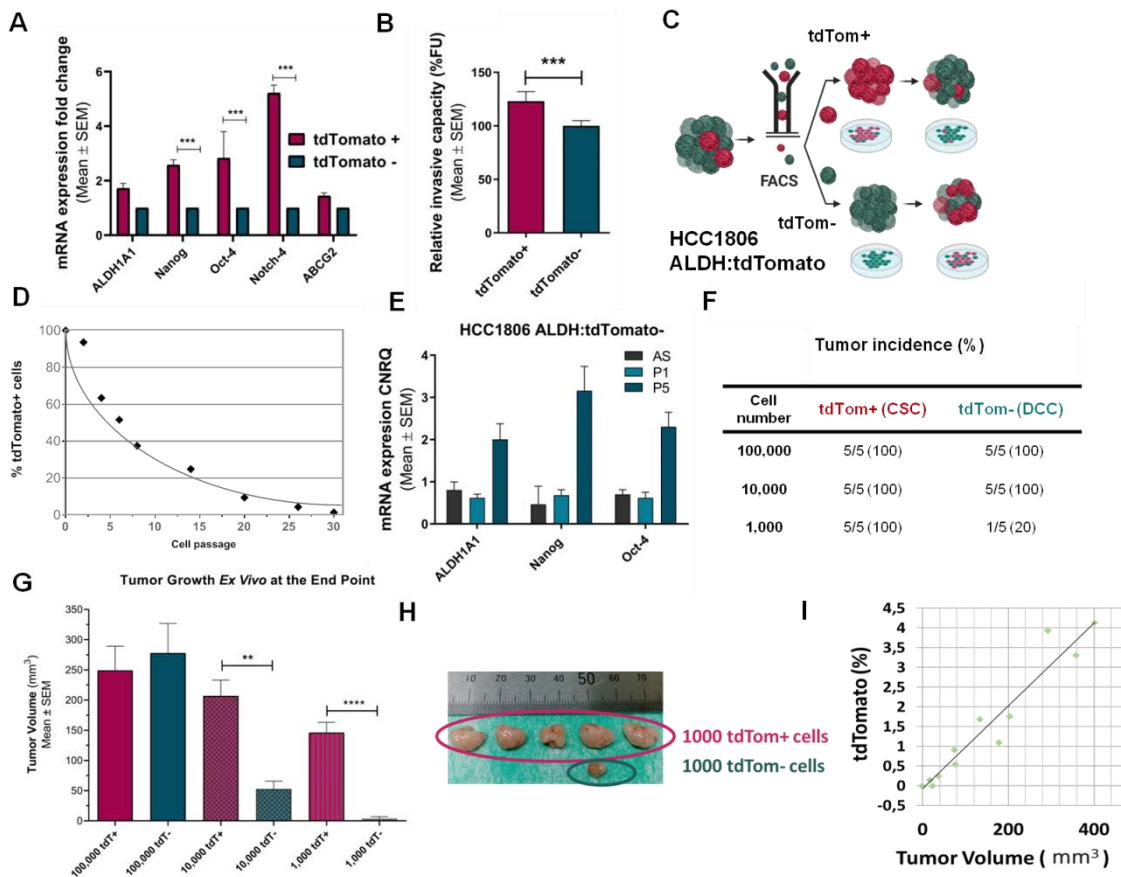


Figure S1. HCC1806 ALDH1A1/tdTomato cancer stem cell (CSC) model. After transfection with reporter vector ALDH1A1/tdTomato, CSC-like cells express fluorescent reporter (tdTomato) which allows CSC subpopulation isolation by fluorescence-activated cell sorting (FACS) (A). Stemness gene expression profile of tdTomato+ cell population (CSC) compared to tdTomato- cell population (DCC), assessed by RT-qPCR just after isolation by FACS (P0). (B) Invasive potential in 2D models of tdTomato+ cells compared to tdTomato- cells. (C) Schematic representation of tdTomato+ and tdTomato- cells behavior in attachment culture conditions after FACS isolation. (D) tdTomato+ cells tend to lose fluorescence over cell passages as CSCs differentiate into DCCs. (E) Dedifferentiation of tdTomato- into cells with increased expression of stemness reporter genes after few passages, assessed as shown by RT-qPCR analysis. (F) HCC1806 *in vivo* model. Tumor incidence in mice inoculated orthotopically with HCC1806 tdTomato- (DCC) and HCC1806 tdTomato+ (CSC) in each cell dilution group. (G) *Ex vivo* tumor growth. (H) Detailed images of tumors grown in mice inoculated with 1000 tdTomato+ and tdTomato- cells. (I) Correlation between tumor volume and % of tdTomato+ cells. Results are expressed as mean ± SEM. (* $p < 0.05$; ** $p < 0.01$, *** $p < 0.001$)

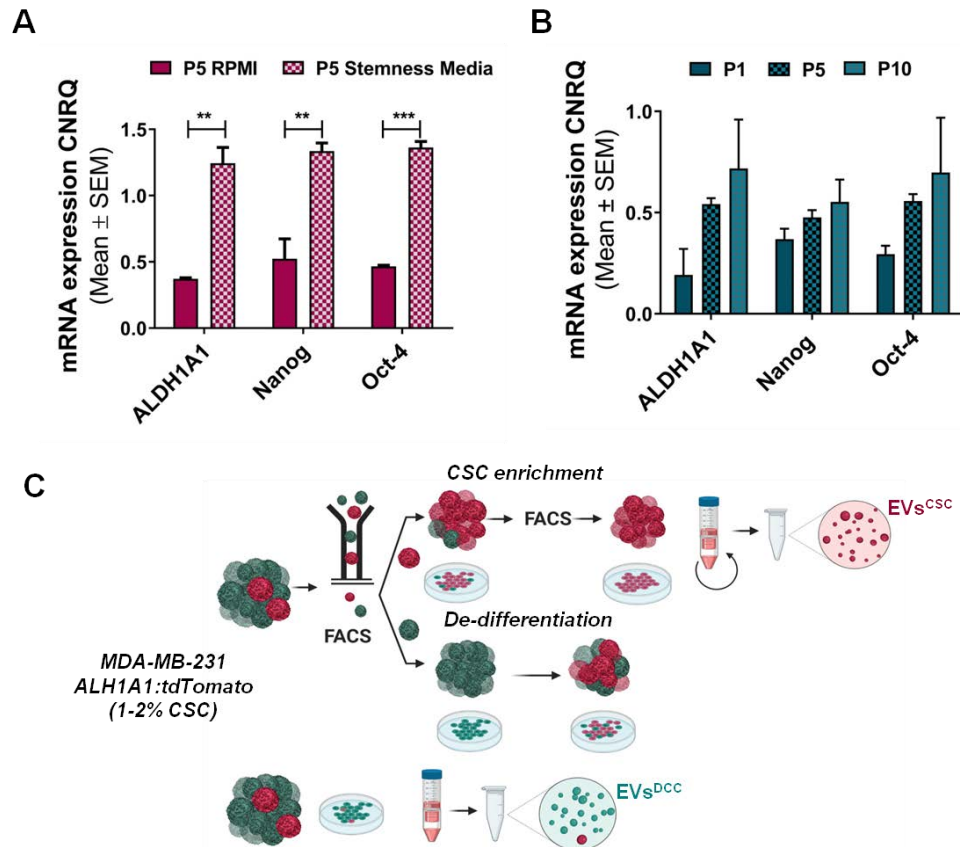


Figure S2. CSC and DCC in vitro culture optimization in MDA-MB-231 cells. (A) Stem gene expression of MDA-MB-231 tdTomato⁺ cells at passage 5 (P5) after cell sorting in different culture conditions: RPMI conventional media vs. stemness media. (B) Stem gene expression profile of MDA-MB-231 with 1-2% content of tdTomato⁺ cells maintained in culture at different passages (1, 5 and 10). (C) Schematic illustration of EVs isolation procedure created with BioRender.com. Briefly, MDA-MB-231 tdTomato⁺ cells were cultured with stem cell maintenance media. EVs^{CSC} were isolated from the CM of these MDA-MB-231 CSC cells, which presented high expression of stemness reporters CSC. Due to tdTomato⁻ sorted cells tendency to de-differentiate into CSC, EVs^{DCC} were isolated from a stable MDA-MB-231 cell subpopulation with a minimal content in CSC (1-2%) that exhibited low expression of stemness reporters, as most cells were DCC.

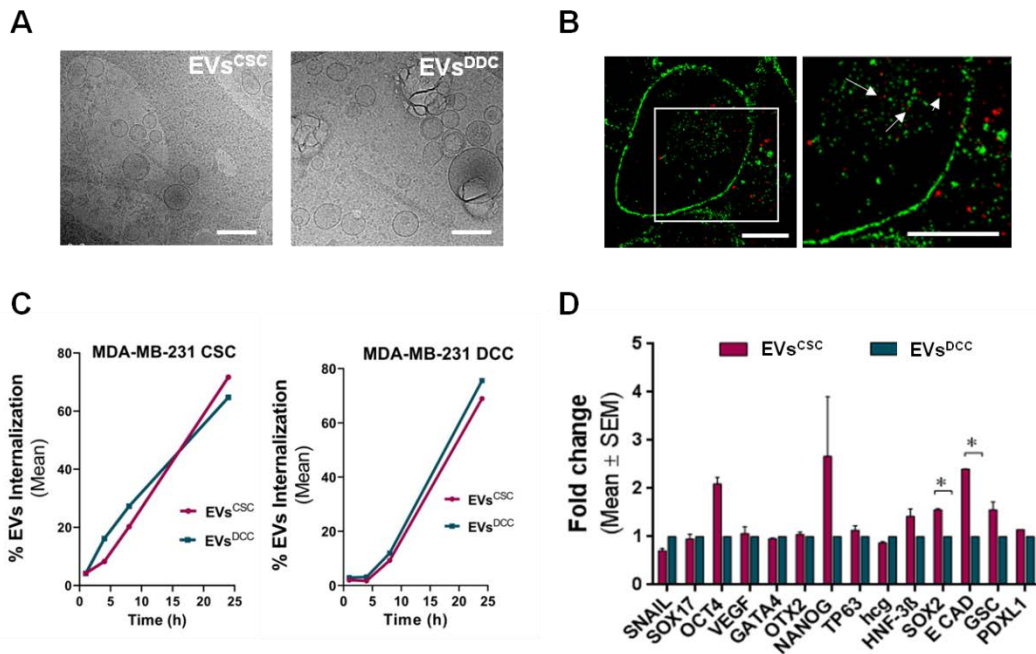


Figure S3. MDA-MB-231 EVs^{CSC} and EVs^{DCC} characterization. (A) General view by CryoTEM of isolated EVs^{CSC} and EVs^{DCC}. Scale bar = 200 nm. (B) STORM detailed images of EVs internalization into MDA-MB-231 parental cells. Arrows indicate DiD labeled EVs (red). Scale bar=10 μ m. (C) Internalization kinetics of EVs^{CSC} and EVs^{DCC} in MDA-MB-231 DCC and CSC subpopulations. (D) Pluripotent stem cell protein expression profile of EVs^{CSC} and EVs^{DCC}. Array results are expressed as integrated density intensity. * $p < 0.05$.

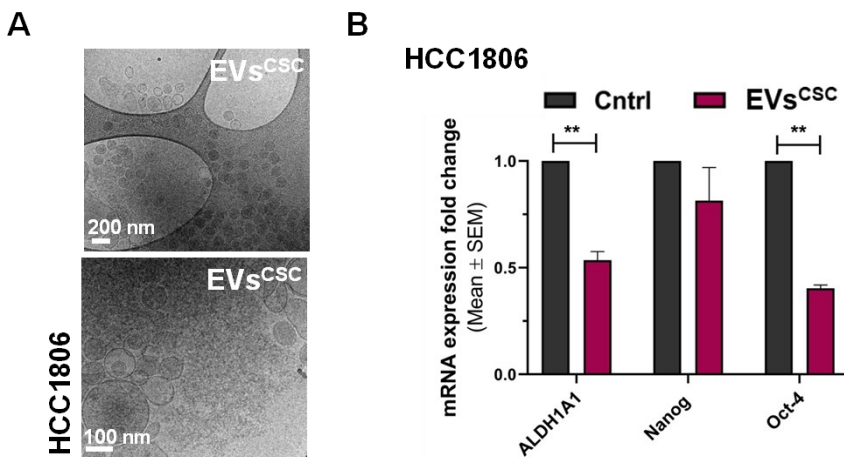


Figure S4. HCC1806 derived EVs^{CSC} effect on CSC/DCC plasticity. (A) CryoTEM images of EVs^{CSC} isolated from HCC1806. (B) Effect of EVs^{CSC} on stemness gene expression profile of parental HCC1806 cell line analyzed by qPCR. Results are expressed as NRQ (relative normalized quantities) mean \pm SEM ($n \geq 3$); * $p < 0.05$; ** $p < 0.01$.

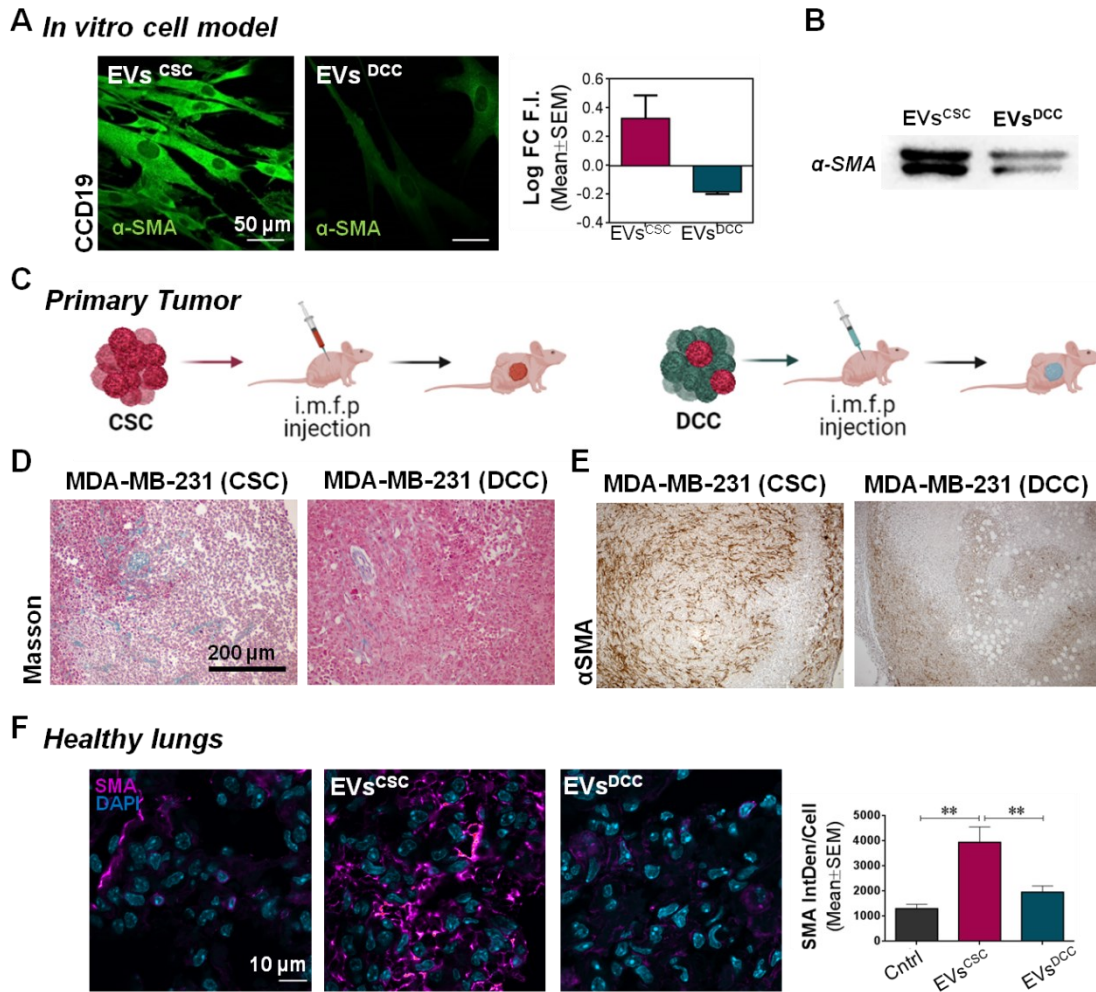


Figure S5. MDA-MB-231 EVs' effect on fibroblasts activation towards CAFs phenotype. (A) Representative images and quantification of fluorescence immunostaining for α -SMA in CCD19 cells educated with MDA-MB-231 EVs^{CSC} and EVs^{DCC} analyzed by confocal microscopy. Scale bar = 50 μ m. (B) EVs^{CSC} and EVs^{DCC} α -SMA cargo examined by Western blotting. (C) Schematic representation of the orthotopic breast cancer mouse model generation. CSC and DCC isolated from MDA-MB-231 ALDH:tdTomato cells were inoculated into the mouse mammary fat pad. Tumors were let to grow till achieving >250 mm³, excised and processed for histological studies (panels D and E). Created with BioRender.com. (D) Masson's Trichrome staining and (E) α -SMA expression in primary tumors of mice orthotopically inoculated into the right mammary fat pad with MDA-MB-231 CSC or MDA-MB-231 DCC and euthanized 9 weeks post-inoculation. Scale bar = 200 μ m. (F) Representative images and quantification of fluorescence immunostaining for α -SMA in lung sections of healthy mice i.v. inoculated with MDA-MB-231 EVs^{CSC} and EVs^{DCC} after 24h. ** $p < 0.01$.

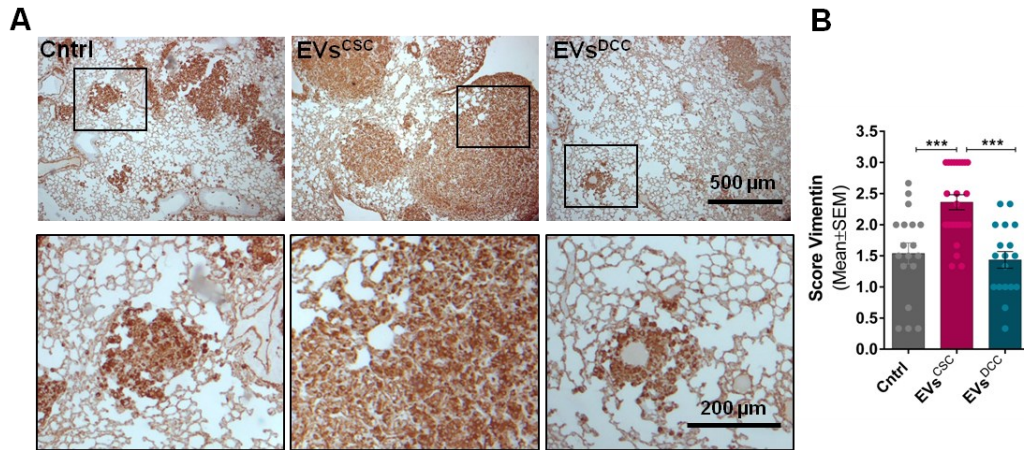


Figure S6. EVs' effect on lung metastasis. (A) Representative images of vimentin staining on lungs showing metastatic foci in different treatment groups. (B) Graph displaying vimentin semi-quantitative scoring of the extension of vimentin staining (ranging from 0 -0 % covered area- to 3 -100 % covered area-). (* $p < 0.05$; ** $p < 0.01$; *** $p < 0.001$).

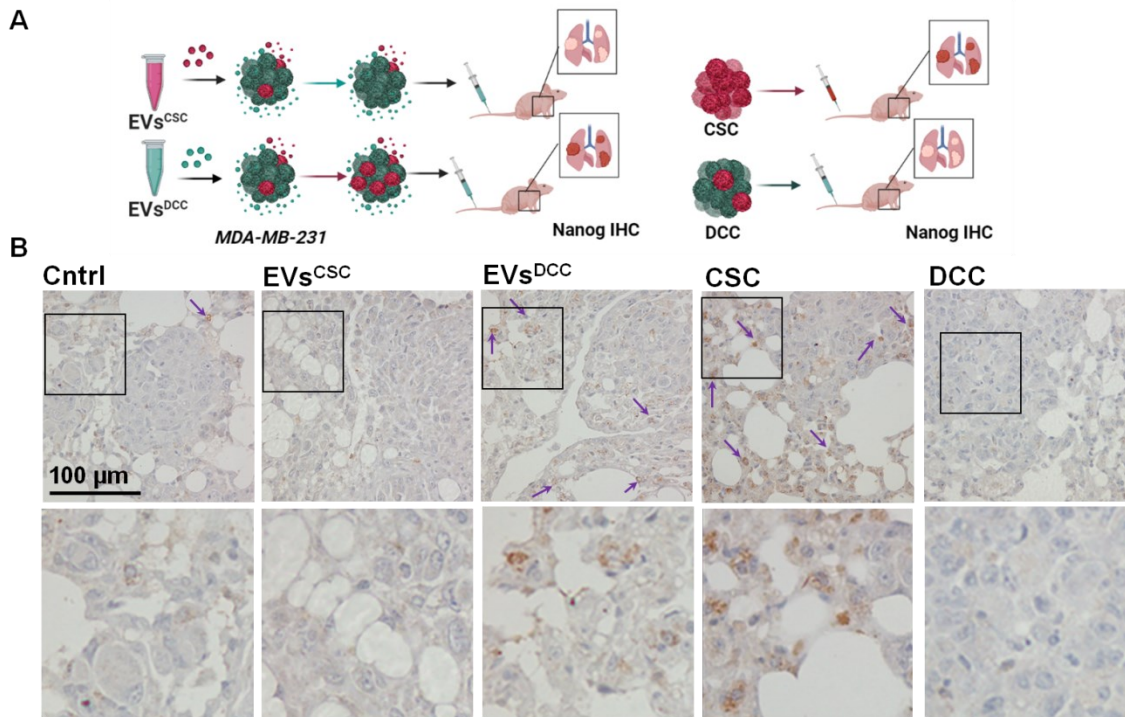


Figure S7. NANOG protein expression in MDA-MB-231 lung metastases. (A) Scheme displaying the distinct conditions tested with the lung metastasis mouse model. Specifically, MDA-MB-231 cells previously conditioned with EVs^{CSC} or EVs^{DCC} and CSC or DCC cells isolated from MDA-MB-231:ALDH:tdTomato cells were injected into the tail vein and metastasis let to grow for 2 months. At the experimental endpoint lungs were excised and processed for histological analysis. Created with BioRender.com. (B) NANOG protein expression in metastatic lungs of mice i.v. injected with MDA-MB-231 cells that were previously treated for 72 h with EVs^{CSC} or EVs^{DCC} before injection. MDA-MB-231 CSC and DCC cells directly i.v. injected are also displayed as additional NANOG staining controls. Scale bars= 100 μm .

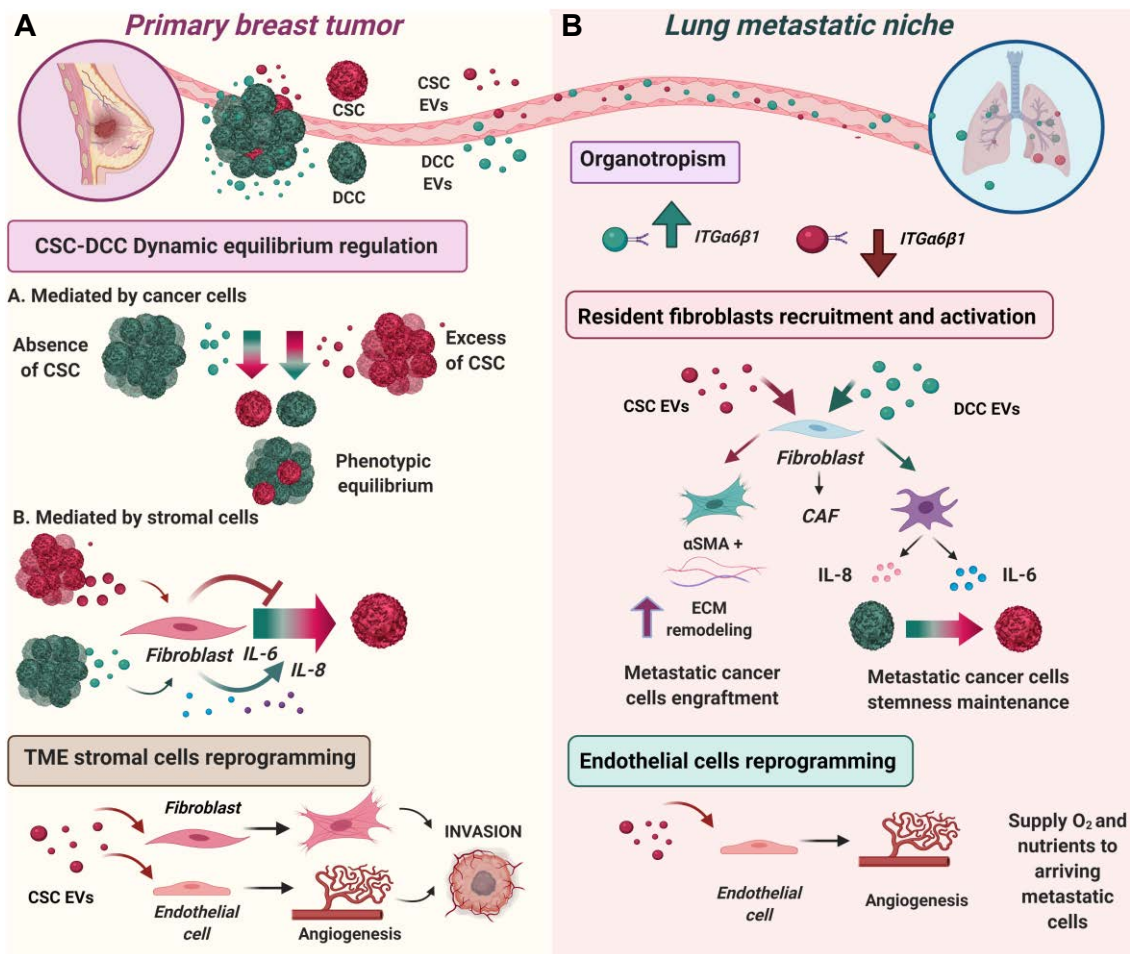


Figure S8. CSCs and DCCs secreted EVs' role in tumor maintenance and metastatic progression. (A) Primary breast tumors are composed by heterogeneous CSC and DCC subpopulations that present phenotypic equilibrium between both cell states. Tumor secreted EVs mediate this phenotypic equilibrium as they can promote cancer cells plasticity towards differentiation or de-differentiation depending on tumor requirements. While an excess of EVs from CSCs (EVs^{CSC}) triggers cancer cells differentiation, EVs^{DCC} induce the opposite effect, enhancing tumor cells de-differentiation to restore CSC/DCC balance. EVs^{DCC} also induce stromal fibroblasts to restore missing CSC subpopulations through IL-6 and IL-8 signaling. Of note, EVs^{CSC} do not produce this effect since CSCs are no longer required in the system. However, EVs^{CSC} are needed to induce CAFs activation and angiogenesis. (B) Primary tumor CSCs and DCCs secrete EVs that travel through the blood circulation and reach the lungs. EVs^{CSC} impacts on lung resident cells by inducing the activation of fibroblasts' into α SMA+ CAFs. In addition, EVs^{CSC} also promote pro-angiogenic activity of endothelial cells. EVs^{DCC} induce resident fibroblasts to secrete pro-stem factors (e.g. IL-6 and IL-8) supporting cancer cell transition towards CSC-like states of arriving metastatic cells. The ability of EVs to induce distinct microenvironmental changes at distant, potential metastatic, sites is critical to determine if metastatic cancer cells will survive, remain dormant, or form macrometastases to spawn a secondary tumor growth. Created with BioRender.com.

Received: 12 May 2020 | Revised: 16 December 2020 | Accepted: 5 January 2021

DOI: 10.1002/jev2.12058

RESEARCH ARTICLE

WILEY

Extracellular vesicles from recombinant cell factories improve the activity and efficacy of enzymes defective in lysosomal storage disorders

Joaquín Seras-Franzoso^{1,2} | Zamira V. Díaz-Riascos^{1,2,4} | José Luis Corchero^{2,3} |
 Patricia González^{1,2} | Natalia García-Aranda^{1,2,4} | Mònica Mandaña^{1,2,4} | Roger Riera⁵ |
 Ana Boullosa^{1,2,4} | Sandra Mancilla^{1,2,4} | Alba Grayston⁶ | Marc Moltó-Abad^{1,7} |
 Elena García-Fruitós^{2,3} | Rosa Mendoza^{2,3} | Guillem Pintos-Morell^{1,7} |
 Lorenzo Albertazzi⁵ | Anna Rosell⁶ | Josefina Casas^{8,9} | Antonio Villaverde^{2,3} |
 Simó Schwartz Jr^{1,2} | Ibane Abasolo^{1,2,4}

¹ Drug Delivery & Targeting, CIBRIM-Nanomedicine, Vall d'Hebron Institute of Research, Universitat Autònoma de Barcelona, Barcelona, Spain² Networking Research Center on Bioengineering, Biomaterials and Nanomedicine (CIBER-BBN), Barcelona, Spain³ Institut de Biociències i de Biomedicina (IBB) and Department of Genetics and Microbiology, Universitat Autònoma de Barcelona (UAB), Bellaterra, Barcelona, Spain⁴ Functional Validation & Preclinical Research (FVPR), CIBRIM-Nanomedicine, Vall d'Hebron Institut de Recerca (VHIR), Universitat Autònoma de Barcelona (UAB), Barcelona, Spain⁵ Nanoscopy for Nanomedicine Group, Institute for Bioengineering of Catalonia (IBEC), Barcelona, Spain⁶ Neurovascular Research Laboratory, Vall d'Hebron Institut de Recerca (VHIR), Universitat Autònoma de Barcelona (UAB), Barcelona, Spain⁷ Division of Rare Diseases, Reference Center for Hereditary Metabolic Disorders (CSUR, XUEC, MetabERN, and CIBER-ER), Vall d'Hebron University Hospital, Barcelona, Spain⁸ RUBAM, Biological Chemistry, Institute of Advanced Chemistry of Catalonia (IQAC-CSIC), Barcelona, Spain⁹ Networking Research Center on Hepatic and Digestive Diseases (CIBEREHD), Barcelona, Spain

Correspondence

Simó Schwartz Jr and Ibane Abasolo, Drug Delivery & Targeting, CIBRIM-Nanomedicine, Vall d'Hebron Institute of Research, Universitat Autònoma de Barcelona, 08035 Barcelona, Spain.
 Email: simoschwartz@vhir.org and ibane.abasolo@vhir.org

Present address

Elena García-Fruitós, Department of Farmaceutic Production, Institut de Recerca i Tecnologia Agroalimentàries (IRTA), 08140, Caldes de Montbui, Spain.

Abstract

In the present study the use of extracellular vesicles (EVs) as vehicles for therapeutic enzymes in lysosomal storage disorders was explored. EVs were isolated from mammalian cells overexpressing alpha-galactosidase A (GLA) or N-sulfoglucosaminase sulfohydrolase (SGSH) enzymes, defective in Fabry and Sanfilippo A diseases, respectively. Direct purification of EVs from cell supernatants was found to be a simple and efficient method to obtain highly active GLA and SGSH proteins, even after EV lyophilization. Likewise, EVs carrying GLA (EV-GLA) were rapidly uptaken and reached the lysosomes in cellular models of Fabry disease, restoring lysosomal functionality much more efficiently than the recombinant enzyme in clinical use. In vivo, EVs were well tolerated and distributed among all main organs, including the brain. DiR-labelled EVs were localized in brain parenchyma 1 h after intra-arterial (internal carotid artery) or intravenous (tail vein) administrations. Moreover, a single intravenous administration of EV-GLA was able to reduce globotriaosylceramide

ABBREVIATIONS: BSA, bovine serum albumin; DHFR, dihydrofolate reductase; ERT, enzyme replacement therapy; EVs, extracellular vesicles; GAGs, glycosaminoglycans; Gb1, globotriaosylceramide; GLA, alpha galactosidase A; Ia, intra-arterial; Iv, intravenous; LAMP1, Lysosome-associated membrane protein 1; LSDs, lysosomal storage disorders; MTX, methotrexate hydrate; PEI, polyethylenimine; SGSH, N-sulfoglucosaminase sulfohydrolase; SN, supernatants

This is an open access article under the terms of the [Creative Commons Attribution License](https://creativecommons.org/licenses/by/4.0/), which permits use, distribution and reproduction in any medium, provided the original work is properly cited.

© 2021 The Authors. *Journal of Extracellular Vesicles* published by Wiley Periodicals, LLC on behalf of the International Society for Extracellular Vesicles

J Extracell Vesicles. 2021;10:e12058.
<https://doi.org/10.1002/jev2.12058>

[wileyonlinelibrary.com/journal/jev2](https://onlinelibrary.com/journal/jev2) | 1 of 14

(Gb3) substrate levels in clinically relevant tissues, such as kidneys and brain. Overall, our results demonstrate that EVs from cells overexpressing lysosomal enzymes act as natural protein delivery systems, improving the activity and the efficacy of the recombinant proteins and facilitating their access to organs neglected by conventional enzyme replacement therapies.

KEYWORDS

alpha-galactosidase A, drug delivery, enzyme replacement therapy, Fabry disease, lysosomal storage disorders, N-sulfoglucosamine sulfohydrolase, Sanfilippo syndrome

1 | INTRODUCTION

The use of recombinant proteins to treat a wide variety of clinical indications, including cancer, autoimmune and genetic diseases, is still a challenge (Leader et al., 2008). Lysosomal storage disorders (LSDs) are congenital rare diseases caused by the lack or malfunction of proteins involved in lysosomal biogenesis and activity. There are more than 70 different LSDs, among them, Gaucher, Fabry, Pompe and Sanfilippo syndromes (Platt et al., 2018). All LSDs share the accumulation in the lysosomal compartment of complex molecules such as glycosaminoglycans, glycoproteins and sphingolipids, rendering in most cases severe clinical manifestations (Platt et al., 2018). Patient symptomatology depends on the disease and the particular mutation but often, LSDs derive in a systemic illness affecting multiple organs, including the central nervous system (CNS), liver, kidneys, heart and the musculoskeletal system. Regrettably, LSDs have been historically neglected by the pharmaceutical industry. Their individual low incidence has discouraged active search for treatment due to the high difficulties to organize clinical trials and poor expected post-commercialization profits. Nevertheless, in the last years, enzyme replacement therapies (ERTs) based on the systemic administration of a functional version of the defective enzyme, have gained clinical relevance in LSD healthcare. Hence, ERTs using recombinant proteins are currently available for 10 LSDs, (Concolino et al., 2018) including Fabry disease. Unfortunately, systemically administered enzymes are not able to reach the brain parenchyma, leaving without effective treatment LSD patients with CNS affection (Solomon & Muro, 2017).

Fabry disease is an X-linked disease characterized by the accumulation of globotriaosylceramide (Gb3) and other glycosphingolipids in cellular lysosomes, caused by a deficient activity of the alpha-galactosidase A (GLA) enzyme, secondary to pathogenic genetic variants of the *GLA* gene. Endothelial cells are one of the most affected cell types. Without proper treatment, alterations in the micro- and macro-vasculature in different organs eventually lead to a multisystemic failure and early death (Rombach et al., 2010). Two products, agalsidase beta (Fabrazyme), and agalsidase alfa (Replagal), are currently approved for ERT in Fabry disease (Beck et al., 2004; Eng et al., 2001). Other treatment approaches based on chaperones, (Hughes et al., 2017) substrate reduction (Guérard et al., 2018) and gene therapy (Huang et al., 2017; Medin et al., 2019) have been either approved recently for Fabry disease (migalastat), or are under study, but with limited efficacy and/or applicability, so far. Conversely, ERT has shown to delay the disease progression in Fabry patients with an early diagnosis (Mehta et al., 2009). Nevertheless, the success of ERT in Fabry disease and other LSDs is often limited by the generation of autoantibodies against the exogenous recombinant proteins, low plasma half-life and poor biodistribution of the enzymes that fail to effectively target organs such as kidney, heart, brain and bone, among others (Safary et al., 2018).

In fact, many LSDs have not yet benefited from ERT due to the impossibility of recombinant enzymes to cross the blood brain barrier (BBB). This is the case of Sanfilippo syndrome, caused by four different genetic defects affecting lysosomal heparan sulfate degradation, each one defining a different disease subtype A, B, C and D. In this regard, Sanfilippo A represents 60% of all diagnosed cases and is caused by a deficiency of the heparan N-sulfatase enzyme, also known as N-sulfoglucosamine sulfohydrolase (SGSH). As with the other subtypes, the accumulation of partially degraded glycosaminoglycans (GAGs) in the brain causes progressive cognitive decline and severe behavioural disturbances. Although no therapy is still approved for Sanfilippo disease, several clinical trials are being conducted using intrathecally applied recombinant protein, gene therapy and substrate reduction therapy (Gaffke et al., 2018).

In this scenario, the use of nanotechnological approaches increasing the efficiency of recombinant enzymes and targeting them to specific cell types is regarded as a powerful approach to introduce new effective therapies for LSDs (Muro, 2010). Different types of nanoparticles have been tested as vehicles for ERT in Fabry disease including liposomes, (Cabrera et al., 2016) chitosan polyelectrolytes (Giannotti et al., 2016) and polystyrene nanoparticles (Hsu et al., 2014). Moreover, other nanocarriers from a biological origin, such as nanoparticles made of albumin and 30Kc19 protein (Lee et al., 2016) have also been studied at the preclinical level. Unfortunately, none of these synthetic nanoparticles have been able to advance towards clinical application in LSDs.

In parallel, extracellular vesicles (EVs) have been also proposed as delivery vehicles for recombinant proteins (Sutaria et al., 2017). EVs, including microvesicles (100-1000 nm) and exosomes (30-150 nm), naturally contain biomolecular cargos such as

miRNA, mRNA and proteins from the donor cells. They have been described as fully biocompatible submicron-sized vehicles with higher *in vivo* transfection capacity and lower immunogenic responses than other non-viral platforms (Srivastava et al., 2016). Importantly, EVs have been shown to be fully tunable using genetically modified cells as source. For instance, Alvarez-Erviti et al. (Alvarez-Erviti et al., 2011) modified dendritic cells to express Lamp2b, a lysosomal membrane protein, fused to the neuron-specific RVG peptide to target EVs into the brain parenchyma. Furthermore, EVs can be also chemically and mechanically loaded after their production and isolation, allowing the introduction of siRNA, enzymes and chemotherapeutics by sonication, saponification or simple incubation. (Batrakova & Kim, 2015; Sutaria et al., 2017)

Notably, the delivery of a therapeutic biomacromolecule often requires previous production and purification of the soluble form of the biopharmaceutical and its further load into the vehicle. This increases the complexity of the production and the final cost. Therefore, an all-in-one process in which the carrier and the therapeutic cargo are produced jointly may provide an optimal strategy to improve the production process and further, the efficacy of protein-based therapeutics. This is especially relevant in the case of LSDs, in which ERT is often regarded as ideal standard of care.

In this work, we investigate the use of protein loaded EVs from protein recombinant cell factories for the delivery of therapeutic lysosomal enzymes such GLA and SGSH, by purifying EVs precisely from the same cells used to produce the recombinant enzyme. Enzyme loaded EVs retain highly active GLA and SGSH recombinant enzymes, withstand lyophilization, and are fully biocompatible. Moreover, *in vitro* and *in vivo* efficacy assays using GLA loaded EVs, have shown clear advantages on the use of EV-loaded system vs. the naked recombinant enzymes.

2 | RESULTS AND DISCUSSION

2.1 | Mammalian cell factories produce EVs with high quantities of GLA and SGSH enzymes

Enzymatic deficiency of GLA and SGSH proteins cause Fabry and Sanfilippo A diseases, two of the LSDs with higher prevalence (Meikle et al., 1999). In this work we aimed at testing the feasibility of EVs as enzyme delivery systems for GLA and SGSH proteins, as a way to improve ERT in these two diseases. Consequently, EVs were isolated from CHO DG44 and HEK293 cells transfected with plasmids coding for GLA and SGSH enzymes, respectively. Stable clones were obtained from CHO DG44 cells for GLA expression, while transfections in HEK293 cells were conducted transiently for SGSH.

EVs obtained from CHO DG44 and HEK293 cells were purified using charge neutralization-based precipitation method and later characterized by cryoTEM and Western blot. EVs presented spherical and pseudo-spherical morphologies that ranged from 30 to 300 nm in diameter by cryoTEM and Nanosight assessment (Figure 1A-C). Additional cryoTEM images at lower magnification are available in Figure S1. Western blot analyses showed very low content of cytosolic β -tubulin within the vesicles and the presence of exosome markers CD63, CD81-tetraspanin and TGS101 (Théry et al., 2018) (Figure 1D) indicated that EVs purified from CHO DG44 and HEK293 cell-factories were enriched in exosomes (50 to 150 nm) and small-sized microvesicles, with some of large microvesicles and apoptotic bodies (Figure 1A). Such mixed population of vesicles was expected because the size-range of exosomes partially overlap with other types of EVs and purification protocols currently in use, mainly based on ultracentrifugation and precipitation methodologies, do not render pure populations of different types of EVs (Kowal et al., 2016). Noteworthy, significant amounts of the protein of interest, GLA and SGSH, were found in EV lysates in comparison to whole cells lysates (Figure 1D). Of note, EVs and lysosomes are both originated from the multivesicular endosomes (MVE) (Raposo & Stoorvogel, 2013) and this common origin could explain the high GLA and SGSH enzyme concentration within the EVs. Although other possibilities, such the release of lysosomal proteins in EVs due to autolysosomal dysfunctions, could not be excluded (Goetzl et al., 2015). Notwithstanding, other endogenous lysosomal proteins such as the membrane protein cystinosis and the beta-glucocerebrosidase (GBA) enzymes, were also found enriched in EV-GLAs, suggesting EV could be an adequate platform for naturally loading a broader spectrum of lysosomal proteins (Figure 1E).

Regarding the presence of the therapeutic proteins in the EVs, the fact that 4.48% and 10.25% of the total protein in the EVs corresponded to GLA and SGSH respectively when isolated by polymer co-precipitation method is remarkable (Figure S2A). Of note, although EV precipitation is a convenient method for preclinical studies, due to its simplicity and speed, it can also co-isolate contaminant proteins in their soluble form. In order to characterize the extent of this phenomenon an alternative purification method, namely tangential flow filtration (TFF) (Busatto et al., 2018) was carried out, we detected the production yield dropped a 42% when using TFF method compared to the precipitation kit used in the isolation of EVs for *in vitro* and *in vivo* studies. However, we also found that the enzymatic activity within the EVs was the major contributor to the increased activity seen in the original EV-GLA samples, as demonstrated by the high enzymatic specific activities in the TFF-purified samples, non-significantly distant from the original EV-GLA (Figure S2A). This indicated that the efficacy seen upon EV-GLA treatment of cell cultures or Fabry animals could be mainly attributed to the effect of the GLA in the EV lumen and not to the GLA co-purified with the EVs. Since the solely TFF might not remove all the free soluble proteins (Corso et al., 2017), to further confirm the higher performance of GLA loaded into EVs in comparison to its soluble counterpart co-isolated during EV precipitation, precipitated EV-GLA were submitted to an additional sucrose cushion purification step (Théry et al., 2006). With this purification method,

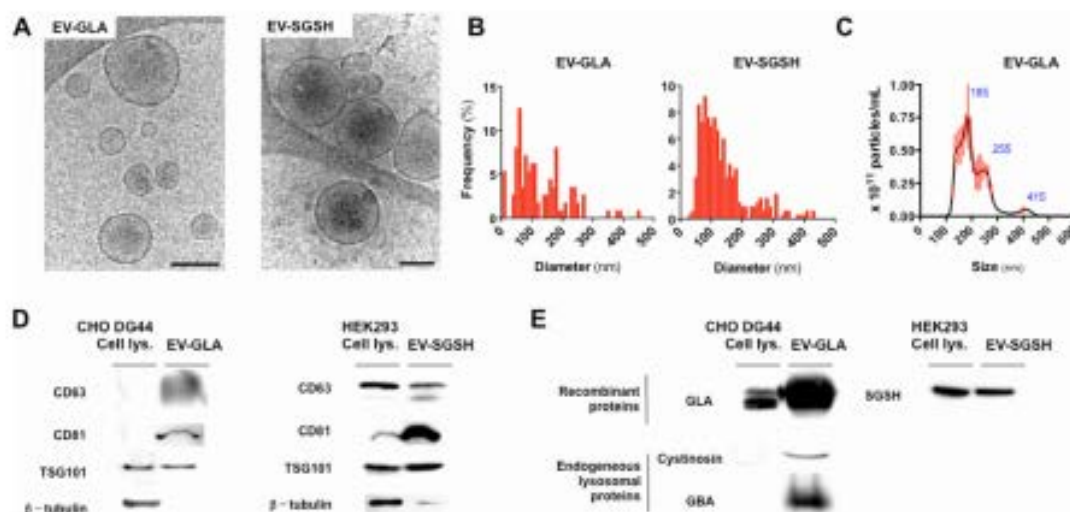


FIGURE 1 Characterization of EVs containing GLA and SGSH lysosomal enzymes (EV-GLA and EV-SGSH). A) Characterization by cryoTEM imaging of vesicle morphology. Magnification bar corresponds to 200 nm. B) Size distribution of EV-GLA and EV-SGSH measured in cryoTEM images. C) EV-GLA size distribution and concentration determination by nanoparticle tracking analysis. Blue values correspond to the size of the main peaks in the histogram. D) Molecular characterization of isolated EVs by Western blot of EV markers. Cell lysates and a cytosolic protein (β -tubulin) were also included as controls. E) Lysosomal protein content in EVs by Western blot. *Panel above*, detection of over expressed protein of interest, GLA and SGSH. *Panel below*, detection of additional lysosomal endogenous protein (Cystinosin and GBA) in EV-GLA. 10 to 20 μ g of total protein loaded per lane in both D and E panels

the relative amount of GLA decreased a $60.5 \pm 0.6\%$ in comparison to the original sample (Figure S2B). However, enzymatic activity of GLA inside EVs was significantly higher, 6 times more active, than its soluble co-isolated counterpart (Figure S2B). Regarding SGSH protein the amount of soluble protein co-purified was higher reaching the $85.9 \pm \%$ of the initial enzyme in the EV-SGSH precipitated samples. These results were in agreement with the ones observed for TFF purification and ratified the major contribution of EV-GLA to the efficacy observed *in vitro* and *in vivo*. Further, an iodixanol density gradient separation (Lobb et al., 2015) onto EV-GLA precipitated samples was carried out (Figure S2C) and revealed significant levels of GLA protein in different density fractions. Considerable amounts of GLA were found in low density fractions ($< 1.06 \text{ g/cm}^3$), probably corresponding to soluble protein interacting with Low Density Lipoprotein (LDL) particles (Karimi et al., 2018). This phenomenon was likely enhanced by the high concentration of samples subjected to sucrose gradient, at least 1 order of magnitude above those subjected to TFF or sucrose cushion methods. Remarkably, GLA was also found, as expected, at densities corresponding to EVs ($1.08 - 1.14 \text{ g/cm}^3$) that retained a significant part of the enzymatic activity (Figure S2C) whilst expressing EV makers (Bobrie et al., 2012).

Overall, considering the above results we found the actual protein loading capacity at 2.96 fg GLA per vesicle. Of note, this loading capability is almost 30 times higher than the one previously reported for alternative lysosomal enzymes in macrophage-derived EVs (0.1 fg/EV) (Haney et al., 2019). Altogether these data suggest that protein loading in EVs can be significantly boosted by selecting cell factories optimized for protein production (Geisse & Fux, 2009). Differences between GLA and SGSH protein content in EVs might be related to the fact that transient transfections, used in this case to obtain EV-SGSH, usually render higher protein yields than stable transfections (Bandaranayake & Almo, 2014). On the other hand, recombinant protein content in EVs was also compared to the amount of soluble protein found in cell supernatants. Interestingly, supernatants from stably transfected CHO cells contained $41.4 \pm 7.14 \mu\text{g}$ of GLA per ml of cell culture, while $0.517 \pm 0.01 \mu\text{g}$ of GLA in EVs were obtained per ml of cell culture. Nonetheless, even though the content of GLA in EVs is 80-fold lower than in cell supernatant, it is worth mentioning that EV loading of GLA is considerably higher than the loading of GLA found in artificial liposomes (Cabrera et al., 2016) or previously reported in EVs loaded with alternative lysosomal proteins (Haney et al., 2019).

2.2 | Recombinant EV-GLA restores lysosomal GLA enzymatic activity in GLA defective cells

The capacity of EVs to act as drug delivery system for lysosomal proteins was studied *in vitro* through the assessment of cell uptake, intracellular trafficking, protease sensitivity and enzymatic activity assays. Fluorescently labelled EVs efficiently internalized in different type of cells, including kidney cells (HEK293T cells, Figure S3) and endothelial cells (MAEC, Figure 2A) at a concentration of 2.5 μg EVs/ml (c.a. 125 ng GLA/ml). These later cells were included since endothelial cells are central in the

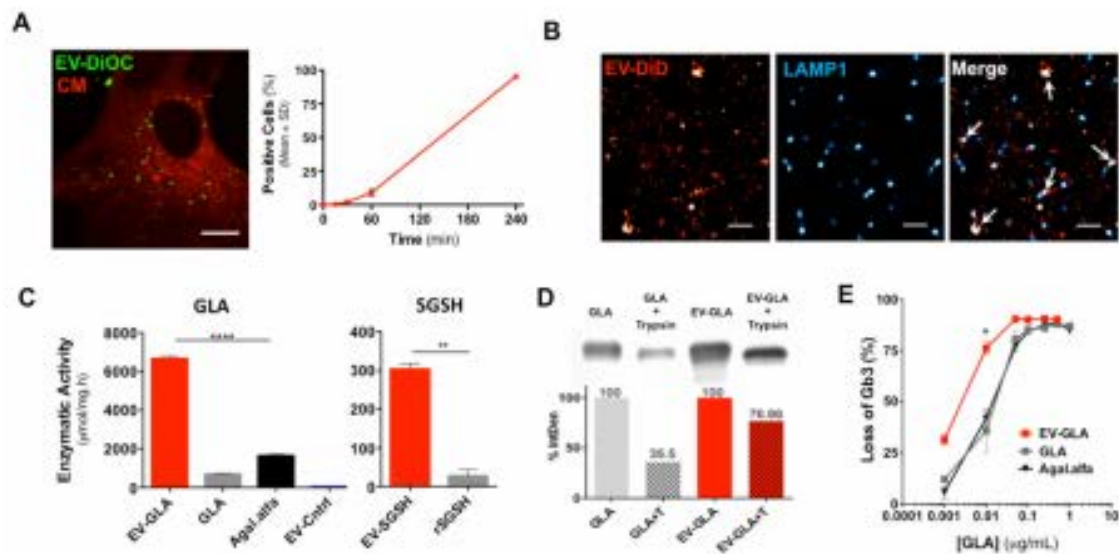


FIGURE 2 In vitro assessment of EVs as drug delivery systems for lysosomal proteins. A) Internalization of EVs by confocal microscopy (4 h incubation) and flow cytometry in primary cultures of mouse aortic endothelial cells (MAEC) derived from Fabry KO mice. EVs were labelled with DiOC (green) and cell membranes were labelled with Cell Mask (red). Magnification bar corresponds to 10 μ m. B) Inset of HEK293 cytoplasmic region of a single cell showing colocalization (white arrows) of EV-GLA labelled with DiD (red) with lysosomal marker LAMP1 (blue) by STORM imaging. Magnification bar corresponds to 1 μ m. C) Enzymatic activities for alpha-galactosidase A (left) and heparan sulfatase (right) measured in EVs obtained from cells overexpressing GLA and SGSH proteins, respectively. EVs from non-transfected CHO cells were also included as controls (EV-Control). D) Protease digestion assay of EV-GLA (red bars) and their naked GLA counterparts (grey bars). T stands for trypsin treatment. %IntDen refers to the percentage of the integrated density. E) Efficacy of EV-GLA reducing the Gb3 deposits in MAEC primary cultures at different GLA protein concentrations

pathophysiology of Fabry disease (Bodary et al., 2007). After short 4 h incubation with fluorescently labelled EVs, nearly 100% of MAEC showed strong fluorescent signal by flow cytometry. Confocal microscopy further confirmed that fluorescently labelled EVs were located inside the cells and not merely attached to the cell membrane. The release of EVs into lysosomes of destiny cells has been extensively described in different cellular models (Do et al., 2019; Hansen et al., 2020; Joshi et al., 2020). In our specific case, EVs preferred cell uptake pathways were further explored by the assessment of diverse internalization inhibitors performance during EV-GLA uptake process (Figure S3). Multiple routes were found involved in the internalization of EV-GLA as highlighted by the impairment in cell fluorescence intensity after 2 h of EVs incubation in cells pretreated with: dynasore (DYN) 80 μ M –inhibition of endocytic vesicle scission from cell membrane–, chlorpromazine (CHP) 20 μ M –inhibition of clathrin mediated endocytosis–, nystatin (NYS) 50 μ M –inhibition of caveolae mediated endocytosis– and 5-(N-ethyl-N-isopropyl) amiloride (EIPA) 100 μ M –inhibition of macropinocytosis– (Figure S3D, left graph). Interestingly, looking at longer EVs incubation times, 4 h, only EIPA maintained the magnitude of the inhibition while the other inhibitors became ineffective (DYN and NYS) or reduced their effect (CHP) (Figure S3D, right graph). These results suggested a predominant contribution of clathrin mediated endocytosis and macropinocytosis in our EV-GLA uptake, in agreement with previous reports (Li et al., 2020).

Further, final intracellular fate of EVs was assessed in HEK293 cells by the co-localization of EV-GLA with LAMP1 lysosomal marker by stochastic optical reconstruction microscopy (STORM), a technique that allows the visualization of individual EVs (Nizamudeen et al., 2018). Co-localization between EVs' signal and LAMP1 was marginally detected 4 h post administration (Figure S4) and clearly observed after overnight incubation, representing the $4.2\% \pm 1.7\%$ of the total number of EV internalized (Figure 2B). EVs have been shown to enter the cells by different routes, and not all of them necessarily ending into the lysosomal compartment (Mulcahy et al., 2014). According to our results, a significant part of the EVs were uptaken through endocytosis, reaching the lysosome after the endosomal maturation and allowing content release of GLA and the hydrolysis of its substrate. A similar process of cellular uptake has been recently described for EVs containing GBA (Do et al., 2019) and TPPI³⁵ lysosomal enzymes.

Once we confirmed that enzyme-loaded EVs reached the lysosomal compartment, we further explored if GLA and SGSH enzymes kept their activity when delivered in EVs. Remarkably, not only protein quantity but specific enzymatic activity was also significantly increased in GLA and SGSH encapsulated in EVs (Figure 2C). Thus, in EV-GLA, 10-fold higher enzymatic activity was detected compared to the activity of soluble GLA from cell supernatants ($P < 0.0001$). Also, 11-fold increase in activity was found in EV-SGSH, compared to commercially available recombinant SGSH (rSGSH, $P = 0.0042$). GLA enzymatic

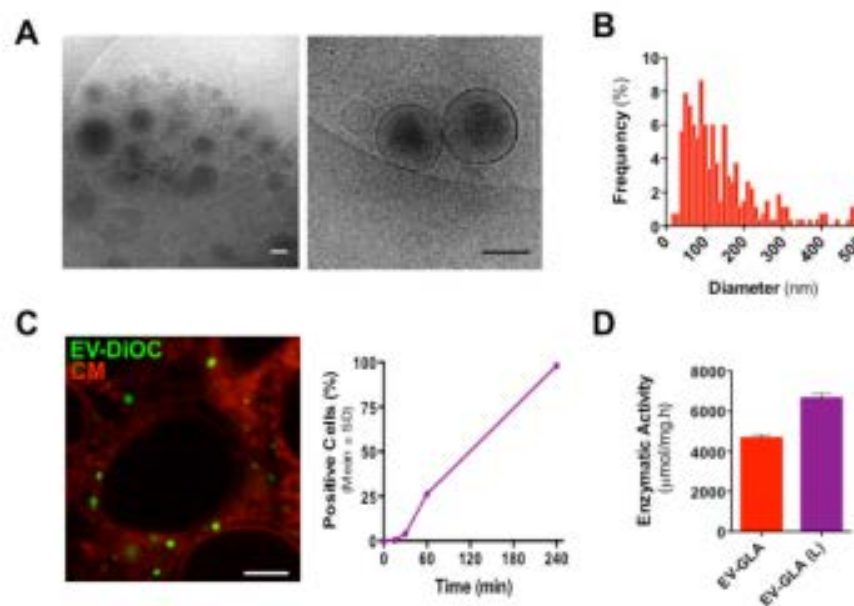


FIGURE 3 EVs stability after lyophilization. A) CryoTEM images of EV-GLA after lyophilization. Magnification bars correspond to 200 nm. B) Size distribution of EV-GLA post-lyophilization. C) Cell internalization of lyophilized EV by confocal microscopy (left panel) and flow cytometry (right panel) in HEK293 cells. For microscope imaging, EVs were labelled with DiOC (green) and cell membranes stained with Cell Mask (CM, red). DiD-labelled EV-GLA were used for cell cytometry. Magnification bar corresponds to 5 μm. D) Specific enzymatic activity of GLA in EVs before (red bar) and after lyophilization (purple bar)

activity was also measured in non-transfected CHO cells, rendering very low but detectable enzymatic activity levels. It is possible that such significant increases in GLA and SGSH activities inside EVs could be due to a higher stability of the enzymes within a more physiological environment, namely acidic pH and a membranous scaffold, as previously described for GLA loaded into artificial lipid structures (Cabrera et al., 2016). Nevertheless, no increments in enzymatic activity have been reported for other lysosomal enzymes loaded in EVs by cell transfection over the cell lysates, namely TPP1, (Haney et al., 2019) HGSNAT (Fedele et al., 2018) and GBA (Do et al., 2019). Therefore, further research is needed to unveil protein conformational quality attributes within EVs and determine whether other enzymes and proteins with catalytic activity could also benefit from EVs encapsulation. In addition, previous studies have suggested that EVs offer natural protection to the enzymes from the action of proteases (Haney et al., 2019). This is also the case for EV-GLA. As shown in Figure 2D, incubation EV-GLA with trypsin, a serine protease that will degrade GLA or any protein/peptide having serine residues, resulted in a 25% loss of protein content, whereas such loss was increased to a 65% when naked GLA was trypsin-treated using the same conditions. The loss of GLA in EV-GLA samples could be attributed to the presence of free GLA co-precipitated with the EV-GLA during the isolation procedure (Figure S2)

Overall, cell internalization and crude enzymatic activity assays suggested that EVs are suitable delivery systems for lysosomal enzymes. For further confirmation that EVs could be therapeutically effective, in vitro efficacy assays were conducted in MAEC derived from Fabry KO mice, a very handful in vitro model of the Fabry disease (Shu et al., 2005). Indeed, due to the lack of endogenous alpha-galactosidase A activity, these cells accumulate high levels of Gb3, the predominant storage product in Fabry patients and the main responsible of the clinical manifestations of the disease (Desnick et al., 2001). In MAEC cells, at 0.001 μg/ml of GLA, EV-GLA were four to five times more efficacious hydrolyzing Gb3, than soluble GLA (Figure 2E, $P = 0.0381$). Remarkably, EV-GLA also overcame the efficacy of agalsidase alfa, the enzyme used in the clinical setting ($P = 0.0286$, at 0.001 μg/ml of GLA).

2.3 | EVs withstand lyophilization and are safe for intravenous administration

Knowing that pharmaceutical development of EVs would require an off-the-shelf product with preserved bioactivity, we studied the stability of EVs after lyophilization. Even in the absence of cryopreservants, EV-GLA withstood lyophilization with minor changes in the vesicle morphology (Figure 3A, B). Lyophilized EVs maintained enzymatic activity values comparable to those of non-lyophilized EVs and kept the ability to cell-internalize, showing that lyophilization was not largely affecting EVs' biofunctionality (Figure 3C, D). Certainly, freeze drying was previously shown to be a useful method to preserve enzymes in EVs (Frank

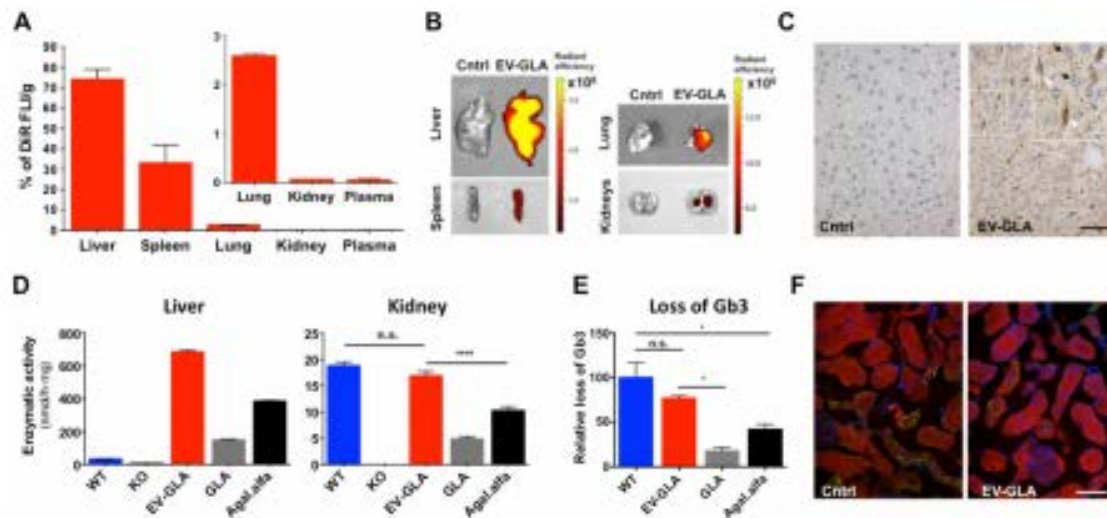


FIGURE 4 In vivo biodistribution and single-dose efficacy of EV-GLA in Fabry KO mice. A) Biodistribution of DiR-labelled EVs in Fabry KO mice 1 h after i.v. administration (100 μ g of protein) showed a widespread distribution of the fluorescent signal in different organs. B) Ex vivo fluorescence images of the liver and kidneys. C) GLA protein detected by immunohistochemistry in liver tissues of GLA KO mice administered with vehicle (Ctrl) or EV-GLA. Magnification bar corresponds to 50 μ m. Inset contains a magnified area to identify hepatocytes (black arrows) and Kupffer cells (with arrowheads) (D) GLA enzymatic activity measurements of mice treated with a single administration of EV-GLA, free enzyme GLA or agalsidase alfa at 1 mg GLA/kg and euthanized 1 h post-administration in liver and kidneys. WT animals and non-treated KO animals were also included in the assay. E) Loss of Gb3 in KO mice treated with a single dose of EV-GLA, free enzyme GLA or agalsidase alfa (1 mg/kg) and euthanized 1 week after. F) Immunofluorescence of Gb3 (green signal) in kidneys of KO animals, vehicle-treated (Ctrl) or receiving one i.v. dose of EV-GLA (1 mg/kg). Nuclei were stained with DAPI (blue) and cells with rhodamine-phalloidin (red). Magnification bar corresponds to 40 μ m

et al., 2018), although sugar additives were thought to be indispensable to prevent EV aggregation and functionality (Bosch et al., 2016).

Because ERT based on EVs would likely rely on the intravenous (i.v.) administration of EV-GLA, hemocompatibility and safety studies were also conducted (Figure S5). Results showed that EV-GLA did not alter cell proliferation capacity (Figure S5C), caused damage to red blood cells nor did they induce any platelet significant aggregation (Figure S45,B), which allowed further testing in animal models. Accordingly, C57BL6 mice were administered with 7 i.v. doses of EVs. As expected, none of the animals showed adverse effects as a consequence of the repeated administration of the EVs or enzymes. Moreover, body weights were comparable to control (non-treated) mice, also suggesting an adequate safety profile (Figure S5D). These results are in agreement with previous studies showing the safety of EVs (Fleury et al., 2014; Li et al., 2016; Somiya et al., 2018; Wiklander et al., 2015).

In addition, biodistribution assays were conducted with DiR-labelled EV-GLA Fabry KO mice were sacrificed 1 h post-administration and tissue samples taken for ex vivo fluorescence imaging. In the first biodistribution assay (Figure 4), EV signal was mainly observed in liver and spleen, while minor but significant amount of fluorescence was also detected in kidneys and lungs (Figure 4A,B). No signal has been observed in the heart, brain, skin and muscles (not shown). These results agree with previous studies on EV biodistribution showing major accumulation in liver and spleen after systemic EV administration (Wiklander et al., 2015). Furthermore, the delivery of the GLA along with the EV was first confirmed by the immunodetection of the GLA protein in livers of Fabry KO mice (Figure 4C). Thus, both, hepatocytes and Kupffer cells from the livers of KO mice treated with EV-GLA showed strong GLA signal, whereas non-treated KO mice showed a complete absence of the GLA protein. EV distribution was also confirmed by measuring GLA enzymatic activity in organs of mice administered with 1 mg/kg of GLA protein as EV-GLA, free GLA or clinically approved agalsidase alfa (Figure 4D). Activity assays were in agreement with the tissue biodistribution of EV-GLA shown by fluorescence imaging and GLA immunohistochemistry. In our hands, for the same GLA dose, more enzymatic activity was seen in livers and kidneys from animals administered with EV-GLA compared to those receiving free GLA or agalsidase alfa. In the case of the liver, administration of exogenous GLA, either naked or encapsulated in EV, resulted in a significant increase of enzymatic activity in the organ, far beyond the endogenous activity seen in wild type (WT) animals. This is probably related to the fact that most of the administered dose is accumulated in the liver. Conversely, in kidneys where few EVs arrived according to fluorescence biodistribution ($0.377\% \pm 0.04\%$ of the total fluorescent signal), GLA enzyme delivered by the EVs increased the enzymatic activity up to the normal levels detected in healthy WT animals (no statistically significant differences among groups), while the free GLA or the clinically approved agalsidase alfa only recovered 60% of the activity seen in kidneys of WT mice ($P < 0.0001$). Hence, for the same GLA administered dose, EVs bring

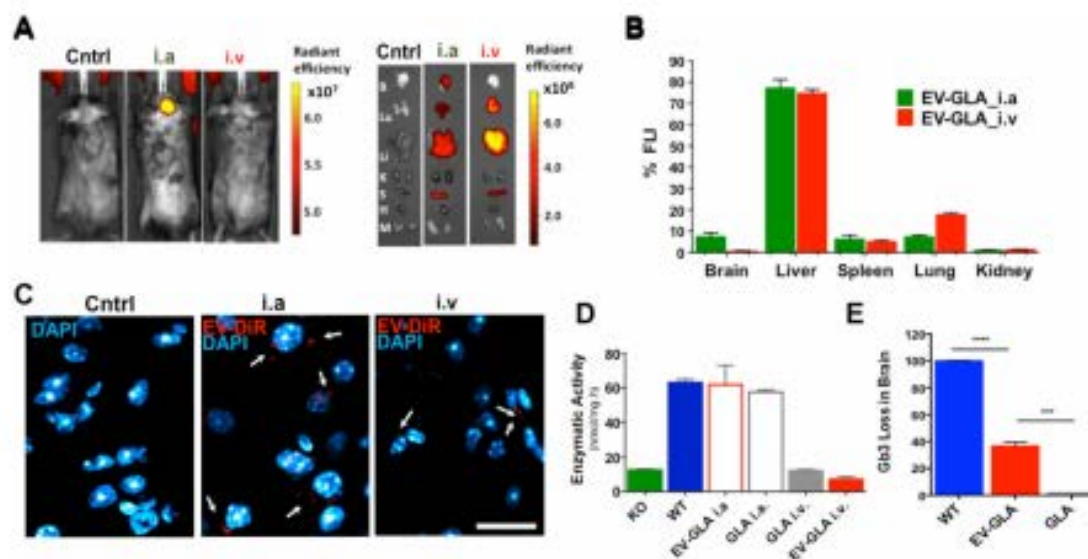


FIGURE 5 EV-GLA in the brain parenchyma. A) In vivo (left panel) and ex vivo (right panel) fluorescence imaging (FI) of Fabry KO mice receiving either intra-arterial (i.a.) or intravenous (i.v.) administration of DiR-labelled EV-GLA (1 mg/kg of GLA) compared to the non-treated controls (Cntrl). Ex vivo imaging included brain (B), lungs (La), liver (Li), kidneys (K), spleen (S), heart (H) and muscle (M). B) FI signal quantification comparing biodistribution of EV-GLA after i.v. or i.a. administration. C) Confocal images of brain parenchyma showing DiR fluorescent signal of EV-GLA (red) and DAPI-labelled cell nuclei (blue). Magnification bar corresponds to 20 μ m. D) GLA enzymatic activity 1 h post-administration in brains of Fabry KO mice treated with GLA or EV-GLA via i.v. or i.a. administrations E) Loss of Gb3 in KO mice treated i.v. with a single dose of EV-GLA, as measured by LC-HRMS 1 week after dosing

significantly more enzymatic activity to the kidneys' than non-encapsulated enzyme. This is probably due to the fact that the delivery of enzyme within EVs allows the combination of three different phenomena: increased intrinsic enzymatic activity, protection against protease degradation, and advantageous differential uptake. In the context of ERT, it is worth noting that the distribution and tissue accumulation of the free GLA are governed by presence of mannose-6-phosphate receptors (M6PR), which are highly expressed in the liver (Sly et al., 2006). However, as cell internalization of EVs does not depend on the presence of M6PR, other tissues with lower M6PR expression such as kidneys, might particularly benefit from ERT treatments based on EVs. This could be especially relevant in Fabry disease, where most of classic male and some female patients present advanced stages of chronic kidney disease (Sunder-Plassmann, 2006).

To measure the impact of EV-GLA treatment in the kidneys, Gb3 levels were determined in KO animals receiving a single dose GLA, EV-GLA or agalsidase alfa (Figure 4E, Figure S6). Our results showed that a dose of 1 mg/kg of EV-GLA was able to reduce Gb3 deposits to wild type (WT) levels ($P = 0.333$), hydrolyzing four times more Gb3 than free GLA at the same concentration ($P = 0.0286$). Reduction of Gb3 levels was also observed by immunofluorescence in the kidneys of KO mice treated with EV-GLA (Figure 4F).

2.4 | EV-GLA cross the BBB and reduce Gb3 deposits in brain

Crossing the BBB to reach the brain parenchyma is hampered when performing i.v. administration of lysosomal proteins. This prevents the use of current ERT in diseases affecting the central nervous system. However, there are several examples of EVs crossing the BBB in the literature, most of them dealing with the delivery of siRNA or microRNA in EVs after intranasal administration. (Guo et al., 2019; Haney et al., 2015) Among them, those using i.v. administration of EVs took profit of the natural brain tropism of EVs derived from brain endothelial cells (Yang et al., 2015), used macrophage derived EVs in diseases coursing with neuroinflammation (Haney et al., 2019; Yuan et al., 2017) or modified EVs to overexpress BBB crossing peptides (Alvarez-Erviti et al., 2011; Yang et al., 2017). Therefore, in an attempt to evaluate if EV-GLA would overcome this barrier, we explored the brain accumulation of fluorescently labelled EVs administered through, i.v. by tail administration and intra-arterially (i.a.) through the cannulation of the external carotid artery (ECA). While in the i.v. route, exogenously administered compounds only reach the brain circulation after passing through the heart and lungs, in the i.a. administration, cannulation of the ECA allows higher exposure of the compound to brain endothelia (Joshi et al., 2008). In this second biodistribution assay, fluorescent in vivo imaging showed strong DiR fluorescent signal in the brain of mice administered through the carotid (Figure 5A, B), precisely

in the hemisphere where arterial cannulation was performed. Ex vivo images were obtained after withdrawing the circulating blood and perfusing the animals with PBS. Our data confirmed that fluorescent signal reached brain parenchyma to a significant extent through the i.a. route ($7.49\% \pm 2.32\%$ of total fluorescence intensity). On the contrary, brain accumulation of DiR after i.v. administration could not be distinguished from background signal. In agreement to this, DiR signal was also located in brain parenchyma of EV-treated mice, 1 h post-administration, using confocal microscopy. Fluorescent signal was intense in the case of mice that received the EV-GLA by arterial infusion, and much lower, although detectable, in animals treated intravenously (Figure 5C).

We wondered whether the i.a. administration could also facilitate the crossing of the BBB. To confirm this hypothesis, GLA KO animals were i.a. or i.v. treated with EV-GLA and also free recombinant GLA enzyme that is known to be unable to cross the BBB in conventional i.v. ERT. The enzymatic activity of GLA was measured in brain tissues 1 h post-administration. Accordingly, no GLA enzymatic activity could be detected in brains of KO mice administered i.v. with free GLA or with EV-GLA. However, significant enzyme activity was observed when the naked enzyme and EV-GLA were administered i.a. (Figure 5D). These data suggest that GLA (free and EV-GLA) cross the BBB in higher amount when using intra-arterial administration instead of i.v. Nonetheless, because the sensitivity of the techniques used to measure GLA activity and biodistribution in the brain have important limitations, we also evaluated Gb3 levels in mice, 1 week after a single i.v. administration of GLA and EV-GLA (1 mg/kg of GLA, Figure 5E and Figure S6). Remarkably, our results clearly showed that EV-GLA was able to significantly reduce Gb3 deposits in a $36.6 \pm 2.97\%$ while free GLA did not induce any reduction of the substrate ($P = 0.0009$). Overall these results indicate that i.v. administered EV-GLA is able to reach the brain parenchyma and restore the therapeutic activity at the lysosomal cell compartment. Noteworthy, we show here that EVs, derived from non-cancerous and non-dendritic cells and with no specific modifications to reach the brain, are able to cross the BBB after i.v. administrations. The avidity of GLA protein for lipids might explain, at least in part, its ability to trespass the hematoencephalic barrier (Spencer & Verma, 2007) although the exact mechanisms used by EVs to cross the BBB need further investigation.

3 | CONCLUSION

Protein-loaded EVs directly obtained from mammalian cell factories and isolated by polymer co-precipitation methods work as highly efficient protein delivery platforms for ERT in lysosomal disorders. EVs from CHO and HEK cells transfected with GLA and SGSH genes, respectively, are biocompatible, withstand lyophilization and contain high quantities of the recombinant enzymes with increased biological activity. This activity is remarkably higher than the one exhibited by the soluble recombinant proteins in cell supernatants. Further, in Fabry disease mice models, a single dose of GLA containing EVs outperform the activity of the non-encapsulated enzyme and the clinical marketed reference. After a single intravenous administration, EV-GLA significantly reduces disease biomarkers Gb3 and LysoGb3 in target tissues including kidneys and brain parenchyma. This proof-of-concept work sets the basis for a potential implementation of EVs-driven replacement therapy in different LSDs, opens the way for a potential treatment strategy in disorders showing CNS involvement.

4 | EXPERIMENTAL SECTION

Plasmid preparation and mammalian cell line transfection: The alpha-galactosidase A (GLA) gene was obtained from the commercial vector pReceiver-M10 (EX-Q0172-M10, OmicsLink ORF Expression Clone), coding for the cDNA version of the GLA gene (NM_000169), with c-myc and 6xHis tags fused to the C-terminus for detection and purification purposes. The gene was subcloned to pOptiVEC-TOPO (Invitrogen, ThermoFisher) that allows the expression of the gene of interest along with the dihydrofolate reductase (DHFR) as auxotrophic selection marker. CHO DG44 *dhfr* cells (a dihydrofolate reductase deficient cell line) were transfected (FreeStyle MAX, ThermoFisher) and further selected under methotrexate hydrate (MTX, Sigma) up to $4 \mu\text{M}$. A single clone (namely CHO-DG44-GLA clone #3) was isolated and cryopreserved. For EVs harvesting, CHO-DG44-GLA clone #3 was grown in CD OptiCHO medium with 8 mM L-Glutamine to a final cell concentration of 2×10^6 cells/ml. Cell supernatants containing EVs and soluble, free GLA enzyme were harvested by centrifugation at 3900 rpm for 15 min.

The sequence of human N-sulphoglucosamine sulphohydrolase (SGSH, BC047318.1) was cloned into the pTriExL1-Hygro vector. Due to the cloning strategy, an extra triplet encoding for an alanine residue was added after the first methionine codon, obtaining a final SGSH protein, with 510 aminoacids in length and a molecular weight of 57.7 kDa. To obtain EVs, SGSH protein was transiently overexpressed in human embryonic kidney cell line (HEK293FT). Briefly, plasmid DNA was polypeplexed with polyethylenimine (PEI) at a ratio 1:3 (w/w) in OptiMEM serum free media and added to cells cultured in exosome-free media (Gibco). Four hours after transfection, valproic acid (4 mM, Sigma-Aldrich) was added to improve protein expression. Supernatants were collected for EVs isolation after 72 h of incubation at 37°C and 5% CO_2 in a humidified incubator. Commercially available SGSH protein (Bionova) was purchased to compare the enzymatic activity of the SGSH purified from EVs.

Purification of EVs: Supernatants (SN) coming from protein producing cell cultures were used to isolate EVs. In detail, cryovials of CHO-DG44-GLA clone #3 (containing 10 million total cells) were thawed and expanded under standard procedures. Briefly, in each passage, cells were diluted to a final cell density of 1×10^6 viable cells/ml. In the last passage before supernatant harvesting, cells were diluted to a final cell concentration of 2×10^6 cells/ml. Finally, supernatant containing extracellular vesicles and soluble, free enzyme was harvested by centrifuging the cell culture at 3900 rpm for 15 min. SN were centrifuged at 300 g at 4°C for 10 min in order to remove dead cells. Additional centrifugation steps at increasing centrifugation speed 2000 g, 10 min 4°C and 10,000 g 20 min 4°C were carried out to remove potential sub-cellular debris. Clarified SNs were concentrated via VIVAspin 30,000 KDa (Sartorius) centrifugation, 7000 g, and 10 min 4°C. Concentration factors varied from 50X to 100X depending on the sample. EVs were precipitated from concentrated SN through the addition 1:1 (v/v) of 'Total Exosome Isolation Reagent', (Invitrogen) and overnight incubation at 4°C. Samples were centrifuged at 16,000 g for 1 h at 4°C and pellets containing the EVs resuspended in PBS. SN of non-transfected CHO cells were also subjected to the same procedures to obtain control EVs (EV-Control)

Soluble, free GLA protein with the cmc- and His-tag of CHO cell supernatants was purified by affinity chromatography with a HisTrap Excel, 5 ml column (GE Healthcare) according to the manufacturer's instructions. Briefly, supernatant was directly injected to the column and later eluted by applying an imidazole gradient (20 to 500 mM). Protein was dialyzed against 0.01 M acetic acid (pH 5.5) and then centrifuged (3900 rpm, 15 min) and filtered (0.2 μ m) to discard putative aggregates. Purified enzyme was stored at -80°C for further uses.

EVs characterization: Morphometric assessment of purified EVs was carried out by CryoTEM analysis. A 3 μ l drop of the samples were deposited onto holey carbon on a 400-mesh copper grid, previously treated by glow discharge. The grid was mounted on a plunger (Leica EM GP), water excess removed by blotting with filter paper and EVs suspension straightforward vitrified by rapid immersion in liquid ethane. Samples were mounted on a Gatan 626 cryo-transfer system and inserted into a Jeol JEM 2011 Cryo-electron microscope. It was operated at 200 kV using different degrees of defocus (500–900 nm) to obtain an adequate phase contrast. Images were recorded using a Gatan Ultrascan US1000 CCD camera and further processed using ImageJ NIH software (Eliceiri et al., 2012). EVs diameters were measured and size distributions generated from at least 250 particles from random fields. Particle size distribution and concentration were further studied by Nanoparticle Tracking Analysis (NTA) with Nanosight NS300 (Malvern Panalytical, Malvern, UK). Appropriate dilution of the sample in PBS was performed in order to adjust the range of particles per frame to the working range of the system (10^6 – 10^9 particle/ml). A total of 3 videos were captured at cell temperature of 22°C and syringe speed of 30. >1400 tracks were acquired per video. Data was further processed using NanoSight Software NTA 3.1 Build 3.1.46 with a detection threshold of 5.

EVs or cell lysates were prepared by diluting EVs samples 1:5 in CellLytic reagent (Sigma), homogenized ultrasonic homogenizer (Labsonic M, Sartorius), and total protein amount was determined by BCA method (Pierce, Rockford, IL, USA). GLA and SGSH quantifications were performed by western blot, using known amounts of recombinant proteins, algalidase alfa (Replagal, Shire) or recombinant SGSH (rSGSH, Bionova) and specific antibodies against GLA (ProteinTech) and SGSH (Sigma) at 1:2,000 dilution. Antibodies against CD63 (1:200, SantaCruz), CD81 (1:200, SantaCruz), TSG101 (1:1000, Abcam), β -tubulin (1:1,000, Invitrogen), cystinosin (1:1000, Mybiosource) and GBA (1:1000, Abcam) were also used to characterize EVs. 20 μ g of total protein was loaded per lane with the exception of β -tubulin and GLA detection in which 10 μ g of total protein were employed. Secondary anti-mouse HRP-conjugated antibody (1:10,000, Dako) was developed using Immobilon reagent (Millipore), and images were digitally acquired (LI-COR Odyssey Fc imaging system) and quantified (ImageJ NIH). Protease resistance was determined by incubating 1 μ g of GLA and equivalent amounts of its EV-GLA counterpart in 0.2% trypsin at 37°C for 45 min. After Trypsin digestion appropriate volumes were loaded into 10% PAA gels and GLA immunodetected as detailed above. Densitometry analysis of GLA bands was carried out using ImageJ NIH software. Band signal was defined with the IntDen or integrated density, an Image J descriptor consisting in the product of mean intensity and band area.

Enzymatic activity determinations: GLA enzymatic activity was determined fluorometrically as described previously^{16,17} by monitoring the transformation of the substrate 4-Methylumbelliferyl β -D-galactopyranoside (4-MUG, Sigma) into fluorescent 4-methylumbelliferone (4-MU). SGSH enzymatic activity was assessed by two consecutive enzymatic reactions as previously detailed by Karpova and co-workers, (Karpova et al., 1996) using the same standardized procedure followed in clinical diagnosis of MPSIIIA. Accordingly, substrate 4-methylumbelliferyl- α -D-N-sulfoglucosaminide (4MU- α GlcNS, Enantia) was incubated with EV-SGSH and rSGSH samples for 17 h at 37°C to generate 4-MU- α GlcNH₂. Fluorescent 4-MU was then released by α -glycosidase (Sigma) after 24 h of incubation at 37°C. Different dilutions of the EV and protein samples were tested to ensure that obtained 4-MU fall within the linear range of the technique. Final values for enzymatic activity were given in μ mol of 4-MU product generated per hour and mg of GLA or SGSH enzyme or referred to total protein content when dealing with tissue activities.

Cell culture conditions: HEK293T cells (CRL-3216, ATCC) were routinely maintained in RPMI medium supplemented with 10% foetal bovine serum (Life Technologies, Paisley, UK), 2 mM L-Glutamine (Life Technologies), 1 X Non-essential aminoacids (Life Technologies), 1X antimycotic-antibiotic (Life Technologies) solution at 37°C and 5% CO₂. Mouse endothelial aortic cells (MAEC) were isolated from descending aorta of GLA deficient mice (GlatmKull) at the ICTS NANBIOSIS (U20) following procedures previously established procedures (Giannotti et al., 2016; Nazareus et al., 2015; Shu et al., 2005). Endothelial origin of isolated cells was confirmed by CD105 staining (12-1051, eBioscience) and flow cytometry (FacScalibur, Becton Dickinson).

EV fluorescent labelling: DiOC, DiD, or DiR (Invitrogen) were incubated to a concentration of 250 $\mu\text{g}/\text{ml}$ with EVs for 30 min at 37°C. Samples were dialyzed (Slide-A-Lyzer MINI Dialysis Device, 3.5K MWCO, 0.1 ml, Thermo Scientific) against PBS, to remove unbound fluorophore and avoid potential artifacts. The absence of significant fluorescent signal after dialysis on labelling controls, namely diluent at an equivalent fluorophore concentration than the used to label EVs, was confirmed (data not shown).

Flow cytometry: DiOC labelled EVs were added to HEK293 cultures, 2.5 μg EVs/ml, and incubated for 15, 30, 60 and 240 min. After incubation plates were treated with trypsin 0.05 % (w/v) (Biological Industries) to detach cells, and neutralized in complete RPMI medium supplemented with DAPI (1 $\mu\text{g}/\text{ml}$ final concentration), in order to remove dead cells from analysis. Cell fluorescence intensity was analyzed in a LSR Fortessa flow cytometer (Beckton Dickinson). Data were further processed using FCS express 4 software (De novo software) and median fluorescence intensity represented. All time points were tested in duplicate.

Confocal microscopy: HEK293 or MAEC cells were seeded in an 8 chambered coverglass (Lab-Tek II, Eppendorf) and incubated 24 h at 37°C and 5% CO_2 . Then, 2.5 $\mu\text{g}/\text{ml}$ DiOC labelled EVs were added and incubated for 4 h. Cell medium was removed and cells were stained with 5 $\mu\text{g}/\text{ml}$ Cell Mask™ (Invitrogen) and fixed in 4% paraformaldehyde (PFA). Image acquisition was carried out by spectral confocal microscopy FV1000 (Olympus) with a PLAPON 60XO objective. Z projections sections were acquired with a step size between 0.4 and 0.6 μm and further reconstructed using ImageJ.

STORM: HEK293 cells were incubated with 2.5 $\mu\text{g}/\text{ml}$ DiD-labelled EVs during 4 h, 8 h or O.N in cell culture conditions. After fixation with 4% PFA, cells were permeabilized (300 mM sucrose, 50 mM NaCl, 20 mM HEPES, 3 mM MgCl_2 and 0.5% Triton X100, 5 min at 4°C) and blocked with 1% BSA in PBS, prior to the incubation with anti-LAMP1 (1:1000, Abcam), 1 h at RT. After washing, Alexa 488-labeled anti-mouse secondary antibody (1:200, Invitrogen) was incubated for an additional hour. Samples were imaged in STORM buffer (5% w/v glucose, 100 mM cysteamine, 0.5 mg/ml glucose oxidase and 40 $\mu\text{g}/\text{ml}$ catalase in PBS) to ensure an adequate photoswitching of the fluorophores. DiD-labelled EVs were imaged with a 647 nm laser (160 mW) and Alexa 488 immunolabelled lysosomes with a 488 nm laser (80 mW) using NIS-Elements software in Nikon Eclipse Ti microscope (Nikon Europe, Amsterdam). The sample was illuminated using a total internal reflection fluorescence (TIRF) alignment system and the z-level was kept constant by Nikon perfect focus system. Fluorescence was collected by a Nikon 100x, L49 NA oil immersion objective and images acquired with a Hamamatsu 19 ORCA-Flash 4.0 camera. For each channel 20,000 frames were acquired and analyzed by fitting a 2D Gaussian function to obtain the localizations of fluorophores. Co-localization was determined using the *Analyze Particles* tool in ImageJ setting a minimum size of 0.02 μm^2 (corresponding to a circular object with an 80 nm radius) and no constraints on circularity. The centre positions of lysosome channel images and EVs channel images were loaded onto a custom Matlab script considering a particular EV being inside a lysosome when its centre was closer than 50 nm to the centre of a lysosome.

In vitro efficacy (NBD-Gb3 assays): MAEC at passages 2 to 5 were seeded in 24 well plates 24 h after seeding 8 μM of fluorescent N-Dodecanoyl-NBD-ceramide trihexoside (NBD-Gb3, Matreya LCC) was added to the cultures along with specified concentrations of tested compounds. After 48 h incubation, cells were trypsinized and NBD-Gb3 fluorescent signal was analyzed by flow cytometry (FacsCalibur, Beckton Dickinson) and FCS Express v4 software. To calculate the percentage of NBD-Gb3 signal, fluorescent signal in control cells (without treatment) was established as 100% and the values accordingly normalized.

Lyophilization: Aliquots of 150 μL of EV-GLA (8.4 mg/ml of total protein), previously frozen at -80°C, were lyophilized in a VirTis sentry 2.0 freeze dryer (Sp scientific). No additives or cryopreservants were added. Morphology and functionality of EVs post-lyophilization was assessed as described above.

In vivo assays: All animal experimentation, including the obtention of MAEC, was performed following procedures previously approved by the Ethical Committee for the Use of Experimental Animals (CEEAA) at the Vall d'Hebron Research Institute (VHIR), Barcelona and the local government (CEA-OH/9572). Male GLA deficient mice (GlatmKull1, C57BL/6 background) with ages ranging from 2 to 4 months were used for biodistribution and efficacy studies.

Biodistribution: In the first assay, each mouse ($n = 3$) was treated by tail vein injection with 100 μg , total protein (5 μg of GLA/mouse), of DiR-labelled EVs and euthanized 1 h post-administration. In the second assay, i.v. (tail vein) and i.a. administrations were compared in mice ($n = 3$ per group) treated with 1 mg/kg in GLA equivalents of DiR-labelled EVs (c.a. 35 μg of GLA/mouse) and euthanized 1 h post-administration. I.a. administrations were adapted for mice following previously described procedures in rats and using procedures (Janowski et al., 2013). In both biodistribution assays, fluorescent images of ex vivo tissues were acquired (IVIS Spectrum), quantified (Living Image software) and referred to the weight of the wet tissue when required. EV visualization was performed in PFA fixed and OCT embedded tissues sections counterstained with DAPI (Sigma-Aldrich) by confocal microscopy. GLA enzymatic activity was measured in harvested tissues, following procedures described above, a referred to the total protein content determined by the BCA method (Pierce, ThermoFisher).

Immunohistochemistry: The presence of GLA antigen in liver was analyzed by pre-treating paraffin-embedded formalin fixed sections with 100 mM citrate buffer (pH 9) in a pressure cooker. Sections were incubated with 10% normal goat serum (NGS) in antibody diluent (1% BSA in 100 mM Tris buffer) and then of 1:150 dilution of anti-GLA antibody (HPA00237, Sigma). Secondary antibody consisted in a HRP conjugated system (EnVision+ System-HRP Labelled Polymer anti-Mouse), which was later visualized with DAB and counterstained with Harris haematoxylin. Gb3 deposits were identified using anti-Gb3 monoclonal antibody (1:50, Clone BGR23, Amsbio) in paraformaldehyde fixed and OCT embedded frozen tissues. Sections were incubated with a

secondary antibody (1:1000, A10684, Invitrogen) and counterstained with DAPI and rhodamine-phalloidin (Sigma-Aldrich). Visualization was performed by confocal microscopy as explained above.

Efficacy assays in vivo: Fabry KO mice ($n = 24$) were randomized in four different groups (vehicle, agalsidase-alfa, GLA and EVs-GLA), and received a single doses of 1 mg/kg of GLA protein. Vehicle treated animals receive the corresponding volume of PBS and additional group of non-treated WT male littermates was also included. Animals were euthanized 24 h or 1 week after dosing. Tissue samples were snap frozen and kept at -80°C upon analysis. Gb3 and LysoGb3 levels were determined with LC-HRMS at Institute of Advanced Chemistry of Catalonia (IQAC-CSIC) (Supplementary Information).

Statistical analysis: All graphs show the mean and the SEM, unless otherwise stated. For statistical analysis, whenever data followed a normal distribution (Kolmogorov-Smirnov test) unpaired Student's *t*-test was used for peer comparisons between EV-GLA and controls. Alternatively, non-parametric Mann-Whitney test was applied. The significance threshold was established at $P < 0.05$, and significance levels were schematically assigned * ($0.01 \leq P < 0.05$), ** ($0.001 \leq P < 0.01$), *** ($0.0001 \leq P$). All the analyses and graphs were performed using GraphPad Prism 6 software (GraphPad, San Diego).

5 | ASSOCIATED CONTENT

Supporting Information. Methodology for EV isolation methods by TFF, sucrose cushion and iodixanol gradient, lyophilization and LC-HRMS determinations, as well as results on EV isolation, characterization, cell internalization and in vivo safety and efficacy are available as supplementary information.

ACKNOWLEDGEMENTS

Apart from the funding stated below, we are grateful to the technical contribution of Alexandre Garcia with the Gb3 and LysoGb3 determinations, Judit Tomsen-Melero for aiding with the TFF purification and Marta Martínez-Vicente for helping with the identification of lysosomal proteins. We are also thankful to Martí de Cabo and the 'Servei de Microscòpia' of the Autonomous University of Barcelona (UAB) for technical assistance with electron microscopy and to Dr. J.A Bernabé for support with NTA. AV received an ICREA Academia Award.

CONFLICTS OF INTEREST

Joaquín Seras-Franzoso, José Luis Corchero, Simó Schwartz Jr and Ibane Abasolo are co-applicants of a patent describing the use of engineered EV for the producing highly active enzymes (P201930056, 24/01/2019).

AUTHOR CONTRIBUTIONS

The manuscript was written through contributions of all authors. All authors have given approval to the final version of the manuscript.

FUNDING SOURCES

This study has been supported by ISCIII (PI18_00871 co-funded by Fondo Europeo de Desarrollo Regional (FEDER)), and CIBER-BBN (EXPLORE) granted to IA. Different CIBER-BBN units of ICTS 'NANBIOSIS' have participated in this work (<https://www.nanbiosis.es/plattform-units/>), more specifically the UI/Protein Production Platform for protein purification, Unit 6 for NTA analysis and TFF purification and U20/FVPR for in vivo assays.

REFERENCES

- Alvarez-Erviti, L., Seow, Y., Yin, H., Betts, C., Likhaj, S., & Wood, M. J. A. (2011). Delivery of siRNA to the mouse brain by systemic injection of targeted exosomes. *Nature Biotechnology*, 29(4), 341–345.
- Bandaranayake, A. D., & Almo, S. C. (2014). Recent advances in mammalian protein production. *FEBS Letters*, 588(2), 253.
- Batrakova, E. V., & Kim, M. S. (2015). Using exosomes, naturally-equipped nanocarriers, for drug delivery. *Journal of Controlled Release*, 219, 396–405.
- Beck, M., Ricci, R., Widmer, U., Dehout, F., De Lorenzo, A. G., Kampmann, C., Linhart, A., Sunder-Plassmann, G., Houge, G., Ramaswami, U., Gal, A., & Mehta, A. (2004). Fabry disease: overall effects of agalsidase alfa treatment. *European Journal of Clinical Investigation*, 34(12), 838–844.
- Bobrie, A., Colombo, M., Krumeich, S., Raposo, G., & Théry, C. (2012). Diverse subpopulations of vesicles secreted by different intracellular mechanisms are present in exosome preparations obtained by differential ultracentrifugation. *Journal of Extracellular Vesicles*, 1, 18397.
- Bodary, P. F., Shryman, J. A., & Eitzman, D. T. (2007). Alpha-Galactosidase A in vascular disease. *Trends in Cardiovascular Medicine*, 17(4), 129–133.
- Bosch, S., de Beaurepaire, L., Allard, M., Mosser, M., Heichette, C., Chretien, D., Jegou, D., & Bach, J. - M. (2006). Trehalose prevents aggregation of exosomes and cryodamage. *Scientific Reports*, 6(1), 36362.
- Busatto, S., Vilanilam, G., Ticer, T., Lin, W. - L., Dickson, D., Shapiro, S., Bergese, P., & Wolfram, J. (2018). Tangential flow filtration for highly efficient concentration of extracellular vesicles from large volumes of fluid. *Colloids*, 7(12), 273.
- Cabrera, I., Abasolo, I., Corchero, J. L., Elizondo, E., Gil, P. R., Moreno, E., Farado, J., Sala, S., Bueno, D., González-Mira, E., Rivas, M., Melgarejo, M., Pulido, D., Albericio, F., Royo, M., Villaverde, A., García-Parajo, M. F., Schwartz, S., Ventosa, N., & Veciana, J. (2016). α -Galactosidase-A loaded-nanoliposomes with enhanced enzymatic activity and intracellular penetration. *Advanced Healthcare Materials*, 5(7), 829–840.
- Concolino, D., Deodato, E., & Parini, R. (2018). Enzyme replacement therapy: efficacy and limitations. *Italian Journal of Pediatrics*, 44, 120.

Review

For reprint orders, please contact: reprints@futuremedicine.com

Nanomedicine



The potential of nanomedicine to alter cancer stem cell dynamics: the impact of extracellular vesicles

Petra Gener¹, Patricia Gonzalez Callejo^{1,2}, Joaquín Seras-Franzoso¹, Fernanda Andrade¹, Diana Rafael^{1,2}, Ibane Abasolo^{1,2} & Simo Schwartz Jr^{*,1,2}

¹Drug Delivery & Targeting Group, Molecular Biology & Biochemistry Research Centre for Nanomedicine (CIBBM-Nanomedicine), Vall d'Hebron Institut de Recerca, Universitat Autònoma de Barcelona, 08035 Barcelona, Spain

²Networking Research Centre for Bioengineering, Biomaterials & Nanomedicine (CIBER-BBN), Instituto de Salud Carlos III, 28029 Madrid, Spain

* Author for correspondence: simo.schwartz@vhik.org

The presence of highly resistant cancer stem cells (CSCs) within tumors as drivers of metastatic spread has been commonly accepted. Nonetheless, the likelihood of its dynamic phenotype has been strongly discussed. Importantly, intratumoral cell-to-cell communication seems to act as the main regulatory mechanism of CSC reversion. Today, new strategies for cancer treatment focusing into modulating tumor cell intercommunication and the possibility to modulate the composition of the tumor microenvironment are being explored. In this review, we summarize the literature describing the phenomenon of CSC reversion and the factors known to influence this phenotypic switch. Furthermore, we will discuss the possible role of nanomedicine toward altering this reversion, and to influence the tumor microenvironment composition and the metastatic spread of the disease.

First draft submitted: 6 March 2020; Accepted for publication: 5 October 2020; Published online: 16 November 2020

Keywords: cancer stem cells • dynamic phenotype • extracellular vesicles • nanomedicine

Cancer stem cell models (the hierarchic model, stochastic model & dynamical tumor initiation model)

Remarkable similarities between embryonic development and tumor growth were acknowledged as early as the 19th century [1]. Later, in 1953, Dixon and Moore postulated for the first time that tumor cells possess characteristics similar to germinal cells and concluded that, in most cases, undifferentiated cells are the origin of tumor development [2]. However, the real breakthrough regarding the cancer stem cell (CSC) theory of tumor development came 40 years later from studies on the origin of acute myeloid leukemia [3]. Those studies demonstrated that only few rare cells (CSCs) were capable of initiating leukemia in mice. A strong resemblance of these cells with hematopoietic stem cells (HSCs) was also shown. They expressed typical HSC markers ($lin^-CD34^+CD38^-$) and showed high capacity for self-renewal and differentiation. Notably, tumors that appeared after the *in vivo* transplantation of only few CSCs in mice were composed of a mixture of cells that was very similar to the one found in the initial tumor [3,4]. Since the first description of leukemic stem cells, CSCs have been identified in many types of cancers, including solid tumors [5–9]. Ever since, the CSC theory has been constantly modified based on growing knowledge, mostly disputing CSC characterization principles and the basis of tumor initiation [10–13].

The CSC model was originally referred to as a hierarchic model in which cancer cells originate from a precursor stem cell (CSC). This precursor cell divides either symmetrically, giving two identical CSCs or two differentiated cancer cells (DCCs), or asymmetrically, giving one CSC and one DCC [3]. Accordingly, the distinctive ability of these cell types regarding tumor initiation has been considered as an indispensable feature to distinguish CSCs from DCCs [3,14,15]. The presence of CSCs that fits into the hierarchic model has been demonstrated in some models of breast cancer where as few as a hundred CSCs were able to form tumors in mice, whereas tens of thousands of cells

Future
Medicine

with alternate phenotypes failed to form tumors [16]. Additional studies on brain and colon cancers also identified such subpopulations of rare cells that produce tumors *in vivo* [17,18].

In this context, even though clinicians often observe tumor shrinkage at the first stages of multimodal treatment, often remaining resistant clones of CSCs survive and eventually cause tumor relapse and very aggressive tumor types with limited treatment alternatives [19–21]. According to the hierarchic model, only the complete abolition of CSCs can eradicate a tumor [22,23]. Thus, considerable efforts have been invested to find what distinguishes CSCs from normal stem cells and/or DCCs, to allow specific therapeutic targeting of CSCs without affecting normal cells. However, it has not been possible so far to find a marker that would solely identify cancer cells with 'stem' characteristics in distinctive tumors and tumor cell lines. Most markers identified in some cell lines that segregated cells with tumor-initiating capacity were not confirmed in other cell lines, even from the same origin. Several CSC markers have been discarded since cells expressing them have not been able to show higher tumor-initiating capacities than other tumor cells. Often, identified markers distinguish cells of mesenchymal characteristics (i.e., CD44⁺/CD24⁻ in breast cancers) that confer tumor cells' more aggressive potential and the ability to induce metastatic growth. These markers, however, are not useful in tumor cell lines of mesenchymal origin. Some additional inconsistencies of the hierarchic model came from the observation that in some cases, even if CSCs were successfully eradicated, tumor growth and spread was evident [24,25]. The original CSC hypothesis has been further challenged by studies demonstrating that in some leukemias, more mature progenitor cell types or even cells expressing lineage markers can serve as leukemia-initiating cells as well [26–28].

These discrepancies raise the possibility that tumor-initiating cells might also come from differentiated cells that reacquire self-renewal capabilities [29]. Accordingly, an alternative stochastic model of tumorigenesis has been suggested. This model postulates that under a permissive environment, every cancer cell has the ability to self-renew and can recapitulate the phenotype of the disease because of the possibility of interconversion among cell phenotypes [30–33]. Indeed, under stress conditions or after eradication of the CSC repository, some DCCs can switch their phenotype into a stem-like phenotype to ensure tumor survival and progression [15,30,34–36].

In cell cultures in attachment conditions, CSCs divide asymmetrically, reaching a final steady state with a stable CSC population rate characteristic for each cancer cell line. In addition, when DCCs are plated alone, CSCs appear after a few days in culture to regenerate the CSC population [24]. In low attachment conditions, where DCCs are not able to survive, these cells can also undergo de-differentiation to ensure survival. However, when cell culture conditions are again favorable (i.e., in attachment), the equilibrium of CSCs versus DCCs is re-established. This is accompanied by an adjustment of the stemness gene expression and invasive potential of these cells. Accordingly, de-differentiated cells in low attachment conditions rapidly express high levels of CSC genes, whereas in attachment conditions, the stemness expression signature of these DCCs is reverted. Similarly, cells cultured in low attachment are more invasive [24]. DCC to CSC reversion can be also observed *in vivo* [24,37]. There is evidence that intestinal epithelial cells and hepatocytes have CSC potential in colon and liver cancer models, respectively [24,38,39].

Of note, this plasticity process seems much more common than previously believed. In fact, a similar feature also occurs with healthy differentiated cells, which are known to reach a stemness state under traumatic conditions [40].

Importantly, since tumors are composed of various cell types and not only of cancer cells, the interconversion does not affect only DSCs and CSCs. In fact, a complex tumoral microecosystem that includes immune cells and stromal cells exists within a tumor, forming the so-called tumor microenvironment (TME) [41]. Cancer cells directly interact with other cells within the TME through paracrine signaling and/or direct cell-to-cell contact signaling to create a favorable physical and molecular signaling environment, to ensure tumor progression [42].

Cancer cells interact with other cells through a combination of mechanical interactions, enzymatic modification of the structure of the extracellular matrix (ECM) and signaling interactions, all of which have an effect on tumor progression and the dissemination of cancer cells (Figure 1) [43,44]. To acknowledge all of these important players, recently a new dynamical tumor initiation model for a mixed population has been proposed. It involves CSCs, DCCs and other cell types, such as quiescent cells, immune cells and fibroblasts, among others (Figure 1) [45]. In this dynamic model, each cell population becomes a nonlinear dynamical system based on its own proliferation rates controlled by chemical and/or biological pathways, and physical interactions. The dynamics are governed by the possibility of full tumor extinction, but also of overshooting dynamics after a period of remission or postsurgical relapse [45]. Importantly, implementation of the realistic complexity of tumor growth regulation changed the view of its effective eradication. Based on the dynamical tumor initiation model, the most promising strategies to fight cancer spread should be the ones that target the activator of the CSC phenotype rather than CSCs because of the feedback loops between CSCs and DDCs. New therapeutics (including nanomedicines) should thus emerge in

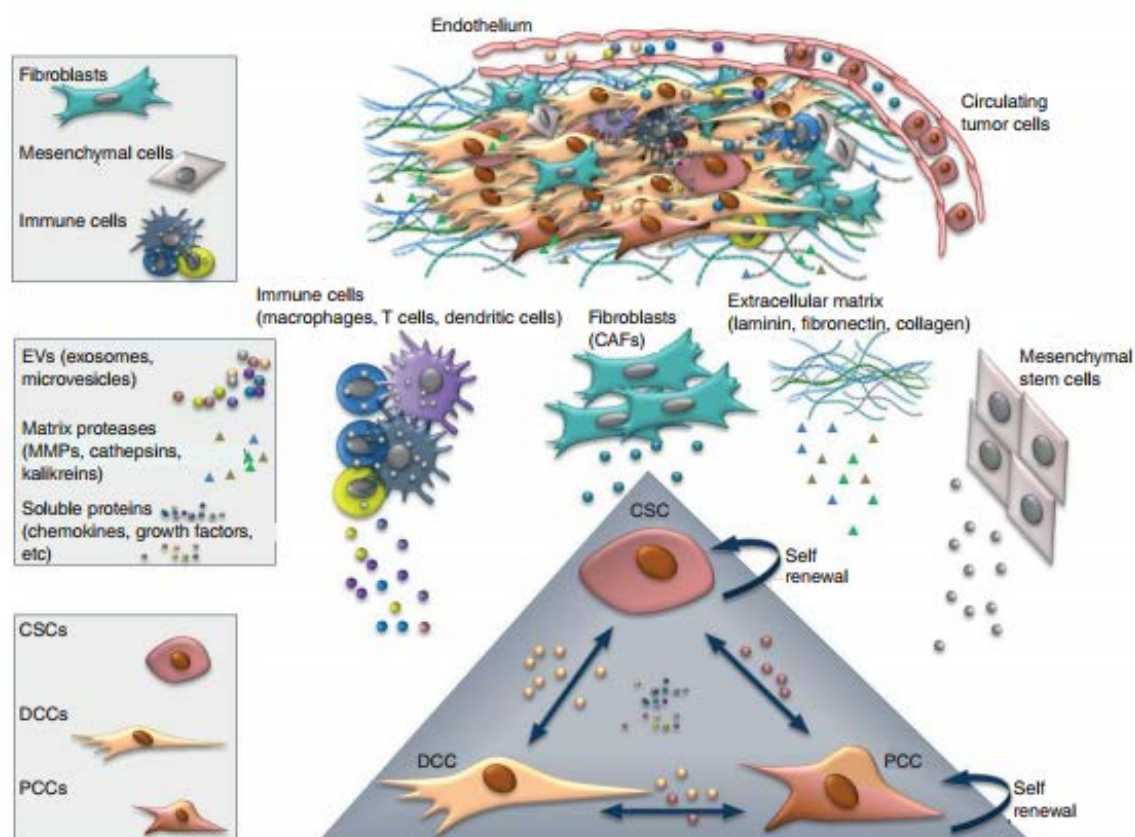


Figure 1. Dynamic cancer stem cell model. A tumor is a highly complex heterogenic dynamic entity that involves cellular components (CSCs, DCCs, fibroblasts, immune cells, mesenchymal cells, etc), cell-secreted functional molecules (growth factors, hormones, metabolites, cytokines, chemokines, etc), EVs (exosomes, vesicles, etc) and the extracellular matrix. Cancer cell subpopulations (CSCs, DCCs, PCCs) within tumors are characterized by their respective densities and rates, and the alteration of these densities and rates alters the equilibrium state of the tumor as a whole biological system. Self-renewal and differentiation rates of cancer cells are finely tuned by all tumor microenvironment players (fibroblasts, immune cells, mesenchymal cells, the extracellular matrix) to ensure tumor progression. CAF: Cancer-associated fibroblast; CSC: Cancer stem cell; DCC: Differentiated cancer cell; EV: Extracellular vesicle; PCC: Pluripotent cancer cell.

this direction [46,47]. With numerical simulations, the model highlights how modifications of the environment, in which the tumor expands, can abruptly change its long-time behavior [45].

Regulation of phenotypic dynamism via intratumoral communication

A role for extracellular vesicles

A tumor should be regarded as a highly complex heterogenic dynamic entity that evolves over time, best adapting to its local microenvironment and the immune system to ensure its survival. Cell-to-cell interactions, affecting CSCs' dynamic phenotype and tumor immunological response, should thus be carefully considered when proposing new anticancer nanomedicine-based therapies. Indeed, tumors from patients with recurrent resistant tumors show higher numbers of CSCs [48]. This clearly suggests the need to develop new effective treatments targeting CSCs, since CSCs account for therapy resistance and represent a cellular depot responsible of tumor regrowth and its metastatic spread [11]. Moreover, modifiable immune cells at the niches also have an important role in tumor spread, cell adaptability and survival [49].

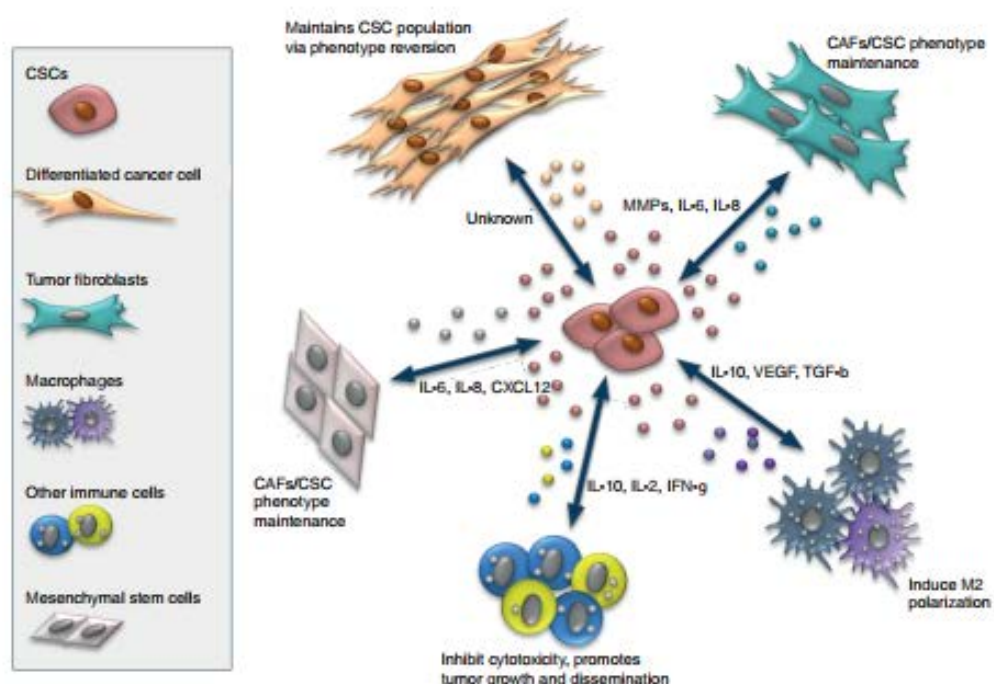


Figure 2. Signaling within the tumor niche. Complex pathways are necessary for the maintenance of the homeostasis of the CSC population. All cellular components (CSCs, DCCs, fibroblasts, immune cells, mesenchymal cells, etc.) of the tumor niche perceive the modulator effects of EVs and soluble proteins emitted by CSCs, resulting in exasperated functional capabilities. In turn, other cells from the TME produce paracrine signaling to ensure CSC growth and dissemination.
CAF: Cancer-associated fibroblast; CSC: Cancer stem cell.

Both cellular and noncellular components of the tumor niche contribute to maintain the required equilibrium and to regulate cellular plasticity [50,51]. Within the tumor niche co-exist cellular components (CSCs, DCCs, fibroblasts, immune cells, mesenchymal cells, etc), cell-secreted functional molecules (growth factors, hormones, metabolites, cytokines, chemokines, etc), extracellular vesicles (EVs; exosomes, vesicles, etc) and a sophisticated ECM that take part in integrating multiple external and internal signals to calibrate self-renewal and differentiation rates of CSCs (Figure 1) [52]. These complex pathways are essential for the maintenance of the homeostasis of the CSC population. In this regard, cell subpopulations within tumors are characterized by their respective densities and rates, and the alteration of these densities and rates alters the equilibrium state of the tumor as a whole biological system. These alterations immediately initiate the process of cell phenotypic interconversion to maintain the balance. All cellular and molecular components of the tumor niche receive the modulator effects of CSCs, resulting in exasperated functional capabilities, which in turn produce a propitious environment for CSC growth and dissemination (Figure 2).

Nonetheless, the exact molecular mechanisms that control the dynamic phenotype of CSCs still remain widely unknown. In melanoma, maintenance of the slow-cycling (JARD1B-positive) stem cell subpopulation has been proved to be dynamic. Sorted JARD1B positive cells (CSCs) gave a rise to JARD1B-negative cells, and, conversely, a single JARD1B-negative cell (DCC) originated in a heterogeneous progeny including JARD1B-positive cells [53]. Similarly, in breast cancer, it was demonstrated that basal-like mammary epithelial cells are able to spontaneously de-differentiate into stem-like cells [54]. This further reinforces the hypothesis of the existence of a controlled balance

between CSC and DCC populations, and suggests that cancer cells opt for de-differentiation as a survival mechanism under stress conditions (i.e., chemotherapeutic treatments) [30,34]. In fact, it has also been shown that several external factors, cell interactions and paracrine cell-to-cell communication are involved in the regulation of this process. As an example, in bladder cancer, prostaglandin E2 that is secreted by apoptotic cancer cells after chemotherapy promotes proliferation of adjacent CSCs [55]. Similarly, in breast cancer, IL-6 is secreted by DCCs to induce CSCs, to maintain this dynamic equilibrium via IL-6-JAK1-STAT3 signaling [56]. Further, various aspects like cell pluripotency, invasion, proliferation, differentiation, tumor recurrence and resistance to apoptosis/treatment, among others, are regulated by constant paracrine cell-to-cell communications in both tumors and metastatic sites [13,57]. Late evidence suggests that this communication is at least partially mediated by EVs (Figure 2).

EVs encompass a very heterogeneous population of lipoproteic vesicles that are released into the extracellular space [58]. The main subtypes of EVs are microvesicles (MVs), exosomes and apoptotic bodies. EV subtypes differ substantially in their origin and biogenesis and thus also in their composition and size. MVs are formed by direct outward budding of plasma membrane, whereas exosomes are formed by an inward budding of the early endosomes. The maturation into multivesicular bodies is necessary during this process. However, apoptotic bodies are formed by a separation of the plasma membrane from the cytoskeleton as a result of an apoptotic process, during which dying cell contract due to increased hydrostatic pressure [59].

Although specific features have been proposed for each EV subpopulation, the identification of specific markers of each subgroup is still under debate [60]. Recently, the minimal feature requirements regarding EV characterization and a guideline to standardize studies performed with EVs have been summarized and consented [61]. Exosomes, MVs and apoptotic bodies are currently categorized based on size (small, medium or large), density (low, medium or high) and some specific markers (Alix, TSG101, HSC70 and HSP90 β) [61].

Due to their biogenesis, EVs may contain a high variety of molecular cargo of their cell of origin, such as DNA, proteins, mRNA, microRNA and lipids, which can affect multiple signaling pathways inside target cells [62]. Subsequently, EVs may trigger phenotypic changes after the interaction with their target cells, whereas single molecules that bind to a single receptor at the cell surface would often activate a single molecular pathway. Indeed, tumor cells secrete EVs bearing immunosuppressive molecules and facilitate the immunogenic escape of a growing tumor [63]. For these reasons, EVs are now considered as leading actors of the intercellular communication signaling, mediating both physiological and pathological responses.

Within EVs, big interest is centered toward exosomes, as it was shown that exosomes participate in cell-to-cell communication, cell maintenance and tumor progression. In addition, exosomes have been found to stimulate immune responses by acting as antigen-presenting vesicles [58,64]. Importantly, the contents of the exosomes are not a random array of signaling molecules from undergoing intracellular events but a specific set of proteins, genetic information and lipids that essentially come from the plasma membrane and the cytosolic compartment, with very limited amounts of compounds from other intracellular compartments, such as the nucleus, the endoplasmic reticulum and the Golgi apparatus. This makes exosomes clearly different from other membrane vesicles (i.e., vesicles released by apoptotic cells). Thus, the so-called hEXO motif (an RNA-binding protein) that is responsible for miRNA sorting toward exosomes via direct binding has been recently identified [65]. Further, Wani and Kaul reported that miR-2909 is packaged in tumor exosomes by a specific 30-end post-transcriptional modification of the miRNA [66]. However, knowledge regarding exosome constitution is still missing, and strong efforts are currently devoted to unraveling how to target specific content to exosomes and EVs.

In 2007, a group led by Jan Lötvald revealed that mRNA and/or microRNA from EVs (exosomes) could be translated into proteins in target cells, providing the first demonstration of a genetic information cell-to-cell transfer mediated by exosomes [67]. Equally, EVs released by embryonic stem cells can reprogram hematopoietic progenitors by horizontal transfer of specific mRNA and proteins. Comparable 'information exchange' represents one of the critical components of conditioning premetastatic niches and is involved in the control of CSC self-renewal and tumor expansion. Released EVs can directly stimulate surrounding cells by interacting with specific surface receptors or transferring from one cell to another various bioactive molecules, including membrane receptors, proteins, mRNA, microRNA and even whole organelles (Figure 1).

The colonization by metastatic cells requires the existence of a hospitable microenvironment in distal sites that allows an adequate hosting of the metastatic arriving cells, fostering their survival. Accordingly, EVs derived from tumor cells can remain at the extracellular space, can remain at the site of origin or can enter into biological fluids, reaching distal sites and participating in the creation of premetastatic niches. Moreover, exosomes from other cells involved in the TME (i.e., fibroblasts, stromal cells, immune cells) influenced CSC-DCC balance in a bidirectional

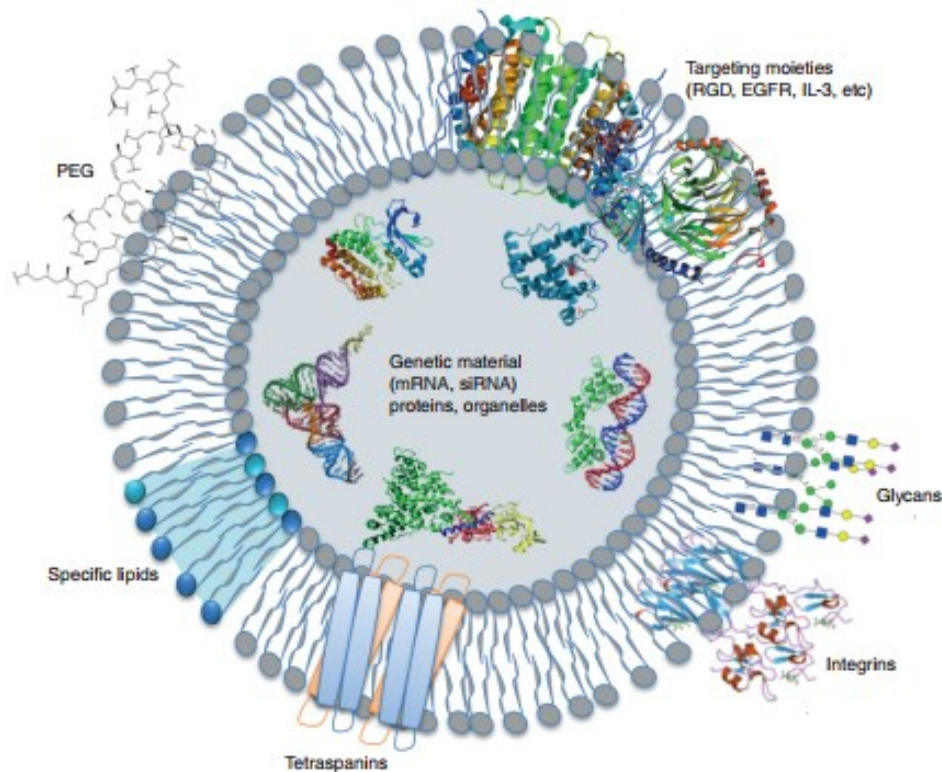


Figure 3. Structure of extracellular vesicles. Extracellular vesicles are lipid vesicles with a complex membrane composition. They express multiple families of proteins, such as tetraspanins (CD63, CD81, CD9), heat shock proteins (HSC70), lysosomal proteins (Lamp2p) and fusion proteins, such as CD9, flotillin and annexin, at the membrane. Within the inner core, they may contain mRNA, miRNA, proteins and organelles, among others.

This approach was first used by Alvarez-Erviti *et al.* to produce EVs displaying the neuron-specific RVG peptide on their surface [79]. Importantly, the authors demonstrated brain-targeting capability of the engineered EVs that delivered stable siRNA after systemic administration in mice. A similar approach has been used to deliver imatinib and siRNA to leukemic cells, using EVs with overexpressed IL-3 on their surface [80].

Another way to tailor-make EV surface targeting peptides is through membrane functionalization by covalent modification. Accordingly, this technique modifies directly isolated EVs rather than modifying their cells of origin. In this regard, EVs with both imaging and therapeutic properties by loading paramagnetic iron oxide nanoparticles and curcumin have been proposed for a glioblastoma theranostic approach. Targeting of glioma has been increased by adding the neuropilin-1-targeted peptide to the exosomal membrane by click chemistry [81]. Alternatively, the membrane of EVs was functionalized by a cationic lipid and pH-sensitive peptide (GALA) conjugation to improve EV cellular uptake and cytosolic release [82]. It was also demonstrated that it is possible to increase the specificity of EVs to target cancer cells through an RNA nanotechnology approach. To this aim, cholesterol-conjugated RNA aptamers harboring a specific targeting domain for cancer cells were developed. Resultant EVs conjugated with RNA nanoparticles harboring EGFR aptamers and loaded with survivin siRNA were able to inhibit breast cancer growth in mice [83]. Some examples of successful preclinical EV development are summarized in Table 1. Nonetheless, even though EVs have demonstrated clear prospects as natural delivery systems, many

Table 1. List of modified extracellular vesicles designed to alter the tumor microenvironment.

Extracellular vesicle source	Extrinsic cargo	Extrinsic targeting	Cancer type	Ref.
Bone marrow-derived MSCs	TRAIL	N/A	Various cancers	[84]
Various carcinoma cells	Doxorubicin, cisplatin, methotresate	N/A	Various cancers	[85]
B16-F10 melanoma cells	SPIONs	N/A	Melanoma	[86]
LNCaP, PC-3 cancer cells	Paclitaxel	N/A	Prostate cancer	[87]
Immature dendritic cells	Doxorubicin	iRGD-Lamp2b	Breast cancer	[88]
Bovine milk	Paclitaxel	N/A	Lung cancer	[89]
B16BL6 melanoma cells	CpG DNA	N/A	Melanoma	[90]
HEK293T	Imatinib, BCR-ABL siRNA	IL3-Lamp2b	Leukemia	[76]
H22 hepatocarcinoma cells	Doxorubicin, 5-FU	N/A	Hepatocarcinoma	[91]
Raw 264.7 macrophages	Doxorubicin	DEAP	Colon cancer	[92]
HeLa cervical cancer cells	Dextran	GALA	Cervical cancer	[82]
Primary dendritic cells	VEGF siRNA	AS1411 aptamer (nucleolin targeting)	Breast cancer	[93]
Divers origins	SPIONs and curcumin	RGERPPR (neuropilin1 targeting)	Glioma	[81]
Macrophages	Paclitaxel	N/A	Lewis lung carcinoma	[94]
HEK293T	TP52 siRNA	LAMP2b-DARPin G3 (HER2/Neu targeting)	Breast cancer	[78]
Mesenchymal stromal cells	Paclitaxel	N/A	Pancreatic cancer	[95]
Red blood cells	miR-125b-2, Cas mRNA	N/A	Leukemia, breast cancer	[96]
Plants (grapefruit)	miR-17, miR18s	N/A	Brain and colon cancer	[97,98]

MSC: Mesenchymal stem cell, N/A: Not applicable.

aspects of their stability, integrity and reproducibility need to be considered during scale-up production. In fact, the great interest and expectations toward the use of EVs as nanocarriers is hampered by a current low-production rate to high-production cost ratio. In addition, some regulatory aspects regarding the clinical use of modified EVs have not been entirely defined. Specific guidelines and regulation regarding EV isolation and characterization (content, surface, isolation method) is thus required to speed up the translation from bench to bedside of EV-based nanomedicines.

Nanomedicines to modulate the tumor microenvironment & reduce tumor spread

As mentioned earlier, the interaction between stromal and tumor cells within a specific TME plays a critical role in tumor growth and dissemination. Cancer cells require mechanical support, blood supply and growth factors secreted by stromal cells to guarantee continuous growth [99]. In fact, the initiation of tumor growth and metastatic growth is linked with the alteration of the healthy stroma and the appearance of a pro-tumoral environment (i.e., inflammatory signatures). This process includes neoangiogenesis, infiltration of fibroblasts and immune cells, and extensive remodeling of the ECM, and exhibits strong similarities to normal wound healing [100]. Cancer stroma thus not only supports but rather directs cancer progression and dissemination.

The most abundant cells of the tumor stroma are cancer-associated fibroblasts (CAFs), which significantly influence cancer growth and progression through TME control [101]. As mentioned previously, a bidirectional paracrine communication between CAFs and CSCs/DCCs is indispensable to maintain the required balance of cell populations within the TME. Of note, normal fibroblasts are activated into overproliferative CAFs by sonic hedgehog proteins that CSCs secrete into the niche. These in turn activate CAFs via upregulation of the WNT/hedgehog signaling pathway [102]. However, CAFs are the main source of multifunctional cytokines (IL-6, IL-8) that regulate CSC–DCC balance and neoangiogenesis within the TME [103–105]. Importantly, paracrine CAF/tumor cell signaling could also be mediated by EV signal transfer as described previously. In addition, CAFs secrete a variety of growth factors (i.e., transforming growth factor β (TGF β), vascular endothelial growth factor and platelet-derived growth factor, interleukins and ECM components (i.e., collagens, fibronectins and metalloproteinases) that support tumor growth, generate a physical barrier against drugs and immune infiltration, and facilitate cancer invasion [101,103–105]. Indeed, CAFs may directly influence tumor infiltrating immune cells and modulate the immune microenvironment.

paracrine setting (Figure 2). Fibroblasts have been reported to secrete diverse bioactive factors such as cytokines (IL-6, IL-8) that can mediate the conversion of DCCs into CSCs [68]. Further, the communication between tumor cells and stromal cells in the metastatic niche, mediated by EVs released by the primary tumor, has a critical role in facilitating cancer metastasis. It has been shown based on specific expression patterns of integrins and glycans that tumor-derived EVs are uptaken by tissue-specific cells to prepare premetastatic niches [69,70].

Furthermore, the resistance of tumor cells to chemotherapeutic treatments also involves cellular intercommunication mediated by EVs, as intratumoral CSC/DCC content is relevant to define the treatment response and recurrence of tumor. Released EVs evacuate pro-apoptotic proteins or directly withdrawn therapeutic drugs from cells. Indeed, resistant CSCs release significantly more EVs than cells responsive to antitumor therapy. Moreover, EVs also appear to favor CSC survival by reducing the responsiveness of T cells or directly inducing apoptosis in activated antitumor T cells [57]. In fact, fibroblasts and immune cells at the tumor niches are substantially involved in tumor spread, adaptability and survival [49]. Understanding the tight relationship among CSCs, the TME and the immune response is essential for developing effective anticancer nanomedicine-based treatments (Figure 2).

EVs as natural nanocarriers engaged in cell-to-cell intercommunication

Despite that nanomedicine is regarded as one of the most promising fields of research to bring new treatment strategies in cancer care, only very few (2%) nanocarrier-based treatments have successfully entered into clinical trials. Moreover, only a limited handful (15) of these formulations have reached clinical practice [4]. There are a variety of reasons for this still suboptimal translation from bench to bedside, like inadequate physicochemical features of nanomaterials, improper preclinical efficacy and safety, and regulatory and manufacturing issues. Further, changes of the properties and complexity of the nanomaterials when in biological fluids (i.e., protein corona, cargo release, opsonization) are difficult to compute and significantly alter the functionality of nanomedicines after administration [71]. There are multiple factors that modulate the toxicity of nanomaterials, such as size, shape, porosity and surface charge. Another major hurdle is the feasibility of manufacturing nanomedicines under good manufacturing practices. Although most clinical and preclinical studies have been made from small amounts of materials, large-scale production requires great effort to maintain their physicochemical properties and release capabilities. Currently, a lot of effort is put into amelioration of large-scale synthesis (i.e., CELLLine Bioreactor Flask) that is required for the EV's clinical translation. The other option is the production of synthetic EV-based drug delivery systems (DDS) that could be produced as a large-scale homogeneous population with standardized protocols [72]. In this regard, EVs demonstrate clear prospects as nanocarriers, as they have a biological origin, little toxicity and lack of immunogenicity [73]. EVs are also very promising as delivery systems due to their capacity to directly release their cargo into the cellular cytoplasm of targeted cells. After internalization, EVs can also fuse with the endosomal membrane and release their content [58,64]. Their structure resembles that of liposomes, but their lipid layer has a more complex composition. They are characterized by the presence of multiple families of proteins such as tetraspanins (CD63, CD81, CD9), heat shock proteins (HSC70), lysosomal proteins (Lamp2p) and fusion proteins such as CD9, flotillin and Annexin (Figure 3). The complexity of their membrane composition may help EVs escape endosomes, thus allowing delivery of material into the nucleus, whereas artificial nanocarriers will require complex protein and peptide modifications [74]. However, EVs are known to be nonimmunogenic, which is certainly an advantage to reduce potential treatment resistance if using protein-based therapies, particularly as enzyme replacement therapies. Moreover, EVs might be the best option when dealing with nondruggable target candidates. Further, one of the challenges of drug delivery systems is to optimize their targeting properties to release the therapeutic compounds only in specific organs/tissues of the body, avoiding or reducing systemic toxicity. In this regard, there is strong data in the literature reporting preferential delivery of EVs (exosomes) to specific target tissues according to their integrin and glycan receptor profile of their membrane surface [69,70]. This is one of the reasons that might explain why EVs from different tumor types have a tendency to modify and condition specific distal tissues to host tumor cells as metastatic niches for each particular tumor type.

In this context, modifying EV-producing cells may lead to the design of EVs with adequate profiles that are required to target specific tissues. Previously, EVs donor cells were transfected with pDisplay™ encoding the transmembrane domain of platelet-derived growth factor receptor fused to a peptide that specifically binds to the EGFR. Subsequently, released EVs efficiently delivered miRNA to EGFR+ cancer cells [75]. Alternatively, to further enhance the display of targeting peptides on the EV's surface, a donor cell may be transfected with the engineered vectors that contain a gene of a protein of the exosomal membrane (e.g., Lamp2b) fused with targeting peptides. EVs released from such modified cell lines will display the targeting peptides on their surface [76–78].

Table 2. List of alternative nanomedicines that modulate the tumor microenvironment/immune system.

Nanoparticles	Therapeutic cargo	Targeting	Cancer type	Ref.
Artificial extracellular matrix	N/A	RGD-YIGSR motif (cancer cell targeting)	Breast cancer	[113]
Binary prodrug nanoparticles	Oxaliplatin, NLG919	N/A	Breast cancer	[114]
Carboxymethylcellulose nanoparticles	Docetaxel	N/A	Pancreatic cancer	[115]
Core-shell structured peptide nanoparticles	Doxorubicin	FAP- α antibody (CAF targeting)	Prostate cancer	[116]
Ferritin nanoparticle cage	ZnF 16Pc	Anti-FAP scFv (CAF targeting)	Breast cancer	[117,118]
Hydrogel	Losartan	N/A	Breast cancer	[119]
Immunoliposomes	N/A	Anti-FAP scFv (CAF targeting)	Fibrosarcoma	[120]
IND-liposomes	Indoximod (IND), doxorubicin	N/A	Breast cancer	[121]
Lipid bilayer nanoparticles	Gemcitabine, cisplatin	N/A	Bladder cancer	[122]
Lipid calcium phosphate nanoparticles	Quercetin	Anisamide motif (CAF targeting)	Bladder cancer	[123]
Lipid calcium phosphate nanoparticles	CXCL 12 trap plasmid	N/A	Colon, breast cancer (liver metastasis)	[124]
Lipid nanoparticles	Paclitaxel	Sulfatide	Breast cancer	[125]
Lipid nanoparticles	CXCL 12, PD-L1 trap plasmids	N/A	Pancreatic cancer	[126]
Lipid-protamine-DNA nanoparticles	IL-10, CXCL 12 trap plasmid	N/A	Breast, pancreatic cancer	[127]
Lipid-protamine-DNA nanoparticles	sTRIAL plasmid DNA	Anisamide motif (CAF targeting)	Bladder, pancreatic cancer	[128]
Liposome-protamine-hyaluronic acid nanoparticles	Wnt16 siRNA	Anisamide motif (CAF targeting)	Bladder cancer	[129]
Liposomes	Paclitaxel, marimastat	Hyaluronic acid	Breast cancer	[130]
Nanoemulsion	Fraxinellone	N/A	Melanoma	[131]
Peptidic spherical nanoparticles	Paclitaxel	Anti-FAP peptide (CAF targeting)	Breast cancer	[132]
pH-responsive nanocores	PHIS/RB4B, doxorubicin	Hyaluronic acid	Breast cancer	[133]
PLGA nanoparticles	Tumor antigens	N/A	Breast cancer	[134]
PLGA-PEG nanoparticles	Doxorubicin	Hyaluronidase	Breast cancer	[135]
SPIONs	Relaxin 2	N/A	Pancreatic cancer	[136]

CAF: Cancer-associated fibroblast; FAP: Fibroblast activation protein; N/A: Not applicable.

Activated CAFs express TGF- β , α -SMA, FAP, PDGFR- α/β and S100A4, among others. After activation, CAFs fail to reacquire an inactive status, and therefore they constantly exert a pathophysiological response producing a desmoplastic TME. Further, CAFs may induce epithelial to mesenchymal transition by secreting carbonic anhydrase IX, which causes acidification of the ECM and further enhances the activity of MMP-2 and MMP-9 metalloproteases, which in turn facilitates the local invasion of cancer cells into their surrounding tissues [106]. This has been observed in pancreatic cancer, prostate cancer, squamous cell cancer and melanoma, although with a variable degree of desmoplasia [107–110]. Because of this, new strategies that either reduce stromal desmoplasia or inactivate CAFs have been explored over the past years (Table 2). In this regard, a recent study showed that the anticancer compound minnelide is able to disrupt TGF- β signaling and revert activated CAFs into a quiescent form by decreasing α -SMA expression. Moreover, the application of all-transretinoic acid promotes a quiescent form of pancreatic stellate cells by modulating Wnt- β catenin signaling, reducing tumor progression [111]. Furthermore, hydrophobic drugs with activity against CAFs have been also encapsulated into nanocarriers to improve their solubility. Accordingly, various types of nanocarriers with distinct functions have been proposed against CAFs, including liposomes, polymeric nanoparticles, nanoemulsions and inorganic nanoparticles. In addition, surface moieties have been conjugated to nanocarriers that have been modified to increase their stability in circulation and to enhance targeting efficiency (Table 2). Alternative strategies have been also tested to modify the ECM to enhance the tumor penetration of drugs while reducing metastatic spread of the disease. An example is the use of a PEGylated recombinant formulation of human hyaluronidase (PEGPH20) aimed to improve the tumor penetration efficiency of chemotherapeutics. In fact, hyaluronic acid is a major component of the ECM and increases the interstitial pressure inside tumors. Hyaluronic acid degradation by PEGPH20 normalizes the interstitial pressure within the tumor and enhances the delivery of cytotoxic agents. In this context, PEGPH20 has been successfully tested in combination with cytotoxic drugs in clinics (i.e., nab-paclitaxel/gemcitabine and doxorubicin). Although phase

I–II studies showed promising results in patients with high hyaluronic acid-expressing tumors, the phase III study of PEHPH20 was not as successful and thus its further development is currently on pause. Additional intrinsic factors, such as lack of significant neoantigens, low tumor mutational burden, and epithelial to mesenchymal transition, should be considered [112]. Currently, PEHPH20 is still tested in combination with pembrolizumab (MK-3475) for patients with previously treated hyaluronan-high metastatic pancreatic ductal adenocarcinoma (NCT03634332) and in combination with FOLFIRINOX in patients with newly diagnosed metastatic pancreatic cancer (NCT01959139).

Recently, in addition to chemotherapy, nanocarriers have also been designed to improve the efficiency of cancer immunotherapy. Lipid-calcium-phosphate (LCP) nanoparticles have been successfully used as a peptide vaccine delivery system to stimulate anticancer T-cell response [137]. Another strategy has elegantly combined an LCP-based vaccine with targeted silencing of TGF- β expression at the TME using liposome-protamine-hyaluronic acid nanoparticles. Since TGF- β acts as immune suppressor within the TME, its silencing enhances the systemic immune response against the tumor. A combination of these two nanoparticles offers a flexible and powerful promising platform for immunotherapy [138]. In this regard, nanoparticles have been also conjugated to the surface of transferred T cells, acting as persistent autocrine-like signals to stimulate the immune response against tumors [139]. Further, inflammation regulators such as cytokines have been loaded into CAFs by using targeted nanoparticles to modify the TME [131,140,141]. Another example is the use of a PEGylated liposome (LPD) with a plasmid-encoding CXCL12 fusion protein (CXCL12 trap), combined with PD-L1. CXCL12 trap facilitates the penetration of T cells into the TME, whereas PD-L1 trap allows infiltrated T cells to kill the cancer cells. A similar setting of lipid-coated calcium phosphate nanoparticles (LCP) also resulted in enhanced infiltration of T lymphocytes while causing a drop in the expression of CXCL12 and immunosuppressive cells in the liver, clearly suggesting a potential impact of nanomedicine in modulating anticancer immune response [126].

Overall, the list of alternative nanomedicines that have been successfully explored in preclinical settings as TME/immune system modulators to reduce tumor progression and metastasis is increasing (Table 2). There is no doubt that in the future, new nanomedicine-based strategies against cancer should focus on the use of nanomedicine to therapeutically intervene in the different aspects that define a tumor and its microenvironment, as well as in the immunological response of the immune system to combat metastasis and the preconditioning of metastatic sites.

Conclusion

A tumor should be regarded as a heterogeneous ensemble of different cell types that are in constant intercommunication to orchestrate the growth and dissemination of the tumor. In addition, cells with metastatic potential communicate with distant tissues to prepare niches for hosting and nesting cancer cells to allow spread of the disease. According to the current dynamic CSC model of tumor growth, new nanomedicine-based therapies under development should focus not only on eradicating cancer cells but should also consider all components of the TME. In fact, after the eradication of the CSC population, specific complex mechanisms (feedback loops, phenotypic reversion and paracrine messaging) become active to re-establish the cellular balance within the TME and guarantee the progression and dissemination of the tumor. In this scenario, a clear understanding of the information exchanged between CSCs and differentiated cells (DCCs) to surrounding cells and, further, the understanding of close interactions among players within the metastatic niche are of utmost importance to develop efficient treatments.

Future perspective

According to the state of the art exposed in this review, a deep characterization of the content from secreted EVs as the main responsible actors of the cell-to-cell intercommunication within the tumors and metastatic sites is needed. Deciphering of EV content would lead to a better understanding of the fundamental nature of CSC/DCC crosstalk, the reversion phenotype of DCCs into CSCs, and their impact on immune response, tumor recurrence, metastasis and future clinical treatment outcomes. Similarly, to decoding ENIGMA during World War II that helped allied troops decipher encoded messages from enemy forces and prompted the end of the conflict, EV cargo will provide new candidate targets for future clinical interventions. Deciphering messages emitted by cancer cells and using nanomedicine-based strategies to modulate these messages should counteract metastatic dissemination and treatment resistance, which are the principal causes of mortality of oncologic patients worldwide. Likewise, a better understanding of the immunological processes occurring at the TME should also open the possibility to design new strategies to combat cancer relapse and metastatic spread.

Moreover, standardized protocols for isolation, modification and loading of EVs are required to prompt EV use in clinical practice. Current lack of quality controls under good manufacturing practices for the evaluation of safety and functionalization of large-scale EV production is preserving their use as DDS.

For all of these reasons, it is necessary to gain insight into fundamental processes of EV biology, to understand the basic mechanisms through which these vehicles can target specific cell types and their precise roles in the TME and develop new methodologies to translate their potential as DDS into clinics. This new knowledge will definitely help in further improving EVs for drug delivery in cancer.

Executive summary

Cancer stem cell models (the hierarchic model, stochastic model & dynamical tumor initiation model)

- A tumor should be regarded as a highly complex heterogenic dynamic entity that evolves over time, best adapting to its local microenvironment and the immune system to ensure its survival.
- The dynamic tumor initiation model for a mixed population describes the cancer stem cell (CSC) dynamic phenotype and cancer initiation.

Regulation of phenotypic dynamism via intratumoral communication

- Cancer cells directly interact with other cells within the tumor microenvironment (TME) through paracrine signaling and/or direct cell-to-cell contact signaling to create a favorable physical and molecular signaling environment, to ensure tumor progression.
- Extracellular vesicles (EVs) play an important regulatory role in TME modulation and CSC dynamics.

EVs as natural nanocarriers engaged into cell-to-cell intercommunication

- EVs and nanomedicines designed to modulate the TME should be regarded as effective anticancer therapy rather than CSC elimination.

Nanomedicines to modulate the TME & reduce tumor spread

- To inhibit tumor growth and dissemination, nanomedicines should directly target cancer cells and should also modulate the TME.

Author contributions

P Gener drafted the work and figures. P Gonzalez Callejo, I Seras-Franzoso, F Andrade and D Rafael contributed to the writing, and I Abasolo and S Schwartz Jr revised it critically for important intellectual content and approved the final version.

Financial & competing interests disclosure

This work was partially supported by grant PI17/02242 from Fondo de Investigaciones Sanitarias (FIS) of Instituto Carlos III (ISCIII), co-financed by the European Regional Development Fund (FEDER), and EvoNano project, funded by European Union's Horizon 2020 FET Open Programme under grant agreement no. 800983. The authors have no other relevant affiliations or financial involvement with any organization or entity with a financial interest in or financial conflict with the subject matter or materials discussed in the manuscript apart from those disclosed.

No writing assistance was utilized in the production of this manuscript.

Open access

This work is licensed under the Attribution-NonCommercial-NoDerivatives 4.0 Unported License. To view a copy of this license, visit <http://creativecommons.org/licenses/by-nc-nd/4.0/>



References

Papers of special note have been highlighted as: • of interest

1. Capp JP. Cancer stem cells: from historical roots to a new perspective. *J. Oncol.* 2019, 5189232 (2019).
2. Dixon FJ, Moore RA. Testicular tumors; a clinicopathological study. *Cancer* 6(3), 427–454 (1953).
3. Bonnet D, Dick JE. Human acute myeloid leukemia is organized as a hierarchy that originates from a primitive hematopoietic cell. *Nat. Med.* 3, 730–737 (1997).
- First article describing the existence of cancer stem cells.
4. Lapidot T, Sirard CF, Vormoor JF *et al.* A cell initiating human acute myeloid leukaemia after transplantation into SCID mice. *Nature* 367(6464), 645–648 (1994).
5. Dionne L, Driver E, Wang X. Head and neck cancer stem cells: from identification to tumor immune network. *J. Dent. Res.* 94(11), 1524–1531 (2015).

Review Article

Dynamism, Sensitivity, and Consequences of Mesenchymal and Stem-Like Phenotype of Cancer Cells

Petra Gener ^{1,2}, Joaquin Seras-Franzoso,¹ Patricia González Callejo,^{1,2} Fernanda Andrade,^{1,3,4} Diana Rafael,^{1,2} Francesc Martínez,¹ Sara Montero,^{1,2} Diego Arango,⁵ Joan Sayós,⁶ Ibane Abasolo,^{1,2,7} and Simó Schwartz Jr. ^{1,2}

¹Drug Delivery and Targeting Group, CIBBIM-Nanomedicine, Vall d'Hebron Institut de Recerca (VHIR), Vall d'Hebron Barcelona Hospital Campus, 08035 Barcelona, Spain

²Networking Research Center on Bioengineering, Biomaterials and Nanomedicine (CIBER-BBN), 08035 Barcelona, Spain

³IS- Instituto de Investigação e Inovação em Saúde, Universidade do Porto, Porto, Portugal

⁴INEB-Instituto de Engenharia Biomédica, Universidade do Porto, Porto, Portugal

⁵Biomedical Research in Digestive Tract Tumors, CIBBIM-Nanomedicine, Vall d'Hebron Institut de Recerca, Universitat Autònoma de Barcelona, Barcelona, Spain

⁶Immune Regulation and Immunotherapy, CIBBIM-Nanomedicine, Vall d'Hebron Institut de Recerca, Universitat Autònoma de Barcelona, Barcelona, Spain

⁷Functional Validation and Preclinical Research (FVPR), CIBBIM-Nanomedicine, Vall d'Hebron Institut de Recerca, Universitat Autònoma de Barcelona, Barcelona, Spain

Correspondence should be addressed to Simó Schwartz Jr.; simo.schwartz@vhir.org

Received 29 June 2018; Accepted 17 August 2018; Published 10 October 2018

Academic Editor: Roberta Fusco

Copyright © 2018 Petra Gener et al. This is an open access article distributed under the Creative Commons Attribution License, which permits unrestricted use, distribution, and reproduction in any medium, provided the original work is properly cited.

There are remarkable similarities in the description of cancer stem cells (CSCs) and cancer cells with mesenchymal phenotype. Both cell types are highly tumorigenic, resistant against common anticancer treatment, and thought to cause metastatic growth. Moreover, cancer cells are able to switch between CSC and non-CSC phenotypes and vice versa, to ensure the necessary balance within the tumor. Likewise, cancer cells can switch between epithelial and mesenchymal phenotypes via well-described transition (EMT/MET) that is thought to be crucial for tumor propagation. In this review, we discuss whether, and to which extent, the CSCs and mesenchymal cancer cells are overlapping phenomena in terms of mechanisms, origin, and implication for cancer treatment. As well, we describe the dynamism of both phenotypes and involvement of the tumor microenvironment in CSC reversion and in EMT.

1. Differences and Similarities of Mesenchymal and Stem-Like Phenotypes of Cancer Cells

Our understanding of cancer biology and genetics has changed sustainably over the past 10 years. We consider tumor to be a highly complex heterogenic dynamic entity that evolves in time, always trying to adapt and survive to adverse conditions. For example, in order to survive to multimodal therapy, which includes resection, chemotherapy,

and radiation, tumor cells undergo dynamic clonal evolution. As a result, tumors become a mass of highly heterogeneous cell populations undergoing constant dynamic phenotypic changes [1]. In addition, somatic mutations and phenotypic variations might generate cancer cell clones that develop resistance to treatment and remain progressing while current treatment eliminates only sensitive clones. In fact, a tumor may initially shrink after multimodal treatment, while remaining resistant clones which will survive

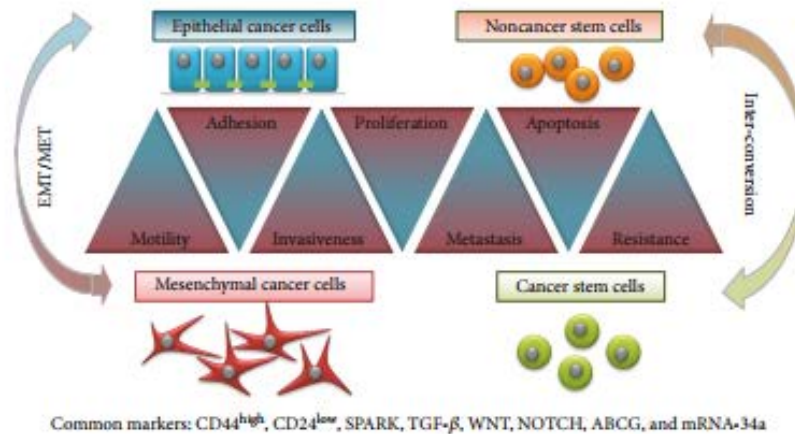


FIGURE 1: Cancer stem cells versus mesenchymal cancer cells. There are remarkable similarities in the properties of CSCs and cancer cells with mesenchymal phenotype, which oppose from characteristics of non-CSCs and epithelial cancer cells, respectively. Both are highly invasive, tumorigenic, resistant against common anticancer treatment, and thought to cause metastatic growth. Both cell types share several cell markers. Besides, both phenotypes are reversible and can be interchanged via EMT or CSC phenotype interconversion.

and eventually cause tumor regrowth and relapse, often rising very aggressive tumor types with unfortunately very limited treatment alternatives [2, 3].

Notably, tumors from patients with recurrent resistant tumors show higher numbers of CSCs and cells with epithelial-mesenchymal transition (EMT) phenotype. Indeed, poor survival has been associated with the presence of both cell types in various clinical trials [4].

CSCs represent a fraction of undifferentiated cancer cells that exhibit stem cell-like features. They have the ability to differentiate and to self-renew. Owing to the phenotypic differences with the rest of tumoral cells, CSCs account for therapy resistance and represent the cellular reserve responsible for tumor regrowth and metastatic spread [5]. CSCs overexpress ATP-dependent drug efflux transporters like P-glycoprotein (P-gp), the multidrug resistance-associated proteins (MRP), and ATP-binding cassette (ABC) transporters at the cell surface, which decrease intracellular drug accumulation. Besides, detoxifying enzymes like aldehyde dehydrogenase 1 (ALDH1A1) and bleomycin hydrolase (BLMH) provide CSCs with further protection against chemotherapy. CSCs are able to enter to a stable quiescence state in hypoxic conditions, overpass the stress condition, and proliferate afterwards [5]. In the last years, many research groups employed big efforts in order to identify biomarkers which could specifically characterize the different subpopulations of CSCs within a tumor [6]. Interestingly, most of the identified CSC markers can be also found in cells with mesenchymal phenotype (CD44⁺/CD24⁻, SPARK, WNT, NOTCH, ABCG, mRNA-34a, etc.). Moreover, the characterization of cancer cells, which have acquired mesenchymal features by EMT, is quite similar to the description of CSCs (Figure 1). EMT cells are essential for tumor progression, including tumor metastasis, therapy resistance, and disease recurrence. A majority of tumors (90%) are epithelial in nature (carcinomas); therefore, the activation of an EMT program, which originally plays a crucial role in organogenesis during

embryonic development as well as wound healing and tissue regeneration, can transform epithelial cancer cells into a more aggressive mesenchymal phenotype, promoting local invasion and dissemination at distant organs [7].

During EMT, epithelial cells lose their cell-cell adhesion and apical-basal polarity, gaining the ability to individually migrate and invade basement membrane and blood vessels [7]. This conversion correlates with a decrease in epithelial markers (E-cadherin, cytokeratin, integrin $\alpha 6 \beta 4$, laminins, collagen type IV, ZD-1, etc.) and an increase in mesenchymal markers (N-cadherin, vimentin, fibronectin, cadherin-11, integrin $\alpha 5 \beta 1$, collagen types I and III, etc.) [8–11]. Interestingly, several recent studies pointed out an increase in CSC signature during EMT processes in many carcinomas such as pancreatic, hepatocellular, and colorectal as well as in human mammary epithelial cells [12–15] (Figure 2).

Even though in the past CSCs and EMT were studied independently, accumulating evidence suggests strong parallels between EMT activation and CSC formation. EMT is relevant to the acquisition and maintenance of stem cell-like characteristics and is sufficient to endow differentiated normal and cancer cells with stem cell properties. Recently, proteasome activator subunit 3 (PSME3) has been shown to induce epithelial-mesenchymal transition of breast cancer cells together with induction of CSC marker expression and further to influence the tumor immune microenvironment [16]. Moreover, CSCs often exhibit mesenchymal properties within epithelial tumor cells [6, 7, 15, 17–20]. Most likely, heterogeneous cancer cell subpopulations, including CSCs and cells with activated EMT signaling, function in a complementary manner at the collective level to achieve therapeutic resistance and ensure disease progression. The idea of tumors as a highly dynamic heterogeneous mass of cells with an unstable and reversible hierarchy, which seems to be influenced by the origin and biological context of each tumor, is gaining acceptance. According to this scenario, a new concept of tumor plasticity, an “EMT score,” has been proposed

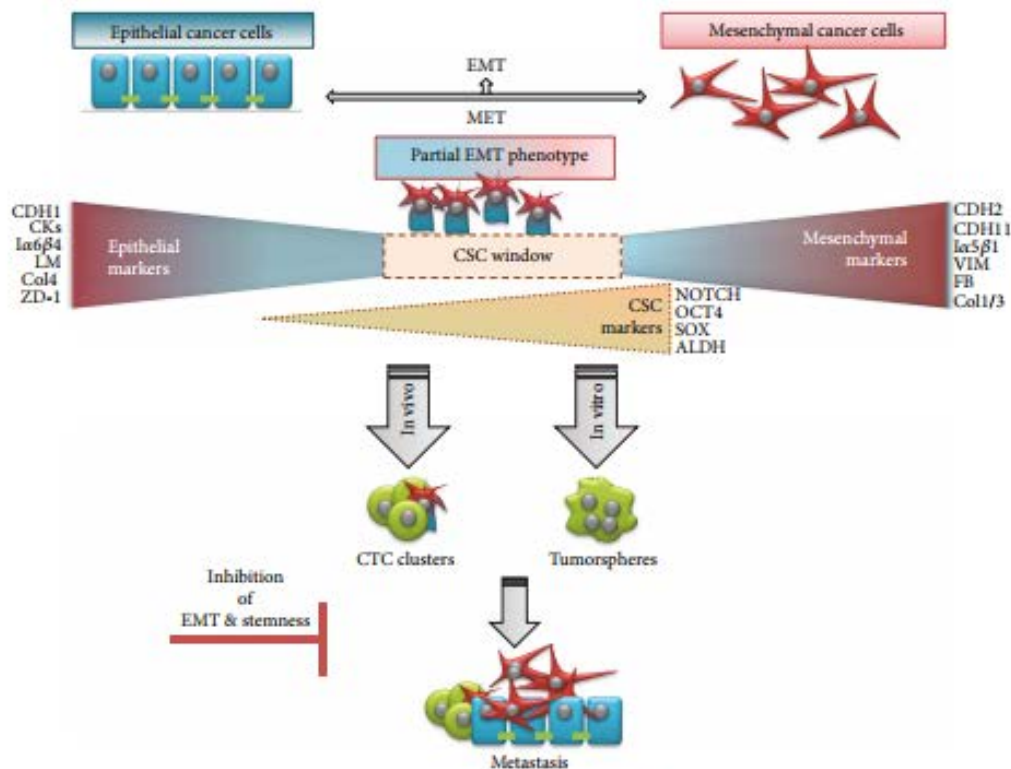


FIGURE 2: E/M hybrid phenotype. E/M hybrid phenotype of tumor cells represents an ideal window for *stemness* reversion. In this state, cancer cells coexpress epithelial and mesenchymal genes and promote expression of *stemness* genes. This results in formation of a tumor sphere *in vitro* and metastatic spread *in vivo*. Also, a majority of circulating cancer cell (CTC) clusters coexpress epithelial and mesenchymal markers together with stem cell markers. An inhibition of EMT and/or *stemness* phenotype should lead to hindrance of advanced cancer.

to represent the EMT-grade characteristic of each cell line and primary tumor [14, 21]. Tan and colleagues established a universal and quantitative EMT scoring to define an EMT spectrum across various cancers (ovarian, breast, bladder, lung, colorectal, and gastric cancers) [14, 21]. Tumor-specific gene expression was used to establish an EMT scoring method and quantitatively estimated the degree of EMT (−1.0 to +1.0) in a large collection of cell lines and tumors, reflecting epithelial and mesenchymal states as well as the intermediate states that occur during transition. Good correlation between EMT and poorer disease-free survival was observed in ovarian and colorectal cancers, but not in breast cancer or carcinomas. Importantly, a distinct response between epithelial and mesenchymal-like ovarian cancers to therapeutic regimes administered with or without paclitaxel *in vivo* was also observed [14, 21].

Of note, the observed intermediate, mixed epithelial and mesenchymal phenotype (E/M hybrid phenotype), is thought to represent the ideal window for *stemness* reversion [18, 22, 23] (Figure 2). This theory is supported by the fact that repression of EMT is required for effective tumor initiation [24–27] and that CSC reprogramming often involves mesenchymal to epithelial transition (MET) [28, 29].

Further, coexpression of epithelial and mesenchymal genes promotes mammosphere formation and expression of *stemness* genes [22] and drives tumor growth *in vivo* [18, 23]. Besides, according to mathematical models of *stemness*-decision circuits, it has been suggested that a hybrid E/M state is more likely to gain *stemness* than complete EMT is [14, 30]. These observations are consistent with experiments showing that a majority of circulating cancer cells (CTCs) coexpress epithelial and mesenchymal markers together with stem cell markers [31]. CTCs in a semimesenchymal phenotype have higher proliferative and invasive abilities than cells with complete EMT phenotype and are able to originate distant metastasis [32, 33] (Figure 2). The association of a hybrid E/M phenotype with *stemness* is not specific to tumor progression but has been also reported in physiological conditions in adult hepatic stem/progenitor cells (HSCs) and adult renal progenitors upon tissue injury and show to mediate tissue repair and regeneration [34–36].

2. Dynamic Cancer Cell Phenotype

There is increasing evidence showing that some cell subpopulations are subjected to a dynamic phenotype within a

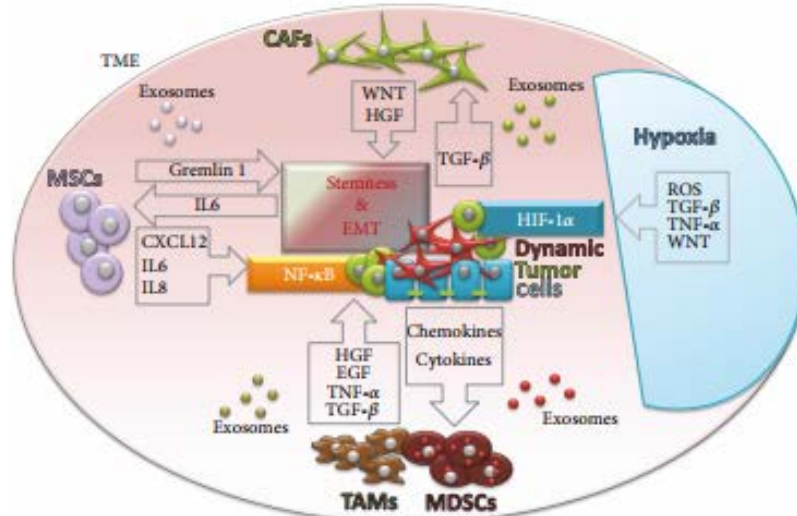


FIGURE 3: Tumor microenvironment and cancer cell phenotype. Schematic representation of TME influence on *stemness* and mesenchymal properties of cancer cells. The dynamic phenotype of cancer cells (*stemness*, EMT) is regulated by several signaling pathways. TGF- β and NF- κ B signaling pathways are activated by different microenvironmental factors like MSCs, CAFs, TAMs, MDSCs, or hypoxia. Exosomes derived from respective cell types play an important role in intercellular paracrine communication.

tumor. Although the importance of the differentiation state of tumor cells on their malignant capacity has been reported since the 80s, the study of the underlying mechanism controlling these cellular states has been neglected until recently [37]. Currently, the most studied phenomenon of cellular differentiation/dedifferentiation processes undergone by tumor cells with influence in cancer progression is transition from epithelial to mesenchymal phenotype and their counter pathway mesenchymal to epithelial transition. Both phenomena have been reported in several cancer types including colorectal cancer, breast cancer, prostate cancer, pancreatic cancer, bladder cancer, and lung cancer, among others. EMT cellular conversion has been extensively studied during the last decade. In this regard, three main molecular pathways leading and regulating this process have been proposed: (a) SMAD/TGF- β pathway, (b) WNT/ β -catenin signaling, and (c) ECM integrin signaling cascade. In any case, these diverse EMT routes render upregulation of specific sets of transcription factors, including SNAIL, SLUG, ZEB, and TWIST, that would further control the cellular conversion process [20, 38, 39].

CSCs and non-CSC populations have also been proved able to interconvert each other depending on external stimuli, namely, factors coming from the microenvironment or in response to treatment. Some examples of differentiated cells undergoing this reversion process to become CSCs, or cells in an intermediate state showing stem-like properties, have been reported for colorectal cancer, breast cancer, and melanoma, among others [17, 40–42]. Interestingly, two of the EMT pathways (SMAD/TGF- β and WNT/ β -CATENIN) have been associated also with the acquisition of stem-like properties [13].

Moreover, another important common activator of CSC reversion and EMT is hypoxia (Figure 3). Hypoxia induces the overexpression of OCT4 that in turns triggers a molecular cascade leading to enrichment of cells with CSC-like phenotype in melanoma [43]. Hypoxic condition also induces the overexpression of hypoxia-inducible factors (HIFs), which can directly induce EMT in various cancer models, mostly conducted by the HIF-1 α factor (Figure 3) [44, 45]. Importantly, HIF-1 α can directly increase NOTCH signaling, enhancing *stemness* [46]. Hypoxia also promotes CSC survival and EMT through reactive oxygen species- (ROS-) activated stress response pathways and through ROS-induced TGF- β and TNF- α signaling pathways, in breast cancer (Figure 3) [47]. In glioma cells, the activation of TGF- β as well as WNT signaling pathways by hypoxia induces *stemness* by promoting an undifferentiated cellular state [48]. Furthermore, hypoxia seems sufficient to promote CSC phenotype and invasion and accelerate metastatic outgrowth in liver tumor cells after surgery. In addition, transcription factors recognized as pluripotency markers in embryonic stem cells such as NANOG, SOX2, and c-MYC have been reported to be upregulated in the acquirement of the CSC profile [49].

Despite some scraps of evidence from distinct tumor types showing the acquirement of *stemness* properties by differentiated cells in specific conditions, the general process by which differentiated tumor cells undergo a dedifferentiation process is still far from being completely elucidated. However, what seems clear is that the dynamism described for CSCs is analogous to the dynamism observed for EMT processes. Despite that signals and subsequent pathways triggering both processes are not necessarily shared, the

acquisition of CSC phenotype and EMT partially overlaps, which goes in line with partial EMT phenotype and the CSC window theory discussed before (Figure 2). Nonetheless, the fact that signaling cascades for both processes differ by enhancing the expression of distinct subsets of transcription factors is remarkable. Therefore, although in some cases EMT and non-CSC to CSC reversion produce similar responses related with an increased malignancy of the disease, they should be considered distinct processes, both highly dependent on the cancer type.

3. Tumor Microenvironment and Cancer Cell Phenotype

Another important modulator of the phenotypic plasticity of cancer cells may come from the tumor microenvironment (TME), also called tumor niche (Figure 3). TME is composed of a complex network of stromal, immune, and inflammatory cells; soluble factors; signaling molecules; and the extracellular matrix [50]. Both cellular and noncellular components of the tumor niche contribute to maintaining the *stemness* of tumor cells and regulating EMT/MET and CSC plasticity [45, 51, 52].

The most abundant cell population within TME are fibroblasts [53]. Solid evidences show that cancer cells are capable of producing factors, like TGF- β , that once secreted to the TME can transform normal fibroblasts into cancer-associated fibroblasts (CAFs) [54]. CAFs have a battery of unique features when compared with normal fibroblasts that promote cancer progression [55]. It has been demonstrated that TGF- β is carried to the tumor stroma by cancer cells, enhancing CAF phenotype. Once activated, CAFs promote tumor cell progression by multiple mechanisms, in a bidirectional crosstalk between CAFs and tumor cells [56]. One of the most important players in cell-to-cell communication in the TME are exosomes [57]. Exosomes are specialized membranous nanosized vesicles (30–150 nm) derived from endocytic compartments that are released by many cell types. They contain sophisticated RNA and protein cargos from the cell of origin, enabling intercellular communication [58]. Exosomes released by activated CAFs have been associated with the promotion of EMT, *stemness*, and angiogenesis in prostate tumors [59–61]. Special relevance has been attributed to the WNT pathway, a crucial signaling cascade for these processes. The upregulation of WNT10b in CAF exosomes induces EMT of breast cancer cells [62]. A study with endometrial cancer cells has also demonstrated that upregulation of WNT10b in CAFs results in increased migration and aggressiveness of tumor cells [63]. Besides, in lung cancer models, CAFs obtained from lung cancer tissue produce hepatocyte growth factor (HGF), thereby activating the EMT-related c-Met pathway (Figure 3) [64].

Moreover, TME also contains mesenchymal stem cells (MSCs) that are considered key regulators of tumoral physiology through multiple mechanisms [65–67]. These multipotent stromal cells are implicated in the restoration of CSCs in the TME. Similar to CAFs, MSCs can promote cancer *stemness* and EMT phenotype also through TGF- β [68]. Moreover, MSCs can stimulate tumor progression by producing

Gremlin 1 to promote the undifferentiated state of cancer cells [69]. Furthermore, MSCs can provide tumor cells with CSCs properties by suppressing FOXP2 expression [70]. Exosomes released by MSC cells are important for communication of MSCs with TME, although further studies are needed to better elucidate completely their role (Figure 3). Another area of great interest is the influence of the TME in modulating tumoral immunity [68]. Accumulating data is pointing out that tumor-polarized immune cells resident in the TME enhance EMT phenotype and ultimately promote migration and invasion of CSCs [71].

The TME is characterized by chronic inflammation which leads to a phenomenon called immunosuppression in the tumor niche that stimulates tumor cell proliferation and metastasis. Tumor-associated macrophages (TAMs) and myeloid-derived suppressor cells (MDSCs) are an example of immunosuppressive cell types recruited by chemokines and cytokines that are secreted by cancer cells. TAMs are derived from polarized macrophages that acquire protumor phenotypes that enhance tumor growth and metastasis [72]. Similarly to previous examples, tumor-derived exosomes have been shown to play a key role in macrophage polarization. Within inflammatory TME, TAMs and CD4⁺ T cells secrete TNF- α which upregulates NF- κ B signaling, induce EMT, and increase the crosstalk with the TGF- β signaling pathway, stimulating *stemness* [71]. In agreement to this, gastric cancer-derived exosomes have been shown to induce NF- κ B activation in macrophages promoting the proliferation of gastric cancer cells. Similar results show that breast cancer-derived exosomes also stimulate the NF- κ B pathway in macrophages [73]. On the other hand, MDSCs are a heterogeneous population of cells from monocytic and granulocytic origins, which are also involved in promoting EMT and in CSC maintenance [74]. Indeed, in a spontaneous murine model of melanoma, MDSCs induce EMT via TGF- β , EGF, and HGF signaling [75]. Similarly, platelet-derived TGF- β secreted by MDSCs activates TGF- β /Smad and NF- κ B pathways in lung cancer cells, resulting in EMT and enhanced metastasis *in vivo*, in lung cancer models [76, 77].

4. Implication of Cancer Cell Phenotypes in Anti-Tumoral Treatment Strategies

Understanding the tight relationship among CSCs, EMT, and the tumoral microenvironment opens the door to new strategies for developing more effective anticancer treatments.

Because many CSC-related pathways are involved also in EMT, new treatments should eliminate CSCs while reverting the EMT phenotype and vice versa. For example, in order to target EMT, different strategies have been reported, usually targeting (i) adhesion-related proteins (e.g., E-cadherin), (ii) microenvironment factors (e.g., SPARC), (iii) cell membrane molecules (e.g., integrins, TGF- β), (iv) intracellular transcription factors (e.g., ZEB, SNAIL, SLUG, TWIST, and E47), (v) microRNAs (e.g., miRNA200, miRNA29), and a wide range of other possibilities [78]. On the other hand, the elimination of CSCs is pursued through different

TABLE 1: Different cancer therapeutic approaches based on CSCs and/or EMT.

CSC	EMT	Therapeutic target	Therapeutic approach	Cancer type	Development stage	References
x	x	AKT/mTOR signaling pathway	Tunicamycin	Colon cancer	Preclinical (<i>in vivo</i>)	[87]
x	x	AKT2	siRNA	Breast cancer	Preclinical (<i>in vivo</i>)	[79]
x		ALOX5	Zileuton	Leukemia	Clinical (phase 1)	*NCT02047149 *NCT01130688
x		Bmi-1	Nigericin	Nasopharyngeal carcinoma	Preclinical (<i>in vivo</i>)	[88]
x		Bmi-1	shRNA	Nasopharyngeal carcinoma	Preclinical (<i>in vivo</i>)	[89]
	x	EGR-1	shRNA against EGR-1	Breast cancer	Preclinical (<i>in vitro</i>)	[90]
	x	EGR-1	Oxytocin	Lung cancer	Preclinical (<i>in vitro</i>)	[91]
	x	EGR-1	Syntactic catalytic DNA	Liver cancer	Preclinical (<i>in vitro</i>)	[92]
	x	EGR-1	2'-Benzoyloxyctinamide hydrolyde	HNSCC	Preclinical (<i>in vivo</i>)	[93]
	x	EGR-1	siRNA	Breast cancer	Preclinical (<i>in vivo</i>)	[93]
		Hedgehog signaling	Cyclopamine	Colon cancer	Preclinical (<i>in vivo</i>)	[94]
	x	HMG2	LBI589	Glioblastoma	Preclinical (<i>in vivo</i>)	[95]
	x	IAP family	AT-406, SM-164, and TRAIL	Prostate cancer	Preclinical (<i>in vivo</i>)	[96]
	x	IAP I2	Ruxolitinib	Nasopharyngeal carcinoma	Preclinical (<i>in vivo</i>)	[19, 97]
	x	Krüppel-like factor 5	Metformin	Pancreatic cancer	Preclinical (<i>in vivo</i>)	[98]
	x	Lysine-specific demethylase 1	Pargyline	Ovarian cancer	Preclinical (<i>in vivo</i>)	[99]
	x	mTOR	Rapamycin	TNBC	Preclinical (<i>in vivo</i>)	[100]
		n.d.	Metformin	Prostate cancer	Preclinical (<i>in vivo</i>)	[101-103]
		n.d.	Salinomycin	Gastric cancer	Preclinical (<i>in vivo</i>)	[101-103]
		n.d.	Salinomycin analogs	Breast cancer	Preclinical (<i>in vitro</i>)	[86]
		n.d.	EpCAM/CD3 antibody	Colon cancer	Preclinical (<i>in vitro</i>)	[104]
		n.d.	Anti-CD33 antibody	Pancreatic cancer	Preclinical (<i>in vivo</i>)	[105]
		n.d.	Quecetin	Glioblastoma	Preclinical (<i>in vivo</i>)	[106]
		n.d.	All-trans retinoic acid	Pancreatic cancer	Preclinical (<i>in vivo</i>)	[107]
		n.d.	Mithramycin	Gastric cancer	Preclinical (<i>in vivo</i>)	[108]
		n.d.	Drug combination	Various neoplasms	Clinical (phase 2)	*NCT02859415
		n.d.	Epirubicin + cisplatin + capecitabine	Glioblastoma	Clinical (phase 1)	*NCT02654964
		n.d.	DECA-14	Gastric cancer	Clinical (phase 3)	*NCT01697072
		n.d.	shRNA	Neuroblastoma	Preclinical (<i>in vivo</i>)	[100]
		NADH dehydrogenase			Preclinical (<i>in vivo</i>)	[80-82, 109]
		Nestin				

TABLE 1: Continued.

CSC	EMT	Therapeutic target	Therapeutic approach	Cancer type	Development stage	References
x	x	Nestin	siRNA	Glioblastoma	Preclinical (<i>in vivo</i>)	[84, 110]
x	x	p53 mutant cells	Metformin	Lung carcinoma Pancreatic cancer	Clinical (phase 2)	*NCT01579812 *NCT02978547
x	x	PI3K-AKT; ERK1/2 pathways	LY294002; U0126	Ovarian cancer FTFPG, pancreatic cancer	Preclinical (<i>in vitro</i>)	[111]
x	x	SNAIL	Trichostatin A	Breast cancer	Preclinical (<i>in vitro</i>)	[112, 113]
x	x	Snail-p53 interaction	GN-25; GN-29	Lung cancer	Preclinical (<i>in vivo</i>)	[114]
x	x	STAT3	LLL12; shRNA	Pancreatic cancer	Preclinical (<i>in vivo</i>)	[115]
x	x	STAT3	BB1608	Breast cancer	Preclinical (<i>in vivo</i>)	[116]
x	x	STAT3	Salinomycin	Various cancers	Preclinical (<i>in vitro</i>)	[85]
x	x	STAT3 pathway	Oncostatin M	Breast cancer	Preclinical (<i>in vitro</i>)	[117]
x	x	WNT pathway	Nigericin	Hepatocellular carcinoma	Preclinical (<i>in vivo</i>)	[118]
x	x	ZEB1	shRNA	Lung cancer	Preclinical (<i>in vitro</i>)	[19]
x	x			Pancreatic cancer	Preclinical (<i>in vivo</i>)	[19]

n.d.: not described. *ClinicalTrials.gov identifier. Abbreviations: HNSCC: head and neck squamous cell carcinoma; FTFPG: fallopian tube; primary peritoneal cancer.

therapeutic strategies involving signaling pathways related with (i) CSC survival and proliferation pathways (e.g., PI3K-AKT, JAK/STAT, and NF- κ B) and (ii) signals linked to the *stemness* properties of CSCs, like self-renewal and pluripotency (e.g., Notch pathway, WNT pathway, and Hedgehog signaling) [5]. However, the molecular pathways studied as potential EMT targets are also involved in CSCs *stemness*, and the ones studied as CSC pathways are usually representative of EMT. Studies characterizing the effect of specific molecular players on the regulation of both CSC malignancy and EMT occurrence are still scarce. As an example, the PI3K-AKT pathway regulates the expression of TWIST, one of the most important transcription factors regulating EMT; however, the same pathway is also reported as crucial for *stemness* properties and CSCs survival [79].

As referred, CSCs and EMT cells partially share signaling pathways of EMT and *stemness* and since CSCs could undergo EMT, it is virtually impossible to characterize a therapeutic target or approach as CSC- or EMT-specific. Moreover, many studies regarding treatments directed against CSCs do not assess the therapeutic effect on EMT and vice versa, making more difficult to comprehend the interactive effects between both phenomena.

An example is Nestin, a class VI intermediate filament protein involved in mitosis. It was originally described as a neural stem cell/progenitor cell marker. However, expression of Nestin has been reported to be associated with migration and metastasis of various types of tumors and as a CSC marker [80–83]. Transfection of the tumor cancer cell line PANC-1 with a short hairpin RNA (shRNA) targeting NESTIN results in decreased NESTIN expression, increased expression of filamentous F-actin and E-cadherin, reduction of cell migration and invasion abilities, and less formation of metastasis *in vivo*, demonstrating its involvement in EMT [80]. Additionally, NESTIN and CSC markers like ALDH1A1 and ABCG2 are found overexpressed in metastasis-derived cancer cells presenting low levels of E-cadherin. NESTIN silencing in pancreatic cancer results in reduced sphere formation, tumor growth, and metastasis development, not only suggesting the correlation between the CSC-like phenotype and EMT but also validating NESTIN as a therapeutic target [84].

The effects of a drug in CSCs and also in the EMT process are dependent on the cell and cancer type. In triple-negative breast cancer (TNBC), salinomycin was described to cause marked suppression of cell migration and invasion as well as inhibition of mammosphere formation and effective reduction of the CD44⁺/CD24⁻ stem-like/mesenchymal subpopulation [85]. On the other hand, in case of head and neck squamous cell carcinoma, salinomycin treatment induces apoptosis and decrease in stem cell properties, despite the activation of EMT via AKT [86]. These observed differences between studies and cancer type could be explained by the previously referred *stemness* window theory (Figure 2).

The best strategy to prevent tumor remission should be the elimination of all kinds of aggressive cells within the tumor together with the bulk tumor cells since these cells have interconversion capacity and could originate new clones of CSCs or mesenchymal cell via the EMT process. Therefore,

the ultimate goal for the cancer treatment field is to find the way to reach all types of cancer cells. This could be achieved by treatment protocols implying combination of various therapeutic molecules, a combination of gene therapy approaches, or the use of targeted vectors decorated with the most specific ligands found for each type of cell.

Nowadays, different therapeutic approaches have been proposed to target CSCs and/or EMT, ongoing different development stages (Table 1). Since this therapeutic approach is still in its infancy, the majority of present studies are at the preclinical phase, with a small percentage enrolling clinical evaluation. More examples of treatments under clinical trials against CSCs and/or EMT can be found at [5].

5. Summary

The *stemness* of CSCs, non-CSC reversion to CSCs, and EMT processes are regulated by similar signaling pathways. Provided data show that when TGF- β and NF- κ B signaling cascade is activated by different microenvironmental factors, cancer cells from various cancer types tend to undergo EMT, and this is frequently accompanied by a maintenance of a CSC stem phenotype. Based on this knowledge, strategies to prevent tumor remission should carefully consider not only eliminating potential aggressive CSCs and EMT cells within the tumor but also targeting those signaling pathways responsible for the interconversion capacity of non-CSCs to new CSCs and mesenchymal cells via EMT activation. This can be undergone through a combination of molecules, a combination of gene therapy approaches, or the use of targeted vectors decorated with the most specific ligands found for each cell type.

Abbreviations

TME: Tumor microenvironment
 CAFs: Cancer-associated fibroblasts
 MSCs: Mesenchymal stem cells
 TAMs: Tumor-associated macrophages
 MDSCs: Myeloid-derived suppressor cells.

Conflicts of Interest

No potential conflict of interest was reported by the authors.

Acknowledgments

This work was partially supported by grants PI14/02079 and PI17/02242 from Fondo de Investigaciones Sanitarias (FIS) of Instituto Carlos III (ISCIII), cofinanced by the European Regional Development Fund (FEDER), and grant AC15/00092 (Target4Cancer project) from EuroNanoMed II to SS and grant 337/C/2013 (PENTRI project) from Fundació Marató TV3 (Catalonia, Spain) to IA. The Portuguese Science and Technology Foundation (FCT) supported FA with a postdoctoral grant (SFRH/BD/76270/2011). La Asociación Española Contra el Cáncer (AECC) supported

